The Application of Transpiration Cooling as a Thermal Protection System for Hypersonic Vehicles

Imran Naved

St John's College

University of Oxford

A thesis submitted for the degree of

Doctor of Philosophy

Hilary 2022

In the name of God
the Most Gracious, the Most Merciful

Acknowledgements

And so, at last, it ends - after almost four and a half years! As I write these final words, I am deeply thankful to those who have supported me on this journey.

First of all, I am grateful to Matthew McGilvray, my supervisor, for guiding me through this PhD. Thank you for conceiving the project and for your continual support, encouragement, and guidance over these past four years. Thank you for all the long weekend shifts in the HDT during the pandemic, for the long discussions into the night about analytical correlations, and mainly for helping me see the bigger picture when I was stuck in the details.

Thank you also to Tobias Hermann, my co-supervisor. Your feedback at every stage of the project has been invaluable. I really enjoyed our chats at the beginning of the PhD when we worked together on the systems level studies. Thank you for always being available to read or discuss any part of my work.

Thank you also to Chris Hambidge for operating the facilities, without which I would have never been able to complete the experiments that comprised a significant part of this undertaking. Thank you for instilling a keen sense of stresses and material limits; lessons painfully learnt from the 'death wedge'. Thank you also to Luke for teaching me how to correctly produce engineering drawings and showing me the value of diligence and taking one's time to do it properly. To Laurent, thank you for all your help at the beginning when started cobbling together the infrared setup. For always being there to listen and for your support at a challenging time during the pandemic.

Gratitude is extended to the entire Hypersonics group; I have really enjoyed my four years as part of this group. First of all, to Marc, I remember very well the first day that we started together. For all the trips to the Business School and Benito's, and for your help characterising those porous samples. To Hassan, for your smile and eagerness to help with any problem - I don't think I have ever come across a harder worker! To Mailys for running the tunnel and always being ready for 'one more shot'. To Rowland for sharing your wealth of knowledge on all things heat transfer - sometimes I feel you actually enjoy noise hunting.

This work would not have been possible without the staff at the Oxford Thermofluids Institute. Special thanks to Greg and Trevor, who built and instrumented many of my models. To Dave O'Dell, thank you for always advising me on my

designs and pointing me towards what is and isn't possible. To Alex and Anna, for the last minute purchase orders and all your help.

To EPSRC grant 'Transpiration Cooling Systems for Jet Engine Turbines and Hypersonic Flight' (reference: EP/P000878/1) and Reaction Engines for funding my PhD. Particular gratitude to James Barth and Gerrie Mullen for their input and encouragement at the early stages of this work.

To Abdurasheed, Basim and Yousef, for being the best of housemates. For keeping me sane at the height of my experimental testing, even cooking for me when I had no time. A separate thanks to the Oxford Islamic Society for being a home away from home whilst I was at Oxford. I will really cherish my time with such a fantastic community. In no particular order, thank you to Faisal, Taimur, Yunas, Djamshid, Sameer, Muhammad, Yasser, Ezziddin, Hassaan, Zaid, and Younes. A special appreciation to Hazim for proofreading parts of the thesis and providing constructive suggestions.

Finally, to my family. Thank you for encouraging my dreams; I would not have had the courage to start this endeavour without your support. Thank you especially to my parents - I really do believe that it is your prayers which have led me to become the person that I am today. Last, but not least, to Fatima - you have only joined me right at the very end of this journey. Thank you for reading the thesis from back to front (including the appendices!). Your love and support means the world to me, and I am so looking forward to all that we will do together for the rest of our lives.

List of publications

Journal papers

- **I. Naved**, T. Hermann, M. McGilvray (2021), Numerical Simulation of Transpiration Cooling for a High-Speed Vehicle with Substructure., *AIAA Journal*.
- **I. Naved**, T. Hermann, M. Ewenz Rocher, C. Hambidge, L. Doherty, L. Le Page, M. McGilvray, M. Grossman, L. Vandeperre (2022), Heat Transfer Measurements of a Transpiration-Cooled Stagnation Point in Transient Hypersonic Flow., *AIAA Journal of Thermophysics and Heat Transfer*.
- **I. Naved**, T. Hermann, C. Hambidge, C. Falsetti, H.S. Ifti, M. McGilvray, I.S. Tirichenko, L. Vandeperre (2022) Transpiration Cooling Heat Transfer Experiments in Laminar and Turbulent Hypersonic Flows., *AIAA Journal of Thermophysics and Heat Transfer*.
- **I. Naved**, T. Hermann, C. Hambidge, M. McGilvray (2022), Experimental Studies of Hypersonic Shock Impingement on a Transpiration-Cooled Flat Plate., *AIAA Journal of Spacecraft and Rockets*.
- T. Hermann, **I. Naved**, M. McGilvray (2020), Tool for Rapid Transient Transpiration-Cooled Reentry Simulation., *AIAA Journal*.
- T. Hermann, M. McGilvray, **I. Naved** (2020), Performance of Transpiration-Cooled Heat Shields for Reentry Vehicles., *AIAA Journal*.

Conference papers

- **I. Naved**, T. Hermann, C. Hambidge, H.S. Ifti, M. McGilvray, I.S. Tirichenko, L. Vandeperre (2022), Quantifying the Surface Heat Transfer on Transpiration Cooled Porous Materials in Laminar and Turbulent Hypersonic Boundary Layers, *2nd International Conference on High-Speed Vehicle Science & Technology*, Bruges, Belgium.

- **I. Naved**, T. Hermann, M. McGilvray (2019), Numerical simulation of transpiration cooling with a two-dimensional substructure, *International Conference on Flight vehicles, Aerothermodynamics and Re-entry Missions and Engineering*, Monopoli, Italy.

- T. Hermann, **I. Naved**, M. McGilvray (2019), Performance of Transpiration Cooled Heat Shields for Hypersonic Vehicles, *AIAA SciTech Forum*, San Diego, US.

- P.L. Collen, L. Doherty, M. McGilvray, **I. Naved**, R.T. Penty Geraets, T. Hermann, R.G. Morgan, D. Gilfind (2019) Commissioning of the T6 Stalker Tunnel, *AIAA SciTech Forum*, San Diego, US.

Abstract

This thesis investigates the application of transpiration cooling to reduce surface heat transfer on hypersonic vehicles. Such vehicles experience high peak heat fluxes and time-integrated heat loads throughout the ascent, re-entry, and cruise phases. The most significant heat fluxes occur at the stagnation point of sharp leading edges, regions of laminar-turbulent transition, or shock-wave boundary layer interactions. Whilst previous and current hypersonic vehicles employ ablation for many of these regions, such thermal protection systems are neither reusable nor suitable for all scenarios. In this work, the performance of transpiration cooling is assessed for a generic flight vehicle. Subsequently, the application of transpiration cooling to laminar and turbulent flows and shock-wave boundary layer interaction regions is assessed experimentally.

For the first time, the additional benefit of transpiration cooling to the underlying substructure is evaluated numerically. The low fidelity PIRATE code for evaluating transpiration-cooled systems is extended to account for quasi-two-dimensional lateral heat conduction effects, enabling very fast calculations of the two-dimensional transient temperature response of a transpiration-cooled thermal protection system. To solve for the transpiration-cooled outer wall and a two-dimensional solid substructure, PIRATE has been coupled with the commercial finite element package COMSOL, enabling the modelling of the longer-duration thermal effects of the integrated heat load over a flight trajectory. Transpiration cooling using helium coolant has been applied to a wing leading edge with an aluminium substructure. Carbon–carbon ceramic composite and the Ultra-High-Temperature Ceramic (UHTC) zirconium diboride (ZrB_2) were chosen as candidate materials. The substructure temperature history for the Space Shuttle re-entry trajectory was obtained, showing that transpiration cooling can lead to a 35% reduction in peak substructure temperature and a 65% decrease in thermal gradients.

A novel heat transfer measurement method is developed to enable measurements of surface heat transfer in transpiration-cooled porous injectors in short-duration hypersonic facilities. Traditional surface heat flux methods such as discrete thin

film gauges or thermocouples are not suitable for modern micro-porous materials with pore sizes of the order of 10μm. High-speed infrared thermography was employed to measure the surface temperature of the porous material. A bespoke calibration system was developed, and the method was verified experimentally in the Oxford High-Density Tunnel on a flat-faced hemispherical probe, with a porous Alumina injector. Nitrogen, air, argon, krypton, and helium injection gases were used with mass flow rates ranging from 0.01-0.235 kg $s^{-1}m^{-2}$. It was found that the Stanton number reduction matched to within 10% of both CFD results and correlations. The direct measurements provided by this technique enable the acquisition of spatially resolved heat transfer on a porous surface with mass injection.

After the development of the heat transfer measurement technique, this was applied to two different scenarios. The first concerns the need for detailed local heat transfer information on and in the vicinity of the porous injector to design a transpiration-cooled system. In this work, experiments were conducted in the Oxford High-Density Tunnel at Mach 6.1 in both laminar and turbulent regimes. Spatially resolved 2D surface heat transfer measurements were acquired by imaging directly on and downstream of two micro-porous transpiration-cooled injectors (METAPOR CE170 and Zirconia) using high-speed infrared thermography. It was found that a modification to existing relations from film theory successfully correlates the stream-wise heat transfer distribution on the injector for different blowing rates of nitrogen and helium injection at both laminar and turbulent regimes. A key result is that helium performs much better than reported in previous experiments. Finally, the downstream thermal effectiveness is characterised for turbulent flows and an analytical correlation is proposed.

In the final component of this thesis, transpiration cooling is applied to mitigate the peak heat fluxes caused by shock-wave boundary layer interactions. Experiments were again conducted in the Oxford High-Density Tunnel at Mach 6.1 in both laminar and turbulent regimes where a 10° shock generator created a strong oblique shock wave which impinged onto a transpiration-cooled micro-porous injector. For the laminar condition, due to the strength of the incident shock, a laminar-transitional shock-wave-boundary-layer interaction region was formed with peak heating over 50 times greater than the nominal laminar level. Both nitrogen and helium were used as coolants and relatively low injection rates were sufficient to greatly reduce the heat transfer downstream of shock interaction for both regimes. The experimental data are correlated, and both fully turbulent and laminar-transitional cases display a similar trend. Empirical fits are proposed which may be used for initial systems design.

Contents

List of Figures

List of Tables

List of Abbreviations

A	Area, m^2
B_h	Blowing parameter; $\frac{F}{St_0}$
$B*$	Boundary layer blow-off parameter
C^*	Chapman-Rubesin factor at the Eckert reference temperature; $(T_e/T^*)(\mu^*/\mu_e)$
c	Speed of light in a vacuum, 2.99792458 $\mathrm{m\,s^{-1}}$
c_p	Specific heat capacity, $\mathrm{J\,kg^{-1}\,K^{-1}}$
F	Blowing ratio; $(\rho_c u_c)/(\rho_e u_e)$
h	Planck's constant, $\mathrm{m^2\,kg\,s^{-1}}$
h	Specific enthalpy, $\mathrm{J\,kg^{-1}}$
H	Total enthalpy, J
h_v	Volumetric heat transfer coefficient, $\mathrm{W\,m^{-3}\,K^{-1}}$
I	Radiant intensity, $\mathrm{W\,m^{-2}\,sr^{-1}}$
k	Thermal conductivity, $\mathrm{W\,m^{-1}\,K^{-1}}$
k_b	Boltzmann constant, $\mathrm{m^2\,kg\,s^{-2}\,K^{-1}}$
K_D	Darcy coefficient, $\mathrm{m^2}$
K_F	Forchheimer coefficient, m
L	Thickness, m
M	Molecular weight, $\mathrm{g\,mol^{-1}}$
M	Mach number
$\dot{m}_f$	Mass flux, $\mathrm{kg\,s^{-1}\,m^{-2}}$
Nu	Nusselt number
Pr	Prandtl number
$\dot{q}$	Heat flux, $\mathrm{W\,m^{-2}}$

r . . . . . Recovery factor

Re . . . . . Reynolds number

$\mathrm{R_n}$ . . . . . Nose radius, m

s . . . . . Injector width, m

St . . . . . Stanton number

t . . . . . Time, s

T . . . . . Temperature, K

u . . . . . Velocity, $\mathrm{m\,s^{-1}}$

V . . . . . Volume, $\mathrm{m^3}$

W . . . . . Width, m

x . . . . . Distance from the leading edge, m

y . . . . . Lateral distance from the model centreline, m

α . . . . . Absorptivity coefficient

γ . . . . . Ratio of specific heats

δ . . . . . Boundary layer thickness

ε . . . . . Emissivity

η . . . . . Effectiveness, defined by Eq. (5.14)

θ . . . . . Ratio of coefficients with and without mass transfer, defined by Eq. (5.1)

θ . . . . . Angle of emission from the surface normal

λ . . . . . Wavelength, m

μ . . . . . Viscosity, Pa s

ξ . . . . . Correlation parameter, defined by Eq. (5.15)

ρ . . . . . Density, $\mathrm{kg\,m^{-3}}$

α . . . . . Reflectivity coefficient

σ . . . . . Stefan–Boltzmann constant, $\mathrm{W\,m^{-2}K^{-4}}$

τ . . . . . Transmissivity coefficient

ϕ . . . . . Porosity

$\bar{\chi}$ . . . . . Viscous interaction parameter; $\frac{M^3}{\sqrt{Re}}\sqrt{\frac{\rho_w \mu_w}{\rho_e \mu_e}}$

Subscripts and Superscripts

*	Quantities evaluated at Eckert's reference temperature, Eq. (2.13)
0	Uncooled reference
2	Post oblique shock, see Fig. 4.2
3	Post re-compression shock, see Fig. 4.2
atm,ext	External atmosphere
atm,int	Internal atmosphere
aw	Adiabatic wall
bb	Black-body
D	Detector
e	Gas at boundary layer edge
env	External environment
f	Coolant fluid
L	Shock impingement location
obj	Object
pl	Plenum
r	Recovery
wind	Window
wall	Wall
w	Wall
∞	Freestream

Acronyms

C/C	Carbon-carbon
CFD	Computational Fluid Dynamics
CMC	Ceramic Matrix Composite
DNS	Direct Numerical Simulation
HCM	Hypersonic Cruise Missile
HDT	High Density Tunnel
HGV	Hypersonic Glide Vehicle
LEO	Low Earth Orbit

NETD	Noise Equivalent Temperature Difference
PICA	Phenolic-Impregnated Carbon Ablator
PIRATE	Porous Impulse Response Analysis for Transpiration cooling Evaluation
RANS	Reynolds-averaged Navier–Stokes
SEM	Scanning Electron Microscope
SWBLI	Shock-Wave Boundary Layer Interaction
TPS	Thermal Protection System
UHTC	Ultra-High-Temperature-Ceramic

Chapter 1

Introduction

Contents

In February 1949, a V-2 rocket, one of many brought over to the US following the end of World War II, flew at over 5000 mph ($2.2\,\mathrm{km\,s^{-1}}$) - the first time any object of human origin travelled faster than five times the speed of sound [1]. In the following decades, rapid developments in the newly formed field of hypersonics would lead to the first man in space, Yuri Gagarin, in 1961; and finally culminate in the first man to step on the moon, Neil Armstrong, in 1969. The subsequent decades would see continued developments in hypersonics, including the commissioning and regular use of the Space Shuttle and the establishment of the International Space Station.

After several quiet decades from the 1980s to the 2000s, hypersonics is once again experiencing a global resurgence, with interest from both military and civilian applications. In 2020, SpaceX delivered four astronauts to the International Space Station on the Dragon 2 rocket (with the Crew Dragon module); this was the first US developed spacecraft to do so since the retirement of the Space Shuttle, heralding a return of manned space travel to US shores. As a result, NASA awarded

SpaceX a $2.9 billion USD contract to develop a lunar lander by 2024 despite stiff competition from Boeing, Blue Origin and Lockheed Martin [2]. Around the same time, Russia unveiled its new weapon system, Avangard, a hypersonic glide vehicle (HGV) which can travel at speeds of over $3.1\,\mathrm{km\,s^{-1}}$ and is able to reach a target in mainland USA from Russia in under 15 minutes [3]. This has heralded the start of what has been dubbed a "hypersonic arms race" [4]; with the US, Russia and China frantically developing hypersonic weapons capability.

There has been a renewed interest in the development of reusable hypersonic aircraft for intercontinental travel. The German Aerospace Center (DLR) is currently developing Spaceliner, a reusable hypersonic vehicle that can fly from Western Europe to Australia in 90 minutes [5]. Furthermore, for many years, Reaction Engines have been progressing their Skylon spaceplane, which utilises a novel combination of air-breathing and rocket propulsion system [6]. The new generation of hypersonic vehicle concepts requires longer transit times during both ascent and re-entry. In addition, for high-speed passenger transport and affordable low-earth orbit (LEO) access, a rapid turnaround of vehicles is necessary, placing a premium on re-usability for all aspects of the vehicle, including the thermal protection systems. These vehicles would benefit from sharp leading edges to minimise drag and ensure sufficient propulsion. To retain control, these critical aerodynamic elements must be shape-stable. Re-usability and shape-stability are, therefore, some of the key drivers for the next generation of spacecraft.

1.1 Hypersonic Aerodynamic Heating

In 2003, the Space Shuttle Columbia suffered disaster when a piece of the polyurethane foam insulation broke off from the Space Shuttle external tank and struck the reinforced carbon-carbon leading edge of the orbiter's left wing. During re-entry, the damage allowed hot atmospheric gases to penetrate the heat shield and destroy the internal wing structure, causing the spacecraft to become unstable and break apart. After decades of safe Shuttle operation since the Challenger disaster, the failure

of Columbia brought to the fore the incredible heat loads and stresses experienced by spacecraft and the challenges of successfully protecting them.

The hypersonic flight regime is defined by the fact that the physics of the flow is dominated by aerodynamic heating [7]. For this reason, a major goal since the start of aerospace research in the 1930s has been to accurately predict the heating rates and time-integrated heat loads, of vehicles flying at hypersonic speeds, either during atmospheric (re-)entry or sustained flight. As Van Driest [8] puts it

"Two major problems encountered today in aeronautics are the determination of skin friction and skin temperatures of high-speed aircraft"

Atmospheric entries from low-earth orbit are around $7.5\,\mathrm{km\,s^{-1}}$ and the fastest artificial object to enter the Earth's atmosphere was the Stardust sample-return capsule at $12.9\,\mathrm{km\,s^{-1}}$ [9]. Proposed Mars sample return missions are predicted to enter even faster, at 13-15 $\mathrm{km\,s^{-1}}$ [10]. At these velocities, the temperature behind the strong bow-shock, which forms in front of the vehicle, reaches thousands of Kelvins, and peak heating rates to the fore-body of the vehicle can exceed $10\,\mathrm{MW\,m^{-2}}$ - over 5 times that experienced by gas turbine engines. Protection of the crew, cargo, and the vehicle itself from this extreme environment requires robust and reliable thermal protection systems (TPS).

The incoming heat flux is a combination of heating from convection, radiation and surface recombination. They will occur in different proportions depending on the trajectory point and nose radius. Convective heating occurs as energy transfer at the surface of the vehicle due to a temperature gradient. This is given by Fourier's law of conduction as

$$\dot{q_w} = k\left[\frac{\partial T}{\partial y}\right]_w \tag{1.1}$$

where k is the gas thermal conductivity at the wall and $\left[\frac{\partial T}{\partial y}\right]_w$ is the gas temperature gradient at the wall. As the external flow moves past at higher speeds, the flow becomes compressible, and heat is generated by viscous dissipation within the boundary layer. Thus the gas temperature close to the wall rises, reaching the

adiabatic wall temperature, T_{aw}. The adiabatic wall temperature is the temperature the fluid attains for no heat transfer between the fluid and wall and is the amount of the total temperature, T_0, that is recovered close to the wall due to viscous dissipation. Gas radiation, on the other hand, occurs when the temperature of the flowfield around the body is hot enough that significant thermal radiation from the gas to the body takes place. In Earth's atmosphere, radiative heat flux begins to be significant at velocities exceeding 9 $\mathrm{km\,s^{-1}}$ and thus, in this research project, radiative heating is neglected due to the lower speeds considered. At high enthalpies, if dissociated species reach the surface and the material is catalytic, an increasing fraction of the heat transfer will occur through recombination. When two atoms recombine to form a molecule, their dissociation energy is released as heat. This is also commonly referred to as catalytic heating. For wall temperatures below the dissociation temperature (approximately 2000 K), a boundary layer that is in chemical equilibrium will inherently have no atoms existing near the wall. However, if the boundary layer is in chemical non-equilibrium, atoms can significantly exist at wall temperatures below 2000 K. Thus, catalytic heating is more prominent in non-equilibrium boundary layers, which are not the focus of this thesis.

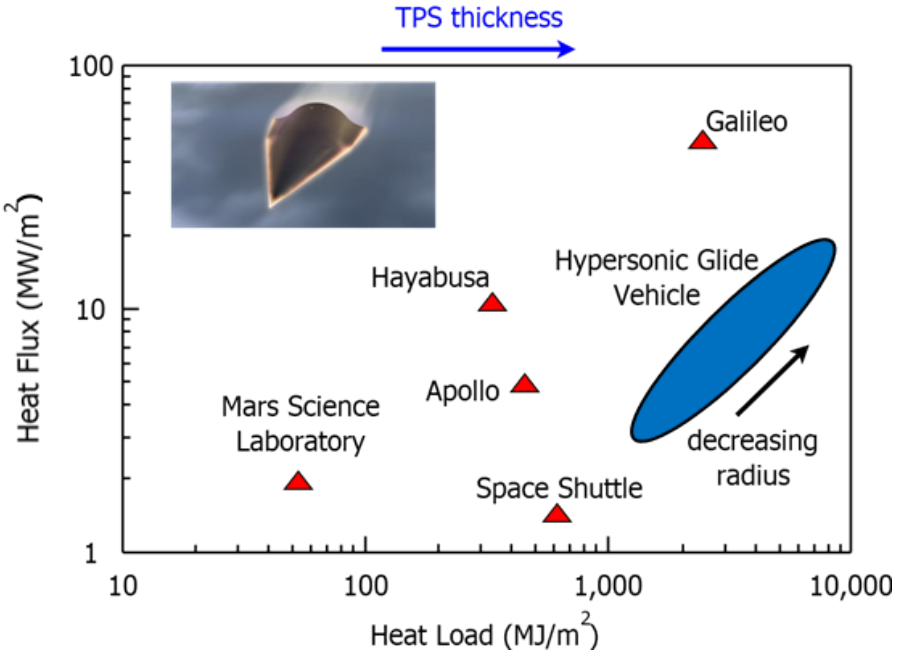

Figure 1.1: Peak heat flux compared to heat load for different hypersonic vehicles.

In addition to the heat flux, another important consideration is overall heat load. This is defined as the time-integrated heat flux over the course of the entire trajectory. Heat load considerations become increasingly important for trajectories that require sustained hypersonic flight in the atmosphere. For aerospace planes (such as the NASP concept and other scramjet vehicles), the ascent trajectory requires the plane to reach close to orbital velocity in the atmosphere. As shown by Tauber et al. [11], these vehicles can reach an order of magnitude higher heat loads than Shuttle re-entry. This is a critical factor for the next generation of Hypersonic Glide Vehicles (HGV) and Hypersonic Cruise Missiles (HCM), all of which require sustained flight at relatively low altitudes to avoid radar detection systems and sharper leading edge radii (Fig 1.1). Any potential TPS system must balance the sometimes contradictory requirement to manage both the peak heat flux and the total heat load. In the following section, two regions in which very high heat fluxes are present, stagnation points and shock-impingement locations, are discussed. However, these are not the only two cases with high heating. Other regimes, such as laminar-turbulent transition regions, also exhibit similar behaviour; however, discussion on those topics is omitted as they are not the focus of this thesis.

1.1.1 Stagnation Point

Typically, the stagnation point is the point of maximum heat flux on a vehicle. This can range from the nose cap of the Space Shuttle, the wing leading edge of a spaceplane, or the inlet of a scramjet. Originally, the convective heat transfer to an axisymmetric stagnation point has been correlated by Fay and Riddell [12] with a mixture of physical and empirical arguments. Since then, Sutton and Graves and others [13–15] developed simpler correlations, assuming chemical equilibrium, to many different atmospheric compositions. For Earth entry, the Sutton-Graves relation with the hot wall correction is

$$\dot{q}_c = 1.7415 \cdot 10^{-4} \cdot \sqrt{\frac{\rho_\infty}{R_N}} \cdot u_\infty^3 \cdot \left(1 - \frac{h_w}{h_\infty}\right) \tag{1.2}$$

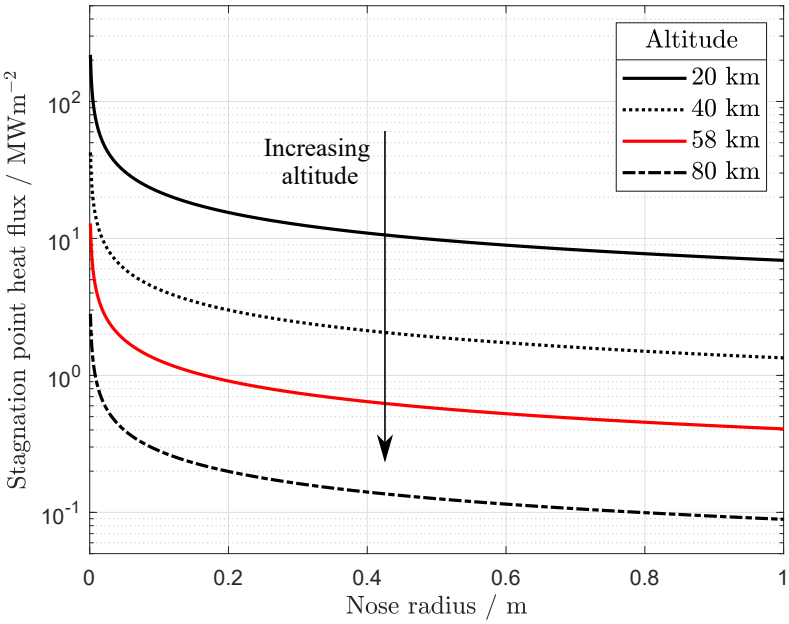

Figure 1.2: Variation of stagnation point heat flux with nose radius at several altitudes. All of the curves are calculated based on a velocity of $5\,\mathrm{km\,s^{-1}}$ with the red line referring to the Space Shuttle peak heating point.

with the freestream density ρ_∞, the freestream velocity v_∞, the nose radius R_N, and the wall and freestream specific enthalpies h_w and h_∞. The axisymmetric stagnation point heat flux may be modified for a 2D wing leading edge by applying the Mangler transform [8]. Figure 1.2 shows the variation in the stagnation point heat flux with nose radius for different altitudes at the stagnation point of a 2D wing leading edge. The heat flux scales with $R^{-0.5}$ and is proportional to the freestream density ρ, i.e. at smaller nose radii; the heat flux increases dramatically. This is more so the case at lower altitudes with increased density. The same is also true for higher velocities where the increased freestream enthalpy leads to higher heat fluxes. The Space Shuttle nose cap had a nose radius of 0.6 m, and this reached a peak heat flux of $600\,\mathrm{kW\,m^{-2}}$. For smaller nose radii, it can be as high as $10\,\mathrm{MW\,m^{-2}}$ [16]. For vehicles with sharp leading edges which require sustained flight at lower altitudes, mitigating the extreme heat fluxes and corresponding wall temperatures is essential.

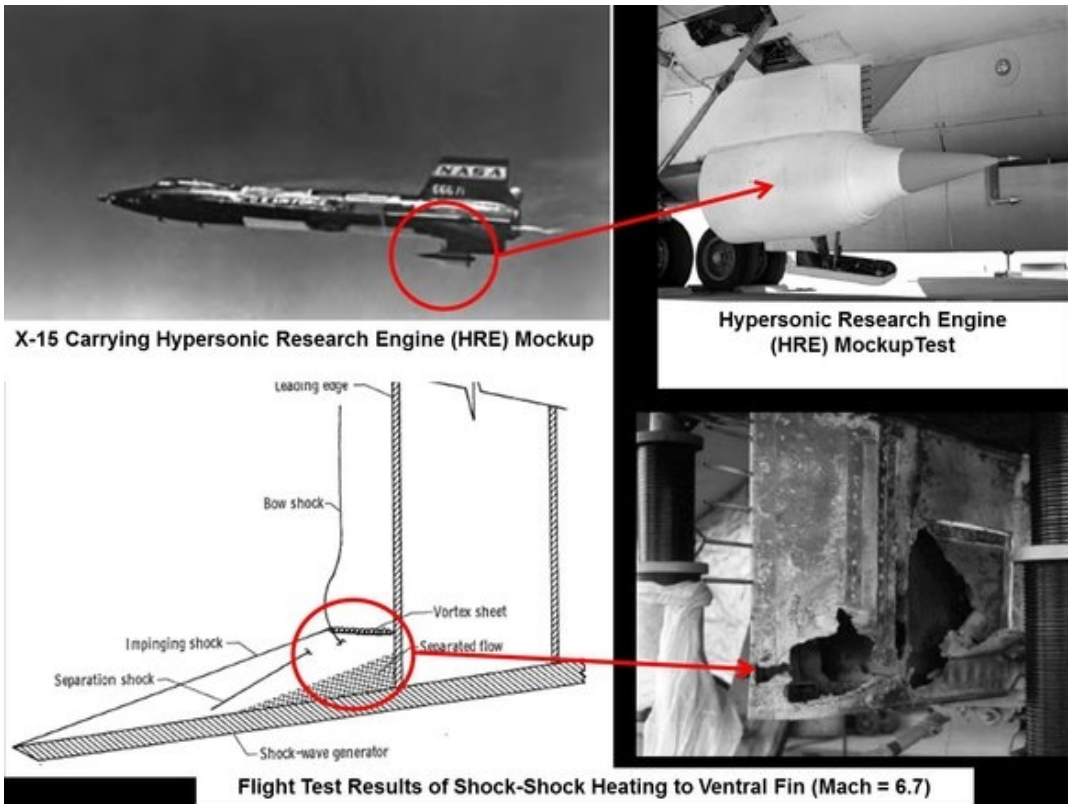

Figure 1.3: Effect of shock-shock interaction heating during X-15A-2 testing of a dummy model of the Hypersonic Research Engine (HRE). Figure from Ref. [17].

1.1.2 Shock-Wave Boundary Layer Interaction Regions

Some of the most serious and challenging problems for the designers of hypersonic vehicles arise due to the severity of the heating loads generated in shock-wave boundary layer interactions. These often take place on deployed control surfaces, at the juncture between vertical fins and the fuselage, and the inlets of hypersonic vehicles [18]. Shock-interaction heating caused the dramatic failure of the pylon support to a ramjet carried beneath the X-15 research vehicle, as illustrated in Fig. 1.3. In addition, the bow shock wave from the pylon, impinging on the bottom surface of the X-15, caused local heating damage. Clearly, from this example, shock-wave-boundary-layer interactions can have serious effects on hypersonic vehicles, and this becomes only more severe at higher Mach numbers. Since transition occurs at very low Reynolds numbers in shock-shock interaction regions, the magnitude of the pressure and heating loads are difficult to predict. The most severe of these

shock-shock interaction types is the Edney Type IV interaction [19], in which the interaction between the two shocks causes a supersonic jet that impinges on the body. The resulting high pressures and heat loads can be over 50 times higher than the undisturbed case. This is of particular concern for modern vehicle designs such as the Skylon spaceplane. As depicted in Fig. 1.4, detailed viscous CFD simulations conducted by DLR showed that shock-shock interaction between the wing and nacelle shock can lead to localised hot spots wherein the surface temperatures can rise well beyond material limits [20]. In the same report, active cooling was proposed as a viable method to reduce the high temperatures in those regions.

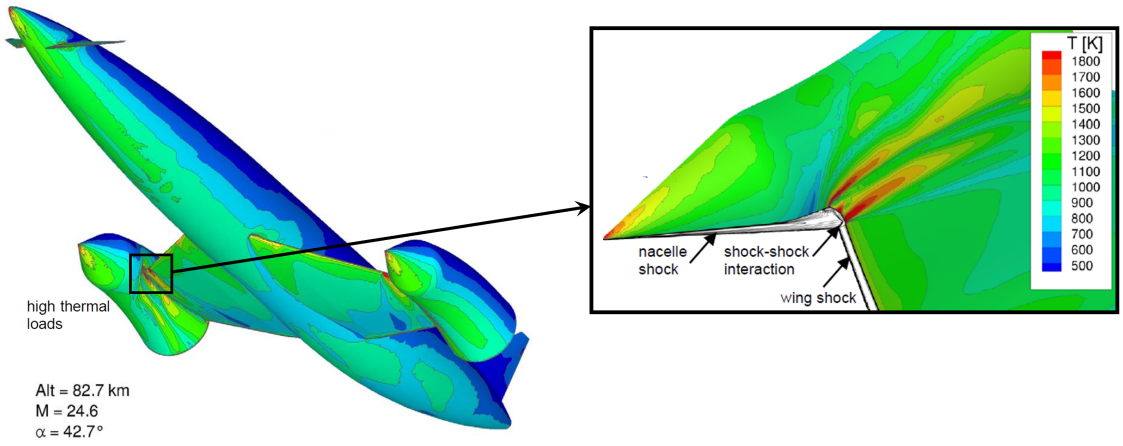

Figure 1.4: View of the thermally critical region on Skylon during re-entry. Adapted from Ref. [20].

1.2 Thermal Protection Systems

To protect hypersonic vehicles from the effects of the harsh high-temperature environment, different thermal protection systems have been proposed depending on the application. These concepts (see Fig. 1.5) can be divided broadly into three overarching techniques: passive, semi-passive, and active [21]

1. **Passive systems**: The passive system is generally the lowest performing TPS and falls into three broad categories: a heat sink, a hot structure, and an insulated structure. The heat sink absorbs most of the incident heat and stores it in a large thermal mass. If the heating rate and duration of the heat

pulse are modest, a high-heat capacity metal heat sink, such as Beryllium oxide, can absorb up to $6.3\,\mathrm{MJ\,kg^{-1}}$ [14]. The hot structure, on the other hand, allows the temperature to rise, so that heat flux is reduced via re-radiation. Re-radiation increases dramatically at high temperatures, according to the Stefan-Boltzmann law

$$\dot{q}_{\mathrm{rad}} = \varepsilon \sigma T_w^4 \tag{1.3}$$

where ε is the emissivity and σ is the Stefan-Boltzmann constant. This process continues until, at a steady state, the heat being radiated from the surface is equal to the incident heating. This is called the radiation adiabatic wall temperature. Passive systems are only restricted by the maximum acceptable surface and backside temperature of the material. Previously, passive TPSs have been used in the Inconel X hot structure of the X-15 research plane, which could withstand temperatures of up to 900 K [22]. This ensured that the heat was mainly re-radiated into space rather than being conducted into the sub-structure. The Space Shuttle also primarily made use of a passive system by employing hundreds of high temperature reusable tiles which were highly insulative, slowing the propagation of the high heat fluxes to the underlying substructure.

2. **Ablatives**: Ablation cooling refers to the uniform process of heat absorption and subsequent removal of surface material utilising the material's thermal capacity for cooling. This is great for providing a very high cooling capacity per unit mass. Ablation occurs at two levels: the outer surface of the material chars, melts, and sublimes, while the layer below undergoes pyrolysis and expels product gases (also known as blowing). A typical modern ablator, which is made of carbon fibres impregnated in a phenolic resin, is the Phenolic-Impregnated Carbon Ablator (PICA). This has been used for the forebody heat shield of Stardust and by SpaceX for its Dragon space capsule [23]. Ablation is a sacrificial method of heat protection since, in order to maintain

acceptable heat conditions, its surface layer is partially destroyed. Whilst ablation is incredibly robust and has been used widely for a variety of missions since the 1950s; it has several drawbacks that make a passive or fully active system desirable for certain vehicles. Ablatives are a single-use TPS system as the surface layer is partially destroyed during the ablative process. As a consequence of the previous point, there is an adverse effect to the vehicle aerodynamics as the ablation material chars and 'ablates', which precludes its usage for slender body vehicles with sharp leading edges where shape stability is an important consideration.

3. **Active**: The active system can adjust the cooling performance depending on the temperature of the material. This accounts for differing heat fluxes and temperatures during the flight trajectory as well as different areas of the vehicle. On the Space Shuttle, regenerative cooling was used to reduce peak temperatures on the wing leading edges. The most widely referred to active cooling methods are film cooling and transpiration cooling. Film cooling refers to the injection of a "cool" fluid into a "hot" boundary layer in such a manner that it forms a thin protective layer over the surface to be cooled. The fluid is injected at one or more discrete locations on the surface through holes or slots. Film cooling is widely used to cool gas turbine blades and rocket nozzle walls. Another use case is protecting the optical windows of supersonic (and hypersonic) interceptor missiles [24]. These windows have very strict cooling requirements to ensure that a clear line of sight to the target object is achieved. Traditionally, they are cooled via tangential film cooling, where the coolant is injected supersonically over the window and interacts with the viscous boundary layer flow that develops over the nose of the interceptor, forming a turbulent mixing layer over the window. A key challenge of such systems is the propensity of the film cooling method to quickly transition to turbulence, causing aero-optical disturbances (such as boresight error, image blur and centroid jitter) [25]. Transpiration cooling has the potential to provide smoother, laminar flows mitigating some of these disadvantages. For

hypersonic applications, ablation products from ablative insulators tend to obscure the sensor's view, which means that such TPS systems cannot be used ahead of or in the vicinity of such optical windows [26].

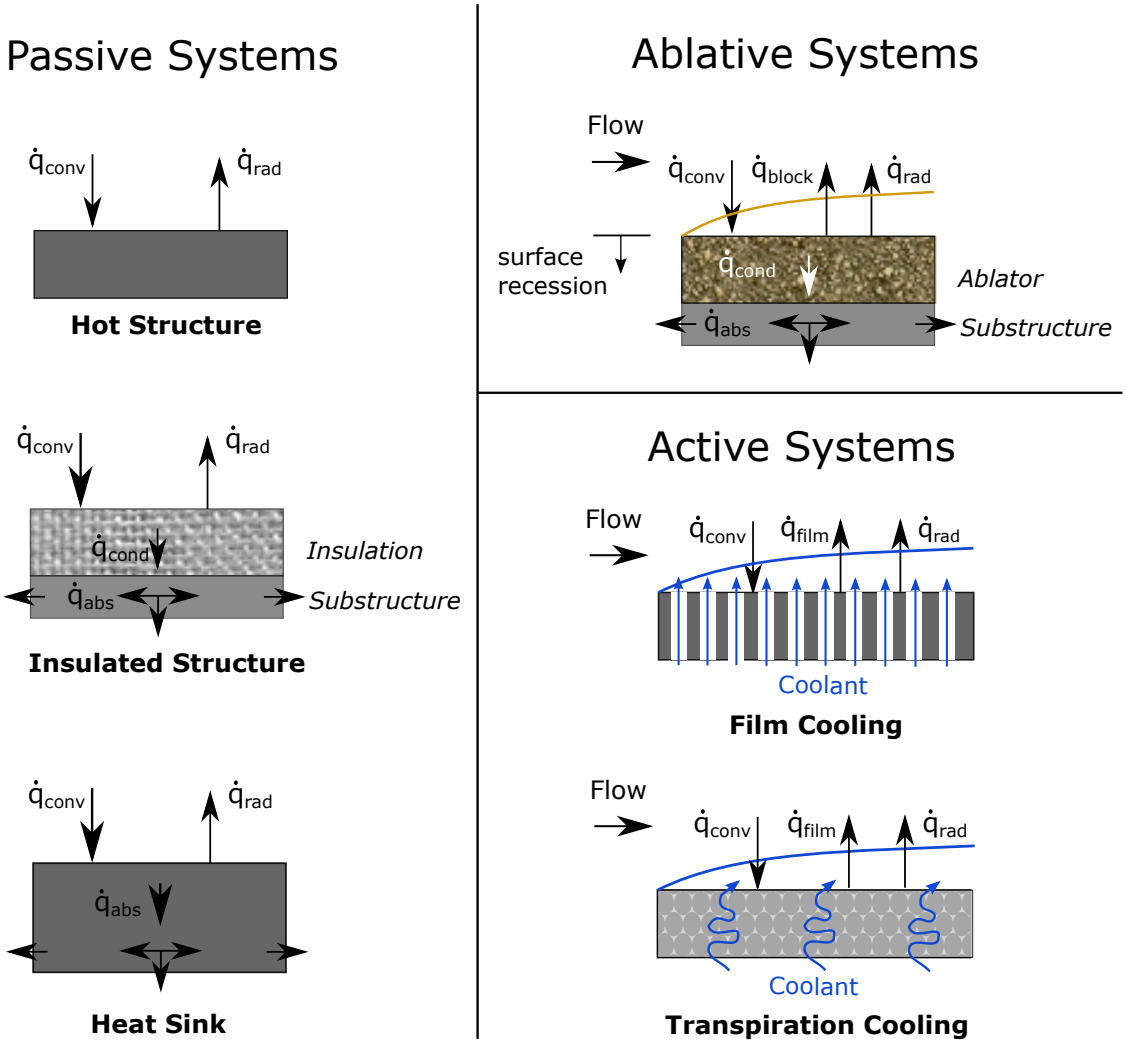

Figure 1.5: Overview of different thermal protection systems.

1.3 Transpiration Cooling

Transpiration cooling is the bleeding of coolant through a porous medium. Transpiration cooling has several advantages over film cooling; primarily, it is envisaged that transpiration cooling can stabilise the boundary layer, reduce skin friction drag and also prevent oxidation if inert gases are used [27]. The stabilisation of

the boundary layer can potentially result in a ten-time decrease in aerodynamic heating [7]. In both film and transpiration cooling, the protective effect of the heat absorption is augmented by the heat transfer blocking action of the coolant as it moves into the boundary layer. In effect, the presence of the coolant on the surface reduces the boundary layer velocity and temperature gradients at the hot surface, thereby decreasing the heat transfer rate to the surface and the skin friction [28].

Research on transpiration cooling first began in the late 1940s in the Jet Propulsion Lab. Rannie [29] developed an analytical approach for the porous-wall temperature by investigating the laminar, transpired sublayer and compared his theory to experiments. Thereafter, experiments in the 1950s [30, 31] confirmed that transpiration cooling is more effective than film cooling, mainly due to its closer packed, smaller pores which lead to a more homogeneous outflow. Subsequent research on the performance and characteristics of this approach has been carried on over many decades [32–40] whilst there has been only one transpiration-cooled flight test, namely SHEFEX II [41]. Some of the key reasons that have led to the very low number of vehicles employing this technique are the following

- A lack of suitable materials that provide the required mechanical and thermal properties. Until very recently, the best available materials were porous metals such as sintered porous stainless steel and bronze. These materials have relatively low melting points ($<$1000 K) which are too low even with the inclusion of transpiration cooling.

- The added complexity of an active cooling system. A transpiration-cooled system requires a considerable quantity of gas under high pressure, a manifold, and a cooling control system. There are high cost, weight, reliability, and volume penalties associated with these systems, which must be carefully balanced against potential benefits. In addition, if the active cooling system fails to activate during flight, this may lead to a catastrophic failure of the flight vehicle.

- Finally, the onset of early transition to turbulence due to gas injection into the boundary layer [42]. Whilst this is not the focus of this thesis, a large number of studies have investigated the effect of blowing on boundary layer transition, as highlighted in a review paper by Schneider [43]. Regardless, this phenomenon is still very difficult to predict and poses a major problem for mission design.

Recent advancements in materials science have made transpiration cooling once again a compelling active cooling technique. Porous injectors made of high temperature metals [44, 45] and carbon-carbon (C/C) type ceramic matrix composites (CMC) have been widely used in recent transpiration cooling studies [38, 46–49]. C/C type CMCs are particularly popular due to their manufacturability, low density, high strength, and a high operating temperature of approximately 1800 K. However, for sustained flight in lower atmospheric conditions with small leading-edge radii (of the order of mm), the temperature limits need to be pushed even further. Ultra-High-Temperature-Ceramics (UHTCs) have an exceptionally high melting point, typically above 3000 K [50]. The high melting point allows a TPS made of a UHTC to remove large amounts of heat through radiative cooling. A limitation, however, is that oxidation occurs for UHTCs above approximately 1000 K. As stated earlier, transpiration cooling with an inert gas can mitigate oxidation [27]. Thus, it is desirable to utilise UHTCs in conjunction with transpiration cooling. In addition, porous UHTCs are made by sintering fine powder grains, which allow for a more uniform distribution of the outflow compared to the coarse, non-uniform outflow exhibited by C/C CMCs [48] and improve internal heat transfer (further discussed in Chapter 2).

The potential regimes of applicability for transpiration may be assessed by considering a velocity-altitude diagram. These maps are widely employed to illustrate the various aerothermodynamic regimes of hypersonic flight [51]. Transpiration cooling is simulated by assuming a sustained, hypersonic cruise at every velocity and altitude point on the trajectory map. At each of these points, transpiration cooling is applied to a 10 mm, 2D leading edge made of a generic ZrB_2 UHTC

(Table 3.1). The PIRATE model (Appendix A) is applied, assuming a thermal steady state for the transpiration-cooled wall. The chosen coolant is nitrogen, and an optimisation procedure is applied, which calculates the required coolant mass flux, and consequently the blowing parameter, B_h, required to keep the surface temperature at or below 2000 K. The maximum temperature is selected assuming partial oxidation protection is acceptable and is the midpoint between the maximum surface temperature without oxidation protection (1000 K) and the maximum temperature with full oxidation protection (3000 K). The blowing parameter is defined as

$$B_h = \frac{F}{St_0} \tag{1.4}$$

where F is the blowing ratio and St is the Stanton number where the subscript '0' denotes the case with no blowing, i.e. $F = 0$. The blowing ratio is the rate of coolant mass injection is typically quantified by the ratio between the coolant mass flux and the freestream mass flux. This is defined as

$$F = \frac{\rho_f u_f}{\rho_e u_e}. \tag{1.5}$$

where the ρ and u are the density and velocity, respectively. The subscripts (f) and (e) denote the coolant and boundary layer edge properties. St is defined as

$$St = \frac{\dot{q}_w}{\rho_e u_e (H_{aw} - H_w)} \tag{1.6}$$

where $\dot{q}_w$ is the net heat flux at the wall, and H_w and H_{aw} are the wall and adiabatic wall total enthalpies, respectively.

Figure 1.6 shows the level of cooling required to keep the material surface temperature below 2000 K for sustained flight at each velocity-altitude point. For very low velocities and high altitudes, passive re-radiation is sufficient to keep the surface temperature below 1000 K (yellow shaded region). At an intermediate region, where the temperature is between 1000-2000 K, some blowing is needed to ensure that the surface does not oxidate (light blue region) [52]. For very

low altitudes and high velocities (red region), B_h is greater than the boundary layer blow-off parameter, B^* (Eq. (4.7)). Exceeding the boundary layer blow-off parameter will blow off the boundary layer, thereby aerodynamically blunting the stagnation point. As the motivation for sharp leading edges is to reduce drag at the expense of increased incoming convective heat flux, this defeats the purpose of using transpiration cooling to enable sharp leading edges. In addition, at very high blowing parameters, there is a system-level downside of requiring to carry more coolant. For such high enthalpy regimes, ablatives are likely to be more effective.

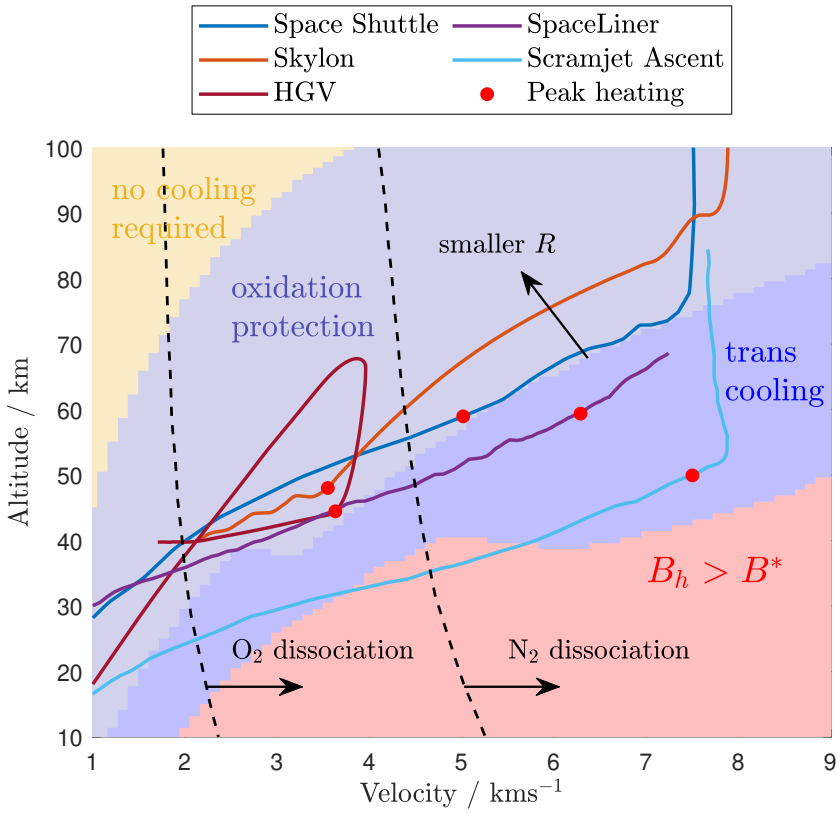

Figure 1.6: Velocity vs altitude maps of different flight trajectories adapted from Ref. [53]. Additional trajectories of Spaceliner [54], HGV and Skylon [55] have been added. Based on a 10 mm leading edge radius.

Between the no cooling region and the region where the blowing parameter is greater than blow-off, there is a corridor where transpiration cooling is highly effective. Overlaid on top of these regions are re-entry and ascent trajectories for a broad range of hypersonic vehicles. These trajectories, assuming a 10 mm leading-edge radius, broadly follow the approximate regime where transpiration

cooling can be highly effective. All of the vehicles avoid the very low altitude, high velocity region on the bottom right, which is characterised by high dynamic pressures and heat loads, as well as transitional/turbulent flows, which are characterised by enhanced heating. At higher speeds, real gas effects become prominent starting with O_2 dissociation at 2-2.5 $\mathrm{km\,s^{-1}}$ with ionisation at 9-11 $\mathrm{km\,s^{-1}}$. A class of vehicles, including spaceplane designs such as Skylon [6] and Spaceliner [54] are characterised by peak heating at lower velocities and relatively low altitudes (40-50 km). Such vehicles also require sharper leading-edge concepts to improve manoeuvrability at lower altitudes. This is also true for scramjet powered vehicles which need to spend a longer time in the atmosphere during their ascent phase [8]. Unlike ablatives, an active cooling TPS has the advantage of re-usability, which makes them an ideally suited TPS system for these vehicles.

Furthermore, reducing heat transfer, and therefore wall temperatures, is of great concern for regions of shock-wave boundary layer interaction (SWBLI) as detailed in Section 1.1.2. Theoretically, a transpiration cooling system is ideally suited to this task as it may be applied locally to any region on the vehicle. Nonetheless, relatively few studies have experimentally investigated the application of transpiration cooling for this problem. This is crucial to validate any computational studies due to the complex flowfields in the vicinity of shock-shock interactions and a coolant layer. In fact, Holden notes that

> *"Predicting the aerothermal loads resulting from the interaction of a shock wave with a cooling layer poses an important design requirement. These flows, which involve the mixing of dissimilar gases, render the calculations far more complex and - as in many other instances in these flows - experimental measurements are extremely important to validate the design of the vehicle component"* [18]

The most sustainable experimental study in these conditions was performed by Holden and others in the 1990s, both on a hemispherical nose [56] and a flat plate in turbulent flow [45]. It was found that whilst transpiration cooling had little effect on peak heat fluxes on a stagnation point subjected to Edney Type IV shock-shock

interactions, on a flat plate, it was highly effective. However, those experiments were conducted on a transpiration-cooled stainless steel plate, perforated with 0.039 inch (1 mm) holes. The surface geometry is vastly different to modern UHTCs, which feature pore diameters in the order of 2 μm. Further experimental testing of shock impingement with UHTCs or UHTC-like materials would be highly beneficial to ascertain the performance of transpiration for cooling these scenarios.

Ultimately, implementing a transpiration-cooled system requires a thorough understanding of the balance between the mass of coolant that needs to be carried out to achieve the target cooling performance, the likely coverage of the coolant, and the overall re-usability of the system. The question of the overall mass budget has been tackled by Hermann et al. [57] for a range of trajectories, with both steady-state and transient simulations. This was completed using the PIRATE numerical code on a generic hypersonic reentry geometry - a 30° half-angle blunted cone with a 0.5 m nose radius and a wall thickness of 10 mm. It was found that injecting close to the stagnation point resulted in good cooling effectiveness downstream as long as laminar flow conditions were maintained. An overall mass budget was less than 0.06 kg of nitrogen for the Space Shuttle trajectory and 1.2 kg for the Hayabusa reentry capsule. Considering that the total mass of the Shuttle is over 2 million kg, the mass of coolant required is ultimately negligible as a proportion of the full system for this case. The greater consideration is designing a system to reliably and safely pressurise the gas and control the injection system to regions and times (during the trajectory) when cooling is needed. In addition, the reusability of a transpiration-cooled system over several flights will likely depend on the material selected. UHTCs, for example, are very brittle and susceptible to cracking under load. Thus, utilising such materials may require detailed inspections between flights akin to the Space Shuttle ceramic thermal tiles. Closely related to this is the problem of thermal gradients, especially due to the large heat transfer gradients close to the stagnation point of hypersonic vehicles. Managing these gradients is essential to ensure the survivability of these materials over the course of several flights. In addition, depending on the trajectory, the pores on the porous material

may get gradually blocked by sand or ash over the course of several flights, degrading its performance and ability to provide uniform coverage of coolant.

1.4 Research Contributions

The overarching aim of this research is to investigate *the heat transfer reduction when transpiration cooling is applied to a hypersonic vehicle.* This has been approached in two ways. First of all, a systems-level study is conducted to explore the performance of transpiration cooling to mitigate heat transfer on a hypersonic wing leading edge. Subsequently, two key regimes in which existing transpiration cooling models are not applicable - a finite length porous injector in hypersonic flow and transpiration cooling applied to a shock-wave boundary layer interaction region - are investigated experimentally. The original contributions of this research are

Assessing the performance of transpiration cooling in reducing heat transfer on a wing leading edge

A numerical model which combined a model for the internal heat transfer between the porous solid and fluid, the external film effectiveness and a substructure was developed. It was found that whilst transpiration cooling can significantly diminish peak surface temperatures, an additional benefit is derived wherein the overall heat load to the vehicle is also reduced.

Development of an experimental method to analyse the heat transfer on a transpiration-cooled surface in hypersonic flow

To build up a better understanding of the heat transfer processes on transpiration-cooled injectors, especially when subjected to complex external flowfields, a non-intrusive diagnostic based on infrared thermography was developed to measure local surface heat transfer. A validation experiment was undertaken by applying the experimental technique to a stagnation point. The results were verified against well-known correlations and CFD.

Investigation of surface heat transfer on transpiration-cooled surfaces

Whilst a large set of experimental data for heat transfer on transpiration-cooled injectors in hypersonic flows exist, past experiments do not have access to 2D, spatial data on the porous injector. In addition, there are no experimental studies in the open literature where the heat transfer on transpiration-cooled micro-porous injectors have been measured in hypersonic flow. Thus, three distinct experimental data sets have been generated over the course of this research project

- A stagnation point experiment at Mach 7 was undertaken over a range of blowing parameters and coolant gases. It is shown that the surface heat transfer on an Alumina injector (mimicking UHTC) corresponds closely to CFD and previous correlations.

- A hypersonic flat plate experiment was undertaken at Mach 6.1 for both laminar and turbulent regimes over a range of blowing parameters with nitrogen and helium coolant gases. The effect of a finite length injector beginning at a point upstream of the leading was investigated, and, for the first time, a correlation parameter was experimentally determined for both laminar and turbulent flows, which accounted for stream-wise variations in heat transfer.

- The same flat plate above was subject to an oblique shock wave on the transpiration-cooled surface. Laminar-transitional and fully turbulent SWBLIs were achieved, and it was found that both regimes displayed similar levels of heat transfer downstream of the interaction. It is shown that relatively little injection dramatically reduced surface heat transfer in shock interaction regions, and a correlation was proposed that may be used for initial system-level design.

1.5 Thesis Structure

This thesis consists of seven chapters, including the Introduction. The remaining chapters are

1. **Chapter 2:** A review of the main literature relating to this research project is provided. The main themes are transpiration cooling, in particular, the heat transfer reduction on transpiration-cooled surfaces both due to external film cooling and internal convective heat transfer. In addition, heat transfer measurement techniques are discussed, including infrared thermography.

2. **Chapter 3:** A numerical model is built up to assess the performance of transpiration cooling to mitigate heat transfer on a wing leading edge. The code is based on the previously developed PIRATE code (Appendix A), which is extended to account for lateral conduction and a substructure. The model is then applied to a 15-degree half-angle wing leading edge with a nose radius of 0.1 m with the Space Shuttle re-entry trajectory. This chapter is based on the journal paper published in the *AIAA Journal* [58].

3. **Chapter 4:** A novel method of employing high-speed infrared thermography to measure surface heat transfer on a transpiration-cooled porous injector in hypersonic flow is described. The technique, including calibration and post-processing methods, is developed on a hypersonic stagnation probe and is validated against CFD and well-developed correlations. This chapter is based on a journal paper published in the *Journal of Thermophysics and Heat Transfer* [59].

4. **Chapter 5:** The technique developed in Chapter 4 is applied to laminar and turbulent hypersonic flows on a flat plate. Two porous injectors (one characteristic of UHTCs) are investigated. The results are presented and compared to existing theories and correlations. This chapter is based on a journal paper published in the *Journal of Thermophysics and Heat Transfer* [60].

5. **Chapter 6:** The technique developed in Chapter 4 is applied to a flat plate subject shock impingement from a 10° shock generator. Laminar-transitional and turbulent conditions are formed as a result of the shock interaction, and the effect of transpiration cooling on the high heat fluxes in these regions is discussed. The results are compared to existing theories and correlations. This chapter is based on a journal paper published in the *Journal of Spacecraft and Rockets* [61].

6. **Chapter 7:** In this chapter the thesis is concluded by summarising the key results, suggesting improvements and recommending future work.

Chapter 2

Literature Review

Contents

This chapter reviews the literature relevant to past advances in film and transpiration cooling research relevant to the aims of this thesis. The fundamental physical processes of transpiration cooling are described, and further details are elaborated specifically on heat transfer measurements for a range of canonical cases relevant to hypersonic flows. A range of coolants and materials are compared, with an assessment of the strengths and weaknesses of different choices. Subsequently, a review of surface heat transfer measurement techniques is provided, focusing on infrared thermography. In the final section, overall systems-level studies of transpiration-cooled systems are assessed. Further literature is also reviewed in each of the subsequent chapters, which are based on submitted or published journal papers that make up this thesis.

2.1 Mechanisms of Transpiration Cooling

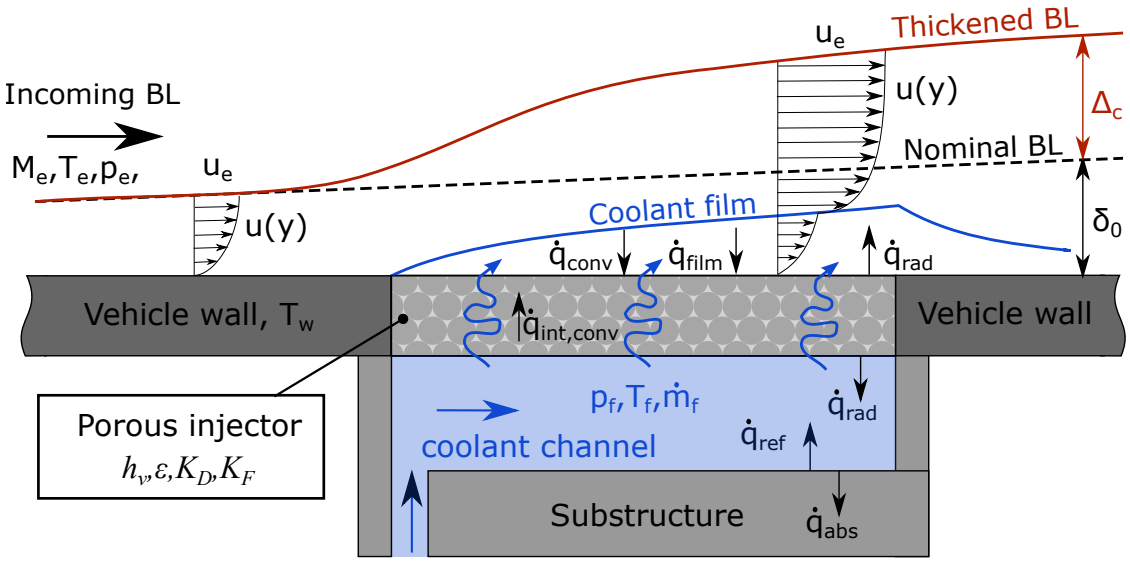

Figure 2.1: Heat flux balance of a transpiration-cooled injector in hypersonc crossflow. Note: not to scale.

There are several coupled processes that occur in transpiration-cooled TPS systems. Firstly, as shown in Fig. 2.1, the coolant is introduced from a pressurised coolant channel located somewhere within the vehicle structure. The pressure gradient between the coolant channel and the external flow drives the coolant flow through the porous material. As the coolant moves through the porous material, if there is a temperature difference between the fluid and the solid, internal convective heat transfer takes place. Thereafter, the movement of the coolant to the surface results in a heat transfer blocking action as it moves into the boundary layer. In effect, the presence of the coolant layer on the surface reduces the boundary layer velocity and temperature gradients at the hot surface, thereby decreasing the heat transfer rate to the surface [28]. The fluid then mixes with the hot external gas as it moves downstream of the porous material.

Additionally, the layer acts as a chemical barrier for catalytic heating and oxidation by protecting the wall from freestream Oxygen, thereby preventing diffusion to the wall. This enables certain materials to operate at a higher temperature and enhances radiative cooling. The success of the latter two processes

depends on the coolant film that is formed on and downstream of the injector (i.e. the coolant needs to be an inert gas). In the following sections, these mechanisms are explored in detail alongside a review of the critical literature.

2.1.1 Porous Media Flow

Fundamentally, transpiration cooling is the use of a porous material as the injector. Thus, an analysis of a transpiration-cooled TPS system is impossible without considering the movement of coolant through a porous material. Once a pressure differential exists between the external flow and the pressure in the coolant reservoir, the resultant mass flux, $\rho_f\, u_f$ is governed by the Darcy-Forchheimer [62] equation, which is given as

$$-\frac{\mathrm{d}p}{\mathrm{d}x} = \underbrace{\frac{\mu_f}{K_\mathrm{D}} u_f}_{\text{Darcy term}} + \underbrace{\frac{\rho_f}{K_\mathrm{F}} u_f^2}_{\text{Forchheimer term}} \tag{2.1}$$

where ρ_f and μ_f are the fluid's density, and dynamic viscosity, respectively. K_D and K_F are material intrinsic permeability coefficients known as the Darcy and the Forchheimer coefficient. $\frac{\mathrm{d}p}{\mathrm{d}x}$ is the pressure gradient across the thickness of the material, and u denotes the superficial or bulk velocity of the through-flow. The first term on the right-hand side of Eq. (2.1) stands for viscous losses, whereas the second denotes the kinetic losses, which become dominant only at higher velocities. If the pressure gradient is assumed to be linear, an integrated form of Eq. (2.1) may be employed

$$\frac{p_\mathrm{in}^2 - p_\mathrm{out}^2}{2 p_\mathrm{in} L} = \frac{\mu_f(T_\mathrm{in})}{K_\mathrm{D}} u_{f,\mathrm{in}} + \frac{\rho_f(p_\mathrm{in}, T_\mathrm{in})}{K_\mathrm{F}} u_{f,\mathrm{in}}^2 \tag{2.2}$$

which is valid for a constant fluid temperature over the thickness of the sample, L. The subscripts (in) and (out) refer to the outflow and inflow quantities, respectively. If there is a temperature gradient across the porous injector, then the viscosity and density would vary at every location depth-wise on the porous injector. For a linear

temperature gradient[1], Langener obtained an alternative analytical solution of the Darcy-Forchheimer equation for a one-dimensional porous material [63]

$$\frac{p_{in}^2 - p_{out}^2}{2p_{in}L} = \frac{\mu_{in}}{K_D} u_f \frac{1}{(T_{in} - T_w)/T_{in}(n+2)} \left[\left(1 + \frac{T_{in} - T_w}{T_{in}} \right)^{n+2} - 1 \right] + \frac{\rho_{in}}{K_F} u_f^2 \left(1 + \frac{T_{in} - T_w}{2T_{in}} \right) \quad (2.3)$$

and validated this against experimental data. A key result from this investigation was that, for a given coolant outflow velocity, the required differential pressure rises as the gas temperature is increased. The effect is larger at lower velocities as the differential pressure is proportional to the viscosity in the Darcy regime (viscous term, Eq. (2.1)) and the gas's viscosity μ increases with rising temperature.

To calculate required plenum pressures and, thus, the mass budget for a transpiration-cooled system, it is necessary to determine the Darcy and Forchheimer coefficients of the chosen injector. Ergun and Orning [64] proposed correlations for K_D and K_F of porous materials with regular, spherical particles. However, for irregular pore structures, as is the case for most materials suitable for hypersonic transpiration cooling systems (C/C ceramics and UHTCs), the permeability coefficients must be determined experimentally. Ifti et al. [65] measured the Darcy and Forchheimer coefficients for a range of different UHTCs in a BS EN ISO 4022 standard rig. An alternative technique described by Innocentini et al. [66] used a pressure-decay, where a tank was pressurised followed by a blowoff and a recording of the transient pressure and mass flow rate data. The fluid expands over the porous sample, and from the pressure loss and mass-flow rate characteristics, the permeability coefficients, K_D and K_F could be determined. A more complicated situation exists for highly two-dimensional flows. Although analytical solutions exist for evaluating pressure distributions [67], those neglect the Forchheimer term and assume an isothermal material. Alternatively, the full two-dimensional Darcy-Forchheimer equation may be solved numerically, including temperature effects as

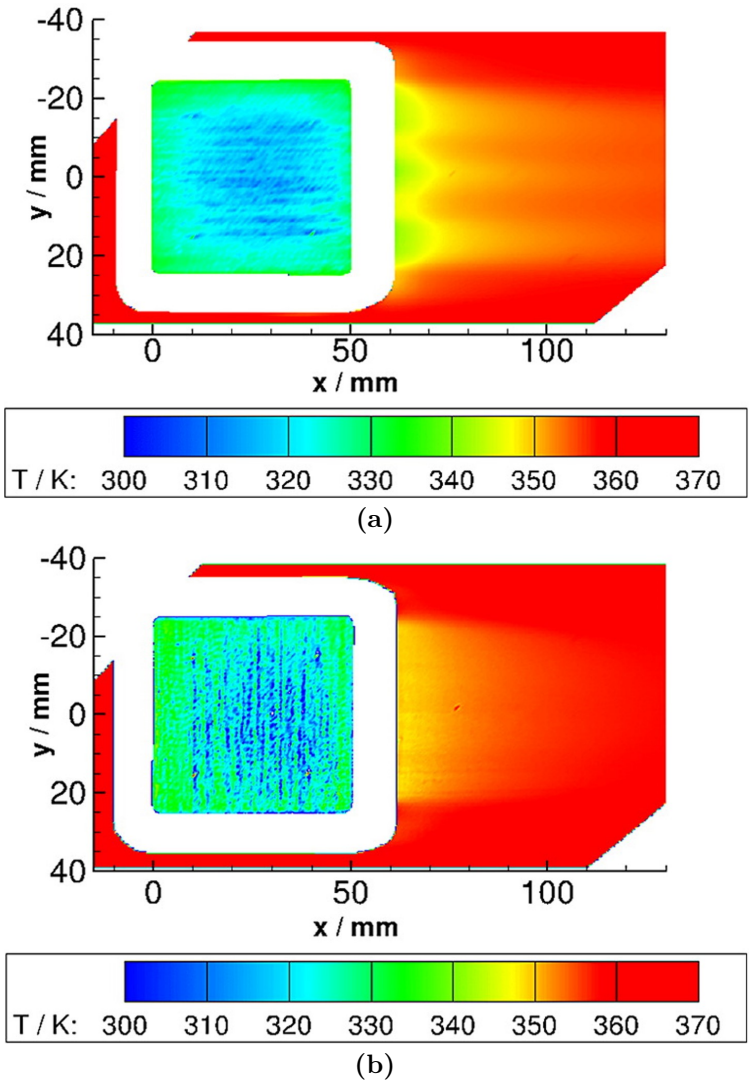

Figure 2.2: Experimentally obtained wall temperature (infrared thermography): (a) C/C plies parallel to flow and (b) C/C plies perpendicular to flow. Blowing ratio both cases: $F = 1\%$. Figure reproduced from König et al. [69].

implemented by Dittert et al. [48] and Prokein et al. [68].

Related closely to the permeability coefficients is the overall porosity of the material. Porous materials are characterised by the total porosity which is then divided into open and closed porosity. When the porous material is immersed in a fluid, the open porosity is the volume occupied by the continuous fluid phase as a ratio to the total volume of the porous material. Conversely, closed porosity refers to the ratio of the unconnected pore volume to the total volume. In a transpiration

[1]A linear temperature may exist for low through-flow velocities and/or materials with low thermal effusivity. Further details in Langener et al. [46]

cooling context, the open porosity is most relevant as this is the path that the fluid will take as it moves through the material and will determine both the overall permeability and the heat transfer coefficient between the fluid and solid. Another widely-used parameter for porous materials is the tortuosity. The tortuosity is essentially a measure of the geometric complexity of a porous material and it is usually defined as the squared ratio between the curved paths followed by a fluid in the porous medium over a straight path [70]. The porosity and tortuosity both affect the effective permeability of a porous material. When there is a more porous volume (high porosity), then, the material is more permeable. When the tortuosity increases, the path that the fluid has to take through the material is more curved, and the effective permeability of the material decreases.

The overall porosity of materials may be measured using a density-based measurement - i.e. comparing the weight of the sample to the theoretical weight of a fully dense one of identical volume. This is how the porosity of the ZrB_2 UHTC samples from Imperial College London were determined [65]. The open porosity may be measured very simply using Archimedes' principle. The material is immersed in a fluid (or gas) and the open porosity is determined by knowing the volume of fluid required to saturate the porous medium. Alternatively, a more accurate technique is the pressure difference method [71]. The volume of an enclosure where a material sample is placed is reduced and, when doing so, the pressure will increase in the enclosure compared to the atmospheric pressure. The increase in pressure depends on the volume of the enclosure and the volume accessible to the air inside the porous medium. By measuring the pressure increase it is possible to determine the open porosity of the material. Finally, optical methods such as X-ray computed tomography can allow you to discriminate easily between closed and open porosity and make both qualitative and quantitative assessments [72].

Related closely to the permeability and porosity is the effect of the type of porous material utilised and the uniformity of the injector. Basore et al. [49] showed that a C/C type CMC injector performed better in reducing the heat flux downstream compared to an Oxygen compatible CMC injector or a Multi-Port Injector Array

(MPIA) in both laminar and transitional hypersonic flows. For UHTCs, Ifti et al. [73] showed that a non-uniform injector could lead to non-uniformities in the downstream film (and presumably on the injector). In fact, similar observations were made by König et al. [69] using C/C injectors, where the authors demonstrated that the downstream film is significantly different for a C/C injector when the orientation of the plies is varied (Fig. 2.2). A non-uniform outflow may lead to potential undercooling for critical regions on or downstream of the porous injector and is a key parameter that underpins the design of a transpiration cooling system.

Finally, a key consideration for the applicability of these materials to realistic geometries is the manufacturability of such materials to suitable, complex shapes. Dittert et al. [48] have shown that it is possible to manufacture porous cones and characterised the 3D permeability of those samples. Numerical simulations of the outflow based on these measurements showed that the area-specific mass flow is significantly lower at the tip compared to the flanks (Fig. 2.3). For the design of a transpiration cooling sharp leading edge where the peak heat fluxes will be at the stagnation point, this is a severe challenge. The authors [48] propose that an optimised wall geometry with smaller wall thicknesses positions where cooling is needed could be one approach or, alternatively, designing a material with anisotropic permeability along the surface. Such materials and geometries which are suitable for transpiration cooling applications are still under ongoing development.

2.1.2 Internal Heat Transfer

As the coolant moves through the porous material, it then heats up the bulk solid through internal convection, $\dot{q}_{\text{int,conv}}$. The internal heat transfer is driven by the magnitude of the internal volumetric heat transfer coefficient, h_v. This value is material-specific and can vary greatly with mass flow rate [74]. This is defined through the Nusselt number as

$$Nu = \frac{h_v K_D}{k_f} \tag{2.4}$$

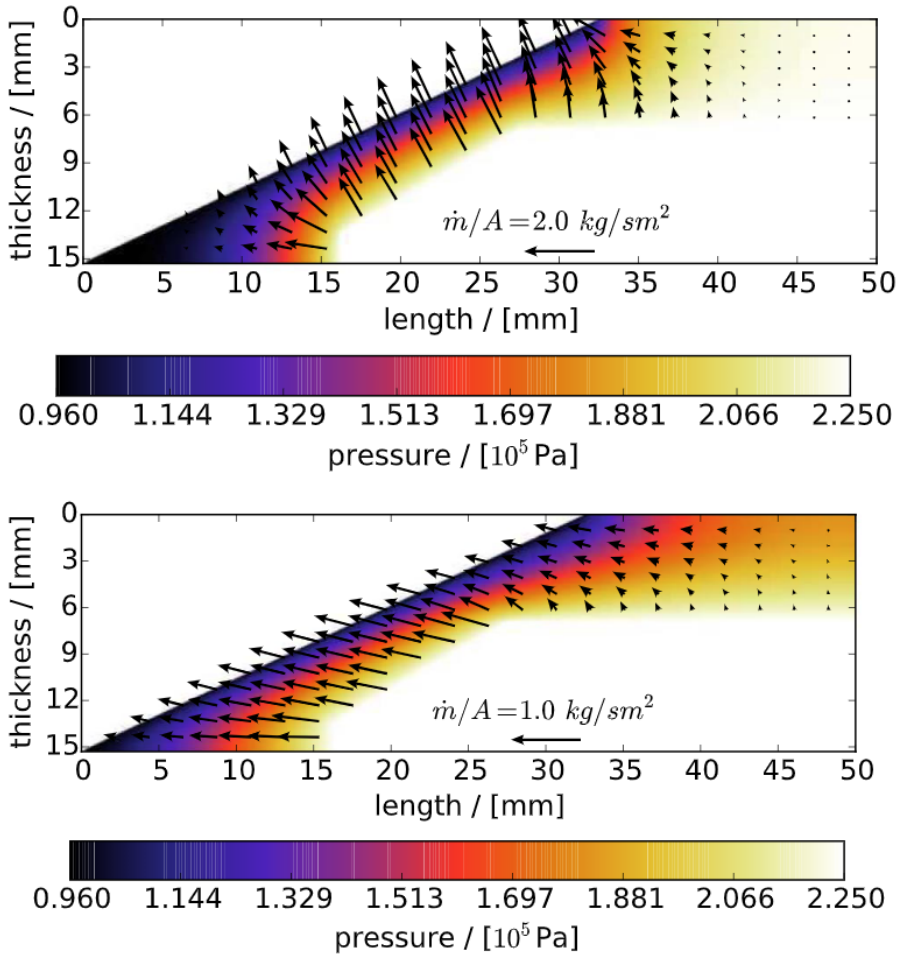

Figure 2.3: Calculated two-dimensional pressure distributions for a cone based on a plenum pressure of 2.25 bar. Figure reproduced from Dittert et al. [48]

where k_f is the thermal conductivity of the coolant fluid. Florio et al. [75] correlated the internal heat transfer coefficient for polymer composite materials

$$Nu = 2.22 \cdot 10^6 \cdot (Re_{\sqrt{K_D}})^{0.703} \tag{2.5}$$

where the Reynolds number is calculated by

$$Re_{\sqrt{K_D}} = -\frac{\rho_f K_D^{1.5} \Delta p}{\mu_f^2 \phi L} \tag{2.6}$$

where Δp is the pressure difference across the porous material and L is the thickness. The full mechanism of the heat transfer between the solid and fluid phases is governed by a set of coupled partial differential equations for the fluid and solid phases respectively [76]

$$\underbrace{(1-\phi)\rho_s c_{p,s}\frac{\partial T_s}{\partial t}}_{\text{Transient heating (solid)}} = \underbrace{k_{y,s}(1-\phi)\frac{\partial^2 T_s}{\partial y^2}}_{\text{Normal conduction (solid)}} + \underbrace{h_v(T_f - T_s)}_{\text{Fluid}-\text{solid heat exchange}} \tag{2.7}$$

and

$$\underbrace{\phi\rho_f c_{p,f}\frac{\partial T_f}{\partial t}}_{\text{Transient heating (fluid)}} = \underbrace{\phi\rho_f c_{p,f}\frac{u_f}{\phi}\frac{\partial T_f}{\partial y}}_{\text{Convection}} + \underbrace{h_v(T_s - T_f)}_{\text{Solid}-\text{fluid heat exchange}} \quad . \tag{2.8}$$

with (s) denoting the solid phase, (f) denoting the fluid phase, the thermal conductivity, k, the porosity, ϕ, the volumetric heat transfer coefficient, h_v, the time, t, and the location, y, measured from the surface. The quantification of the volumetric heat transfer coefficient, h_v, is fairly hard to assess. Existing methods to characterise h_v of a particular material can be found in Refs. [75, 77–81]. These approaches rely on measuring the transient solid and fluid temperatures of a porous material exposed to either a heated flow that is passing through it or transiently heating (e. g., by radiation or electrical current) the solid phase instead. A numerical or analytical model of the material using the known thermophysical parameters is then employed to assess the volumetric heat transfer coefficient. These methods can be quite difficult to apply for the rather low porosity and homogeneous but highly irregular inner structure of Ultra-High-Temperature-Ceramic. For C/C, Schweikert et al. [82] estimated the h_v of C/C to be over the order of $10^6\,\mathrm{W\,m^{-3}\,K^{-1}}$. For UHTCs, h_v, has been experimentally determined by Hermann et al. [74] by surface heating transpiration-cooled ZrB_2 samples with a laser and by measuring the resulting surface and backside temperatures. On the other hand, Chakravarthy et al. [83] applied an optical method to extract the fluid and solid temperatures at the exit of the porous injector, using those values to obtain h_v. Both of the above experiments resulted in values that broadly agreed with the correlation in Eq. (2.5).

Depending on the internal heat transfer coefficient of the porous material, the fluid and solid phases may be in local thermal non-equilibrium (LTNE) over the course of a vehicle trajectory. This has been a focus of research in the past 5-10 years, and several authors have employed LTNE models in numerical codes to

model transpiration-cooled surfaces [84, 85]. A semi-analytical method employing impulse responses has been developed by Hermann et al. [86] to rapidly solve Eqs. (2.7) and (2.8) and obtain the fluid and solid temperatures at the surface and backside of a porous material. This model has further usage in systems-level studies as detailed in Section 2.6.

2.1.3 Surface Cooling

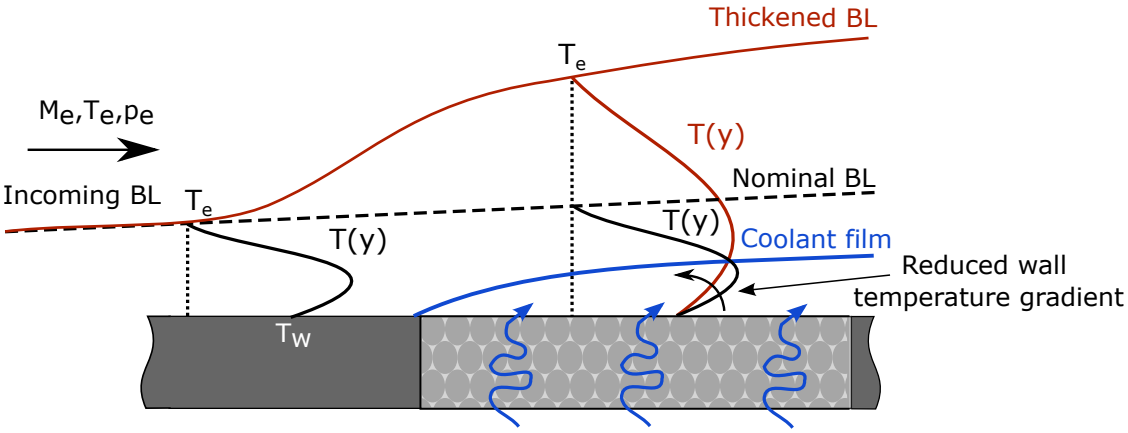

Figure 2.4: Boundary layer temperature profiles for a transpiration-cooled wall. Note: not to scale.

Initially, the introduction of the coolant layer thickens the incoming boundary layer. Mann [87] derived the effective boundary layer displacement thickness with blowing, D^*, for a two-dimensional compressible boundary layer as

$$D^* = \delta^* + \int_0^x \left(\frac{\rho_w u_w}{\rho_e u_e}\right) dx \tag{2.9}$$

where δ^* is the local displacement thickness defined as

$$\delta^* = \int_0^\infty \left(1 + \frac{\rho u}{\rho_e u_e}\right) dy \tag{2.10}$$

This was later extended for arbitrary shape bodies by Hayasi [88].

For a given freestream condition, the boundary layer thickness, δ, is inversely proportional to the distance from the leading edge [8]

$$\frac{\delta}{x} \propto \frac{M_\infty^2}{\sqrt{Re}}. \tag{2.11}$$

Thus, as shown from Eckert's heat transfer correlation for laminar boundary layers [89]

$$St^*_{lam} = \frac{0.332}{\sqrt{Re^*_x}}(Pr^*)^{-2/3} \tag{2.12}$$

the surface heat transfer reduces further away from the leading edge. i.e. as the boundary layer thickens, the surface heat flux reduces. St is the Stanton number, Re_x is the Reynolds number and Pr is the Prandtl number. The superscript '*' denotes quantities that are evaluated at Eckert's reference temperature

$$\frac{T*}{T_e} = 1 + 0.032M_e^2 + 0.58\Big(\frac{T_w}{T_e} - 1\Big). \tag{2.13}$$

As illustrated by Fig. 2.4, the introduction of the low momentum coolant into the sublayer of the boundary layer can significantly reduce the temperature and velocity gradients close to and at the wall [28, 90]. The magnitude of heat transfer and skin friction reduction depends both on the injection rates of coolant and the coolant type.

Before moving on to specific scenarios, it must be highlighted that a key assumption made by a vast majority of transpiration-cooled studies is that the fluid and solid are at local thermal equilibrium at the porous injector wall [91] - i.e. it is assumed that the porous surface is a 100% effective heat exchanger. If the porous wall is thick, or the pores are very small, this may well be the case, but if the wall is very thin, this assumption may not hold. For instance, in the cooling of gas turbine blades, a common configuration is to drill an array of small holes on the surface. Unlike transpiration cooling, the temperature of the coolant will usually be different to the wall temperature because the cooling holes are too short to provide a sufficient heat-transfer area to bring the cooling fluid to surface temperature. Thus, film cooling is characterised slightly differently in terms of an effectiveness parameter

$$\eta = \frac{T_w - T_e}{T_f - T_e} \tag{2.14}$$

where the coolant is injected at temperature T_f to cool a surface downstream at temperature T_w. The film is 100% effective if the coolant has blocked so much heat

that $T_f = T_w$. A non-equilibrium between the coolant and solid at the surface can be an important factor in certain scenarios, for example, transiently during a hypersonic trajectory. Whilst models exist to account for local thermal non-equilibrium within the porous material, the effect at the surface in hypersonic conditions remains to be investigated both experimentally and numerically. In this thesis, it is assumed that the coolant and solid temperatures are in equilibrium at the surface.

Determining the heat fluxes at the wall with blowing requires either detailed experimental testing or numerical simulations. In the following section, key experimental, numerical and analytical studies are presented which have characterised the effectiveness of transpiration cooling to mitigate surface heat transfer for a range of geometries for laminar and turbulent flows.

2.2 External Blockage Transpiration Cooling Studies

Table 2.1 presents an overview of external blockage transpiration cooling studies for flat plates, stagnation points, cones and shock interaction regions. Since the 1950s, studies have been conducted on almost every aspect of the transpiration cooling problem, including complex phenomena such as cooling shock interaction regions.

One of the earliest works by Mickley et al. [92] investigated the effectiveness of transpiration cooling on a flat plate with a laminar boundary layer. It was found that the inclusion of transpiration cooling significantly reduced surface heat transfer and skin friction. The experimental data were compared favourably to a simple analytical model called film theory, further detailed below. Subsequently, Rubsein et al. [93] conducted experiments on a turbulent boundary layer with air injection at Mach 2.7 and compared these against an analytical formulation based on mixing-length theory [107]. Great agreement was found, and the effects of blowing are indicated to be similar for high-speed, compressible flow to those for low-speed, incompressible flow.

[2]Transpiration cooling is applied to one of the faceted surfaces of the SHEFEX II model. This is categorised here as an inclined flat plate.

Table 2.1: Summary of key experimental, numerical and analytical studies on external heat transfer blockage for hypersonic transpiration-cooled systems.

	Experimental	Numerical	Analytic
Flat plate	Mickley (1954) [92] Rubesin (1956) [93] Bartle and Leadon (1960) [94] Kuhn and Hald (2008) [37] Meinhert et al. (2008) [95] Langener et al. (2011) [46] Reimer et al.(2011) [16] Böhrk et al. (2012)[2] [96] Huang et al. (2015) [97] Ibrahim et al. (2016) [98] Hermann et al. (2018) [99] Ifti et al. (2022) [100]	Thompson and Gnoffo (2008) [101] Shi and Wang (2008) [102] Gulli et al. (2013) [103] Dahmen et al. (2014) [104] Cerminara et al. (2021) [105] Ifti et al. (2022) [106]	Mickley (1954) [92] Low (1955) [28] Rubesin (1955) [107] Eckert (1958) [90] Kays (1972) [36] Meinhert et al. (2008) [95]
Stagnation point	Swann and Pittmann (1962) [108] Howe and Sheaffer (1964) [109]	Moyer and Rindal (1968) [110] Sreekanth and Reddy (1995) [111] Thompson and Gnoffo (2008) [101]	Hartnett and Liu (1968) [112] Yoshikawa (1969) [113]
Cone	Pappas and Lee (1970) [114] Wimberly et al. (1970) [34] Stalmach et al. (1971) [33] Kaattari (1978) [115] Van Foreest et al. (2012) [116] Reimer et al. (2011) [16]	Marvin and Pope (1967) [117] Stalmach and Bertin (1978) [118] Thompson and Gnoffo (2008) [101] Brune et al. (2014) [40]	Marvin and Pope (1967) [117]
Shock interaction	Nowak et al. (1990) [119] Holden and Sweet (1994) [45] Jiang et al. (2019) [120] Strauss et al. [121]	Jiang et al. (2019) [120]	
Downstream cooling	Volchkov et al. (1967) [35] Goldstein (1971) [122] Heufer and Olivier (2008) [123] Gülhan and Braun (2011) [39] Hombsch and Olivier (2013) [124] Tanno et al.(2016) [42] Strauss et al. (2017) [121] Ifti et al. (2022) [100]	Kellerand Kloker (2016) [125] Ifti et al. (2022) [106]	Volchkov et al. (1967) [35] Goldstein (1971) [122] Heufer and Olivier (2008) [123] Hombsch and Olivier (2013) [124]

Later, research moved from flat plates to stagnation points and cones. Howe and Sheaffer [109] employed viscous shock layer theory to investigate the effect of blowing on a stagnation point with air injection. They found that for high Reynolds number flow, the heat reduction due to mass addition was not simply correlated as a function of the mass addition rate but required additional variables. Stalmach et al. [118] developed a non-self-similar boundary layer solver to predict heat transfer and skin friction on transpiration-cooled surfaces. The numerical results showed excellent agreement with the experimental tests on a cone by Pappas and Lee [114] including foreign gas injection (helium and argon). Wimberly et al. [34] conducted experiments on a transpiration-cooled slender cone at Mach 12 and 17. They found that both heat transfer and skin friction decreased with

increased mass injection. As a result of reduced skin friction, the slope of the axial force coefficient and normal force was also reduced with increased mass injection, suggesting that transpiration cooling can have a net positive impact to aerodynamics. More recently, Kuhn and Hald [37] performed experiments in an arc jet-heated plasma facility that can recreate the high wall temperatures experienced during flight. They demonstrated successful cooling over the porous injector for a range of injection gases and verified that transpiration cooling could be applied successfully for hot structures at application relevant re-entry conditions.

A key output of the above experimental and numerical investigations is obtaining simplified engineering correlations, which may be used by vehicle designers to assess the performance of a transpiration-cooled system. Generally, authors have produced correlations by expressing the Stanton number reduction as a function of the blowing parameter

$$\frac{St}{St_0} = f(B_h). \tag{2.15}$$

Mickley et al. [92] applied an analytic method called film theory to relate the Stanton number ratio to the blowing parameter.It is less realistic than boundary-layer theory, but it greatly simplifies the analysis of the mass transport between the freestream and the wall. It is shown that an equation of the form

$$\frac{d^2\beta}{dm^2} - \Gamma\left(\frac{d\beta}{dm}\right) = 0 \tag{2.16}$$

with the boundary conditions $\beta = 0$ when $m = 0$ and $\beta = 1$ when $m = 1$ has the following dimensionless gradient at the wall

$$\left(\frac{d\beta}{dm}\right)_w = \frac{\Gamma}{e^{\Gamma} - 1} \tag{2.17}$$

where Γ is a dimensionless measure of mass transfer rate, β is a normalized velocity, temperature, or concentration, and is called generalized profile factor, whilst m is the normalized y coordinate. Furthermore, it is demonstrated that the ratio of non-dimensional gradients corresponds to the ratio of mass-transfer coefficients, θ

$$\frac{\left(\frac{d\beta}{dy}\right)_w}{\left(\frac{d\beta}{dy}\right)_{w,0}} = \frac{\Gamma\frac{\Delta_*}{\Delta}}{e^{\Delta}-1} = \frac{\phi}{\exp\left(\frac{\phi\Delta}{\Delta_*}\right)-1} \tag{2.18}$$

where ϕ is a mass transfer parameter and Δ/Δ_* is the ratio of effective film thicknesses. For heat transfer, θ is the Stanton number ratio and ϕ is the blowing parameter, B_h. Simple film theory assumes that Δ/Δ_* is unity and therefore the equation may be rewritten as

$$\frac{St}{St_0} = \frac{2\lambda B_h}{e^{2\lambda B_h}-1} \tag{2.19}$$

where λ is 0.5 for laminar flows and 0.4 for turbulent [110]. Tauber [14], compiled a range of transpiration-cooled studies for flat plates, cones and stagnation points and provided simple, experimentally based correlations in the form

$$\frac{St}{St_0} = 1 - X \cdot B_h + Y \cdot B_h^2 \tag{2.20}$$

where the values of X and Y vary depending on whether it is the stagnation point, laminar flat plate/cone or turbulent flat plate/cone. These correlations are only suitable for identical gas injection (for example, air-air). For the stagnation point, Swann and Pittman [108] did extensive research on the numerical modelling of ablatives, in particular the recession of the char layer. As the injection of ablation products into the boundary layer was found to cause significant blockage of aerodynamic heating, it had to be included in the model. The blocking effectiveness for three mass transfer rate parameters was obtained from the boundary layer equations for air-to-air injection and correlated as

$$\frac{St}{St_0} = 1 - 0.72 \cdot B_h + 0.13 \cdot B_h^2. \tag{2.21}$$

For stagnation points, an alternative approach, using shock-layer theory, was developed by Yoshikawa [113] which is applicable across a wide range of injection gases and conditions. The derivation and equations are further detailed in Chapter 4. More recently, Langener et al. [46] reported great agreement between the film

theory correlation (Eq. (2.19)) and experimentally obtained data using a porous C/C injector at low blowing ratios, i.e. up to 0.1%, employing air, argon, and helium as the coolant.

A variety of different correlations for stagnation points and flat plates with identical gas injection are plotted in Fig. 2.5. Whilst the Yoshikawa and Swann-Pittmann correlations agree well at the stagnation point; there is great variation between other correlations. This is likely due to differences in the flow field for the experiments in which the experimental data were correlated. In particular, it has been noted in the literature that the blowing parameter, B_h does not capture Mach number dependency [95]. The greatest discrepancies are for the turbulent cases, highlighting the need for further careful experimental and computational studies to refine these correlations.

Stalmach et al. [33] conducted a range of experiments on a 12° half-angle cone with a porous-sintered nickel skin. The model was fitted with a sharp, non-porous nose section nominally 4% of the model length. In laminar flows, it was found that the heat transfer reduction for a large range of experiments with different injection gases, including nitrogen, methane and freon are correlated with a modified blowing parameter

$$\frac{St}{St_0} = f\Big[\frac{\rho_f u_f}{\rho_e u_e} Re_x^{0.5} \Big(\frac{x - x_s}{x}\Big)^{0.5} \Big(\frac{\mathrm{M}_e}{\mathrm{M}_f}\Big)^{0.25}\Big] \tag{2.22}$$

where x is the distance from the stagnation point, x_s is the location of the injector from the leading edge, M is the molecular weight with the subscripts (e) and (f) referring to the freestream and injected coolant, respectively (see Fig. 2.6). Whilst a single expression to correlate the experimental data was not developed, the effect of the non-porous sharp nose was captured with the term $\left(\frac{x-x_0}{x}\right)^{0.5}$. Essentially, this factor accounts for the development of the boundary layer at the point of injection. A correlation parameter was also obtained for turbulent flows in the form $\frac{\rho_f v_f}{\rho_e v_e}\left(\frac{c_{\mathrm{p,f}}}{c_{\mathrm{p,e}}}\right)$.

Ifti et al. [106] conducted RANS (Reynolds-averaged Navier–Stokes) simulations on a flat plate in laminar flows at Mach 7. It was found that at very high blowing ratios, a negative temperature gradient may be present at the wall. The coolant

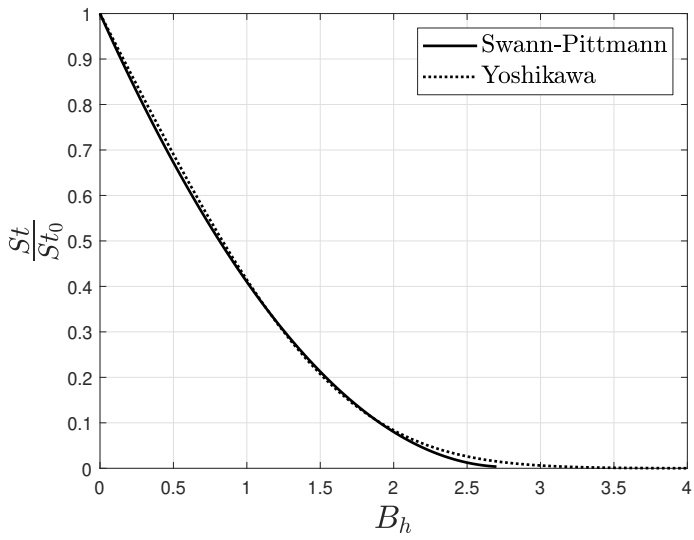

(a) Stagnation point

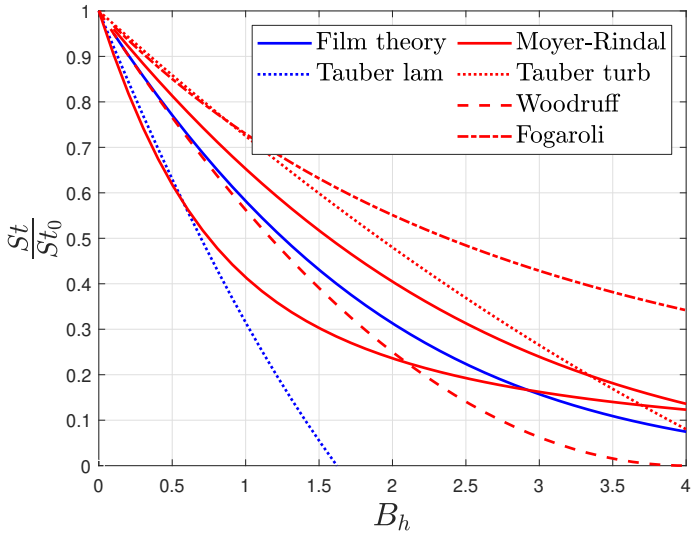

(b) Flat plate

Figure 2.5: Comparison of the Swann-Pittman [108], Film theory [92], Woodruff and Lorenz [126], Fogaroli et al. [127], Yoshikawa [113], and Tauber [14] correlations. Laminar correlations are blue and turbulent red.

is accelerated in the stream-wise direction downstream, promoting dissipation of energy. This results in a reduction in the temperature of the coolant that is injected at wall temperature and thereby induces a negative temperature gradient at the wall that leads to a negative heat flux. Keller and Kloker [125] observed similar results in the context of film cooling holes. This suggests that for laminar flow, transpiration cooling may be even more effective than previously expected. Finally, closely related to the issue of characterising surface heat transfer with cooling is

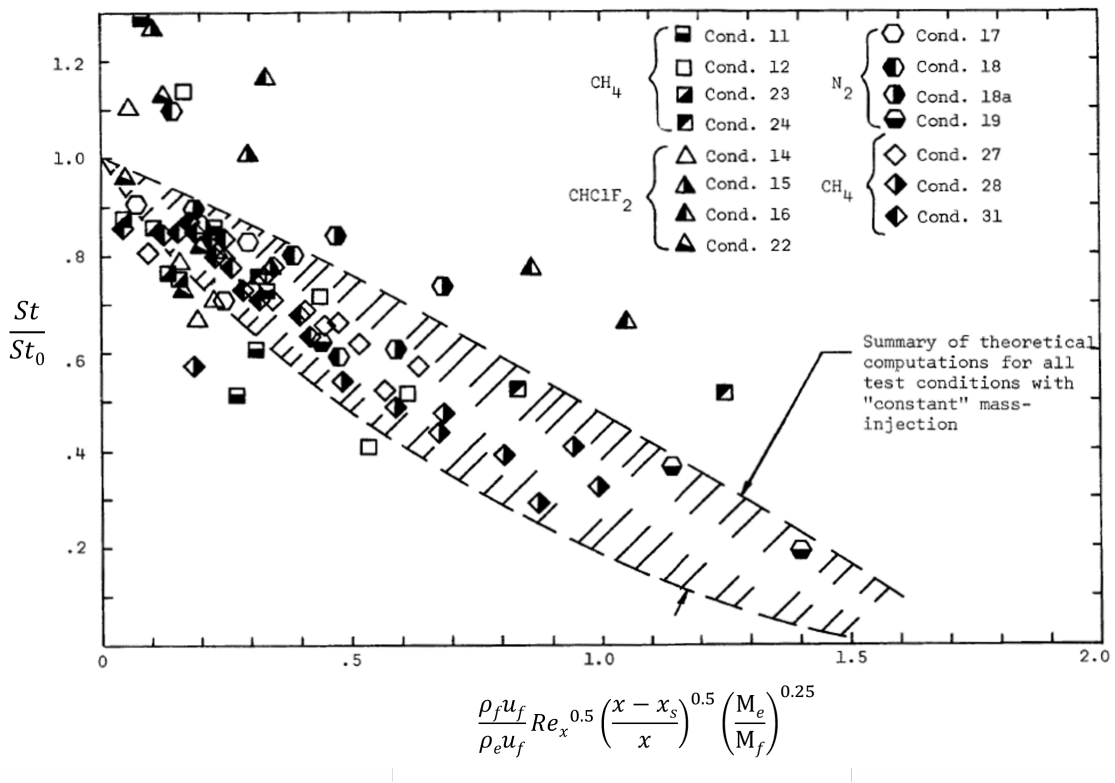

Figure 2.6: Summary of laminar experimental and numerical results of constant mass injection from Ref. [33].

the effect on boundary layer transition. A range of studies, as summarised by this review paper by Schneider [43], have explored the effect of blowing on the transition since the late 1960s. More recently, Cerminara et al. [105] conducted DNS (Direct Numerical Simulation) simulations on a flat plate with a porous injector modelled using spherical elements with equivalent porosity and permeability as a ZrB_2 UHTC. They found that porous injection on an unstable boundary layer leads to a more rapid transition process compared to slot injection, whilst the mixing of coolant within the boundary layer is enhanced in the porous injection case, increasing cooling performance.

Shock Wave-Boundary-Layer Interactions

As discussed in Chapter 1, a major source of peak heating in hypersonic vehicles are regions of shock-shock interaction. Holden and Sweet [45] investigated the effects of an impinging oblique shock on the flowfield and surface characteristics

of a transpiration-cooled wall (flat plate) in turbulent hypersonic flow. A 2D shock generator was used to generate oblique shocks, which impinged onto the transpiration-cooled surface. It was found that transpiration cooling is a very effective method of reducing both the heat transfer and skin friction loads on the surface. Perhaps more surprisingly, it was discovered that the interaction region between the incident shock and the transpiration-cooled boundary layer did not result in significant flow distortions. The increase in heating downstream of the shock impingement point could easily be reduced to the values without shock impingement by a relatively small (5-10%) increase in the transpiration cooling to this region compared to the unshocked case (Fig. 2.7). From the experiments, a simple correlation relationship was developed based on a modified blowing parameter defined as

$$B_{h,s} = \frac{F_3}{St_3} = \frac{\dot{m}_f}{\rho_3 u_3} \cdot \frac{\rho_3 u_3 c_p (T_0 - T_w)}{\dot{q}_w} = \frac{\dot{m}_f c_p (T_0 - T_w)}{\dot{q}_w} \tag{2.23}$$

where St_3 is the Stanton number based on the boundary layer edge parameters downstream of the re-compression shock, $\dot{m}_f$ is the injected mass flux, and the freestream parameters (ρ and u) are determined from local inviscid conditions downstream of the shock denoted by the subscript (3). Based on this, the heat transfer reduction downstream of the shock interaction region in turbulent flows was correlated with the following expression

$$\frac{St}{St_{0,s}} = 1 - 0.92 \cdot \left[1 - \exp\left(- \frac{\left(\frac{\mathrm{M}_\infty}{\mathrm{M}_\mathrm{f}}\right) \cdot B_{h,s}}{4} \right) \right] \tag{2.24}$$

where $(\frac{\mathrm{M}_\infty}{\mathrm{M}_\mathrm{f}})$ is a molecular weight correction to account for the differing molecular weights of helium and nitrogen. This correlation, as shown in Fig. 2.8, was based on fitting a large number of test points with 5°, 7.5° and 10° shock generator angles at Mach 6 and 8 in which transpiration cooling was introduced with both nitrogen and helium gases.

Strauss et al. [121] compared six correlations for a transpiring wall in a turbulent boundary layer, including that of Kays et al. [36] and Meinert et al. [95], with

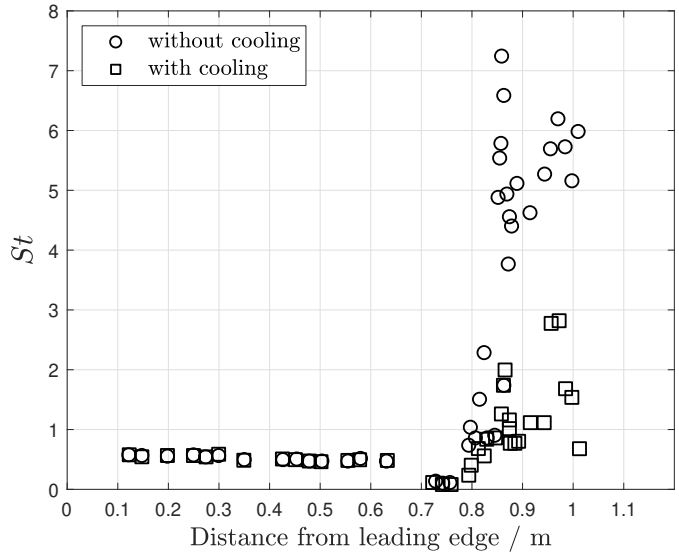

Figure 2.7: Stanton numbers at Mach 6 with and without helium transpiration cooling for shock interaction from a 10.1° shock generator. Figure adapted from Ref. [45].

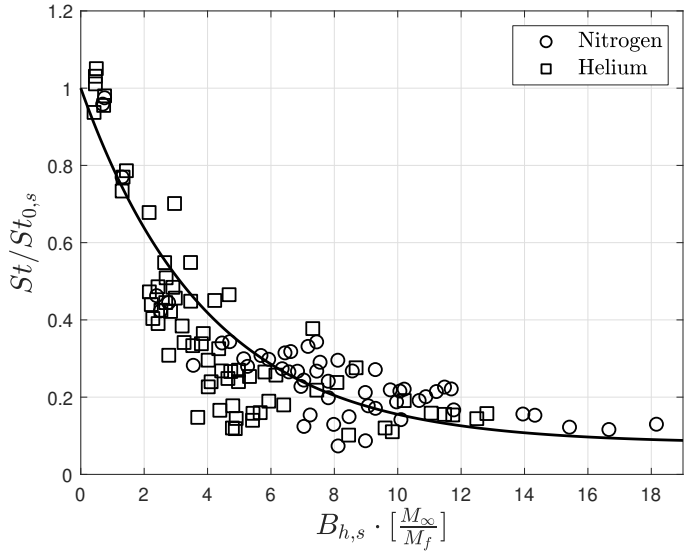

Figure 2.8: Correlation of heating reduction ratio, Eq. (2.24), with modified blowing parameter, $B_{h,s}$ for shock generator angles of 5°, 7.5°, and 10° and both nitrogen and helium coolants. Figure adapted from Ref. [45].

experimentally obtained data employing porous walls made of sintered stainless steel. The authors used K-type thermocouples to measure the transpiring wall temperature in a supersonic flow with blowing ratios up to approximately 8%. It was shown that all of the correlations overestimated the cooling efficiency by up to 25%. Thereafter, the response of the transpiration-cooled surface to shock impingement caused by a 9.3° half wedge was investigated. The results show, encouragingly, that

shock impingement only led to moderate reductions ($\approx 5\%$) in cooling efficiency compared to the case without impingement. This is a promising result though the authors note that hotspots due to shock-boundary layer interaction on the porous wall can be an issue, with locally high thermal loads and an increase in failure of the porous material.

Jiang et al. [120] investigated the influence of shock waves on supersonic transpiration cooling at Mach 2.8 on a sintered bronze plate. The porous wall temperature was measured by an infrared camera and then compared to a 2D CFD model. Transpiration cooling efficiency is reduced due to oblique shock wave impingement with further reduction with an increase in the shock intensity. The numerical results are in good agreement with experimental data showing promise that computational tools may be employed for transpiration-cooled shock interaction regions.

Downstream of the Injector

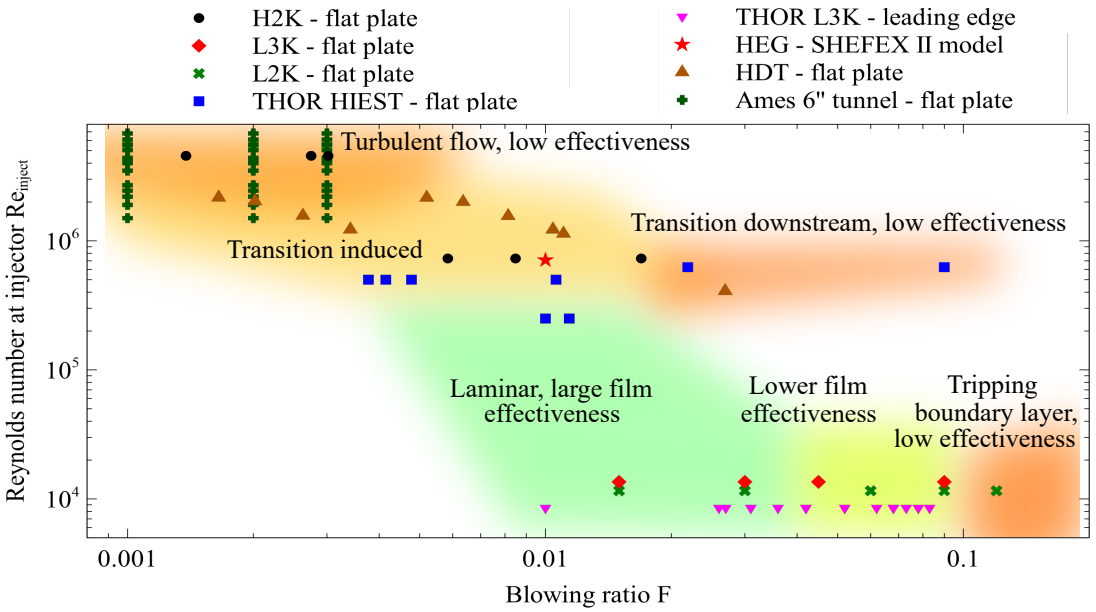

Figure 2.9: Overview of transpiration-cooled experiments on flat surfaces [37, 39, 42]. Figure adapted from Ref. [57].

Significant research has been conducted on the film efficiency downstream of injectors for flat plate models in hypersonic wind tunnels. Figure 2.9 summarises

key investigations in open literature [37, 39, 42]. All of the studies employed very similar models, i.e. a flat plate at various angles of attack with a single injector. The focus of these studies was the characterisation of the downstream film effectiveness, i.e. heat flux or surface temperature distributions were measured, which allowed for the identification of transition. The conclusions of the respective test campaigns are indicated in the figure by a background colour. Notably, the results from the THOR project [42] - which used a carbon-carbon (C/C) type CMC as the porous material, show very clearly that the effect of transpiration cooling is considerably higher for low Reynolds number flows (laminar boundary layers) compared to high Reynolds number flows (turbulent boundary layer). Therefore the coolant injection rates (i.e. the blowing ratio) needs to be controlled; otherwise, this can trip the laminar boundary layer, trigger transition and decrease the effectiveness. As expected, the ideal application of transpiration cooling is in low Reynolds number regimes with low blowing ratios. The laminar flow remains mostly undisturbed, and a coolant film is formed that does not suffer from strong mixing with the hot external flow. Larger blowing ratios lead to early triggering of turbulence and increase coolant-external flow mixing, which decreases the overall effectiveness of the cooling method. Conversely, even low blowing ratios lead to transition when the free stream Reynolds number is increased. Especially poor performance is noticed for high Reynolds number flows with large blowing ratios.

Modelling the mixing between the coolant and freestream downstream of the injector has been extensively studied for over 70 years in the context of film cooling. Several authors have developed correlations for the cooling effectiveness downstream of the injector in turbulent flows based on an energy balance and a turbulent velocity profile. Goldstein [122] reviewed a range of correlations, including those that varied in slot or hole geometry and injection type, i.e. tangential and non-tangential injection. Although the majority of the studies were concerned with slot or hole injectors in subsonic flow, some were conducted in supersonic flows featuring a porous injector [35]. In fact, the correlation of Kutetaldze [35] was selected as the film effectiveness model for the PIRATE numerical code. On the other hand, only

very few studies on the downstream film effectiveness in laminar flows have been published. Heufer and Olivier studied the downstream effectiveness on angled plates and stagnation points [128]. A simple analytical model was provided by curve-fitting their experimental data [124]. Ifti et al. [100] experimentally measured surface heat transfer and coolant concentration downstream of a ZrB_2 UHTC injector on a flat plate in laminar flow. The downstream heat transfer ratio was successfully correlated utilising the same approach as Heufer and Olivier, albeit with different correlation coefficients due to the lower blowing ratios considered.

2.3 Choice of Coolant

Previous work has predominantly focused on gases. The non-toxic noble gases, helium, neon, argon, krypton, are inert and thus most suited to protect the surface from oxidation. Helium and argon were used to transpiration cool a porous flat plate in a hypersonic cross-flow [46] and a nose cone in hypersonic flow [114]. Dichlorodifluoromethane (Freon-12) was commonly used in the literature from the 1950s to 70s for flat plates and cones [33] but was banned due to its damaging effect on the ozone layer. Another commonly used gas is nitrogen which is inexpensive and readily available, thus making it a good gas for initial experiments.

To account for dissimilar gases, various authors have proposed different correction factors to the blowing parameter based primarily on either the ratio of molecular weights or the specific heat capacity. Kays [91] introduced a scaling factor for foreign gas injection on a flat plate. The blowing parameter, B_h, is scaled by the heat capacity ratio of the injectant and the boundary layer edge gas as follows

$$\left(\frac{c_{\mathrm{p,f}}}{c_{\mathrm{p,e}}}\right)^n \tag{2.25}$$

where $n = 1/3$ is used for laminar flows and $n = 0.6$ for turbulent. For a stagnation point, Marvin and Pope [117] suggest the following scaling parameter based on the molecular weight

$$\left(\frac{\mathrm{M_e}}{\mathrm{M_f}}\right)^n \tag{2.26}$$

where n is between 0.25 and 0.4 depending on the reference consulted [117]. For shock impingement regions, Holden and Sweet [45] proposed a scaling parameter $n = 1$ that best fits the experimental data. Generally speaking, these correlations show that a gas that is both lighter and with higher heat capacity performs best. Thus, in past experiments, helium has provided the best cooling performance for a given mass flux due to its high heat capacity and low molecular weight. However, the low molar mass also leads to high outflow velocities, which can be more disturbing to the boundary layer [43].

Liquids have also been considered for transpiration cooling. Water was investigated due to its high cooling capacity per unit mass. As a potential application for Spaceliner, a transpiration-cooled stagnation probe was heated to 2000 K in an arc-heated wind tunnel [116]. Water injection reduced the surface temperature to 300 K and was found to be much more efficient, per unit mass, than nitrogen. However, the formation of an ice beard was observed, which partially blocked the pores. The ice beard would not only block the pores but also disturb the flow field, leading to early transition. For the purposes of this thesis, the focus has been on inert gases due to the additional benefit of oxidation protection.

2.4 Choice of Material

Initially, transpiration cooling systems considered porous metals such as sintered porous stainless steel and bronze [45, 129]. Porous materials with smaller particle sizes were found to perform better due to the enhanced internal convective heat transfer. In addition, a higher thermal conductivity can be beneficial to quickly remove heat from the surface, acting as a heat sink. This may be a disadvantage if the high thermal conductivity causes the underlying substructure, which is often made of lighter materials with lower operating temperatures, to rise above material limits. Recently, the focus has shifted to the usage of porous ceramics and

carbon ceramic composites. These alternatives are lighter with higher operating temperatures. A selection of properties comparing the two is given in Table 2.2. The carbon-carbon (C/C) type CMC has been used extensively for transpiration cooling experiments by DLR. The reason for this is due to the very high operating temperature of approximately 1800 K [46] as well as high specific strength and modulus. Another candidate is the novel use of zirconium diboride (ZrB_2), which is an Ultra High-Temperature Ceramic (UHTC). However, ZrB_2 and UHTCs, in general, are brittle and have low flexural strength, typically $\sigma_f < 200$ MPa. In comparison, C/C is ductile and has a tensile strength of $\sigma_t > 1100$ MPa. In addition, C/C has a lower density than UHTCs. Therefore, C/C features a much higher strength-to-density ratio. Despite this, ZrB_2 is attractive due to its great thermal properties, which can withstand temperatures of over 3000 K. In addition, UHTCs have particle sizes smaller than 10 μm, and therefore eject the coolant in bulk as opposed to individual jets. In fact, as illustrated by Fig. 2.10, Ifti et al. [65] characterised a range of UHTCs samples and found they exhibited a very uniform outflow with an average standard deviation of only 25.1% with respect to the mean value. This is desirable as it minimises the disturbance of the boundary layer and maximises the protection provided by the coolant film.

Table 2.2: Comparison of selected properties between C/C and UHTC. C/C data from Schweikert et al. [130] and UHTC data from Wang and Vandeperre [50].

Material	$\rho_{\phi=100\%}$ kg m^{-3}	σ_t or σ_f / MPa	k / W m^{-1} K^{-1}	Melting point / K
C/C	>1400	<1100	$\approx$ 13.5	$\approx$ 1800
UHTC	6080	<200	56	3505

2.5 Experimental Heat Transfer Measurement Techniques for Transpiration Cooling

The majority of past transpiration cooling experiments have employed conventional heat-flux sensors, such as thin film gauges and thermocouples [32, 34, 45]. Thin film gauges are one of the most common measurement techniques found in short

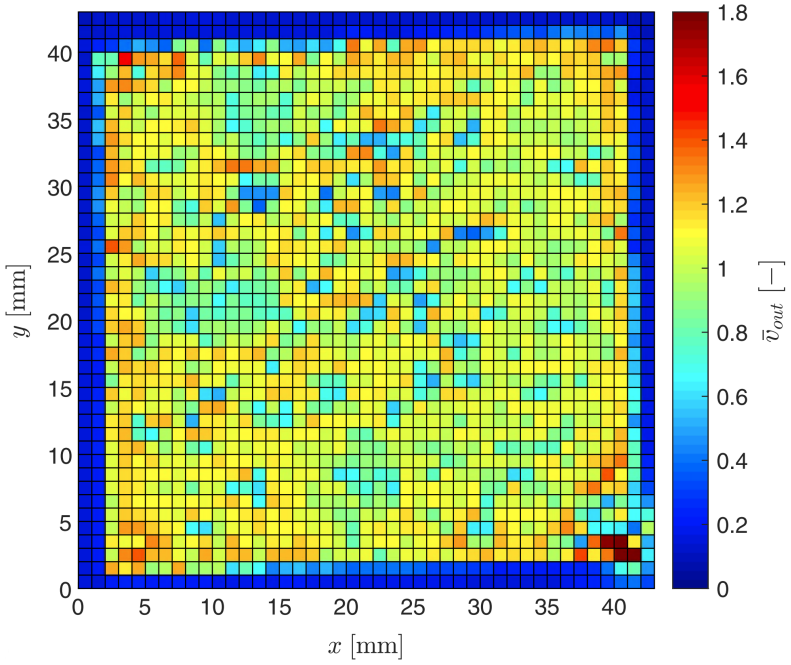

Figure 2.10: Outflow map of a UHTC sample in terms of the nondimensional output velocity $\overline{v}_{out}$. Figure reproduced from Ref. [65].

duration facilities due to their fast response time and accuracy [131]. A thin film gauge consists of a film of conductive material, normally platinum or nickel, deposited in the form of a thin track onto an insulating substrate. For pure metals, resistance increases as temperature increases, and so, when the gauge is heated, the temperature can be measured through a change in resistance. Such gauges have been used successfully in hypersonic wind tunnels for a number of decades.

However, such single-point sensors are limited in terms of the spatial resolution they provide; and moreover, physical constraints may prevent them from being installed in complex geometries. In the context of transpiration cooling, past investigators have primarily used porous materials with relatively large pore sizes or hole diameters. For example, Holden and Sweet [45] employed a transpiration-cooled stainless steel plate with a hole diameter of 1 mm. This contrasts with modern micro-porous injectors, which can have pore sizes of the order of 10 μm. To ensure that the coolant outflow is not disturbed by these modern materials, an alternative, non-intrusive measurement technique is required. Two common non-intrusive heat transfer measurement techniques are infrared thermography

and temperature-sensitive paint (TSP). TSP is a technique where a luminophore, when excited at specific wavelengths, re-emits radiation at a different wavelength, with the intensity of the emission related to temperature. Whilst TSP has been employed successfully at hypersonic facilities [132–134], a key drawback for the current application is that painting on top of porous materials is likely to block the pores and otherwise change the outflow characteristics of the porous injector.

Infrared thermography has several advantages over other surface temperature measuring techniques. It provides a two-dimensional spatial image, is non-intrusive, with very high sensitivity (down to 20 mK) and has a low response time (down to 20 μs) [135]. Some of the disadvantages include the very high cost to purchase a high-performance, high-speed infrared camera; the need for optical access; and the requirement to account for external sources of radiation. This last point can make quantitative infrared measurements in high enthalpy facilities very difficult without judicious use of filters or otherwise [136]. Further details about this technique are elaborated in Appendix B.

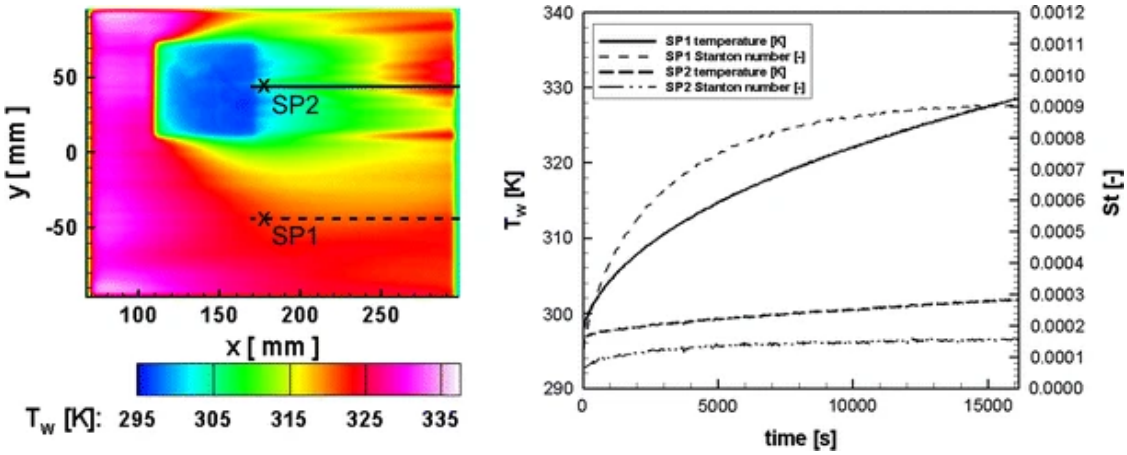

Figure 2.11: Measured surface temperature distribution of the flat plate model with air injection as coolant. Figure reproduced from Ref. [39].

Several transpiration cooling experiments have employed infrared thermography to resolve the surface heat flux. Langener et al. [46] used infrared thermography in a steady Mach 2.1 condition on a C/C porous CMC. The camera was calibrated in situ to obtain quantitative wall temperature maps. A key benefit of infrared thermography was illustrated by the experiments of König et al. [69] where the spatial

temperature measurements reveal inhomogeneities in coolant outflow distribution (see Fig. 2.2), measurements that would be highly difficult or even impossible with discrete gauges. Similarly, for a short-duration blowdown facility, Gülhan and Braun [39] employed infrared thermography to assess the heat transfer reduction downstream and around a C/C porous CMC injector. Quantitative temperature values were achieved by accounting for the emissivity of the PEEK surface and a camera calibration. The full two-dimensional maps show clearly the spread of the coolant downstream of the injector and how this varies with the angle of attack. A key limitation of most infrared cameras is acquisition frequency, with all of the above experiments using cameras with frame rates below 100 Hz. For usage in short-duration facilities with test times of the order of ms or even μs [137, 138], higher frame rate cameras are required in the order of 1s or 10s kHz to capture the transient change in wall temperature. Such experimental testing has been conducted with infrared thermography [136, 139], but none in the context of transpiration cooling.

2.6 System Studies

The engineering correlations and methods described in Section 2.2 are highly useful when applied to low-order models. This is useful for sensitivity analyses and to investigate the performance of transpiration cooling over different trajectories and conditions. Nonetheless, few studies are available in the open literature which investigate the application of transpiration cooling for a given geometry over a complete flight trajectory. One of the earliest such studies by Schneider et al. [140] considered the application of transpiration cooling to a two-dimensional axisymmetric nose tip at steady flight. Two-dimensional effects were found to be highly important for assessing the required plenum pressures for adequate nosetip cooling. Colwell and Modlin [141] investigated hypersonic vehicle leading edge cooling using heat pipe, transpiration and film cooling techniques. Using a finite difference model to simulate transpiration cooling and modelling the heat flux at the leading edge as a simple blunt wedge, they showed that transpiration cooling could reduce the maximum temperature during flight by almost 40% when helium is

used as a coolant. A development of the same numerical method [142] was applied to the case of a scramjet inlet exposed to type IV shock interference heating. It was found that these active cooling techniques can keep maximum surface temperatures to near acceptable values even for this extreme aerodynamic heating environment.

More recently, Böhrk et al. [38] developed a finite difference code HEATS to predict the performance of transpiration cooling for a given flight trajectory. The code utilises a finite difference approach to determine the transient wall heat flux to a transpiration-cooled flat plate under either laminar or turbulent conditions. This code has been validated against ground-based experimental testing and was applied to the SHEFEX II re-entry trajectory. A comparison of flight data and predictions from HEAT showed good agreement (Fig. 2.12), successfully demonstrating its use for transpiration cooling systems design. Dittret et al. [143] considered the design of a transpiration-cooled sharp leading edge for SHEFEX III. An assessment of the mechanical and thermal design of the leading edge was made, in particular the interface between the leading edge and the main body, as well as the infrastructure needed for transpiration cooling. Transpiration cooling was simulated, and this resulted in a reduction from maximum temperatures of over 4400 K at the stagnation point to 3300 K with transpiration cooling. However, this paper simulates transpiration cooling via taking a simple 35% of the nominal heat flux (in line with experimental data from SHEFEX II) and is therefore of little benefit when trying to compare different injection points, injection rates and coolant types.

Hermann et al. [57] conducted a comprehensive systems-level study of transpiration cooling on a 30° half-angle blunted cone with a 0.5 m nose radius and a wall thickness of $L = 10$ mm. The performance of transpiration cooling was assessed by calculating the overall required coolant mass for different steady-state and transient flight scenarios. It was found that the majority of the injection is required on the spherical nose segment of the blunted cone and that both C/C and the UHTC ZrB_2 require similar amounts of coolant injection. A key result was that transpiration cooling is highly effective for flight conditions with velocities

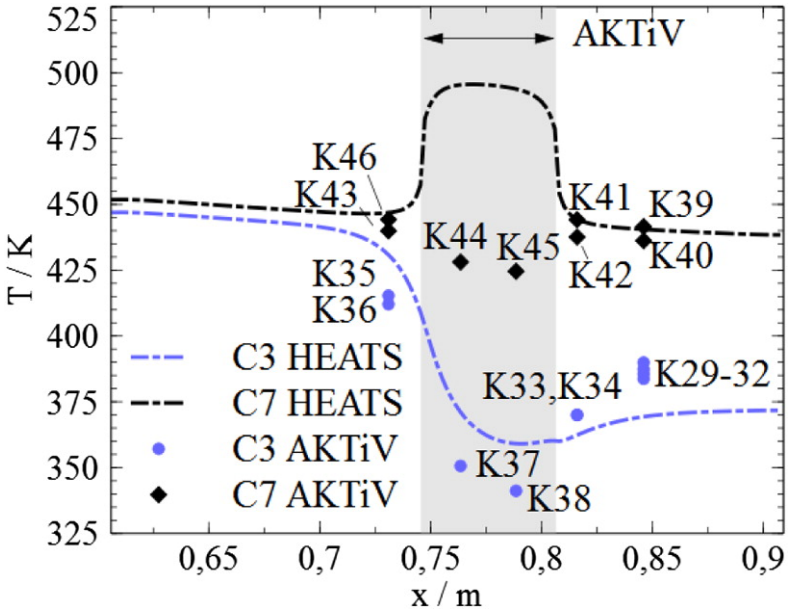

Figure 2.12: AKTiV temperatures along the panel at t = 485.12s. Figure reproduced from Ref. [41].

below 8 km s^{-1} and altitudes above 40 km. However, this study was conducted on a relatively large nose radius of 0.5 m.

Whilst these system studies have explored some of the key design choices for a transpiration-cooled system, none of them extend their analyses to account for the effect of longer-term thermal effects on the underlying substructure. This calculation is generally restricted to full vehicle scale thermal and mechanical simulations such as one conducted for the Space Shuttle in Ref. [144]. However, it is an important consideration, as noted by Steelant et al. [145] in which a constant heat flux was applied to a finite element model of an uncooled SHEFEX II TPS panel. The study showed that, for sustained flight, substructure temperatures could continue to rise well after the outer TPS reaches radiative equilibrium and can potentially violate structural limits.

Chapter 3

Numerical Simulation of Transpiration Cooling for a High-Speed Vehicle with Substructure

Contents

In Chapter 1, it was established that there is a corridor within the altitude-velocity diagram wherein transpiration cooling is likely to be an effective TPS system. In particular, for longer re-entry trajectories (for example Space Shuttle or Skylon), designing a vehicle that incorporates sharper leading edges requires

an active cooling system such as transpiration cooling, otherwise, the maximum temperatures would exceed material limits.

In this chapter, the PIRATE code used for the aforementioned analysis is extended to account for 2D lateral conduction and a substructure. Building upon the steady state study on a 2D stagnation line in Chapter 1, the first part of this thesis applies the updated model to assess the cooling performance of transpiration cooling when applied to a generic wing leading edge and the Space Shuttle trajectory. This work lays down the context and motivation for further experimental studies of transpiration cooling described in subsequent chapters. The following work has been published in the *AIAA Journal* [58]. It is presented in this chapter with small layout changes, but unaltered content. The author contributions are as follows

- Imran Naved: Conceptualisation, Methodology, Investigation, Data Analysis, Writing
- Matthew McGilvray and Tobias Hermann: Supervision

In addition to the published work presented in this chapter, further details of the PIRATE numerical code is detailed in Appendix A.

3.1 Introduction

Hypersonic vehicles are exposed to very high heat fluxes and heat loads during reentry or sustained flight. This requires thermal protection systems to manage these heat fluxes and keep wall temperatures below critical values. Transpiration cooling is an active cooling technology that can enable fully reusable hypersonic vehicles. It relies on a gaseous or liquid fluid that is fed through a porous wall [82]. The coolant leads to internal convective cooling between the porous solid and the fluid, as well as a protective film that keeps the hot external gas away from the surface [27]. Transpiration cooling provides alternative flexibility in the design of future reusable hypersonic vehicles.

Only a few systems-level studies of transpiration cooling have been performed. Colwell and Modlin [141] employed a finite difference code to investigate the feasibility of cooling hypersonic wing leading-edge structures using metal heat pipe and surface mass transfer cooling techniques, including transpiration cooling. Modlin and Colwell [142] then applied this code to the transient thermal behaviour of cooling scramjet inlets using the aforementioned hypersonic leading-edge cooling model, which was modified to include type IV shock interaction surface heating effects [19, 146]. It was found that a combination of transpiration, film, and heat pipe cooling techniques can keep surface temperatures at acceptable levels. Böhrk et al. [38] developed the finite difference code HEATS to determine the transient wall heat flux to a transpiration-cooled flat plate under laminar and turbulent conditions. Both of these models considered an adiabatic backside and did not consider the effects of the integrated heat load to the substructure of the vehicle. Hermann et al. [86] applied the one-dimensional porous impulse response analysis for transpiration cooling evaluation (PIRATE) numerical code to conduct systems studies of transpiration cooling for a blunt cone. This analysis considered radiation coupling between the transpiration-cooled skin and the substructure, but it assumed that the substructure was at a constant temperature. Steelant et al. [145] applied a constant heat flux to a finite element model of an uncooled SHEFEX II (which stands for Sharp Edge Flight Experiment II) TPS panel, showing that substructure temperatures can rise well after the outer TPS reaches radiative equilibrium and potentially violate structural limits.

This paper investigates how transpiration cooling can be applied to wing leading edges to lower the backside temperatures of the porous wall, and therefore the integrated heat load to the substructure. To achieve this, first, the Oxford University in-house PIRATE code is extended to model the two-dimensional effects of lateral conduction within the porous outer wall. Second, the PIRATE code is coupled to the commercial finite element package COMSOL to model the thermal behaviour of the substructure during a particular flight trajectory. The resulting coupled methodology is applied to a 0.1 m nose radius, 15 deg half-angle wing leading edge with the space

shuttle reentry trajectory. The results show a significant substructure temperature reduction due to the application of cooling as well as reduced thermal gradients.

3.2 One-Dimensional PIRATE Model

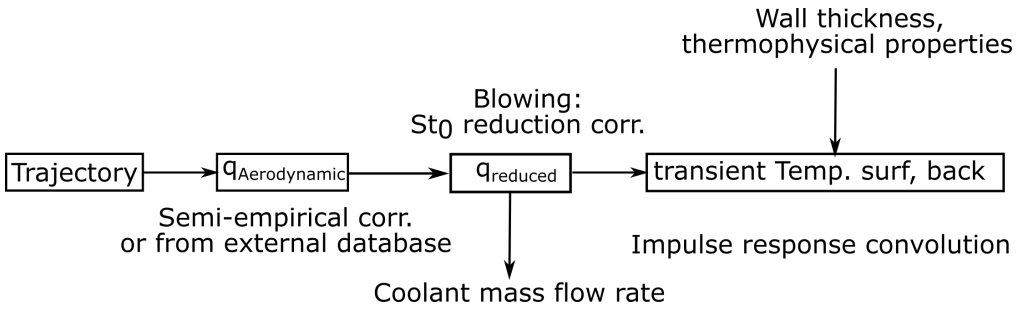

Figure 3.1: Flow chart of the computational approach [86].

The PIRATE numerical code [86] calculates the transient temperature response for a one-dimensional porous material subjected to aerodynamic surface heating. By relying on a method based on impulse response convolution, significantly faster computation times are possible, providing the opportunity to conduct optimization studies for various flight trajectories and geometries. Figure 3.1 shows an outline of the code. For a given trajectory, the aerodynamic heat fluxes with no cooling are calculated from aerodynamic correlations or imported from an external database. The cooling effect of the local heat flux mitigation through blowing and downstream film effectiveness is then taken into account using semi-empirical models [35, 91].

The cooling within the inner structure of a porous material is carried out by convective heat transfer between the material and the coolant. Therefore, the one-dimensional governing equations for the solid and fluid phases are [76]

$$(1-\phi)\rho_s c_{p,s}\frac{\partial T_s}{\partial t} = k_{y,s}(1-\phi)\frac{\partial^2 T_s}{\partial y^2} + h_v(T_f - T_s) \tag{3.1}$$

and

$$\phi\rho_f c_{p,f}\frac{\partial T_f}{\partial t} = \phi\rho_f c_{p,f}\frac{v_f}{\phi}\frac{\partial T_f}{\partial y} + h_v(T_s - T_f), \tag{3.2}$$

where s denotes the solid phase, f the fluid phase, k denotes the thermal conductivity, ρ denotes the density, T denotes the temperature, c_p denotes the specific heat

capacity, ϕ denotes the porosity, h_v denotes the volumetric heat transfer coefficient, v denotes the velocity, t denotes the time, and y denotes the location medially through the material.

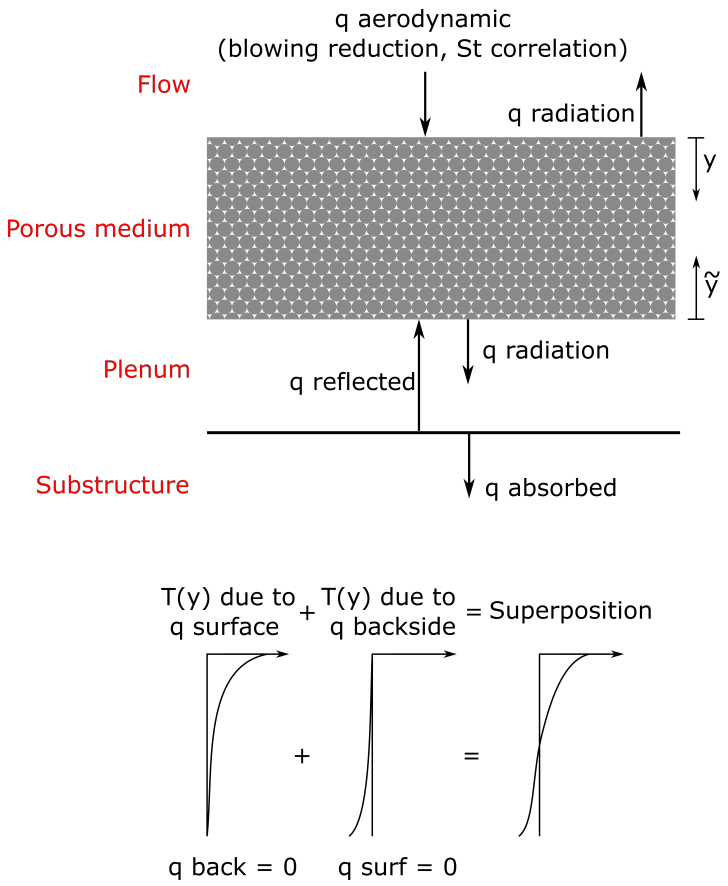

Figure 3.2: Schematic of the one-dimensional thermal model [86].

Figure 3.2 shows a schematic of the one-dimensional thermal model. The temperatures of the solid and fluid phases are calculated based on a given coolant mass flow rate, porous wall thickness, and the thermophysical properties of the solid and fluid phases. The transient temperature calculations are based on an impulse response approach that solves the coupled fluid–solid heat conduction problem with radiation cooling to a constant temperature substructure. As the equations are solved analytically for the normal direction, constant material properties are assumed. This is an inherent limitation of this numerical method and is acceptable given the usage of this numerical code for first-order system studies. In addition, it should be noted that faster computation times are achieved by calculating the surface

and backside temperatures directly, and the temperatures at different intermediate locations through the material are not available without additional computations. This approach is detailed further by Hermann et al. [86].

The PIRATE model has been validated against a variety of experiments: both ground-based and reentry flight testing. In particular, experimental results from the SHEFEX II flight test campaign as well as the RESPACE and IMENS+ campaigns are used [37, 41]. The different validation cases have demonstrated that this numerical model matches experimental data closely and agrees with experimental measurements to within 10%. The relevant effects occurring during transpiration-cooled hypersonic flight (i.e., transient heating, local cooling through blowing, and downstream film coverage) are all replicated to within acceptable accuracy.

3.3 Extension of PIRATE to Quasi-Two-Dimensional Heat Transfer

A key assumption made in PIRATE is that only one-dimensional heat conduction and coolant flow through the porous material are considered. Therefore, when a calculation is conducted across a full body, a series of one-dimensional models are solved independently. Solving for full two-dimensional material conduction and coolant flow is a complex problem that requires knowledge of the complete temperature distribution inside the material. An intermediate solution, suitable for the purposes of rapid system studies, is to only consider two-dimensional conduction and assume coolant flow to be solely in the normal direction. This is a reasonable assumption for many geometries where lateral pressure gradients are small; i.e., the radius of curvature of the surface is much larger than the thickness of the material. Thus, the governing equations for the solid and fluid phases including two-dimensional conduction are

$$\underbrace{(1-\phi)\rho_s c_{p,s}\frac{\partial T_s}{\partial t}}_{\text{Transient heating (solid)}} = \underbrace{k_{x,s}(1-\phi)\frac{\partial^2 T_s}{\partial x^2}}_{\text{Lateral conduction (solid)}} + \underbrace{k_{y,s}(1-\phi)\frac{\partial^2 T_s}{\partial y^2}}_{\text{Normal conduction (solid)}} + \underbrace{h_v(T_f - T_s)}_{\text{Fluid}-\text{solid heat exchange}} \tag{3.3}$$

and

$$\underbrace{\phi\rho_f c_{p,f}\frac{\partial T_f}{\partial t}}_{\text{Transient heating (fluid)}} = \underbrace{\phi\rho_f c_{p,f}\frac{v_f}{\phi}\frac{\partial T_f}{\partial y}}_{\text{Convection}} + \underbrace{h_v(T_s - T_f)}_{\text{Solid}-\text{fluid heat exchange}} . \tag{3.4}$$

By considering only the lateral conduction term in Eq. (3.3), the corresponding governing equation for purely one-dimensional transient conduction in the x (lateral) direction ignoring any convective heat transfer between the solid and fluid phases is

$$\frac{\partial T_s}{\partial t} = \frac{k_{x,s}}{\rho_s c_{p,s}}\frac{\partial^2 T_s}{\partial x^2}, \tag{3.5}$$

where $T_s(x,t)$ is the temperature of the solid material at spatial point x and time t.

To model lateral conduction, a quasi-two-dimensional approach is followed where conduction medially through the material is calculated first using the impulse response method of PIRATE detailed earlier in this paper. Thereafter, the Crank–Nicolson scheme for one-dimensional thermal conduction is applied at every time step to the existing surface and backside temperature history. The advantage of using Crank–Nicholson is its known unconditional stability for both linear and nonlinear heat conduction systems [147]. The Crank-Nicolson scheme can be expressed as

$$\frac{T_x^t - T_x^{t-1}}{\Delta t} = \frac{\alpha}{2}\left[\frac{T_{x-1}^t - 2T_x^t + T_{x+1}^t}{\Delta x^2} + \frac{T_{x-1}^{t-1} - 2T_x^{t-1} + T_{x+1}^{t-1}}{\Delta x^2}\right], \tag{3.6}$$

where x is the spatial step along the x axis (from $x = 0$ to W), t is the time step, Δt is the time step discretisation, Δx is the spatial discretisation and α is the thermal diffusivity defined as $\frac{k_{x,s}}{\rho_s c_{p,s}}$. Neumann boundary conditions are considered such that there is zero heat transfer across the sides (adiabatic boundary condition)

$$\left.\frac{\partial T}{\partial x}\right|_{x=0,\mathrm{W}} = 0. \tag{3.7}$$

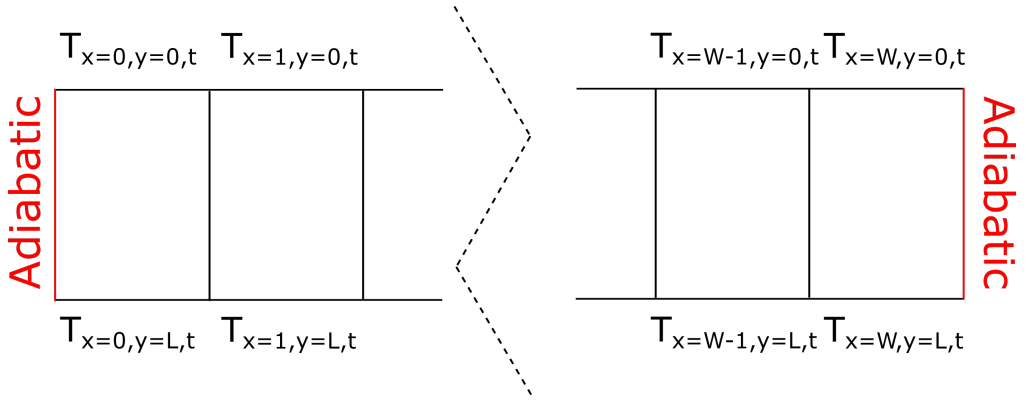

Figure 3.3: PIRATE 1D output temperature field.

This scheme is applied to the existing transient temperature distribution from PIRATE via the following steps:

1. The PIRATE one-dimensional (1D) simulation is applied to each node. As per Fig. 3.3, this results in a temperature field $T_{x,y,t}$ describing every node of the two-dimensional material (x,y) at each time step t.

2. An array of differential temperatures ($dT_{x,y,t} = T_{x,y,t+1} - T_{x,y,t}$,) for the surface and backside are calculated between each time step. These differential temperatures represent an instantaneous temperature rise (or fall) due to the heat flux applied in each time interval dt. As these are based on the 1D conduction model, they have to be relaxed through lateral conduction; i.e., the heat will spill over to neighbouring nodes.

3. The Crank-Nicolson algorithm is applied to the differential temperatures at the surface and backside separately. This results in a t by $\tilde{t}$ matrix where the 1D heat conduction equation is solved in the lateral direction for every spatial node from x = 0 - W at y = 0 (the surface) and y = L (backside):

$$dT^{\text{lat}}_{x,y,t,\tilde{t}} = \begin{pmatrix} dT^{\text{lat}}_{x,y,t_1,\tilde{t_1}} & dT^{\text{lat}}_{x,y,t_1,\tilde{t_2}} & \cdots & dT^{\text{lat}}_{x,y,t_1,\tilde{t_{\text{end}}}} \\ dT^{\text{lat}}_{x,y,t_2,\tilde{t_1}} & dT^{\text{lat}}_{x,y,t_2,\tilde{t_2}} & \cdots & dT^{\text{lat}}_{x,y,t_2,\tilde{t_{\text{end}}}} \\ \vdots & \vdots & \ddots & \vdots \\ dT^{\text{lat}}_{x,y,t_{\text{end}},\tilde{t_1}} & dT^{\text{lat}}_{x,y,t_{\text{end}},\tilde{t_2}} & \cdots & dT^{\text{lat}}_{x,y,t_{\text{end}},\tilde{t_{\text{end}}}} \end{pmatrix}, \tag{3.8}$$

where the new temperature field has values at two distinct times: t and $\tilde{t}$. Both of these range from 0 to t_{end} where t represents the transient change in temperature due to one-dimensional medial conduction at a given time and $\tilde{t}$ represents the change due to lateral conduction. These two separate time variables occur because essentially two independent conduction problems have been solved: in the normal direction by applying the impulse response method of PIRATE, and laterally using the Crank–Nicolson method.

4. The two independent transient conduction solutions are then combined to form the two-dimensional temperature field. This is accomplished by appropriately weighting the contributions of both conduction terms at every time step; i.e., for example, at time step t_2, $T_{x,y,2} = dT_{x,y,2,1} + dT_{x,y,1,2} + T_{x,y,0}$. This process is displayed in Fig. 3.4 where a schematic of the quasi-two-dimensional method is shown for an arbitrary temperature distribution. For example, at t_2, the 1D conduction solution at t_2 is added to the solution at t_1 with lateral conduction applied to $\tilde{t_2}$. This can also be represented as the summation of a diagonal of the matrix in Eq. (3.8) where the resulting temperature field is

$$T^{\text{lat}}_{x,y,t_{\text{end}}} = T^{\text{lat}}_{x,y,0} + \sum_{t=1}^{t_{\text{end}}} dT^{\text{lat}}_{x,y,t,t_{\text{end}}+1-t}, \tag{3.9}$$

where t_{end} is the time step of interest, $T^{\text{lat}}_{x,y,0}$ is the initial temperature distribution and $T^{\text{lat}}_{x,y,t_{\text{end}}}$ is the new temperature distribution with lateral conduction applied.

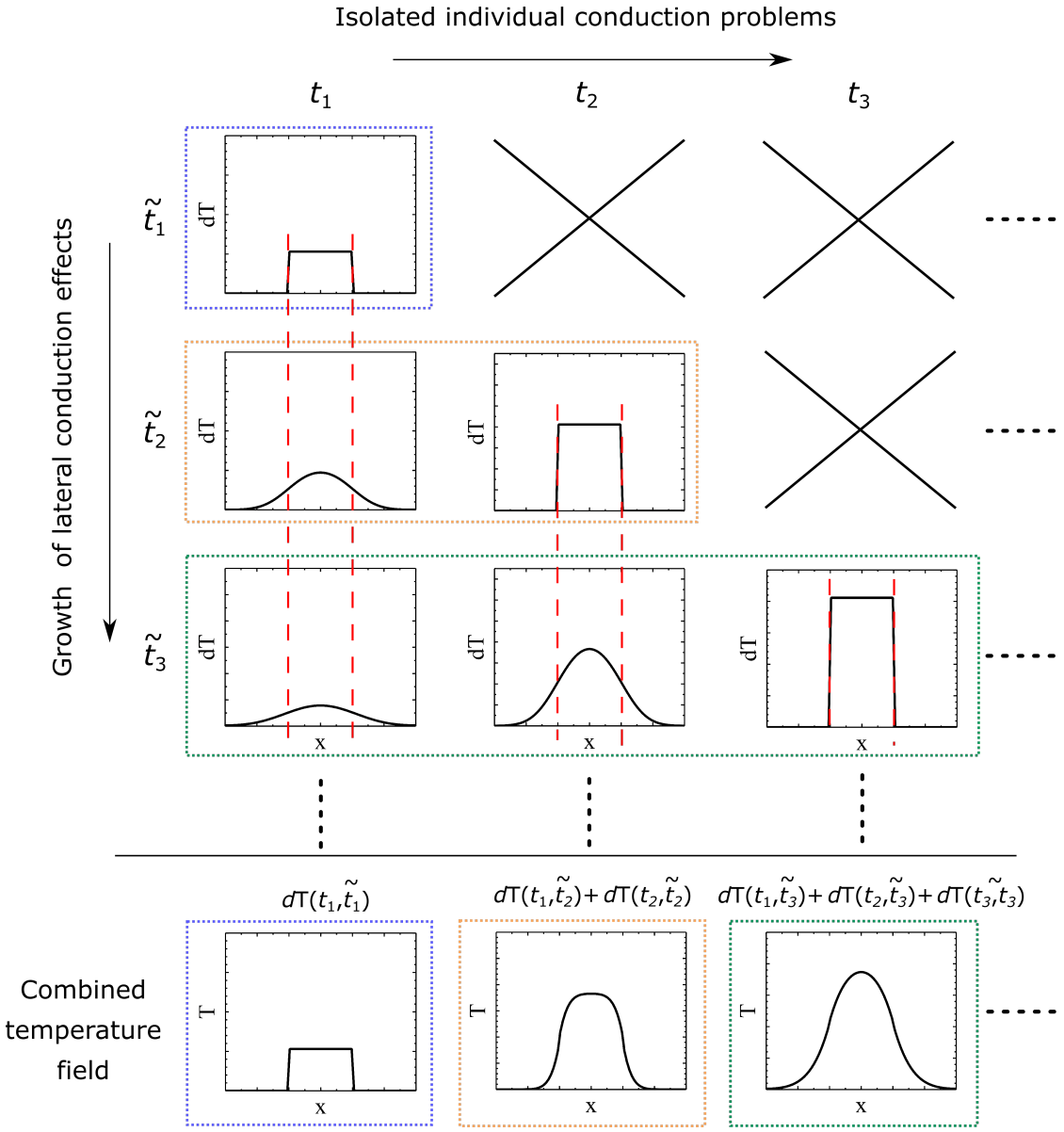

Figure 3.4: Schematic of the 2D conduction method.

The key advantage of this approach is the very short computational time. On top of the one-dimensional calculation time, this method solves for the two-dimensional (2D) field with only a 20% increase in computation time. For a typical calculation with 2000 time steps and 60 spatial nodes, a complete trajectory simulation takes only around 60–75 min. This enables first-order systems studies of the application of transpiration cooling for different trajectories, geometries, and materials to be feasible on a desktop computer. Henceforth, the quasi-two-dimensional version of PIRATE will be referred to as “PIRATE Q2D,” whereas

the original one-dimensional code is "PIRATE 1D."

This method of calculating lateral conduction is applicable for moderate thermal gradients where the effects of variable wall thickness and two-dimensional coolant mass flow do not dominate.

3.4 Validation of the Quasi-Two-Dimensional Heat Conduction Model

3.4.1 Uncooled - COMSOL Finite Element Analysis

First, this method to solve for lateral conduction has been validated by comparing the temperature response of the PIRATE Q2D code with the COMSOL commercial finite element package. For zero coolant mass flux, the differential equations for the solid and fluid phases of the porous material reduce to the well-known equations for two-dimensional conduction. In this case, the temperature response via the quasi-two-dimensional method described here can be compared directly with a commercial finite element package like COMSOL [148].

Two high-temperature porous materials are chosen: the main purpose of which is to confirm that the quasi-two-dimensional approach accurately models the transient change in temperature through the material. These are carbon-carbon (C/C) ceramic composite [82] and the ultra-high-temperature ceramic (UHTC) ZrB_2 [57]. The material parameters used in this study are summarised in Table 3.1. Both materials have been investigated in previous transpiration-cooling studies for high-speed vehicles [27, 41].

The two-dimensional model described in Fig. 3.5 is used as a validation case. Initially, the material is set at 300 K. Subsequently, a step change in heat flux of 0.1 MW m^{-2} is applied at the centre (from x = -0.05-0.05 m) of the model for 20 s and then allowed to thermally dissipate until 100 s. Adiabatic boundary conditions are assumed for the remainder of the boundaries. This represents a highly two-dimensional and transient heat transfer case where the front and backside temperatures initially strongly diverge, eventually approaching equilibrium for the

Table 3.1: Material properties used in this study. Note: The K_D and K_F terms for UHTC were measured using the ISO standard rig of Ifti et al. [65] and C/C by applying the pressure decay method of Innocentini et al. [66]

Material	UHTC [57]	C/C [38, 82]
ϕ	0.41	0.13
ε	0.7	0.85
$k_{x,s}$ / W m^{-1} K^{-1}	41.4	14
$k_{y,s}$ / W m^{-1} K^{-1}	41.4	2
$c_{p,s}$ / J kg^{-1} K^{-1}	437	1650
ρ_s / kg m^{-3}	6100	1400
K_D / m^2	$3.4 \cdot 10^{-14}$	$1.645 \cdot 10^{-13}$
K_F / m	$15.7 \cdot 10^{-8}$	$2.9 \cdot 10^{-6}$
h_v / W m^{-3} K^{-1}	$5.5 \cdot 10^4$	$1 \cdot 10^4$

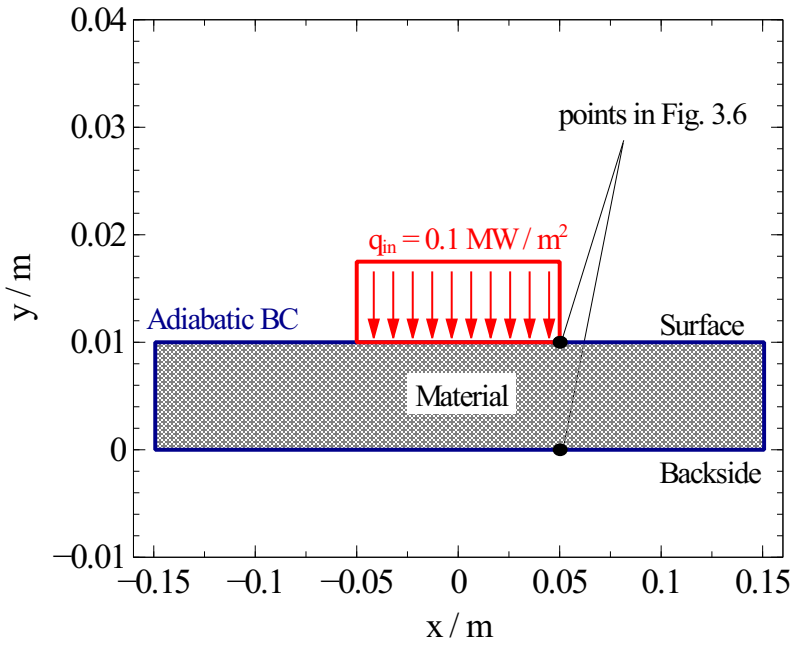

Figure 3.5: Schematic of the validation case.

steady state. COMSOL solves for heat conduction via the finite element method. For this validation model, the COMSOL mesh has a maximum element size of 0.003 m leading to 891 domain elements and 209 boundary elements. Time stepping is achieved with a relative tolerance of 0.0001.

Mesh sensitivity analysis has been carried out for the COMSOL simulation. Three meshes were compared: a coarse mesh with 47 elements, a medium mesh with

891 elements and a fine mesh with 84062 elements. Less than 0.01% difference in the final solution was found between the medium and fine meshes. For this reason, the medium COMSOL mesh was used for all subsequent simulations.

Table 3.2: Time step sensitivity study. Note: ΔT_{max} is the maximum temperature difference between PIRATE Q2D and COMSOL. This is recorded in both absolute and percentage terms.

dt / s	ΔT_{max} / K	ΔT_{max} / %	Simulation time / s
0.5	35.57	6.68	13
0.25	26.81	5.02	28
0.1	18.11	3.39	86
0.05	13.26	2.48	280
0.025	9.60	1.79	1286

Table 3.3: Spatial discretisation sensitivity study with dt = 0.05 s.

dx / m	ΔT_{max} / K	ΔT_{max} / %	Simulation time / s
0.02	64.79	16.14	1658
0.01	31.38	7.82	3002
0.005	12.66	3.15	4710
0.0025	4.59	1.14	11196

The advantage of the impulse response method is that the temperature distribution vertically through the material can be solved analytically with the accuracy of the final solution only dependant on the time step, dt. Firstly, a time step sensitivity study is conducted by setting up a PIRATE 1D simulation (no lateral conduction effects considered) at the centre of the validation model ($x = 0$ m) with the C/C material. The transient surface temperature evolution of COMSOL and PIRATE 1D, with several different time steps from dt = 0.025 to dt = 0.5 s, are shown in Fig. 3.6a. For each time step, the time taken to complete each simulation and the peak temperature difference between PIRATE 1D and COMSOL are shown in Table 3.2, where the simulations are completed using a six-core 3.2 GHz desktop computer with 64 GB of RAM. To achieve numerical accuracy whilst ensuring quick calculation times, dt = 0.05 s (highlighted in cyan) is chosen for all subsequent

simulations. For this time step, there is a peak temperature difference of 2.48% (or 13.26 K) compared to COMSOL with a simulation time of 280 s.

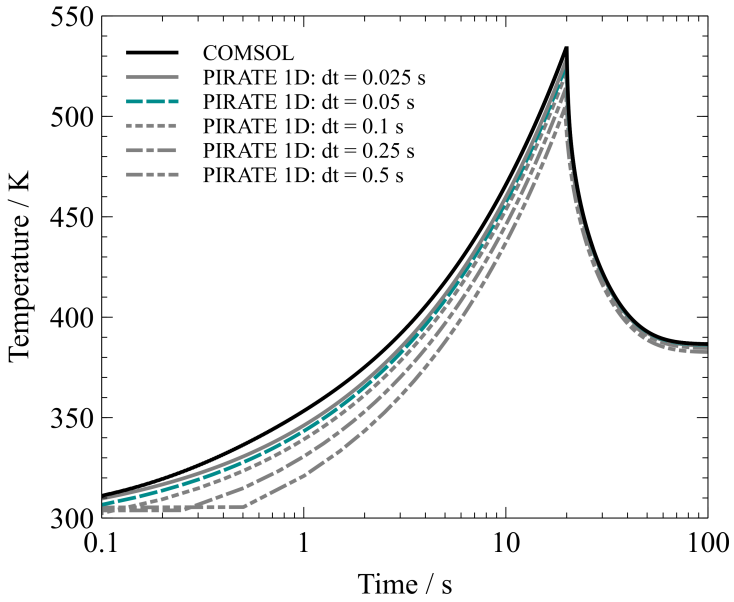

(a) Time discretisation, at $x = 0\,\mathrm{m}$

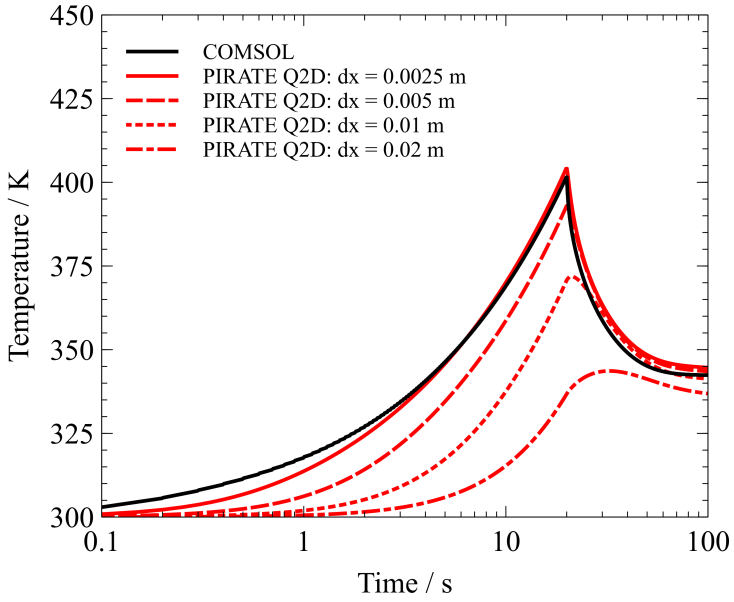

(b) Spatial discretisation, assuming dt $= 0.05\,\mathrm{s}$ at $x = 0.05\,\mathrm{m}$

Figure 3.6: Surface temperature evolution - comparing COMSOL and PIRATE 1D/Q2D for C/C uncooled.

In addition, a similar study is conducted to investigate the sensitivity of temperature distributions to spatial discretisation in the x direction, dx. This is important for the validation case due to the very large spatial thermal gradient imposed at the lateral boundary of the surface heat flux. As shown in Fig. 3.6b, the temperature distributions are highly sensitive and a suitable dx needs to be picked on a case-by-case basis. Assuming dt = 0.05 s, for the subsequent simulations dx = 0.0025 m is chosen which represents a peak temperature difference of 1.14% (or 4.59 K). The simulation time for this fully 2D simulation is 11196 s, or around 3 hours (Table 3.3). It should be noted that a very fine spatial discretisation is required for this validation case, due to the large thermal gradients imposed. It is envisaged that for more uniform spatial heat flux distributions, sufficient accuracy can be achieved with a coarser mesh.

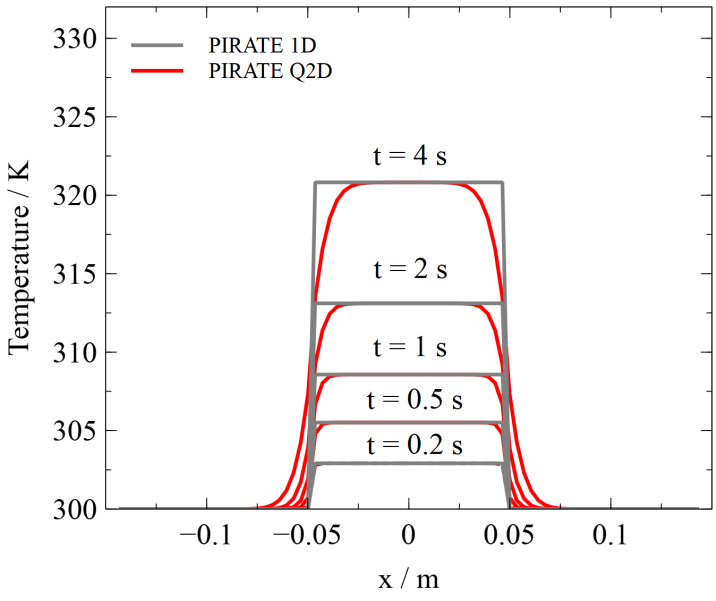

Figure 3.7: Surface temperature evolution along the x axis: C/C uncooled.

Figure 3.7 shows the evolution of the surface temperature over several time steps for the C/C case. Comparing the PIRATE 1D to the PIRATE Q2D code, it is clear that at later time steps, more heat flux dissipates toward the sides, leading to a "smoothing" of the surface temperature profile along the x axis. This

demonstrates that PIRATE Q2D correctly models the transient lateral distribution of surface temperature.

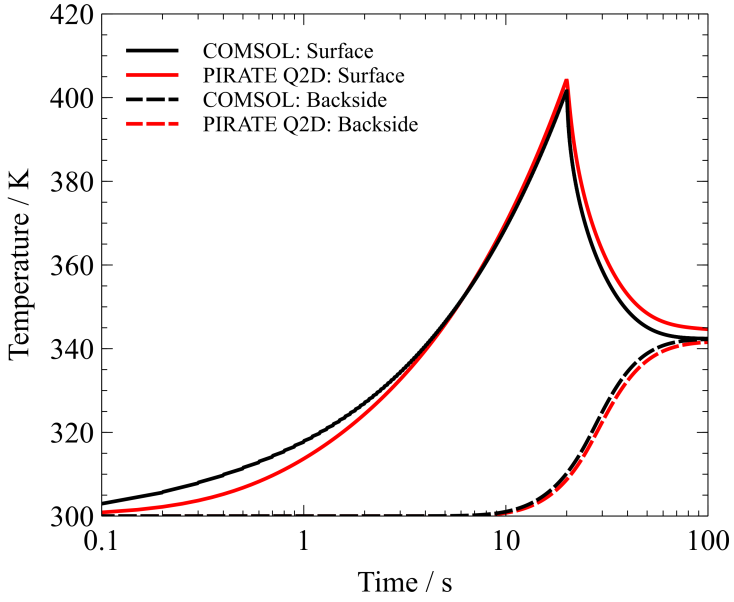

(a) C/C

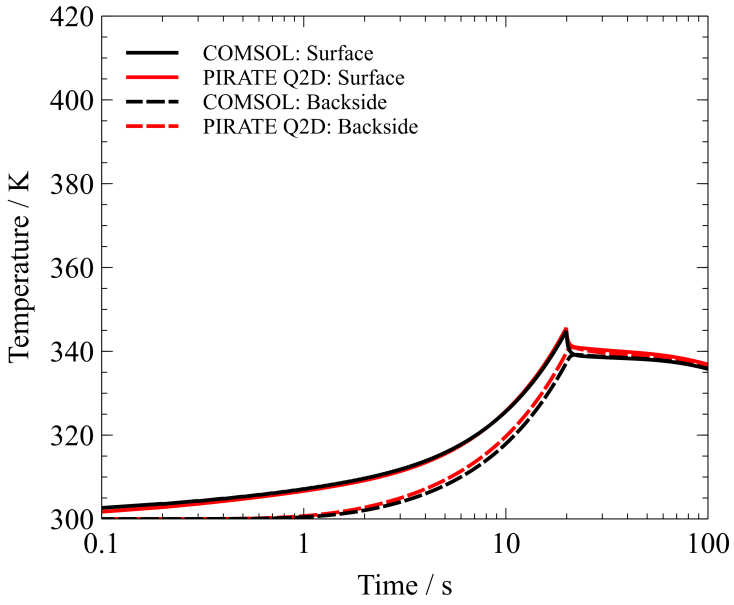

(b) UHTC

Figure 3.8: Transient temperature evolution at $x = 0.05\,\mathrm{m}$ - uncooled.

Figure 3.8 shows the transient surface and backside temperatures at the point x = 0.05 m for both materials. This point represents the intersection between the heat flux input boundary condition and the adiabatic boundary around the model and is where considerable two-dimensional effects and the largest errors are expected. For the entire time history, the PIRATE Q2D simulations agree within 5% of the COMSOL simulations, capturing the linear rise during the onset of heating and then the drop off as heat dissipates to the rest of the material. For the C/C case, PIRATE Q2D underpredicts the temperature peak by 6 K which can be attributed to the time discretisation error described before. In addition, there is a slight overprediction of 4 K of the final temperature. This is consistent with both materials and is likely only due to a lateral discretisation error (dx = 0.01 m for these simulations). As this point constitutes a very transient and non-linear change in temperature, a very small change in lateral discretisation leads to a large change in temperature.

Figure 3.9, shows the temperature distribution along the body for C/C and UHTC at time 10 s. Reinforcing the results above, the general shape of the temperature distribution for PIRATE Q2D matches closely with COMSOL. For the C/C case, the difference of 12 K in peak surface temperature at t = 10 s can again be attributed to the time discretisation error described before whilst the difference for UHTC is only 2.5 K. Overall, the implementation of the quasi-two-dimensional correction appears to be of suitable accuracy for systems-level calculations.

3.4.2 Cooled: Sharp Edge Flight Experiment II Flight Data

To validate the lateral conduction model with transpiration cooling, the PIRATE code with lateral conduction has been applied to the SHEFEX flight data [41]. The total flight time was roughly 500 s with 52 s of experimental time for the atmospheric re-entry at altitudes between 100 and 30 km. The SHEFEX II flight experiment implemented a transpiration-cooled experiment named Aktive Kühlung durch Transpiration im Versuch (AKTiV). Porous C/C samples (properties from

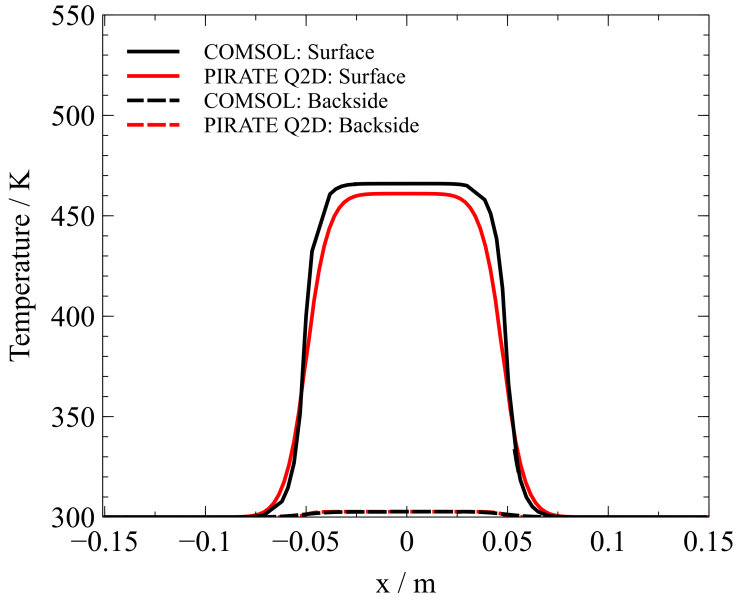

(a) C/C

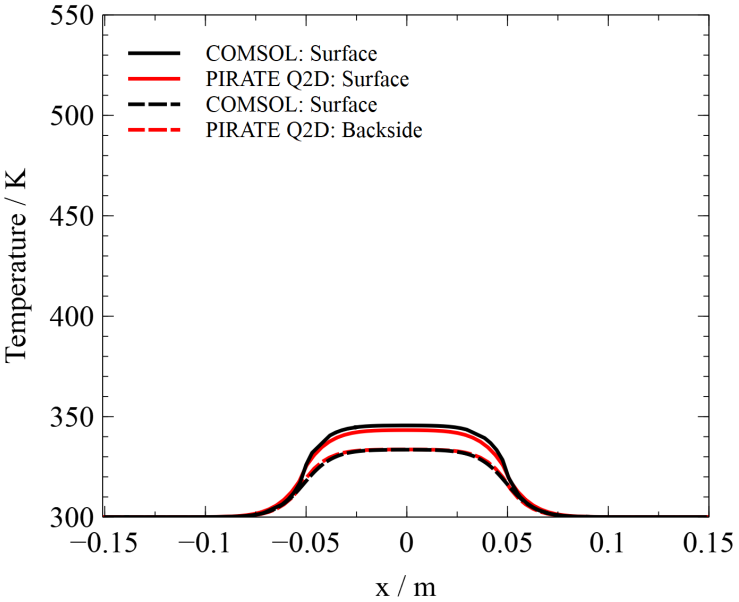

(b) UHTC

Figure 3.9: Temperature distribution along the body at $t = 10\,\mathrm{s}$ - uncooled.

Table 3.1) with a thickness of 5 mm were inserted in the center of a 7 mm thick thermal protection panel made of C/C-SiC [41]. Nitrogen coolant gas was fed through the porous sample at a mass flow rate of $0.4\,\mathrm{g\,s^{-1}}$ with a stainless steel

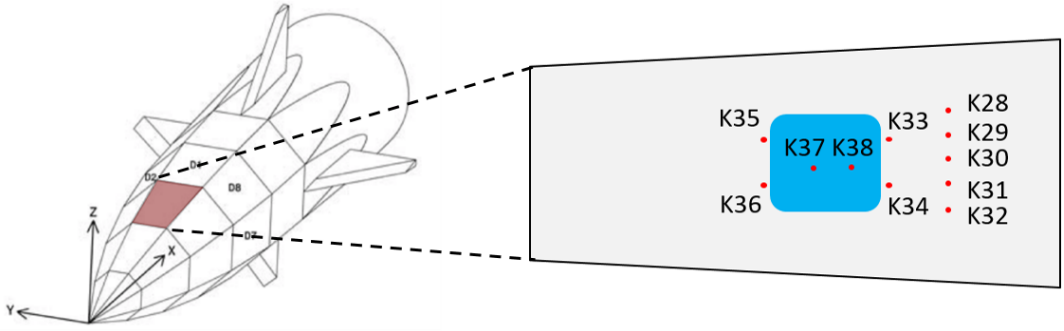

Figure 3.10: AKTiV thermocouple locations on experiment - panel C3 [41].

plenum. Fig. 3.10 shows the locations of thermocouples for the AKTiV experiment at Panel C3. The reservoir temperature is assumed to be 300 K [41]. Before the cooling is started at 431 s, the pre-heating of the model has been simulated by starting from the initial temperature distribution.

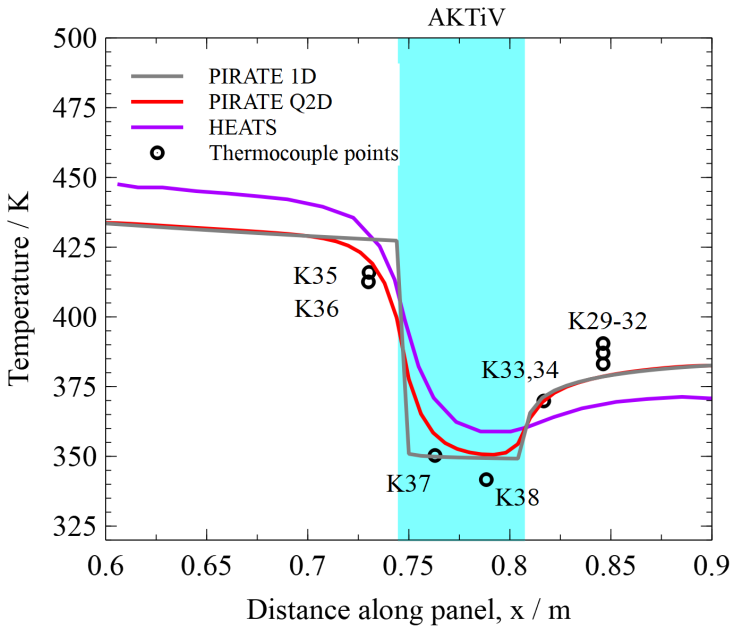

Figure 3.11: Comparison of experimental to simulated temperatures along panel C3 at the surface of AKTiV at $t = 485.12\,\mathrm{s}$ [41].

The temperature distribution for the AKTiV flight experiment is shown in Fig. 3.11 for $t = 485.12\,\mathrm{s}$ where the experimental results from the SHEFEX flight data, the two-dimensional finite difference HEATS simulation data, and the PIRATE

1D and PIRATE Q2D simulations are plotted. The results show very good agreement within 2 K between PIRATE Q2D and the measured thermocouple data upstream of the porous sample (K35 and K36). The HEATS two-dimensional finite difference code follows a very similar trend to PIRATE Q2D. The overprediction of HEATS may be attributed to the fact that PIRATE 1D and Q2D account for the radiation exchange between the backside and the plenum, whereas HEATS considers an adiabatic backside. The prediction of the temperature reduction due to cooling is in good accordance with both HEATS and the experimental data, and it lies within a margin of less than 10 K. There is a slightly different trend in the downstream cooling between HEATS and both PIRATE simulations. This may be attributed to the different models used between HEATS and PIRATE to calculate the downstream film effectiveness. Where HEATS uses a boundary-layer heat balance, PIRATE uses a semi-empirical correlation [86]. Both PIRATE models follow the surface thermocouple data closely, within 10 K for K29-32. Finally, a comparison between the PIRATE 1D and PIRATE Q2D simulations illustrates the increased accuracy attained by considering 2D effects, particularly at the boundary between the thermal protection outer panel and the porous sample. This engenders confidence in the described extension of PIRATE to include two-dimensional conduction with transpiration cooling.

3.5 Coupled Numerical Code

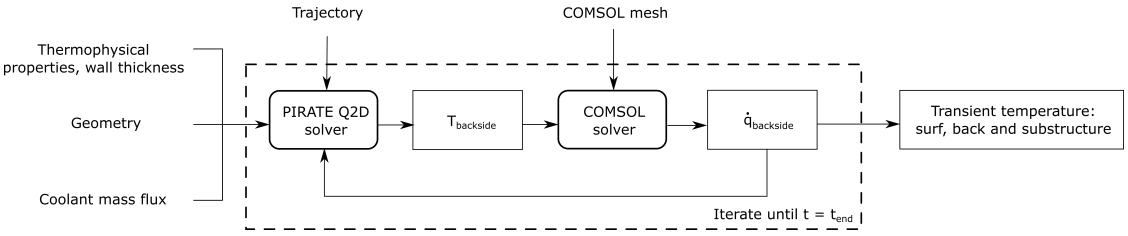

Figure 3.12: Flowchart of coupled numerical model.

One of the key assumptions made by the PIRATE solver is that the boundary condition at the backside of the porous wall is represented as a radiative exchange between the back surface and a cold substructure (Fig. 3.2)

$$\dot{q}_{\text{backside}} = -\frac{\sigma(T^4_{\text{backside}} - T^4_{\text{sub}})}{\frac{1}{\varepsilon_s} + \frac{1}{\varepsilon_{\text{sub}}} - 1} \tag{3.10}$$

where σ is the Boltzmann constant, ε_{sub} is the emissivity of the substructure and ε_s is the emissivity of the porous outer wall. In reality, during a flight trajectory, the substructure temperature (T_{sub}) increases due to the incoming radiative heat flux from the backside of the porous wall. An increase in substructure temperature then leads to a reduction in the net negative backside heat flux, which reduces the transient heat loss from the porous backside as the substructure heats up. Even if critical material temperature limits are maintained for the outer wall, overall failure for the vehicle is possible if the substructure temperature exceeds critical material limits.

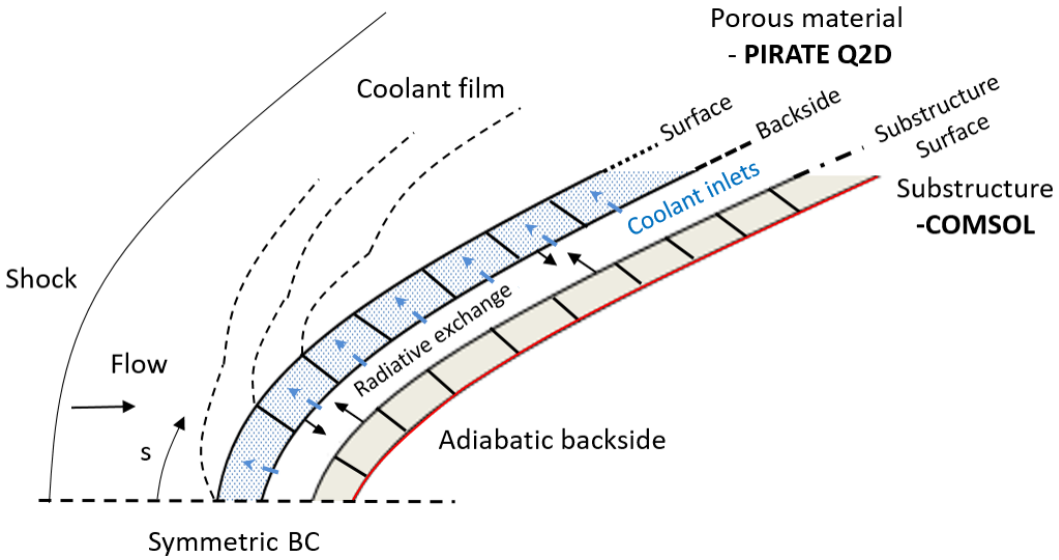

Figure 3.13: Schematic of the two-dimensional model with substructure.

To model this effect, the PIRATE Q2D code has been linked to the COMSOL finite element package using LiveLink$^{\text{TM}}$ for MATLAB. Figure 3.12 outlines a flowchart of the computational model. For each time step, the porous outer wall backside temperature calculated by PIRATE Q2D is taken as an input into a backside material boundary condition in COMSOL. Thereafter, once COMSOL calculates the heat transfer to the substructure for the given time step, the backside radiative heat flux is then taken as an input boundary condition for the porous

wall backside in PIRATE Q2D. Henceforth, the coupled version of PIRATE Q2D with substructure is referred to as "PIRATE Q2D+S."

A schematic of this model is shown for a generalised geometry in Fig. 3.13, where the entirety of the outer surface material (whether porous or solid) is modelled by PIRATE Q2D. For the substructure, an adiabatic boundary condition is assumed for the backside and a symmetric boundary condition is along the stagnation point. For a given flight trajectory, the outer wall heat flux distribution is an input boundary condition calculated either using empirical correlations [86] or via an external database [e.g., from computational fluid dynamics (CFD)].

The coupled numerical model presented assumes negligible convective heat transfer between the coolant channel and the substructure. In addition, the input coolant temperature at the backside of the porous surface is also assumed to at 300 K. It is envisaged that the coolant is to be supplied to appropriate regions via channels through the substructure.

3.6 Transient Flight Analysis with Substructure

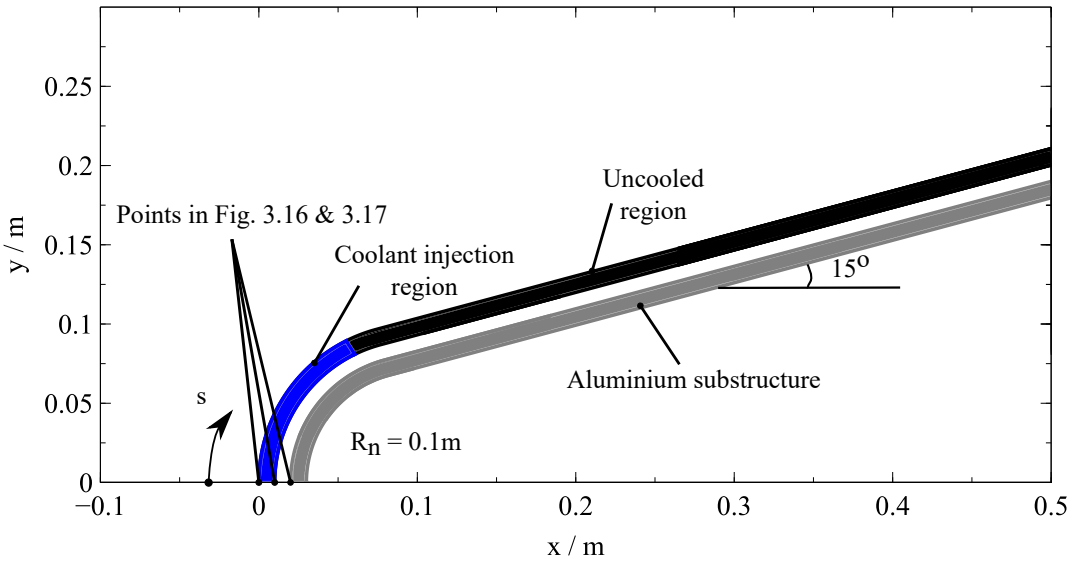

Figure 3.14: Leading edge geometry considered in this study. Coolant injection region from s = 0 - 0.11 m.

To demonstrate an application of the coupled numerical approach detailed above, the study presented in this paper consists of a 15° half-angle wing leading edge

with a 0.1 m nose radius and a consistent wall thickness of L = 10 mm. A simplified 10 mm aluminium thick substructure is considered with a gap of 10 mm between the porous wall and the substructure acting as a coolant reservoir. The total length from the stagnation point along the body profile is 0.57 m and a schematic of the model is displayed in Fig. 3.14.

The external heat flux boundary condition is determined by applying the Sutton-Graves stagnation point correlation corrected for a 2D stagnation line [13]. Laminar flow is assumed at the external surface and the Lees laminar heat transfer correlation is applied for the varying heat flux boundary condition at the external surface [149].

For the porous outer wall, the C/C and UHTC materials are chosen of which the material parameters are summarised in Table 3.1. The aluminium substructure is built up with assumed nominal properties of: emissivity, $\varepsilon_{\text{sub}} = 0.07$; density, $\rho = 2700\,\text{kg}\,\text{m}^{-3}$; specific heat capacity, $c_p = 900\,\text{J}\,\text{kg}^{-1}\,\text{K}^{-1}$ and thermal conductivity, $k = 177\,\text{W}\,\text{m}^{-1}\,\text{K}^{-1}$. Heat transfer through any supports between the substructure and the porous outer wall are neglected as well as any heat transfer between the coolant gas and the substructure. This assumption is sensible as any heat transfer through the supports are likely to be very small if they are made of highly insulating materials [41]. In addition, the primary purpose of this study is to demonstrate the purely radiative heat transfer interplay between the porous wall and the substructure. In addition, it is assumed that there is no radiative shielding and that there are no coatings to reduce the emissivity at the backside of the porous wall which would be present in a real spacecraft.

As per Kays et al. [91], a commonly used parameter to describe transpiration-cooled processes is the ratio of coolant transpired through the wall and the main flow (also known as the blowing ratio) defined as

$$F = \frac{\rho_f u_f}{\rho_e u_e} = \frac{\dot{m}_f}{\rho_g u_g} \tag{3.11}$$

with coolant mass flux, $\dot{m}_f$ (in units of $\text{kg}\,\text{s}^{-1}\,\text{m}^{-2}$), where (e) and (f) denote values for the post-shock boundary layer edge gas and coolant respectively. Further details

regarding the calculation of heat fluxes and blowing ratios from the freestream conditions are detailed in Ref. [86].

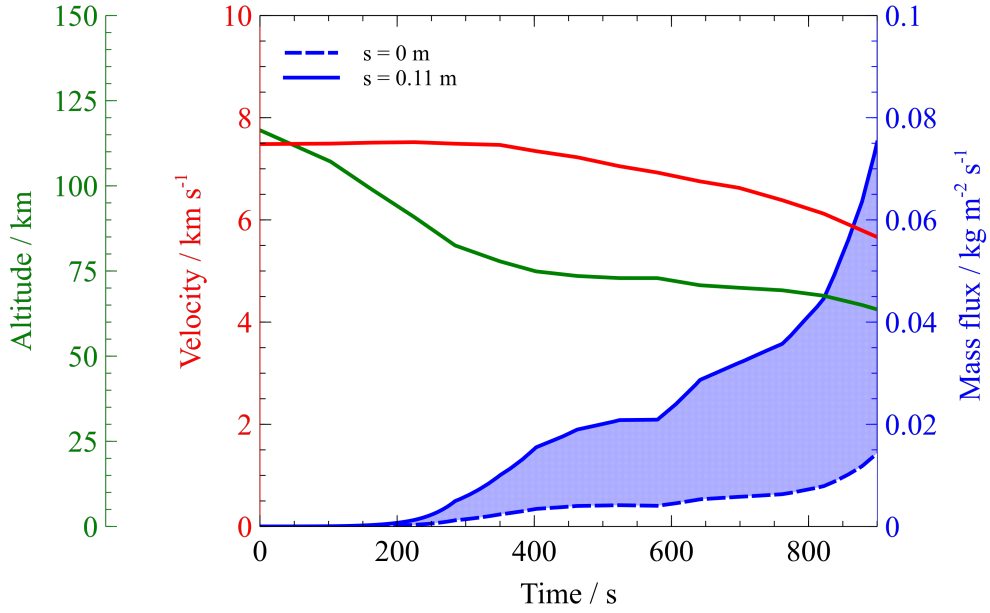

Figure 3.15: Space Shuttle re-entry trajectory with the coolant mass flux distribution within the coolant injection region, $F = 0.04$.

The following simulations are all carried out for the first 900 s of the space shuttle re-entry trajectory [144] where the model is assumed to be at a uniform initial temperature of 300 K. Transpiration cooling is applied by injecting Helium coolant at 300 K at four constant blowing ratios, F, of: 0.01, 0.02, 0.03 and 0.04. Figure 3.14 shows the coolant injection region from $s = 0$ to 0.11 m. This has been chosen based on the conclusions in Ref. [57] which showed for a number of trajectories that transpiration cooling is only needed near the nose to maintain a vehicle below critical temperature limits. The mass flux distribution at the coolant injection region is shaded in Fig. 3.15 over the course of the trajectory for a constant blowing ratio, $F = 0.04$. As expected at later points, to maintain a constant blowing ratio, the coolant injection mass fluxes increase greatly due to the higher freestream gas density at lower altitudes. The boundary layer is assumed to be laminar for the duration of the chosen trajectory. This assumption is justified by considering Ref. [57] which

showed, through a survey of different transpiration cooling experiments, that the boundary layer is not tripped if the blowing ratio is kept below 0.04.

Each PIRATE Q2D+S simulation requires between 9-11 hours to complete. The computation time is significantly slower compared to the PIRATE Q2D simulations detailed in Section 3.4 mainly due to the coupling process between PIRATE and COMSOL. However, this is still well within a reasonable time frame for a complex transient conjugate heat transfer simulation and is highly applicable for large-scale systems studies.

3.6.1 Uncooled Coupled Numerical Simulation

First, the PIRATE Q2D+S code is compared to PIRATE Q2D and PIRATE 1D for the uncooled case (zero coolant injection). Because the PIRATE 1D/Q2D model assumes that the substructure has infinite thermal capacity, this remains at a temperature of 300 K throughout the flight trajectory. PIRATE Q2D+S transiently calculates the change in substructure temperature due to the incoming radiative heat flux from the backside of the porous wall.

Figure 3.16 shows the transient temperature history of the surface and backside of the C/C and UHTC porous wall and the surface temperature of the substructure at the stagnation point. By first comparing PIRATE 1D and 2D, as expected, the 1D simulation significantly overestimates the temperature rise over the trajectory, diverging by 340 K at the final time step. This is due to the large thermal gradients near the stagnation point for the wing leading-edge geometry and justifies the development and application of the quasi-two-dimensional method to account for the significant lateral conduction effects. The lower material emissivity of UHTC results in reduced radiative cooling. This is balanced out by the significantly lower heat capacity, which leads to largely similar surface temperatures between UHTC and C/C for the one-dimensional simulation (2250 K vs 2180 K at the maximum point for PIRATE 1D). However, the appreciably higher thermal conductivity of

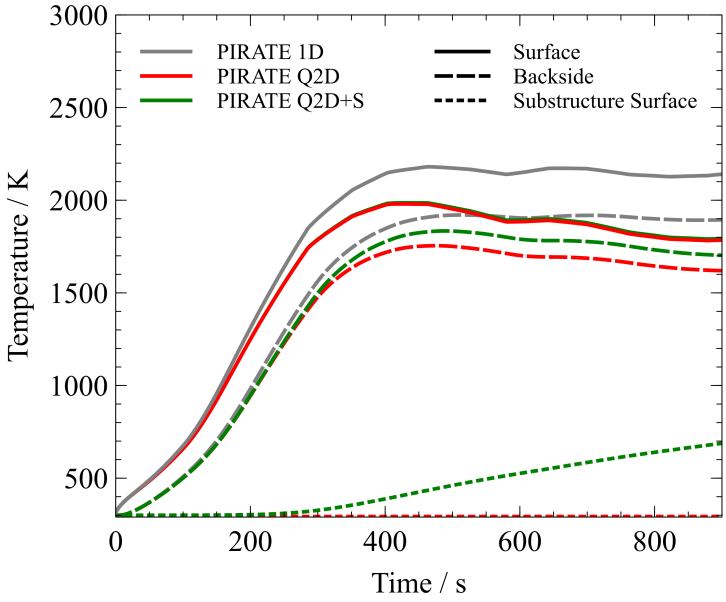

(a) C/C

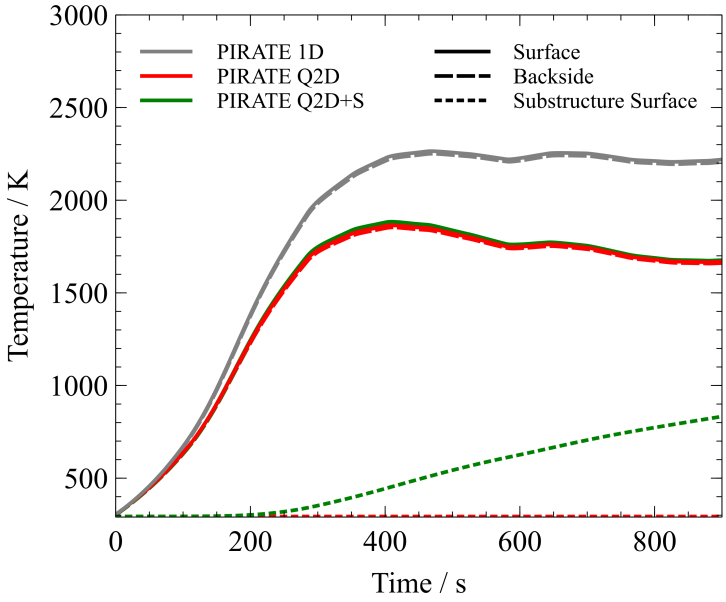

(b) UHTC

Figure 3.16: Transient temperature evolution at the stagnation point ($s = 0\,\mathrm{m}$), comparison of PIRATE 1D, Q2D, and Q2D+S uncooled.

UHTC means that heat is very quickly conducted away from the stagnation point and results in a lower two-dimensional peak temperature.

Considering PIRATE Q2D+S, there is a significant temperature increase of the

substructure over the trajectory, reaching a peak of 700 K for C/C. The steady, linear rise in temperature is plausible as the backside absorbs the total integrated heat flux. The back face of the substructure is assumed to be adiabatic with no further heat transfer into internal structures. In addition, as the aluminium surface temperature increases, there is greater radiation emission leading to a net backside heat flux, which raises the backside temperature. As the emissivity of aluminium is very low, the temperature rise is only a maximum of 70-80 K. For UHTC, the higher thermal conductivity leads to an equilibration between the surface and backside temperatures over the trajectory. The corresponding higher backside heat flux results in a maximum temperature of 850 K at the substructure surface, illustrating that UHTC acts as a hot structure in this trajectory, dissipating heat quickly to the underlying body.

3.6.2 Application of Cooling

Secondly, transpiration cooling is applied within the injection region for the four different constant blowing ratios detailed previously. Figure 3.17 illustrates the effect of gas injection to the stagnation region for the C/C and UHTC materials where $F = 0.04$ of Helium coolant is injected. For C/C, as expected, this leads to a reduction in both the surface and backside temperatures of the porous wall. The reduction in backside temperature then results in a lower heat flux from radiative emission at the substructure, and thereby a significantly lower substructure temperature rise. As the backside temperatures are reduced along the entire trajectory, a moderate reduction in the peak backside temperature of the outer wall (approximately 180 K) leads to a 250 K reduction in the substructure temperature at the final trajectory point to 440 K: a 36% drop compared to the uncooled case. The backside and surface temperatures diverge at later times because maintaining the same blowing ratio requires a greater coolant mass flux, and thus there is increased internal convective cooling. This effect shows that in addition to the use of transpiration cooling to reduce outer wall surface temperatures, there is an advantageous side effect where the integrated heat loads to the substructure can also be lowered when

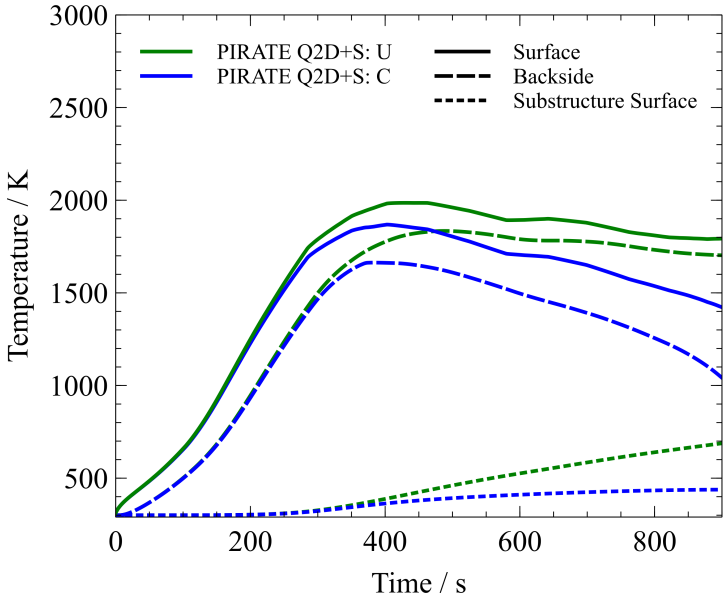

(a) C/C

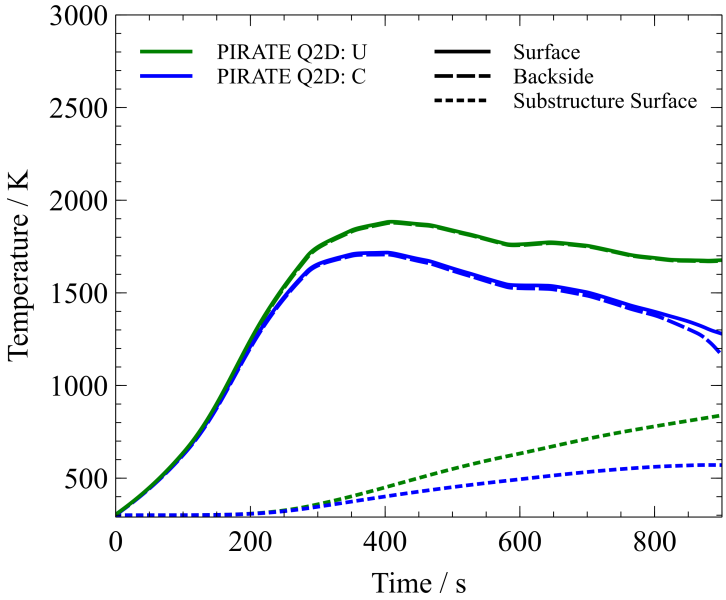

(b) UHTC

Figure 3.17: Influence of coolant injection at the stagnation point. U = uncooled, C = cooled with $F = 0.04$ of Helium coolant injection.

coolant is injected for a large portion of the trajectory. For the UHTC material, at the application of cooling, the final temperature at the stagnation point drops by only 50 K to 880 K. The lower temperature reduction compared to C/C is expected

primarily due to the higher backside temperatures of UHTC, which are caused by the high thermal conductivity of UHTC. Therefore, transpiration cooling has higher benefits for the substructure when heat conduction is slow in the material.

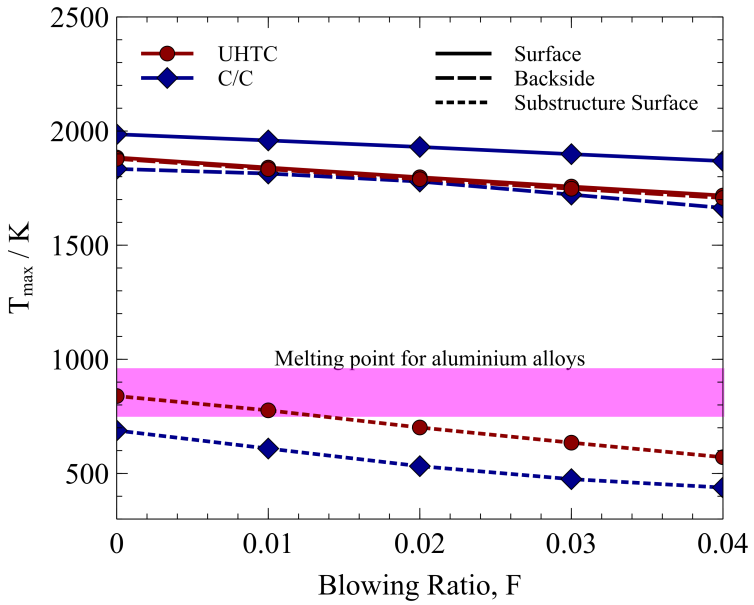

Figure 3.18: Maximum temperature for various blowing ratios. The location of these temperature peaks is at the stagnation point ($s = 0\,\mathrm{m}$).

Figure 3.18 shows how the maximum temperatures of the surface, backside and substructure reduce with increasing blowing ratios. For the surface, both C/C and UHTC show an approximately linear trend where increasing the blowing ratio from 0 to 0.04 reduces maximum temperatures by 125 and 160 K respectively for C/C and UHTC. The substructure temperatures reduce at a greater rate (approximately 250 K for C/C and 165 K for UHTC) as this represents the integrated load over the entire trajectory. Between $F = 0.03$ and 0.04, there is a slowdown in the reduction of substructure temperature ratios; suggesting a reduced marginal benefit with higher blowing ratios. By considering the melting point of various aluminium alloys, it is clear that for this particular trajectory and geometry, even a moderate level of coolant injection is highly beneficial for UHTC and can reduce the substructure temperature below critical limits.

3.6.3 Impact on Thermal Gradients

The extreme thermal gradients present lead to large thermal stress near the stagnation point of hypersonic wing leading edges. These are significant engineering challenges and can frequently violate structural limits. This is important for both the outer wall and the underlying substructure. Here, a baseline study is conducted on the impact of transpiration cooling to the substructure thermal gradients.

The thermal expansion of a material is proportional to its temperature gradient; therefore a variation in temperature, ΔT, across a material induces a thermal stress σ_{th}, given by

$$\sigma_{\text{th}} \propto \Delta T. \tag{3.12}$$

To quantify this benefit, $\Delta T_{\text{sub,lateral}}$ is defined as the change in substructure surface temperature between the stagnation point and at $s = 0.56\,\text{m}$

$$\Delta T_{\text{sub,lateral}} = T_{\text{sub,s=0\,m}} - T_{\text{sub,s=0.56\,m}}, \tag{3.13}$$

where it is assumed that the substructure is fixed at these two locations so that any temperature gradient between these points directly corresponds to increased thermal stress. Focusing on the C/C material only, Fig. 3.19a shows the transient change in $\Delta T_{\text{sub,lateral}}$ for each of the five injection scenarios detailed above. Considering the uncooled case, as expected, there is very little change for the first 200 s as the heat flux slowly propagates from the surface to the substructure. Thereafter, there is a rapid increase peaking at $\Delta T_{\text{sub,lateral}} = 225\,\text{K}$. For coolant injection, the maximum level of cooling of $F = 0.04$ leads to a maximum $\Delta T_{\text{sub,lateral}}$ of 80 K, a 65% reduction. As $\Delta T_{\text{sub,lateral}}$ is directly proportional to the thermal stress, transpiration cooling can be very effective in reducing the high thermal stresses near the stagnation region of the leading edge.

Figure 3.19b shows the substructure temperature distribution along the body at $t = 900\,\text{s}$. The effect of coolant injection is significantly reducing the temperature gradient near the stagnation point of the leading edge. Even though the coolant is

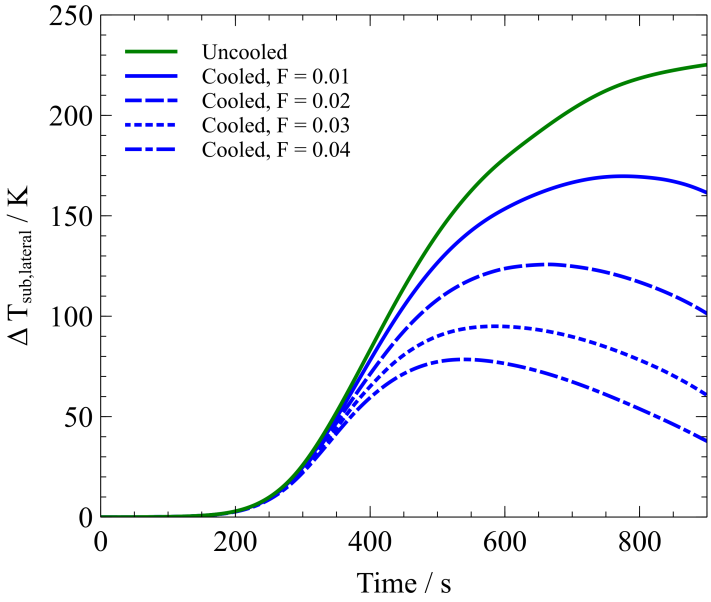

(a) Transient change in $\Delta T_{\mathrm{sub,lateral}}$

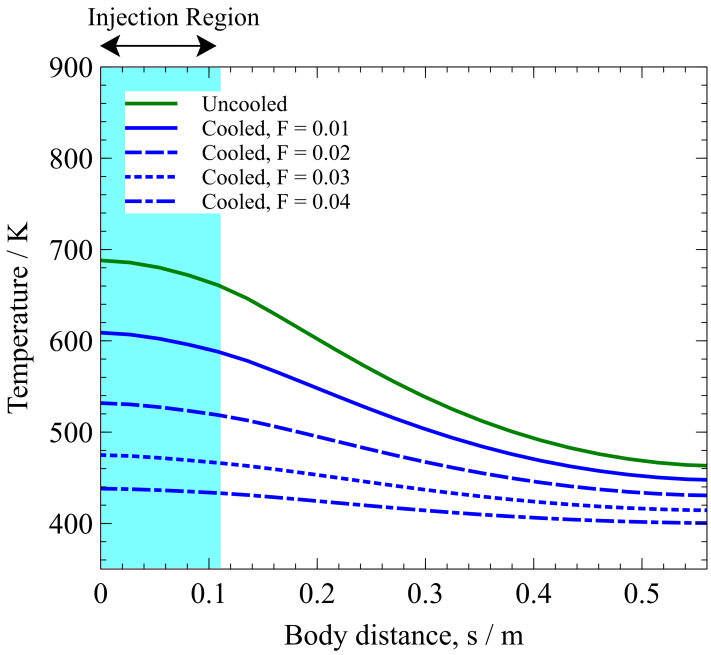

(b) Temperature distribution along the body, $t = 900\,\mathrm{s}$

Figure 3.19: An assessment of the temperature gradient along the substructure surface at the onset of cooling - C/C outer porous wall.

only applied close to the stagnation region, temperatures also reduce significantly far downstream with a 65 K reduction at s = 0.56 m between the uncooled case and a blowing ratio of 0.04. This is primarily due to the high conductivity of

aluminium which quickly conducts heat away from the stagnation point to locations further downstream. In addition, the propagation of the coolant film downstream of the injection region leads to a moderate reduction in the surface temperature and hence a reduction in substructure temperature.

3.7 Conclusions

This paper presents improvements to the PIRATE code developed to perform rapid simulations of the transient temperature evolution of transpiration-cooled heat shields for hypersonic vehicles. The Crank-Nicolson numerical scheme has been applied to the existing PIRATE code, providing the capability to accurately model lateral conduction for geometries with moderate thermal gradients and strictly one-dimensional coolant mass flow. The quasi-two-dimensional method allows for rapid calculations of the transient temperature history, suitable for large-scale systems studies with minimal computational cost. The model is validated against COMSOL and experimental data from the SHEFEX II re-entry flight test. An uncooled validation case using COMSOL showed excellent agreement with the quasi-two-dimensional method, accurately capturing the transient non-linear temperature profile. The comparison between simulation results and the SHEFEX II re-entry flight test experimental data showed good agreement within 10 K, demonstrating that the lateral conduction effects at the onset of transpiration cooling are being resolved.

To model the substructure of a vehicle where transpiration cooling is applied, the PIRATE code is coupled to COMSOL to create a tool by which complete systems studies can be investigated. Preliminary results show the heating up of the substructure is a major factor in choosing appropriate materials for a given mission trajectory. Applying transpiration cooling has the effect of not only reducing temperatures for the outer wall but also significantly reducing the temperature of the substructure. By applying a moderate level of coolant injection ($F = 0.04$ of Helium), the maximum temperature of the substructure surface reduces from over 700 K to 450 K. Furthermore, transpiration cooling can reduce the thermal

stresses at the substructure, with a 65% reduction in the temperature gradient of the substructure surface for moderate coolant injection.

For the purposes of this paper, a generalised wing leading edge geometry and a constant thickness substructure are considered. However, in principle, any heat flux distribution can be applied as input from an external database (e.g. CFD) and a complex substructure built up within the COMSOL environment. In the future, it is envisaged that this tool will be developed to perform optimisation studies for a fully formed and realistic transpiration cooling system.

3.8 Practical Implications to Cooling the Wing Leading Edge

Whilst the analysis presented in this Chapter applies a constant blowing ratio over the trajectory, in reality, a transpiration-cooled system would be optimised to ensure that enough mass flux is supplied to keep surface temperatures below a given threshold. This would likely require the highest mass fluxes at and or near the stagnation point, where the peak heat fluxes and surface temperatures will occur. The challenge in supplying enough cooling to this region is augmented by the fact that viscosity scales with temperature. At very high temperatures, viscosity-driven blockage is a crucial factor that must be accounted for as described in the Darcy-Forcheimer equation (Eq. 2.1). This may be illustrated by considering Fig. 3.20 which shows the pressure and uncooled temperature distribution at t = 500 s for the UHTC material. The highest pressures and temperatures are, as expected, at the stagnation point. Table 3.4 shows the resultant supplied coolant mass flux to the surface at the stagnation point and at $s = 0.1\,\mathrm{m}$ if a constant reservoir pressure of 100 kPa is assumed. This considers both the case at the predicted surface temperature of the vehicle and the case of a cold wall ($T_{\mathrm{wall}} = 300\,\mathrm{K}$). The elevated viscosity at high temperature leads to almost 12 times lower mass flux at the stagnation point and 7 times at $s = 0.1\,\mathrm{m}$, respectively (compared to the cold wall). This illustrates just how difficult it is to deliver sufficient cooling to the stagnation point at high temperatures; especially considering that this is the

location that is most in need of higher coolant mass fluxes. The effect is further exacerbated when moving towards sharper leading edges with nose radii in the order of 0.01-0.005 m. Prokein et al. [68] proposed one solution to this problem - i.e. to design a preferentially fibre-orientated sharp leading edge (made of C/C) to ensure that more flow can be supplied to the stagnation region. However, this issue remains a significant challenge and more creative solutions such as a variable thickness wall (so that the wall is thinner at the stagnation point), a multitude of small plenums to deliver very localised coolant mass fluxes or even adding a slot at the stagnation point location may be required.

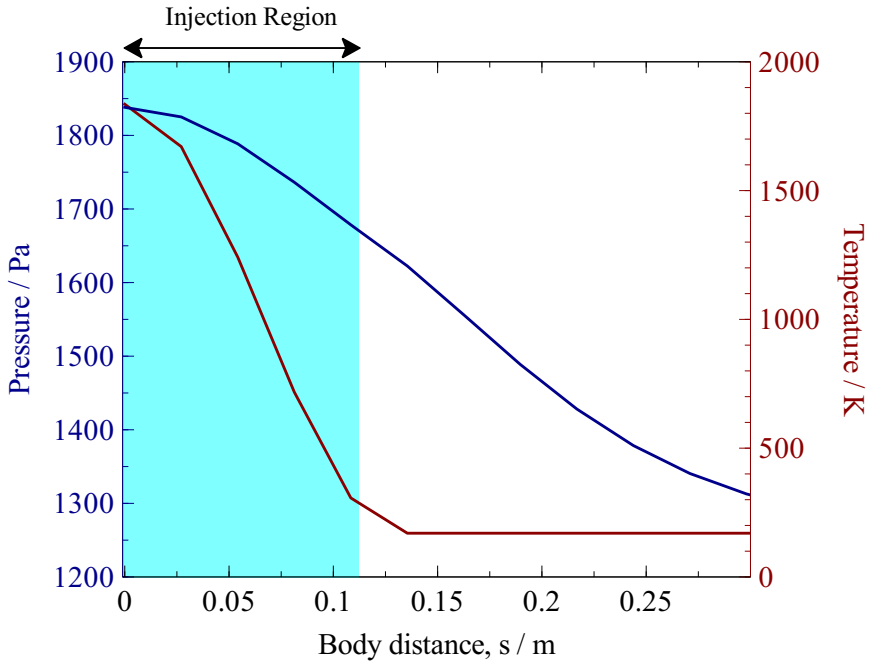

Figure 3.20: Surface pressure and temperature at $t = 500\,\mathrm{s}$ for UHTC uncooled. The temperature is determined using PIRATE Q2D+S.

Table 3.4: Required coolant mass flux assuming a 10 mm thick UHTC porous material with a constant plenum pressure of 100 kPa.

Wall temperature / K	Location / m	Mass flux, $\dot{m}_f$ / $\mathrm{kg\,s^{-1}\,m^{-2}}$
$T_{\mathrm{wall}} = T_{\mathrm{surf}}$	$s = 0$	$1.0315 \cdot 10^{-2}$
$T_{\mathrm{wall}} = T_{\mathrm{surf}}$	$s = 0.1$	$1.0318 \cdot 10^{-2}$
$T_{\mathrm{wall}} = 300$	$s = 0$	$6.6524 \cdot 10^{-4}$
$T_{\mathrm{wall}} = 300$	$s = 0.1$	$9.1569 \cdot 10^{-4}$

Chapter 4

Heat Transfer Measurements of a Transpiration-Cooled Stagnation Point in Transient Hypersonic Flow

Contents

In the preceding chapter, it was established that applying transpiration cooling to a hypersonic wing leading edge can deliver significant temperature reduction not only to the outer surface but also to the underlying substructure. This enables the possibility of using lighter or cheaper materials with lower melting points for the substructure. In addition, the inclusion of transpiration cooling reduces the very

high thermal gradients near the stagnation point of the leading edge.

However, the previous modelling employed simplified correlations for the surface heat transfer reduction in laminar flows. In particular, it was assumed that the local heat transfer reduction on the porous surface can be modelled by film theory, described in Section 2.1.3 (Eq. (2.19)) and the downstream film effectiveness with the correlation of Kutateladze [35]. The Kutateladze relation is in fact a turbulent correlation which has been used due to a lack of an existing laminar correlation in the open literature which can be applied to a wide range of hypersonic flow conditions.

Whilst the existing correlations enabled a sensible first-order estimate to assess the performance of a transpiration cooling system, a more realistic application to a flight vehicle requires higher fidelity modelling, ideally supported by experimental data. In particular, UHTCs and other modern porous materials have very small pore sizes and film theory may not necessarily be applicable. Thus, existing heat transfer models need to be validated and potentially extended for these cases. In addition, film theory assumes that the porous injector begins at the leading edge or stagnation point. For many transpiration cooling applications, this is not necessarily the case (i.e. for cooling local regions).

In this chapter, the development of a new diagnostic tool to measure the surface heat flux on transpiration-cooled surfaces is described. This enables detailed, two-dimensional measurements of transpiration-cooled porous materials in short-duration hypersonic facilities. The tool is fundamental to conducting the experiments in Chapters 5 and 6 which focus on generating novel datasets at representative flow conditions using microporous materials. The following work has been published in the *Journal of Thermophysics and Heat Transfer*. It is presented in this chapter with an additional section describing the experimental facility but otherwise unaltered content. The author contributions are as follows

- Imran Naved: Conceptualisation, Methodology, Investigation, Data Analysis, Writing
- Matthew McGilvray, Tobias Hermann, and Luke Doherty: Supervision

- Chris Hambidge, Laurent Le Page: Assistance with calibration and set-up of the infrared thermography system
- Marc Ewenz Rocher: Design and manufacture of the stagnation probe model
- Madeleine Grossman and Luc Vandeperre: Manufacturing of porous Alumina

In addition to the published work presented in this Chapter, further details of the theoretical background of infrared thermography, the calibration, and sensitivities of the infrared methodology described in this chapter are detailed in Appendices B and D. Furthermore, Appendix C details a modification to the experimental facility to enable infrared measurements using a nitrogen driver gas.

4.1 Introduction

The design of aerospace vehicles is generally constrained by high thermal loads. Regions on a hypersonic vehicle that experience these loads can be both external (thermal protection systems) and internal (combustion chamber walls). The next generation of hypersonic vehicles has the requirement to both be reusable to reduce costs and will likely employ sharper leading edges to improve aerodynamic performance. Transpiration cooling is an active thermal protection system that can be applied to hypersonic vehicles. It involves injecting a coolant through a porous material into the external boundary layer. This cooling process is thus achieved through three primary effects: heat from the wall is convected out by the fluid, the coolant creates a thin film that insulates the wall from the hot external gas, and the coolant film can protect the wall from surface oxidation and surface catalytic heating [27].

Past investigations have shown that transpiration cooling can be highly effective in reducing the surface heat transfer in hypersonic flows [115, 150]. A number of investigations have focused on determining the heat transfer reduction when blowing from a stagnation point using both experimental and numerical tools. The correlation of Swann and Pittmann [108] (Eq. (4.1)) has been applied to a wide

range of conditions and validated extensively through computational fluid dynamics (CFD) and analytic methods [109, 113, 117]. In addition, Pappas and Lee [114] conducted heat transfer measurements on a blunt cone in Mach 13.6 hypersonic flow with mass addition for several different injection gases including air, helium, and argon. They found that the heat transfer reduction at the stagnation point agreed reasonably well with the theory of Yoshikawa [113].

Various porous materials have been used for transpiration cooling experiments in the past including Ultra-High-Temperature-Ceramic (UHTCs) such as ZrB_2 [65]) and carbon fibre reinforced carbon (C/C) ceramic composites [38]. Previously, heat transfer measurements directly on porous media have been conducted by placing heat flux sensors such as thin film gauges or surface thermocouples directly between the porous injection holes [45, 46]. Whilst this is possible when the diameter of the injection holes is relatively large, when moving to very small pore sizes as is common in modern micro-porous materials, it is impractical to place physical sensors without disturbing or impeding the outflow. For this reason, an optical, non-intrusive technique is desirable. For heat transfer, infrared thermography is ideally suited to measure the surface temperature and has several advantages over conventional heat flux sensors, for example, providing a 2D spatial image, high sensitivity, low response time, and most crucially, is non-intrusive [139]. In particular, infrared thermography makes it easier to analyse highly complex geometries such as geometrically scaled vehicle models. Whilst infrared thermography has been successfully employed in previous transpiration cooling experiments [39, 63, 116, 121], this has been in the context of either evaluating the thermal film effectiveness in a steady state experiment or interrogating the flow-field downstream of injection for simple flat plate geometries.

This work investigates novel experiments where direct heat transfer measurements are taken in the outflow from transpiring porous media with infrared thermography in a transient hypersonic flow. Tests were conducted at the Oxford High-Density Tunnel (HDT) using a stagnation probe with a porous Alumina injector. A stagnation probe model has been chosen for these experiments due

to the simpler flow field at a stagnation point which has been well-validated both experimentally and numerically by previous studies. The Stanton number on the porous surface with different coolant gases and injection rates is extracted and the results are then compared against numerical simulations and correlations.

4.2 Theoretical Model

The effect to stagnation point heating of injecting air into an air freestream is well predicted by the Swann and Pittmann empirical correlation [108]:

$$\frac{St}{St_0} = 1 - 0.72B_h + 0.13B_h^2 \tag{4.1}$$

where

$$B_h = \frac{\rho_f u_f}{\rho_\infty u_\infty St_0} = \frac{\dot{m}_f}{\rho_\infty u_\infty}\frac{1}{St_0} = \frac{\dot{m}_A(H_0 - h_w)}{\dot{q}_w} \tag{4.2}$$

is referred to as the blowing parameter where ρ and u are density and velocity, respectively. The subscripts (f) and (∞) refer to the injected gas and the freestream conditions respectively and $\dot{m}_f$ is the mass flux of the injected gas. St is the Stanton number and the subscript 0 refers to the value without any injection. This is defined as

$$St = \frac{\dot{q}_w}{\rho_\infty u_\infty (H_0 - h_w)} \tag{4.3}$$

where $\dot{q}_\mathrm{w}$ is the convective heat flux at the wall which may be found either through experiment or via correlations such as the Fay-Riddell correlation [12]. h_w is the wall enthalpy and H_0 is the total enthalpy of the flow defined as

$$H_0 = h_\infty + \frac{u_\infty^2}{2}. \tag{4.4}$$

This correlation is well validated by experimental data [114]. For foreign gas injection (i.e. where a different gas is injected compared to the freestream gas or vice versa), Tauber [14] suggests a modification to the definition of the blowing parameter according to the molecular weight of the injected gas

$$B_{h,M} = B_h \left[\frac{\mathrm{M}_\infty}{\mathrm{M}_f}\right]^{\mathrm{n}} \tag{4.5}$$

where n is between 0.25 - 0.4 depending on the reference consulted. Marvin and Pope [117] suggest that for injection of gaseous ablation products (i.e. gases typically heavier than the freestream gas), n is 0.25. A limitation of this correlation is that the blowing parameter needs to be adjusted manually for different gases based on an empirical fit rather than based on a physical model.

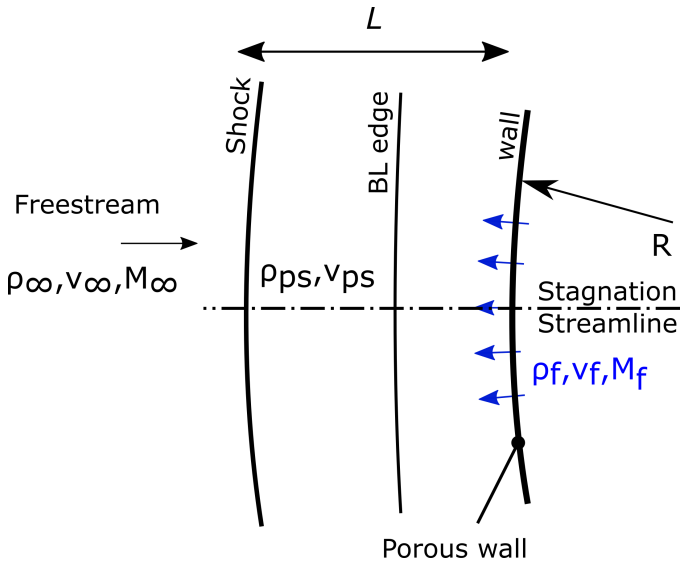

Figure 4.1: Flow geometry at the stagnation point. Adapted from Ref. [113].

A different theoretical approach pioneered by Yoshikawa [113] considers shock layer theory and applies simplifications to derive an analytic solution for the reduction in convective heat transfer due to blowing. This is especially useful for fast engineering calculations. Considering the definitions from the flow diagram in Fig. 4.1, the resultant equation for the reduction in Stanton number at the stagnation point due to blowing is

$$\frac{St}{St_0} = \left[\frac{L}{L_0}\lambda^{(B_h/B_*)}\right]^{-0.5} \frac{\exp(-\frac{1}{\pi}\frac{L}{L_0}\lambda^{(B_h/B_*)}B_h^2)}{1+\mathrm{erf}[\frac{1}{\pi}\frac{L}{L_0}\lambda^{(B_h/B_*)}]^{0.5}B_h} \tag{4.6}$$

where B_* is the blowing parameter for boundary layer blow off defined as [113]

$$B_* = 1.59\sqrt{\frac{\mathrm{M_f}}{28.9}}, \tag{4.7}$$

$\frac{L}{L_0}$ is the ratio of shock stand-off between the uncooled and cooled cases and λ is a gas correction parameter to account for the differences in the molecular weight between the freestream and injected gas

$$\lambda = \sqrt{\frac{\mathrm{M}_\infty}{\mathrm{M}_f}} \bar{N}_f \tag{4.8}$$

where $\bar{N}_f$ is a weighting factor which depends on the type of foreign gas. From numerical results [113], it was found that $\bar{N}_f = \frac{5}{9}$ for a monatomic gas and 1 for diatomic and polyatomic gases. For adiabatic flow, Ref. [151] gives the following correlation for $\frac{L}{L_0}$ for an axisymmetric body as follows

$$\frac{L}{L_0} = 1 + \sqrt{\frac{p_{\mathrm{ps}}}{p_\infty}(\frac{\mathrm{M}_\infty}{\mathrm{M}_f})} St_0 B_h \tag{4.9}$$

where p_{ps} is the post-shock boundary layer edge pressure which may be found through normal shock relations. The full derivation of these equations may be found in Ref. [113].

The Yoshikawa model has been well validated both against numerical simulations and experimental data [117, 151]. Whilst this model does not account for chemical reactions (which are not present in the experiments presented in this paper), it does consider the effect of freestream density and radius in its formulation which makes it suited for modelling flows in a cold flow facility such as the HDT. These theoretical models will be employed to validate the experimental results presented in this paper.

4.3 Experimental Setup

4.3.1 Experimental Model

The porous injector used in these studies is 39% porous Alumina (Al_2O_3) manufactured by the Centre for Advanced Structural Ceramics, Imperial College London. Alumina powder with an average particle diameter of 6.75 μm was sintered for 3 hours at 1700°C to mimic the porosity and micro-structure of ZrB_2 which is currently being explored as a candidate material for transpiration cooling in flight applications [65, 99]. Further details including microscopic images of the porous

Alumina surface are available in Ref. [152]. Porous Alumina is suitable for surface heat transfer measurements due to its relatively low thermal product and high emissivity (Table 4.1), maximising the signal of the infrared measurement.

Table 4.1: Properties of porous Alumina (Al_2O_3) [153].

Parameter	Value
Porosity, ϕ	0.39
Density, ρ_s / $\mathrm{kg\,m^{-3}}$	3800
Thermal Conductivity, k_s / $\mathrm{W\,m^{-}\,K^{-1}}$	25
Specific Heat Capacity, $c_{p,s}$ / $\mathrm{J\,kg^{-1}\,K^{-1}}$	775
Thermal Product, $(\sqrt{\rho c_p k})_{\mathrm{Alumina}}$ / $\mathrm{J\,m^{-2}\,K^{-1}\,s^{-0.5}}$	5234
Darcy Coefficient, K_D / $\mathrm{m^2}$	$3.04 \cdot 10^{-15}$
Forchheimer Coefficient, K_F / m	$1.16 \cdot 10^{-9}$
Emissivity, ε	0.97

Experiments were conducted on a stagnation probe model, shown schematically in Fig. 4.2. A 25 mm radius hemispherical probe head is connected via an adaptor to a 480 mm long hollow sting held in place at the centre axis of the nozzle with a mounting arm. The nose of the probe head was machined to create a 21 mm diameter flat face.

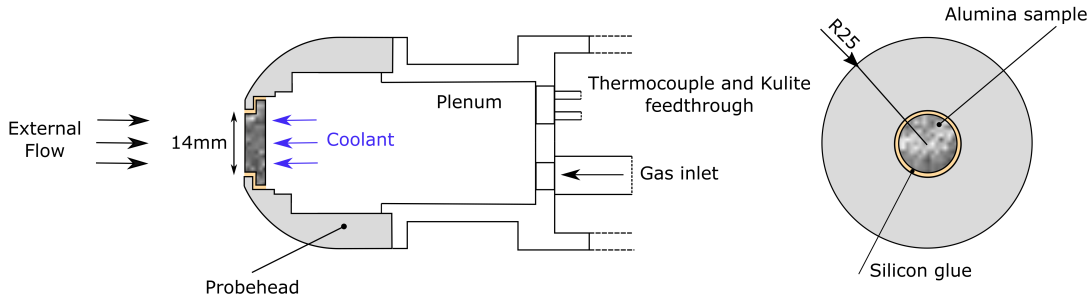

Figure 4.2: Diagram of the experimental model.

The model design is such that the probe head and supporting cylindrical piece form a plenum chamber behind the porous injector. The coolant gas is supplied to the model via the HDT gas injection system (GIS). This features a 5-litre reservoir which is filled with the desired injection gas prior to the experiment. Then, at a specified time, a fast-acting valve is opened to release the gas into the plenum. The temperature and pressure in the plenum is measured by a 0.0762 mm-diam

K-type thermocouple and a Kulite® HEL 375 sensor with a range of 0 to 35 bar absolute. The measured data were acquired using a National Instruments PXIe-8135 controller and one PXIe-6368 card. A sample rate of 200 kHz was used to record all signals of the measurement which includes model and wind tunnel instrumentation.

The permeability of the sample was characterised pre and post-experiment according to the procedure detailed in Ref. [65] using an ISO 4022 standard test rig. The measured Darcy and Forchheimer outflow coefficients are indicated in Table 4.1. In addition, to assess uniformity, the outflow of the transpiring porous samples was investigated using hot-wire anemometry, Air was injected through at 4 bar differential pressure and the obtained velocity map is illustrated in Fig. 4.3. The velocity field is extremely uniform indicating that the pores are small and evenly distributed.

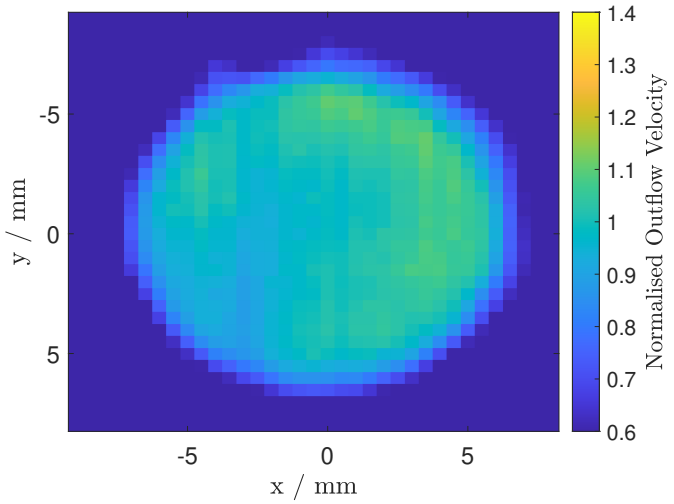

Figure 4.3: Outflow velocity map normalised with the average flow velocity across the sample at 4 bar differential pressure. This is measured with a hot wire with no cross flow [154].

A schematic of the optical setup is shown in Fig. 4.4. The infrared camera used was a FLIR A6751 SLS long-wave infra-ref (LWIR) camera with a wavelength band of 7.5-11 μm. A LWIR camera was chosen due to the spectral emissivity dependence of Alumina which was shown by Rozenbaum et al. [155] to be greater than 0.9 between 7 and 10.5 μm. Due to limited optical access through the upstream face of the test section, the model was viewed in this experiment via. two gold mirrors, each with a nominal reflectivity $> 96\%$. As shown in Fig. 4.4, one mirror

was mounted inside the test section, the other external. The optical path passed through a 50 mm coated Germanium window with an average reflectivity $< 2\%$. The camera was operated at a frame rate of 1 kHz and integration time of 0.1 ms, resulting in a windowed spatial resolution of 128 x 160.

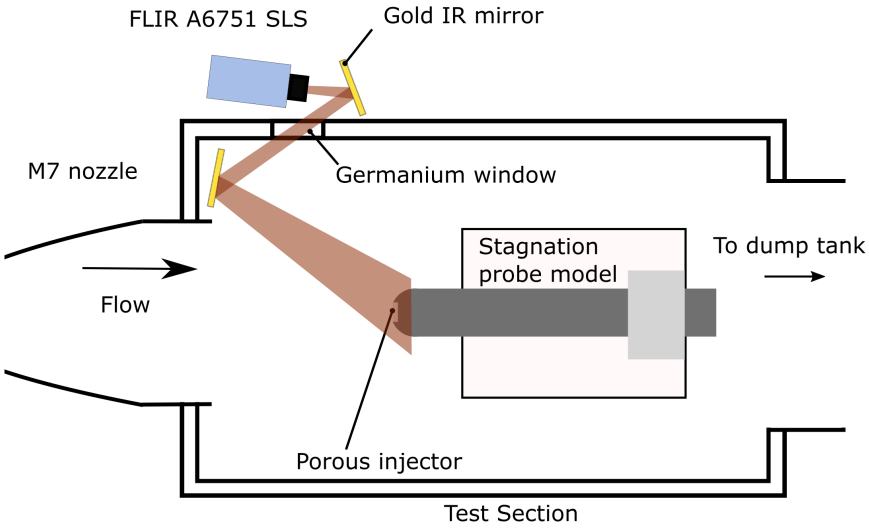

Figure 4.4: Top view of the experimental model in the test section.

4.3.2 Experimental Facility, Test Conditions and Blowing Ratios

The experiments were conducted in the the Oxford High Density Tunnel (HDT) located at the Oxford Thermofluids Institute. The HDT was originally developed by the RAE in the United Kingdom in the 1960's. It was initially operated as a cold hydrogen-driven shock tube and tunnel. The HDT was acquired by the University of Oxford's Osney Thermo-Fluids Institute in 2012. With the addition of a fast-acting plug valve [138], the HDT added the ability to be operated as a Ludwieg Tube or Light Isentropic Compression Heating (LICH) mode.

For this research, the Oxford HDT is run using its Ludwieg tube mode. Each experimental test begins by filling the barrels with air to the pre-determined fill pressure. External electrical heating of the test gas is used to increase the total temperature, up to a maximum temperature of 573 K. The objective is to heat the

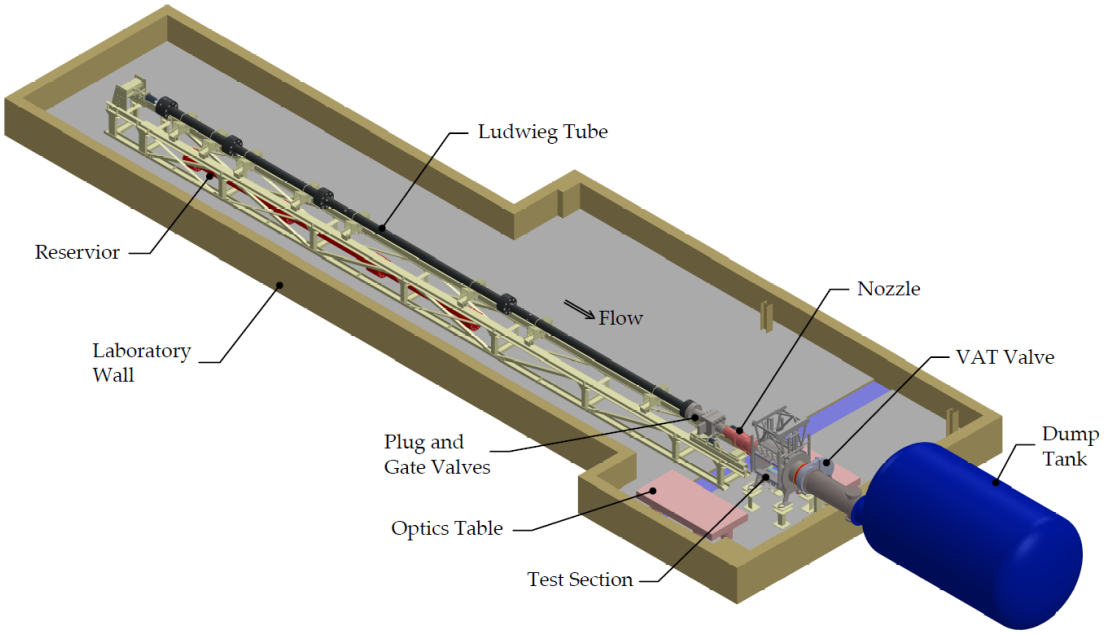

Figure 4.5: An annotated schematic of the Oxford High Density Tunnel (HDT) [138].

test gas enough so that it does not liquefy at the nozzle exit. The Ludwieg tube is attached to a bespoke fast-acting plug valve assembly, which feeds the stagnation plenum of a Laval nozzle. The test time begins when the plug valve is opened, causing the test gas to undergo an unsteady expansion and accelerate through the convergent/divergent nozzle. The facility nozzle exhausts into the test section, and then into a 28 m^3 vacuum tank that is external to the building. The nozzle exit diameter is 350 mm, with a length of 1395 mm between the throat and nozzle exit. The test section has a diameter of 760 mm and a length of 940 mm.

A succession of expansion waves propagates into the high-pressure region when the plug valve is opened. The initial test time is therefore steady until the expansion wave reflects from the far end of the tube and passes through the nozzle again. This results in multiple quasi-steady flows (referred to as "plateaus") between expansion wave reflections, giving a sweep of conditions for an individual shot. The plug valve timings can be modified to control the amount of flow passing through the facility. This allows the operator to dictate the number of steady test time plateaus that are being captured. Details about the fast-acting plug valve can be found in Ref. [138]. More recently [156], two modes have been developed for the HDT: Extended Ludwieg

Mode (ELM) and Plenum Augmented Ludwieg Mode (PALM). ELM produces a test flow that is over fifteen times longer but of comparable steadiness to a Mach 7 Ludwieg Mode plateau. PALM on the other hand results in a test flow that is both ten times the duration of, and significantly steadier (for supply pressure and unit Reynolds number) than a typical Ludwieg Mode plateau though sacrificing the peak supply pressure that can be attained for a given fill pressure compared to Ludwieg Mode, significantly reducing the unit Reynolds number capability of PALM.

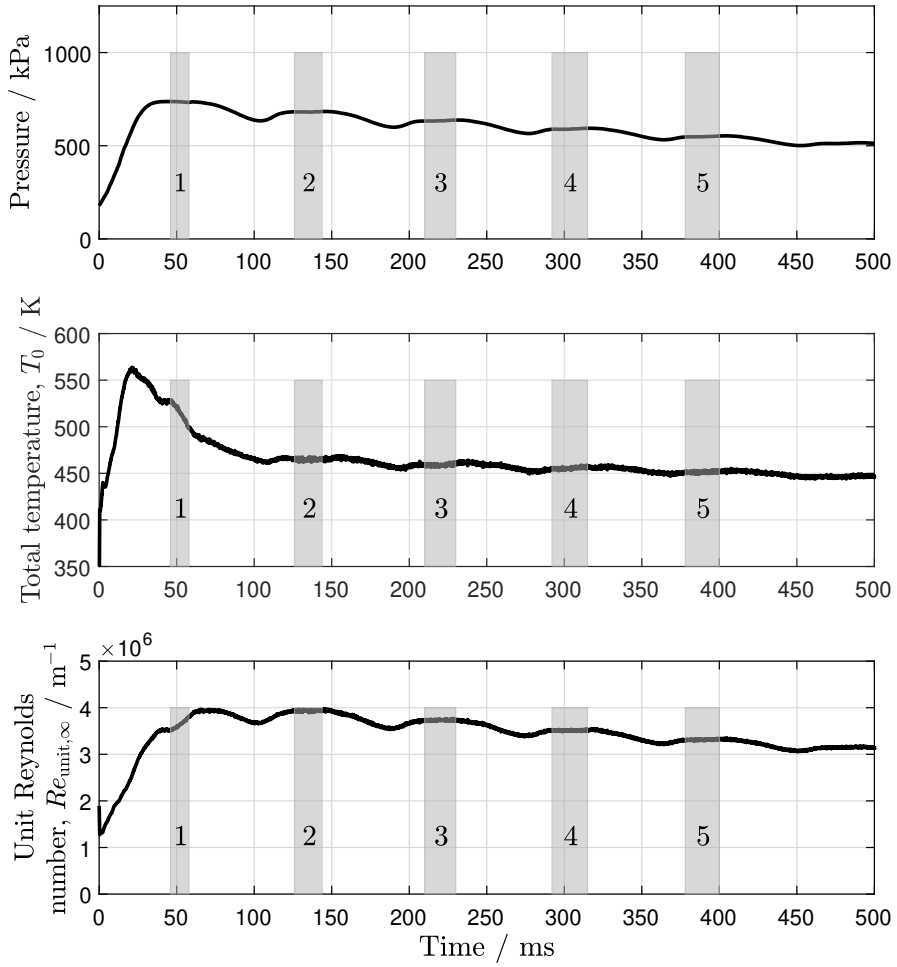

Figure 4.6: HDT facility conditions using the Mach 7 nozzle. The fill conditions are: $P_{\mathrm{fill}} = 777\,\mathrm{kPa}$, $T_{\mathrm{fill}} = 500\,\mathrm{K}$. The quasi-steady plateau test times are illustrated by the grey-shaded areas.

Figure 4.6 illustrates a typical shot in the HDT for these experiments. The pressure in the plenum upstream of the Laval nozzle is measured and approximated as the total pressure, p_0. The total temperature, T_0, is measured in the test section

using differentially heated aspirated thermocouples as described in previous work by Hermann et al. [157]. The various reflected expansion waves enable testing at multiple quasi-steady conditions – each lasting for approximately 30 ms - from one single shot. Condition 1 is typically not considered as it is relatively unsteady. The freestream Mach number is calculated either from the edge static pressure (for example on a flat plate model) or from the pitot pressure (generally measured by a dedicated rake). The edge velocity is calculated by the equation

$$u_\infty = M_\infty \sqrt{\gamma R T_\infty} \tag{4.10}$$

The edge unit Reynolds number is obtained from the equation

$$Re_u = \frac{\rho_\infty u_\infty}{\mu_\infty} \tag{4.11}$$

where μ_∞ is the dynamic viscosity of the flow. Since $T_e < 89$ /,K, the Keyes' viscosity model [158] is given as

$$\mu_\infty = \frac{1.488 \cdot 10^{-6} \sqrt{T_\infty}}{1 + \frac{122.1}{T_\infty} \cdot 10^{\frac{-5}{T_\infty}}} \tag{4.12}$$

For these experiments, the Mach 7 nozzle was used and a single freestream flow condition corresponding to $Re_u = 3.84{\cdot}10^6\,\mathrm{m}^{-1}$ was chosen for these tests. Stagnation and freestream (or nozzle exit) flow properties are provided in Table 4.2. These are taken from a detailed characterisation study of the facility conducted prior to this work. Several injection pressures were prescribed for all of the injected gases and the resultant mass fluxes were then found by solving the Darcy-Forchheimer equation [62] (Table 4.3).

Table 4.2: Flow conditions of the test.

Parameter	Stagnation (tot)	Static (∞)
Pressure, p / Pa	$6.45{\cdot}10^5$	151
Temperature, T / K	459	42.2
Velocity, u / $\mathrm{m\,s^{-1}}$	-	915
Density, ρ / $\mathrm{kg\,m^{-3}}$	-	0.0125
Mach Number, M	-	7.03

Table 4.3: Plenum pressures and the associated mass fluxes and blowing parameters of the injected gases. Note: the value of blowing parameter requires St_0 and has thus been calculated based on the heat transfer to the uncooled stagnation probe.

	Coolant gas				
Parameter	N_2	Air	Kr	Ar	He
Molecular Weight, M / $\mathrm{g\,mol^{-1}}$	28.01	28.96	83.8	39.94	4.003
Plenum Pressure, p_{pl} / kPa	279 - 1041	278 - 1044	151 - 718	258 - 1032	1075 - 1541
Mass flux, $\dot{m}_f$ / $\mathrm{kg\,s^{-1}\,m^{-2}}$	0.0145 - 0.1952	0.0148 - 0.2007	0.0092 - 0.2052	0.0134 - 0.2227	0.0392 - 0.0803
Blowing parameter, B_h	0.104 - 1.38	0.106 - 1.44	0.0654 - 1.45	0.0870 - 1.37	0.065 - 0.496

4.4 Infrared Calibration

Conversion of the raw data recorded by the infrared camera to the surface temperature of the porous sample requires a careful calibration process. This process may be broken down into two distinct stages:

1. A multipoint calibration captured in situ using a black body calibrator. This step calibrates the camera and optical system by correcting any detector or optical system non-uniformities and relates the camera raw signal to the true black body temperature inside the wind tunnel test section.

2. A material emissivity calibration performed using a bench-top setup.

4.4.1 Multipoint Calibration

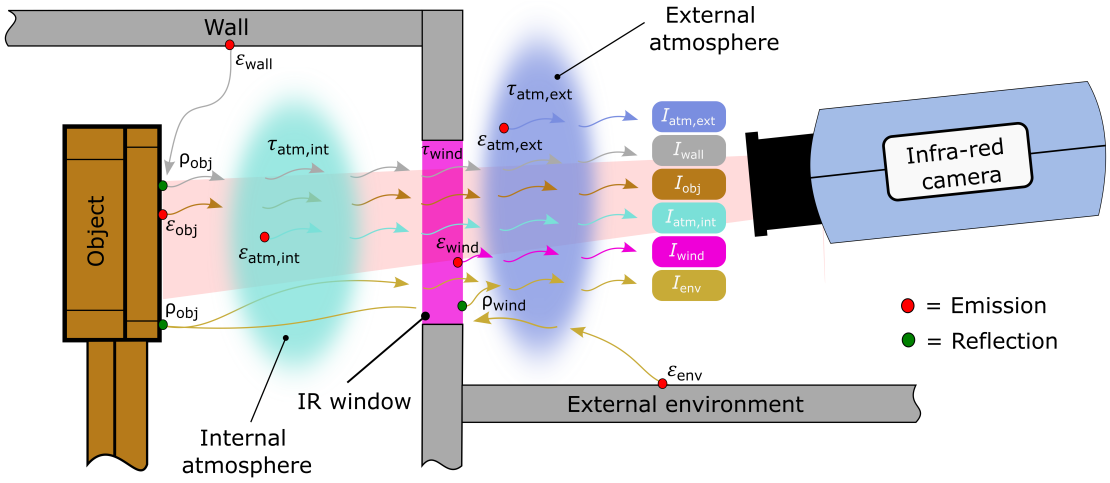

Figure 4.7: Illustration of the dominant optical path signal terms in the wind tunnel test section.

Following the basic principles laid out by Zaccara et al. [139], when a model is placed inside the test section, there are various sources of radiation as shown schematically in Fig. 4.7. The total radiant intensity detected by the camera during a test (I_D) is:

$$I_D(t) = I_{\text{atm,ext}}(t) + I_{\text{wall}}(t) + I_{\text{obj}}(t) + I_{\text{atm,int}}(t) + I_{\text{wind}}(t) + I_{\text{env}}(t) \tag{4.13}$$

where each component term is given as follows

$$I_{\text{atm,ext}}(t) = \varepsilon_{\text{atm,ext}} \cdot I_{bb}^{\text{atm,ext}}(t) \tag{4.14}$$

$$I_{\text{wall}}(t) = \tau_{\text{atm,ext}} \cdot \tau_{\text{wind}} \cdot \tau_{\text{atm,int}} \cdot \rho_{\text{obj}} \cdot \tau_{\text{atm,int}} \cdot \varepsilon_{\text{wall}} \cdot I_{bb}^{\text{wall}}(t) \tag{4.15}$$

$$I_{\text{obj}}(t) = \tau_{\text{atm,ext}} \cdot \tau_{\text{wind}} \cdot \tau_{\text{atm,int}} \cdot \varepsilon_{\text{obj}} \cdot I_{bb}^{\text{obj}}(t) \tag{4.16}$$

$$I_{\text{wind}}(t) = \tau_{\text{atm,ext}} \cdot \varepsilon_{\text{wind}} \cdot I_{bb}^{\text{wind}}(t) \tag{4.17}$$

$$I_{\text{atm,int}}(t) = \tau_{\text{atm,ext}} \cdot \tau_{\text{wind}} \cdot \varepsilon_{\text{atm,int}} \cdot I_{bb}^{\text{atm,int}}(t) \tag{4.18}$$

$$\begin{aligned} I_{\text{env}}(t) = {} & \tau_{\text{atm,ext}} \cdot \rho_{\text{wind}} \cdot \tau_{\text{atm,ext}} \cdot \varepsilon_{\text{env}} \cdot I_{bb}^{\text{env}}(t) + \\ & \tau_{\text{atm,ext}} \cdot \tau_{\text{wind}} \cdot \tau_{\text{atm,int}} \cdot \rho_{\text{obj}} \cdot \tau_{\text{atm,int}} \cdot \tau_{\text{wind}} \cdot \tau_{\text{atm,ext}} \cdot \varepsilon_{\text{env}} \cdot I_{bb}^{\text{env}}(t). \end{aligned} \tag{4.19}$$

For these cases, ε refers to the emissivity, τ the transmissivity, and ρ the reflectivity. The subscript (atm,ext) refers to the external atmosphere outside the test section, (wall) refers to the internal walls of the test section, (obj) refers to the object of interest, (wind) refers to the optical window, (atm,int) refers to the internal atmosphere inside the test section, and (env) refers to the external environment outside the test section such as the camera body, the external test

section wall or other surrounding objects. Finally, (bb) refers to the equivalent radiant intensity if that object were a black body.

In practice, assuming that none of these sources change temperature appreciably during a test—which is a reasonable assumption for a short-duration facility such as the HDT with a total test time of below 1 s — all of these terms except for I_{obj} are essentially constant over the course of a test (I_{bb}^{obj}). Thus, Eq. (4.13) may expressed as

$$I_D(t) = \varepsilon_{\text{obj}} \cdot A1 \cdot I_{bb}^{\text{obj}}(t) + \rho_{\text{obj}} \cdot A2 \cdot I_{bb}^{\text{amb}} \tag{4.20}$$

The $A1$ and $A2$ parameters are obtained by conducting an in-situ calibration. Following a similar procedure to that of Playford [159], a black body calibrator is placed inside the test section at the same position as the model. Any errors with positioning the calibrator relative to the model will lead to an error in the directional emissivity. If the model is a simple flat plate and perpendicular or close to perpendicular to the infrared camera, then a 1-2° misalignment of the black body is unlikely to lead to significant errors. Whilst if the model is complex, with detailed surfaces, then ensuring the black body is at the same position as the model is essential. Further details are in Section 4.4.2. The reference black body used for these tests was the CI-Systems SR-33-7 infrared calibrator which is an extended black body source with a known emissivity of 0.98 and a 178 mm diameter aperture.

The detected infrared signal may then be related to the temperature of the calibrator. Theoretically, for a multipoint calibration, a true black body source is required ($\varepsilon = 1$). As the emissivity of this calibrator is not 1, a correction was applied to give the equivalent black body temperature of the calibrator, T_{bb}^{calib}. The process was completed by following the offset procedure detailed in the Fluke IR calibration handbook [160]. The large diameter aperture of the calibrator encompasses the full field of view of the infrared camera and may thus be used to perform a complete non-uniformity calibration. Before starting a calibration, the frame rate, image resolution and integration time of the camera were set at the value required for the experiment. Thereafter, the multipoint calibration was completed by performing the following two operations:

1. Pixel-wise non-uniformity correction: The black body calibrator is imaged by the infrared camera and the variation of each pixel from the mean value of the whole image is calculated. This was conducted for every temperature step across the full range of temperatures of interest. The temperature range of interest needs to be determined prior to the test based on the model geometry and flow conditions, i.e. the estimated temperature change over the course of a test. This results in the following offset correction

$$\text{Offset}(T_{\text{step}}, x, y) = D(T_{\text{step}}, x, y) - \overline{D}(T_{\text{step}}). \tag{4.21}$$

Since only discrete temperature steps are recorded, a shape-preserving piecewise cubic polynomial interpolation method is employed to derive the intermediate values.

2. Detector characterisation: The mean camera signal at each temperature, $\overline{D}(T_{\text{step})}$ is analogous to a radiant intensity signal. Thus, the mean signal and the radiant intensity of the black body calibrator at each discrete temperature step may be related as

$$\overline{D}(T_{\text{step}}) = A1 * I_{bb}^{\text{calib}}(T_{\text{step}}) + A2 * I_{bb}^{\text{amb}}(T_{\text{step}}) \tag{4.22}$$

where the radiant intensity, I_{bb}^{calib}, is calculated from the equivalent black body temperature, T_{bb}^{calib}. This value is found by applying the integral of Planck's law for the wavelength band of the camera

$$I_{bb} = 2hc^2 \int_{\lambda_{min}}^{\lambda_{max}} \frac{1}{\lambda^5(\exp\frac{hc}{\lambda k_b T_{bb}} - 1)} d\lambda \tag{4.23}$$

where λ_{max} and λ_{min} are the upper and lower wavelength limits of the infrared camera (7.5 and 11 μm, respectively), h is Planck's constant, c is the speed of light in a vacuum, k_b is the Boltzmann constant and λ is the wavelength. The black body temperature at each step, T_{bb}^{calib}, is determined

from the recorded temperature of the black body calibrator and the ambient temperature,T_{bb}^{amb}, from a fixed lab thermometer. The Levenburg-Marquart least squares algorithm is employed to find the constants $A1$ and $A2$. Figure 4.8 shows the resultant offset and calibration curves. For this experiment, the values of $A1$ and $A2$ were 46.46 and 59.09 respectively with a coefficient of determination, R^2, of 0.9986.

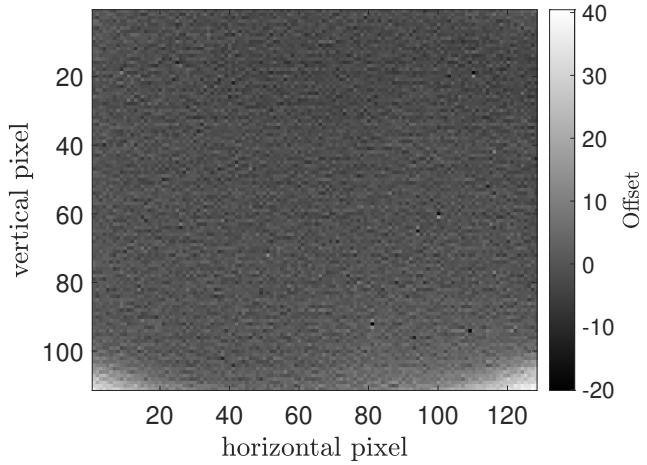

(a) Pixel-wise offset variation at 300 K

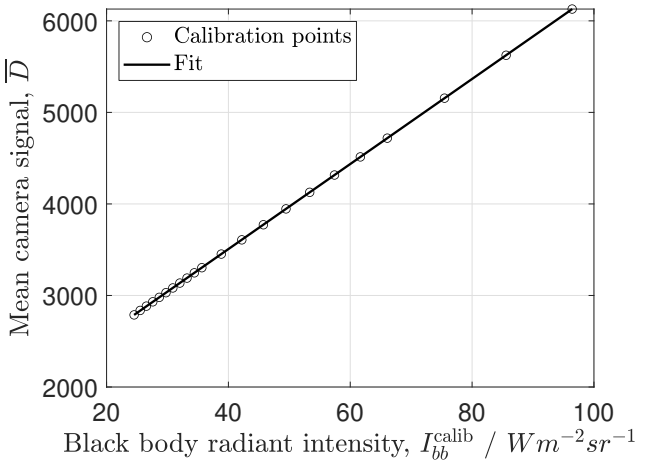

(b) Camera calibration curve

Figure 4.8: Infrared camera calibration curves for this study.

Once the offset, $A1$ and $A2$ are obtained through the above calibration procedure, these values may be applied pixel by pixel to the infrared camera test data as per Eq. (4.20) where $I_D(t)$ is the signal detected by the camera and $I_{bb}^{\text{obj}}(t)$ is the radiant intensity of the object that we are trying to obtain. The final remaining parameter

required is the emissivity of the object surface, ε_{obj}, which is described in the section below. Once the radiant intensity of the object is found, $I_{bb}^{\text{obj}}(t)$ may be converted to the true object temperature, $T_{bb}^{\text{obj}}(t)$ by applying Planck's law, Eq (4.23), in reverse. Overall, the advantage of this method is that pre-existing knowledge of the window transmissivity, internal test section emissivity etc. are not needed, rather all of those effects are captured within the offset and calibration coefficients, $A1$ and $A2$.

4.4.2 Emissivity Measurement

The emissivity of an object is dependent on the surface roughness, the wavelength and the material properties. For this reason, an in-house custom calibration plate was constructed to measure the emissivity (Fig 4.9). The calibration plate consists of a circular silicon heater mat mounted onto a 150 mm diameter, 20 mm thick copper disk. At the opposing surface, a very thin 1 mm groove was cut out where a disk of the material of interest for infrared experiments may be mounted - in this instance Alumina. The copper block is encased with Rohacell® to reduce losses through conduction. The front disk is bonded to the copper using a highly conductive thermal paste and is instrumented with four T-type surface-mounted thermocouples. Temperature control of the copper disk is achieved via a PID heater controller which was able to maintain the copper disk at a set-point level of ± 0.1 K. However, in reality, the uncertainty of the temperature measurement will be in the order of ± 1 K or $\pm 0.75\%$, whichever is greater.

The infrared camera was placed in a radiation-shielded enclosure, painted black, 0.5 m from the calibrator. The camera then recorded the signal from the custom calibrator for two different temperatures - ambient and 45.0°C. For each step, 1 s of data was collected at 1 kHz and the mean value was recorded. The true surface temperature of the Alumina, I_{bb}^{obj} (obtained via the surface mounted thermocouples), was compared against the camera detected signal, I_D, and the emissivity found through the following equation

$$\varepsilon = \frac{I_D(T_2) - I_D(T_1)}{I_{bb}^{\text{obj}}(T_2) - I_{bb}^{\text{obj}}(T_1)}. \tag{4.24}$$

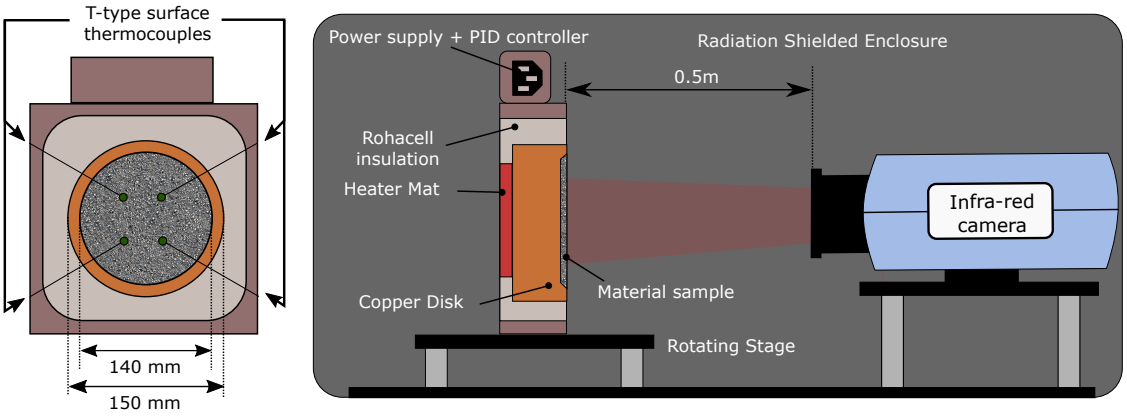

Figure 4.9: Schematic of the in-house bench-top emissivity measurement setup, not to scale.

This equation is valid as long as the environmental temperature inside the radiation-shielded box remains constant. The environmental temperature was monitored over the course of a calibration by two K-type thermocuples mounted on the radiation-shielded box. Next, by mounting the calibrator onto a rotation stage, the directional emissivity of the body was determined. Theoretically, for dielectric materials, i.e. materials with low electrical conductivity such as PEEK or Alumina, the directional emissivity coefficient $\varepsilon_{\lambda,\theta}$ for a smooth opaque medium can be calculated according to the following relationship [161]:

$$\varepsilon_\theta = \frac{2\cos(\theta)\sqrt{n^2 - \sin^2(\theta)}}{(\cos(\theta) + \sqrt{n^2 - \sin^2(\theta)})^2}\left(1 + \frac{n^2}{(\cos(\theta)\sqrt{n^2 - \sin^2(\theta)} + \sin^2(\theta))^2}\right) \tag{4.25}$$

where n is the refractive index of the material and θ is the angle between the direction normal to the emitted surface and the direction of the emitting radiation. In the absence of any knowledge of the refractive index for Alumina, n was varied until the best fit between the experimental points and the theoretical curve is obtained. Figure 4.10 presents a comparison of the experimental measurements with the theoretical curve assuming $n = 1.8$. Ten experimental points were taken and it can be seen that they match the theoretical curve to within 6%, with greater scatter at high viewing angles. The scatter in the measurements at high viewing angles are likely due to errors in the angle set by the rotation stage. However, for the experiments presented in this work, the directional emissivity does not affect

the measurements as the view angle of the Alumina sample on the stagnation probe relative to the infrared camera was measured to be 35° and at this view angle, the measured emissivity essentially constant at 0.97. It must be noted that the Alumina measured during the emissivity calibration is not the same material used for the stagnation probe model. However, several different Alumina samples were tested at $\theta = 0°$ and the emissivity was consistently 0.97 ± 0.1 promoting confidence that the Alumina injector on the stagnation probe is the same.

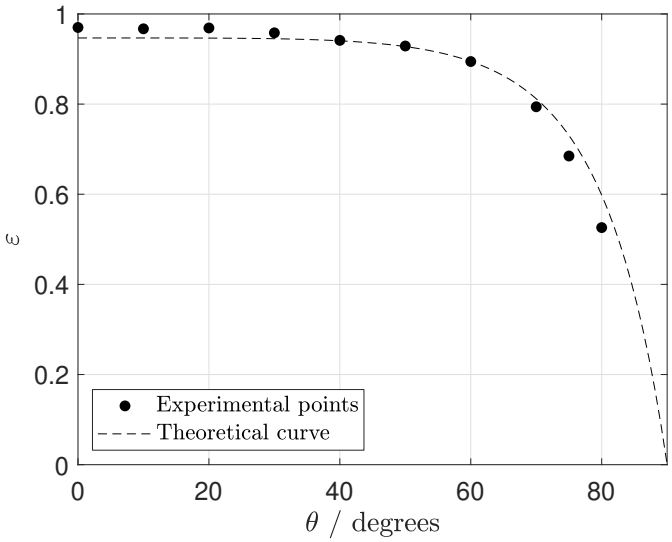

Figure 4.10: Directional emissivity of Alumina. The theoretical curve is based on Eq. (4.25) with $n = 1.8$.

4.4.3 Image Processing

The raw data (Fig. 4.11a) was filtered temporally using a Savitsky-Golay finite impulse response (FIR) smoothing filter. After filtering, the location of the Alumina sample on the flat-faced cylinder was identified and an affine transform was applied to transform the perspective view of the front face to a square mesh (Fig. 4.11b). Due to the simplicity of the geometry in this case, the edges of the sample in the IR image were identified using a canny edge detection algorithm. Following this, the edge of the sample was used to define the moving points for an affine transform to a square. After the calculation of the affine transform, the infrared image gives a final spatial resolution of 1.1 pixels/mm. This transformation was applied for every

temporal infrared frame. Finally, the calibration process described above was applied to convert raw camera signals to quantitative temperature maps such as Fig. 4.11c.

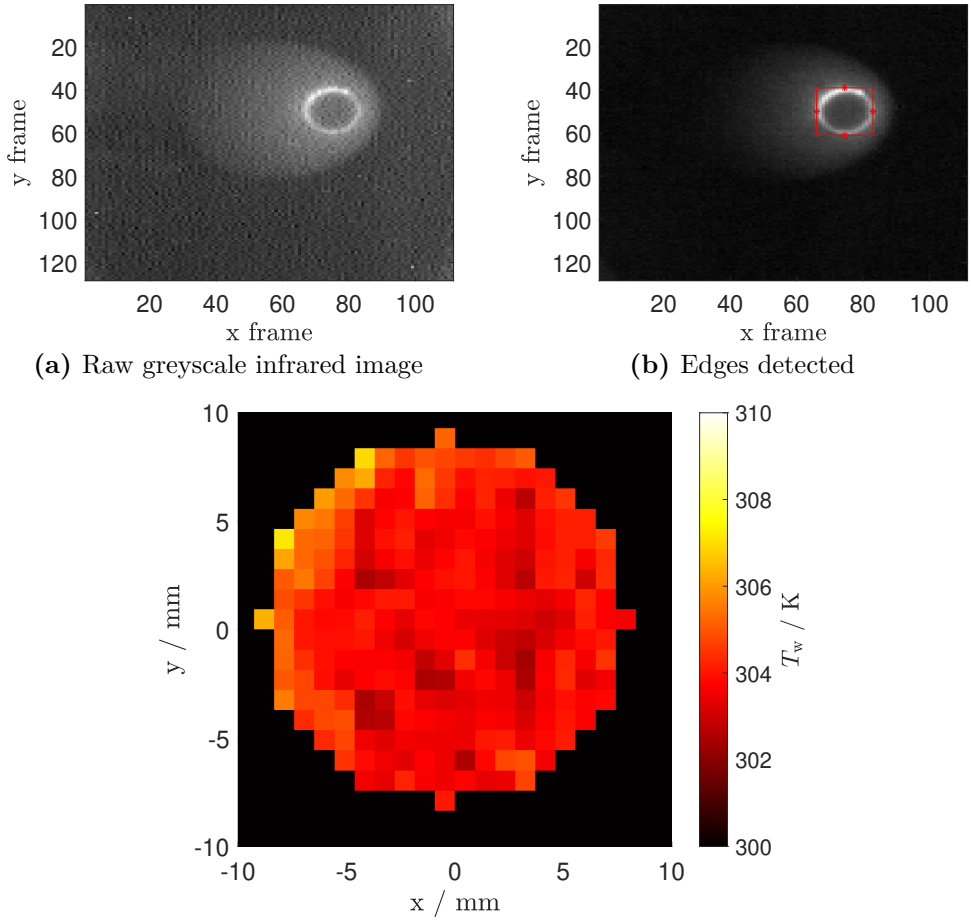

(a) Raw greyscale infrared image

(b) Edges detected

(c) Transforms and infrared calibration applied

Figure 4.11: Image processing steps for the stagnation point infrared experimental data.

4.5 Data Processing

Reduction of the temperature history of a material (measured from sensors or an infrared camera) to the incident heat flux requires an assumed physical model. This model should account for all necessary heat transfer mechanisms present in the experiment. This section describes the data processing steps used in this work to calculate heat flux from the infrared temperature measurement data. The basic physical model is that of conduction, however complications are introduced due to the use of a transpiration-cooled material. As discussed in Ref. [74], for

transpiration-cooled surfaces, it is necessary to model not only heat transfer by conduction in the solid but also the fluid heat transfer process and any interaction between the fluid and solid.

The operation of the gas injection system used in this work results in an unsteady filling of the plenum directory behind the porous injector. As shown in Fig. 4.12, this results in a transient increase in gas temperature in the plenum. To ensure that the injected gas is at thermal equilibrium with the porous material during external flow, the injection was adjusted to begin approximately 3 seconds prior to test flow onset. Nevertheless, the transient heating of the coolant imparts a backside heat transfer boundary condition that must be accounted for through either a numerical model or calibration. The backside heat flux is detected as a temperature change on the porous surface prior to external flow on-set, as seen in Fig. 4.11 (a) for t < 0 s. Resolving this additional heat flux boundary condition requires accurate information of the internal heat transfer coefficient of Alumina as well as the exact plenum gas temperature at the backside of the porous material. This temperature measurement is difficult to measure (even with a fast-response thermocouple) as the injected gas has a very slow velocity at the backside of the porous material, and so the heat transfer to any thermocouple is small and slow.

To overcome this limitation, the heat transfer process between the fluid and solid was accounted for by conducting a calibration run before every test. The calibration consisted of injecting the same pressure gas as a given test and measuring the surface and plenum gas temperature without any freestream test flow (i.e. injecting coolant gas into the test section vacuum). With reference to Fig. 4.13, the corrected surface heat transfer (Fig. 4.11(c)) was determined by subtracting the temporal temperature profile of the calibration (Fig. 4.11(b)) from the experimental temperature profile (Fig. 4.11(a)) for every pixel location of the infrared image. This subtraction process essentially treats the heat transfer process as a linear time-invariant model which assumes that the fluid and solid are in thermal equilibrium at the surface of the porous injector. Using the corrected temperature profile (for each pixel), the heat flux was determined by applying the impulse response method of Oldfield [162] which

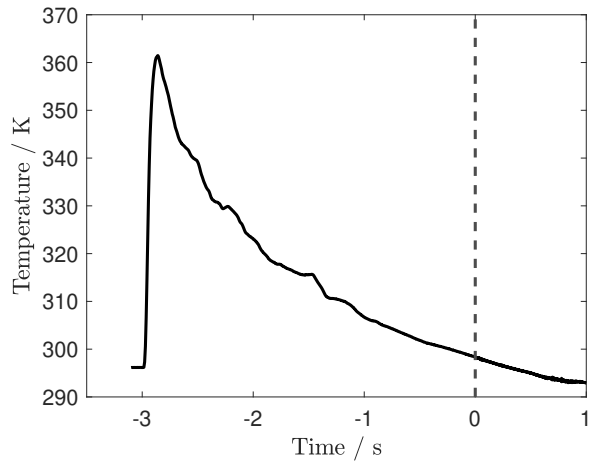

(a) Plenum temperature trace

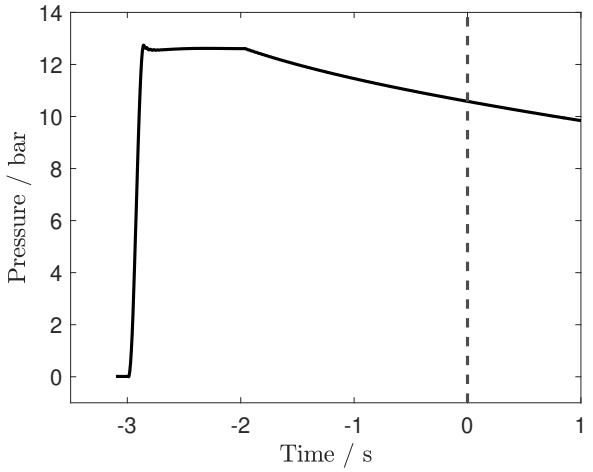

(b) Plenum pressure trace

Figure 4.12: Example plenum temperature and pressure traces for nitrogen injection at an injection mass flux of $0.1952\,\mathrm{kg\,s^{-1}\,m^{-2}}$. The external test flow starts at time = 0 s as indicated by the dashed lines.

assumes that the material thermal response is one-dimensional and semi-infinite. This assumption is considered valid for testing conducted in the Oxford HDT as the time scale for a penetration depth of 5 mm (the thickness of the injector) is over 0.25 s [131]. Finally, the heat flux is averaged over a chosen steady flow period and the Stanton number is found based on the freestream parameters as per Eq. (4.3).

4.6 Numerical Simulations

To support and further validate the experimental data, laminar, transient CFD simulations have been conducted for a subset of nitrogen and helium injection cases.

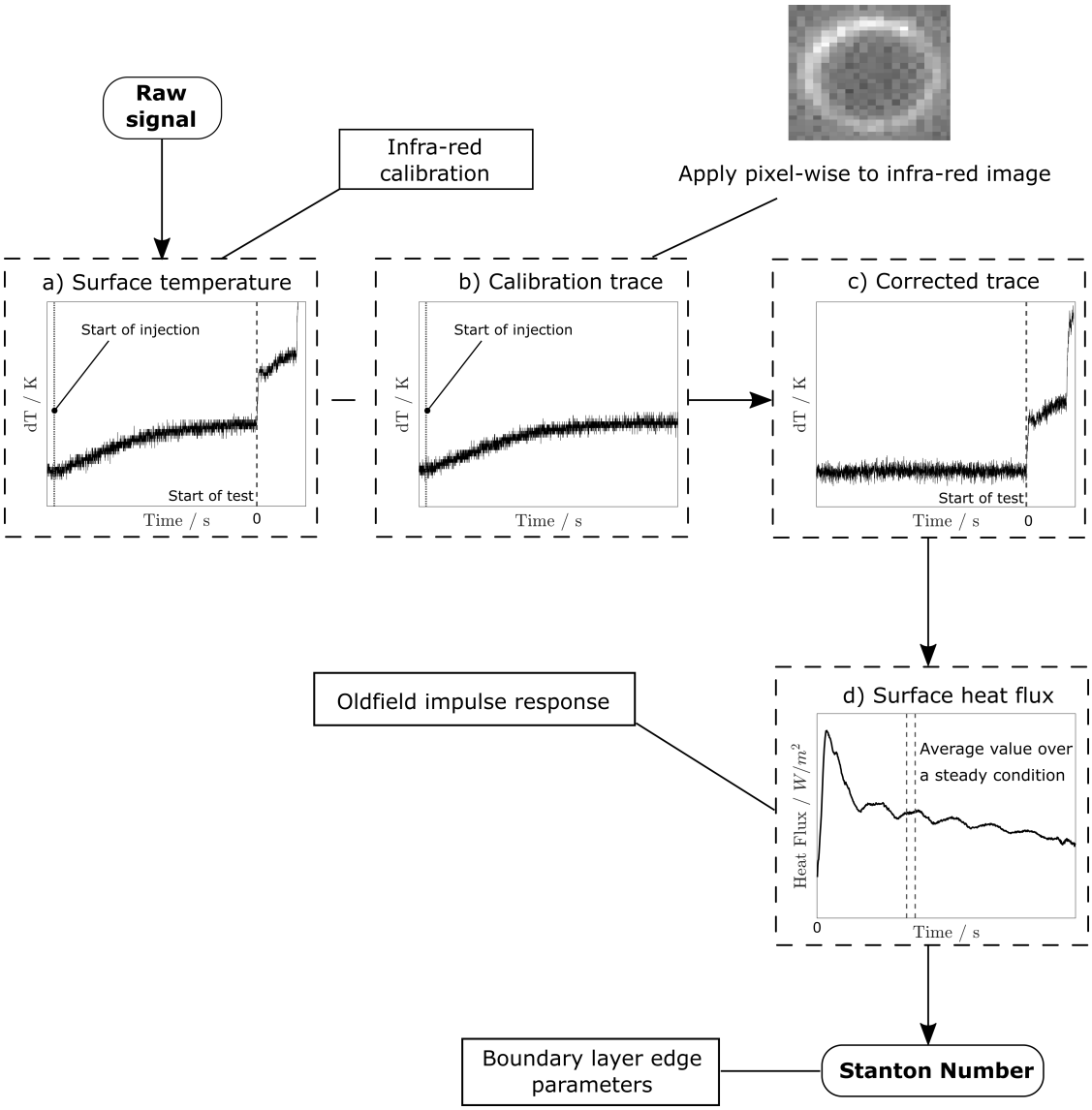

Figure 4.13: Overview of the entire data processing chain. The dashed line on the temperature plots refer to the start of the test and the dotted line to the start of injection.

The simulations were conducted using Eilmer 4[1] which is a high fidelity CFD solver developed for the numerical simulation of transient, compressible gas flows in both two and three dimensions [163, 164]). A two-dimensional axisymmetric simulation was set up with a geometry that matched the physical experimental model i.e. a 50 mm radius hemispherical model with a 21 mm diameter flat face. The domain of computation and the boundary conditions are overlayed onto the post-shock pressure flow-field in Fig. 4.14. The inflow was taken from Table 4.2 and a shock fitting

[1]https://gdtk.uqcloud.net/

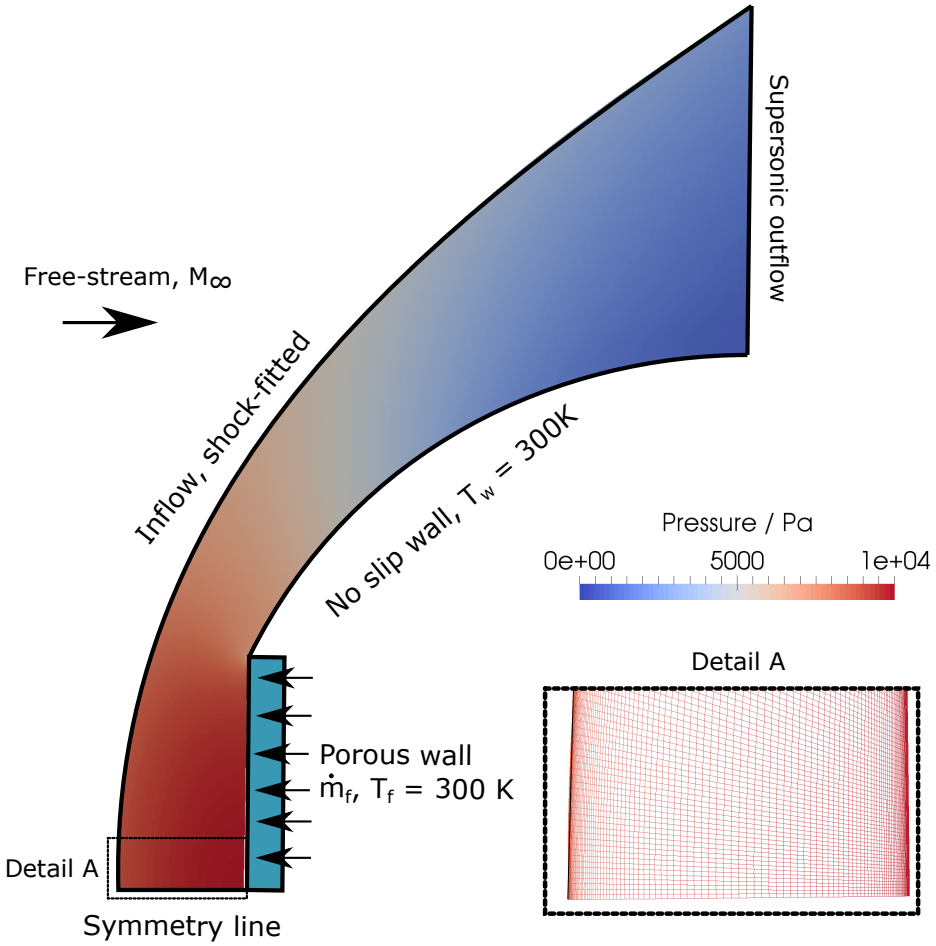

Figure 4.14: CFD boundary conditions overlaid onto the post-shock pressure flow field around the stagnation probe. Wire-frame of detail A, illustrating the mesh size and density near the stagnation point.

boundary condition with the mesh clustered near the shock and boundary layer was used to accurately resolve the shock boundary condition and improve cell density. A no-slip isothermal wall boundary condition with $T_w = 300\,\mathrm{K}$ was used for the model surface. A porous wall boundary condition was defined over a radius of 10.5 mm, matching the size of the experimental porous sample. This boundary condition is applied through a basic diffusion model consisting of Fick's law and diffusion coefficients calculated using the Lennard-Jones parameters. The temperature of the injected fluid at the porous interface is set at 300 K and more details of this boundary condition may be found in Ref. [165]. Both the freestream gas and injected coolant gas were assumed to be perfect gases. A blend of the low-dissipation advection upstream splitting method for the regions away from shocks and a more diffusive

Hänel–Schwane–Seider scheme for the interfaces near shocks was employed as flux calculator. The simulations were run for 0.8 ms to achieve convergence. A mesh sensitivity study was conducted with a final mesh chosen with $2.88 \cdot 10^4$ cells and a first cell height from the wall of $\Delta = 2.8 \cdot 10^{-6}$m. Ensuring that $Re_c < 10$ is a common condition to ensure that the flow gradients in the viscous boundary layer near the wall are accurately resolved [166] and, for this mesh, Re_c never exceeds 6.

4.7 Results and Discussion

The aim of this work was to directly measure the heat transfer on a transpiration-cooled porous injector. Recording calibrated infrared temperature measurements and calculating heat fluxes using the impulse response method are complex processes with many possible sources of error both in the experimental setup and the data reduction algorithm. To validate the combined experimental setup and heat transfer processing methodology, the experimentally derived stagnation point Stanton numbers are compared with the following correlations, analytical solutions and simulations:

1. The Swann-Pittmann correlation for the heat transfer reduction at the stagnation point with identical gas injection (i.e. where the freestream and injected gases are the same), Eq. (4.1).

2. The closed form solution of convective heat transfer reduction with gas injection derived by Yoshikawa, Eq. (4.6). This has been applied to all the gases tested in this study.

3. A perfect gas simulation in Eilmer 4 which has been applied for nitrogen and helium injection.

A rigorous uncertainty analysis was conducted accounting for uncertainties in material properties, the infrared camera calibration and the facility freestream conditions; the details of which may be found in Section 4.9. The total uncertainty in Stanton number is 13.54% and blowing parameter is approximately 15.58%. The largest contributions of uncertainty were from the uncertainty in the material

thermal product, $\sqrt{\rho c_p k}$, the injected mass flux, $\dot{m}_f$, the total temperature, and the freestream Mach number.

Figures 4.15 and 4.16 present all the results of this work. Figure 4.15a depicts Stanton number maps for nitrogen injection at four different blowing parameters while Fig. 4.15b shows the radial average values. The experimental Stanton number distribution for the uncooled case is within 3% of the computational value; this is smaller than the experimental uncertainty. In addition, the experimental curve clearly follows the slight, monotonic increase in the Stanton number further away from the stagnation point. This confirms that the fundamental calibration and processing steps detailed in this study are valid. The cooled cases similarly show good agreement with computational values, with all cases matching within experimental uncertainty bounds. It is noted that the distribution of coolant on the sample is very uniform, with marginally more cooling on the right-hand side in line with the hot wire map in Fig. 4.3.

To directly compare the results from these experiments with existing correlations and numerical simulations, the average Stanton number reduction across the injector was plotted against the blowing parameter. The variation in normalised Stanton number with blowing parameter is presented in Fig. 4.16a while Fig. 4.16b presents the variation against the molecular weight corrected blowing parameter. Referring to Fig. 4.16a, it can be seen that the experimental data show strong agreement with the CFD and correlations for all cases tested in this work. The experimental data is consistently slightly below the simulations for large blowing parameters (this is reflected in radial average values plotted above) and is likely due to either errors in the measurement of the injected mass flux or the assumption that the coolant temperature equals the material temperature breaking down. Future experiments using a different gas injection system in which a constant mass flow rate of coolant is supplied for a long period of time before tunnel fires (so that the coolant is in thermal equilibrium with the porous injector) will be helpful to eliminate temperature dependant effects. In addition, the experimental data points lie within 10% of the predicted values by Yoshikawa and Swann-Pittmann (though

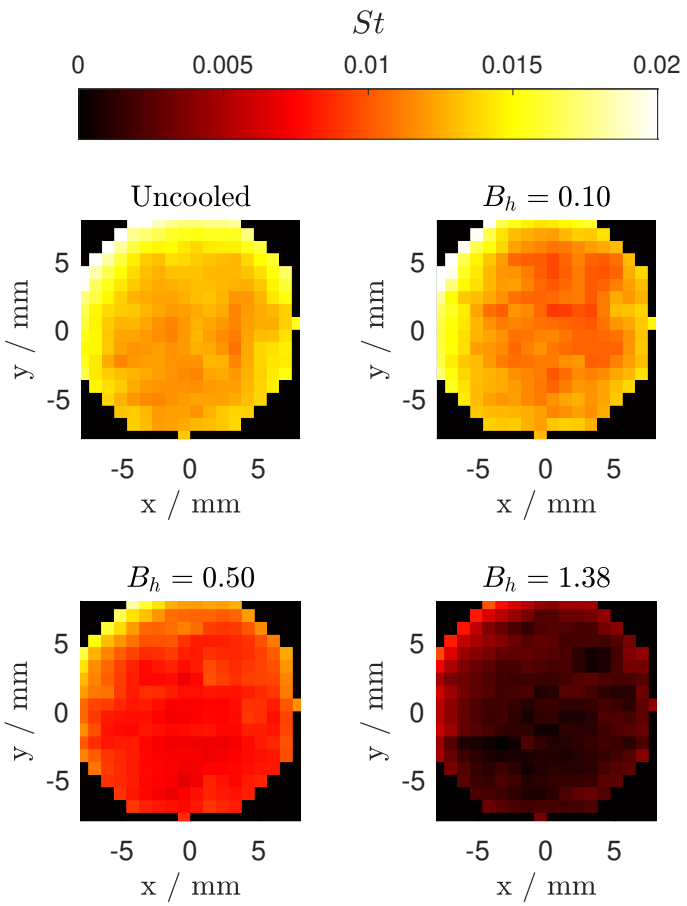

(a) Contour maps.

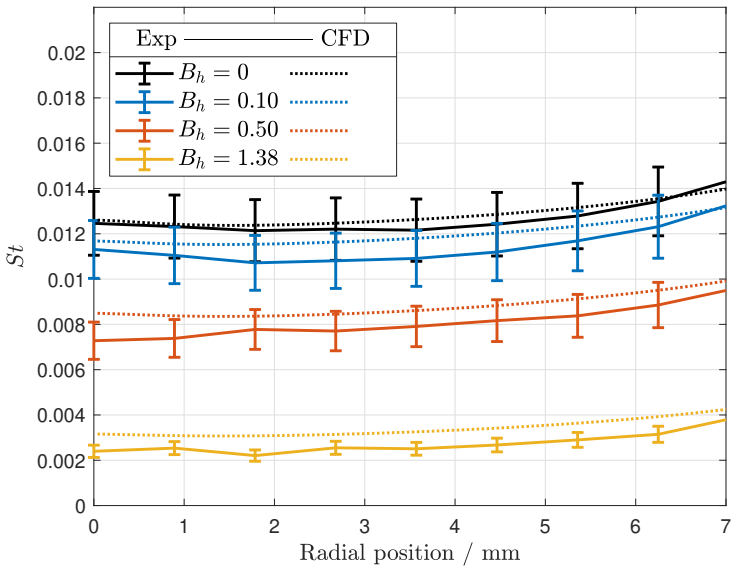

(b) Radially average values.

Figure 4.15: Nitrogen injection at four different blowing parameters.

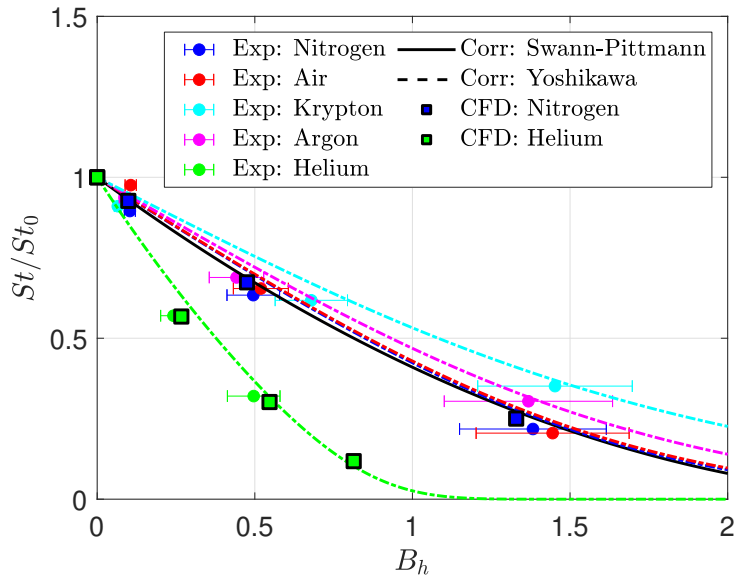

(a) Nominal.

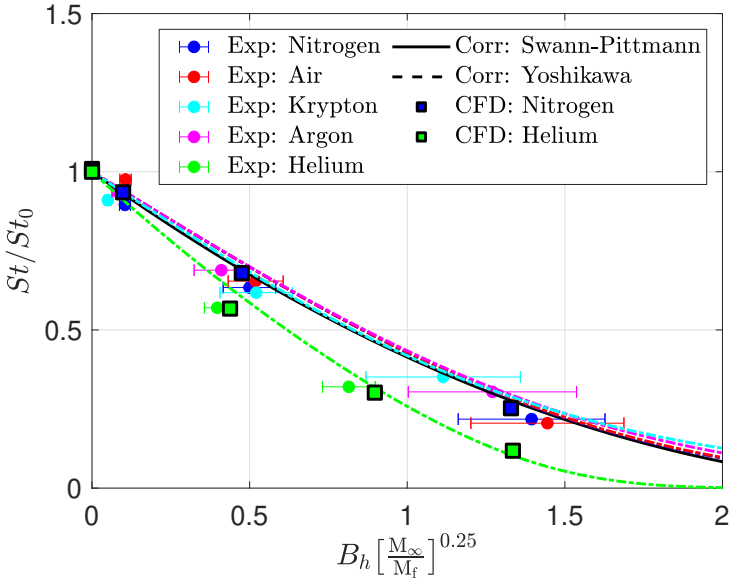

(b) Corrected with the molecular weight factor.

Figure 4.16: Stanton number reduction vs blowing parameter for nitrogen, air, argon, krypton and kelium injection.

Swann-Pittmann is only valid for either air or nitrogen injection). Plotting the blowing parameter (Fig. 4.16b) with the molecular weight correction of Eq. (4.5) collapses all the data except for helium onto one line confirming the empirical findings of Marvin and Pope [117]. This is well substantiated with lighter gases such as helium and hydrogen noted to show less agreement to the molecular weight correlation than the heavier gases (argon, krypton etc.). Overall, these experiments

have substantiated the infrared surface measurement methodology described in this paper for transpiration-cooled surfaces and give confidence in applying this technique to more complicated geometries and flow fields.

4.8 Conclusions

The effect of mass addition on the surface heat transfer at a stagnation point has been measured experimentally using infrared thermography. This has resulted in the first spatial surface heat transfer measurements of a transpiration-cooled porous material in a short-duration hypersonic facility. Increasing the blowing parameter leads to a reduction in surface heat transfer for all cases with helium showing the highest effectiveness and Krypton the lowest. The experimental results have broadly aligned with well-known correlations and computational results for five different injection gases: air, nitrogen, helium, argon and krypton. This serves as a validation study for this experimental method with broad applicability for a wide range of porous materials and geometries. The accuracy of this method may be improved by using a porous material with the lowest thermal product possible, to maximise the signal to the infrared camera. Intricate, 3D geometries may also require a more sophisticated inverse heat transfer model to account for lateral conduction effects. In future work, it is envisaged that this technique may be applied to more complex flow fields and geometries.

4.9 Uncertainty Analysis

The two main independent quantities of interest measured in this paper are the Stanton number and the blowing parameter. To find the total uncertainty in Stanton number and blowing parameter, the Taylor Series Method by Coleman and Steele [167] is employed. For function $r = r(X_1, X_2, ...X_n)$, the uncertainties in the individual measurements are assumed to be uncorrelated. Thereafter, gradients $\frac{\partial r}{\partial X_i}$ are calculated numerically by perturbing the variables X_i in the data

reduction processing code. The Stanton number, from Eq. (4.3), is a function of the following quantities

$$St = f(\dot{q}_w, p_\infty, \rho_\infty, H_0, h_w) \tag{4.26}$$

where u_∞ and ρ_∞ are a function of the Mach number, M, total pressure, P_0, and total temperature, T_0. The total enthalpy, H_0, is a function of the total temperature, T_0, and the specific heat capacity of the freestream gas (assumed to be constant). The heat flux at the wall, $\dot{q}_w$ is a function of the material thermal product, $\sqrt{\rho c_p k}$, and the temperature, T_w.

A key figure of merit used to qualify the temperature output of infrared cameras is the noise equivalent differential temperature (NETD) [135]. This is a signal-to-noise figure that represents the temperature difference which would produce a signal equal to the camera's temporal noise. This value is calculated by dividing the standard deviation of the temporal noise by the response-per-degree (responsivity) and is usually expressed in units of mK. NETD is a useful figure as this value represents the combined effect of the various types of noise present in the infrared camera to a temperature change observed by the camera, i.e. this is the noise floor of the camera system. Those noise sources include dark current noise, shot noise and electronic noise. Another term used for the NETD is the thermal sensitivity. For the FLIR A6751 SLS camera used in this work, a factory calibration determined that the NETD was below 40 mK over the range of temperatures that would be observed. This is significantly smaller than the expected temperature rise of the sample 0.5-5 K. In addition to the NETD, there are additional sources of error from the calibration system described in Section 4.4. This includes the error in the measurement of the reflected temperature when conducting the multipoint calibration, T_{ref}, and the error in the temperature measurement of the CI-Systems black body calibrator, $T_{\text{calibrator}}$. Finally, to go from the black body temperature to the temperature of the material of interest, the emissivity of the material, ε, is required. Table 4.4 lists the different uncertainty contributions to the overall uncertainty in the measurement of Stanton number. The total uncertainty is 13.45% with the greatest contributor

being the uncertainty in the Alumina thermal product. Currently, an uncertainty of 10% is chosen as a nominal level in the absence of in-house materials testing. High-precision materials testing prior to experimental testing may yield a significantly lower uncertainty. The next highest contributions are the uncertainties in freestream Mach number and total temperature. Both absolute uncertainty levels have been chosen based on past experience with usage of the HDT.

Table 4.4: Uncertainty contributions and overall uncertainty in Stanton number.

Parameter	Baseline value	Absolute uncertainty	Relative uncertainty	Uncertainty contribution
NETD / K	0.04	±0.02	50%	<1%
T_{ref} / K	300	±2	6%	<1%
$T_{\text{calibrator}}$ / K	300	±0.1	<1%	<1%
$\varepsilon_{\text{Alumina}}$	0.97	±0.04	4.1%	6.7%
$(\sqrt{\rho ck})_{\text{Alumina}}$ / $\text{J m}^{-2}\,\text{K}^{-1}\,\text{s}^{-0.5}$	5234	±523	10.0%	54.6%
P_0 / kPa	645	±12.9	2%	2.2%
T_0 / K	459	±10	2.2%	14.8%
M	7.03	±0.1	1.4%	21.8%
St_{IR}	0.0094	0.0011	13.54%	-

The blowing parameter relates the uncooled Stanton number and the blowing ratio as per Eq. (4.2). The freestream mass flux cancels out in this equation and the blowing parameter is therefore a function of the following quantities

$$B_h = f(\dot{q}_w, H_0, h_w, \dot{m}_A). \tag{4.27}$$

In this case, there is no dependency on Mach number, M, or total pressure, P_0. The contribution to the total uncertainty in blowing parameter requires the uncertainty of the injected mass flux. It was found after post-experimental testing that the permeability of the porous sample reduced by 5-10% over the course of the test campaign. This may be due to a small leak when measuring the permeability pre-test or due to freestream debris blocking the pores. Thus a conservative estimate of ±10% has been assumed in the results. Table 4.5 lists the different uncertainty contributions to the overall uncertainty in the measurement of blowing parameter for the case of a injected mass flux of $0.2\,\text{kg}\,\text{s}^{-1}\,\text{m}^{-2}$ which represents the maximum

level of air injected experimentally. The two main contributors to the uncertainty in this case are the thermal product, like previously, and the injected mass flux.

Table 4.5: Uncertainty contributions and overall uncertainty in blowing parameter when $\dot{m}_f = 0.19\ \mathrm{kg\,s^{-1}\,m^{-2}}$.

Parameter	Baseline value	Absolute uncertainty	Relative uncertainty	Uncertainty contribution
NETD / K	0.04	±0.02	50%	<1%
T_{ref} / K	300	±2	6%	<1%
$T_{\mathrm{calibrator}}$ / K	300	±0.1	<1%	<1%
$\varepsilon_{\mathrm{Alumina}}$	0.97	±0.04	4.1%	4.6%
$(\sqrt{\rho ck})_{\mathrm{Alumina}}$ / $\mathrm{J\,m^{-2}\,K^{-1}\,s^{-0.5}}$	5234	±523	10.0%	39.8%
T_0 / K	459	±10	2.2%	15.7%
$\dot{m}_A$ / $\mathrm{kg\,s^{-1}\,m^{-2}}$	0.19	±0.019	±10%	39.8%
B_h	1.4368	0.2273	15.85%	-

Chapter 5

Transpiration Cooling Heat Transfer Experiments in Laminar and Turbulent Hypersonic Flows

Contents

5.1 Foreword

In this chapter, the novel infrared-based diagnostic method to measure surface heat transfer on transpiration-cooled porous injectors is applied to the generic case of a flat plate with a finite-length porous injector in hypersonic flow. These experiments are important to extend the simple correlations used for the systems-level study in

Chapter 3 to realistic flight vehicle applications and scenarios. For the first time, the spatial heat transfer distribution on a finite-length injector is correlated and a new analytical relation has been determined for both laminar and turbulent flows. These experiments have the aim of resolving two different objectives. First of all, the heat transfer on micro-porous materials which mimic the behaviour of UHTCs is measured for the first time and compared against well-known correlations. It is established that existing heat transfer relations can broadly predict the local heat transfer, especially for laminar flows, though a modification to account for the length and location of the finite length injector with respect to the leading edge is required. The following work has been published in the *Journal of Thermophysics and Heat Transfer*. It is presented in this chapter with small layout changes, but unaltered content. The author contributions are as follows

- Imran Naved: Conceptualisation, Methodology, Investigation, Data Analysis, Writing.
- Matthew McGilvray, Tobias Hermann, and Chris Hambidge: Supervision.
- Hassan Saad Ifti: Design and manufacture of the flat plate model.
- Chiara Falsetti: Assistance with setup of the infrared thermography system.
- Iullia S Tirichenko and Luc Vandeperre: Manufacturing of porous Zirconia.

5.2 Introduction

During ascent, cruise and reentry, aerospace vehicles travelling at hypersonic speeds are subject to extremely high heat fluxes due to aerodynamic heating [7]. A large fraction of the mass budget is devoted to the thermal protection system (TPS) to protect the vehicle from failure. Although heat sinks (passive) and ablation (semi-passive) are successful for vehicles operated at present, conventional thermal protection systems often have a low degree of reusability, especially on nose tips and leading edges where the vehicle experiences high peak heating. For certain vehicles,

such as atmospheric cruise and glide vehicles, maintaining aerodynamic performance and reusability is highly important. In particular, many of these vehicles utilise radar or optical sensors and require a viewing port or window of some optically or radar-transparent material. Ablation products from ablative insulators tend to obscure the sensor's view which means that such TPS systems cannot be used ahead of or in the vicinity of such windows [26].

For these scenarios, a potential active TPS system is transpiration cooling. This involves passing a fluid through a porous material onto the external boundary layer. The cooling process is achieved through four primary effects: heat from the wall is convected out by the fluid, the coolant creates a thin film which thickens the boundary layer and insulates the wall from the hot external gas, the coolant film can protect the wall from surface oxidation, and allowing for higher wall temperatures enables re-radiation and reduces surface catalytic heating. However, a transpiration-cooled system requires a considerable quantity of gas under high pressure, a manifold, and a cooling control system. There are large cost, weight, reliability, and volume penalties associated with these systems which must be carefully balanced against potential benefits.

There is a vast amount of work in the literature regarding this topic spanning more than 70 years. Transpiration cooling has been successfully applied to nose cones and frustra of hypersonic vehicles [33, 114] as well as for the walls of scramjet combustors [46]. However, relatively little work has considered the two-dimensional spatial effects of a transpiration-cooled injector beginning downstream of the leading edge. Such a scenario would occur if transpiration cooling is applied to the internal wall of a scramjet combustor or placed in the vicinity of an optical window. Furthermore, there is a substantial geometric difference between injectors with holes of the order 100μm [45] and modern micro-porous materials with pore diameters of less than 10μm [65]. A uniform film coverage over and downstream of the injector is essential to ensure the target region is kept below critical temperature limits.

To enable designers to assess the viability of a transpiration-cooled system for such situations, there is a need to build up a detailed two-dimensional ex-

perimental data set in hypersonic conditions. Previously, two-dimensional data has been achieved by placing a large number of discrete heat transfer gauges in between the holes on a transpiration-cooled wall [32, 45]. However, for modern micro-porous materials, discrete gauges are likely to disturb the coolant outflow distribution and a non-intrusive measurement technique is highly desirable. In more recent years, low-speed infrared thermography has been employed in long-duration, supersonic facilities [46, 121] but, additionally, testing in short-duration hypersonic tunnels is desirable.

In this work, the spatial two-dimensional surface heat transfer of a transpiring porous injector was measured experimentally on a flat plate at Mach 6.1 in laminar and turbulent conditions. Two porous injectors made of METAPOR CE170 and Zirconia were tested. The surface heat transfer on and downstream of the porous injector was measured using high-speed infrared thermography employing the same technique described in Naved et al. [59]. For the first time, a modification to existing relations from film theory is proposed that accounts for the growth of the boundary layer at the start of the injector. The surface heat transfer on the injector is successfully correlated across different blowing rates for nitrogen and helium injection. In addition, for the turbulent boundary layer, the thermal film effectiveness downstream of the injector is measured and subsequently correlated across different blowing rates.

5.3 Theoretical Approach

Over the course of transpiration cooling research in the past 70 years, various models have been proposed to predict the surface heat transfer reduction on transpiring porous media in both subsonic and hypersonic flows at laminar and turbulent conditions. Perhaps the simplest of those models is film theory developed by Mickley [92] in which the ratio of transport coefficients (whether that is heat, mass, or momentum) is predicted by making an idealisation that the transition between the main-stream and the wall occur entirely within a thin laminar film of thickness, Δ, lying immediately adjacent to the wall. The thickness of this film

is not predicted by film theory but rather is defined as the thickness which would offer the experimentally observed resistance to the transfer processes. Thus, the variation in transfer coefficients may be written in the form

$$\theta = \frac{\phi}{e^{\phi} - 1} \tag{5.1}$$

where θ is the ratio of the coefficient with and without mass transfer and ϕ is a dimensionless mass transfer rate. For heat transfer, the function in Eq. (5.1) is written in the form

$$\frac{St}{St_0} = \frac{B_h}{e^{B_h} - 1} \tag{5.2}$$

where B_h is a blowing parameter defined as

$$B_h = \frac{F}{St_0}. \tag{5.3}$$

St_0 is the Stanton number in the absence of injection (i.e. when $F = 0$) and F is the blowing ratio which is the ratio of the coolant mass flux to the free stream mass flux at the boundary layer edge

$$F = \frac{\rho_f u_f}{\rho_e u_e} \tag{5.4}$$

where ρ and u are density and velocity respectively. The subscripts (f) and (e) refer to the injected gas and the boundary layer edge conditions respectively. Film theory makes no assumption about the state of the boundary layer and the results of film theory have been applied in the past for both laminar and turbulent regimes [92, 101] with a reasonable agreement to experimental data. Moyer and Rindal [110] noted that a slight modification of the above equation as follows

$$St = St_0 \cdot \left[\frac{0.8B_h}{e^{0.8B_h} - 1}\right] \tag{5.5}$$

yielded a better fit to experimental data for turbulent flows.

Whilst film theory gives reasonable predictions with the injection of an identical gas to the freestream, injection of a foreign gas requires a correction. The most

common correction is either a correction for the ratio of molecular weights between the injected and freestream gas, (M_e/M_f), or the ratio of specific heat capacities, $(c_{p,f}/c_{p,e})$. The logic behind a correction factor is that a lower molecular mass would result in a larger blockage effect, as there is a greater volume of lighter gas in the boundary layer for the same mass flow rate whilst the higher the specific heat capacity, the greater the quantity of heat absorbed for the same mass flow rate. Without knowledge of the surface concentration of coolant, nor the relative weights of these two variables to the overall change in heat transfer, the effect of foreign gas injection may be accounted for purely as a molecular weight factor (M_e/M_f). This may be understood physically as akin to accounting for the differences in the volume of gas that is introduced. If it is assumed that on the porous injector, there is at least some coverage of coolant at all locations which are likely to be at the same temperature as the wall, then the major difference between injecting a heavier and lighter gas is the effect on the oncoming boundary layer. If the gas is lighter, it will take up more volume for a given mass flow rate and thus displace the boundary layer by greater levels. This approach has been successfully employed in previous studies though there is some variation in how the correction factor is weighted to achieve a good fit with experimental data [45, 117]. However, some authors such as Prokein et al. [168] have satisfactorily accounted for foreign gas injection, including helium, argon and CO_2, on the porous injector by employing a heat capacity ratio correction. At this stage, which of the scaling parameters is more robust is unclear and requires further work - especially at different wall temperatures.

The other drawback of film theory is that it is assumed that injection begins at the leading edge and continues downstream for the full extent of the flat plate. However, in many cases, the injector is likely to be of a finite length, beginning at a point downstream of the leading edge. An approach suggested by Stalmach et al. [33] for laminar flows is that the blowing parameter defined above may be modified by a factor $((x - x_s)/x)^{0.5}$ where x is the distance from the leading edge and x_s is the location of the start of the injector. This hearkens to a similar approach in laminar and turbulent downstream film effectiveness theory [122, 124,

128]. In the same way, it is proposed that for turbulent flows, the factor may be expressed as $((x - x_s)/x)^{0.8}$. Thus, the film theory relation above may be rewritten for a finite length injector for laminar flows

$$St = St_0 \cdot \left[\frac{\lambda}{e^{\lambda} - 1}\right], \qquad \lambda = C \cdot B_h \cdot \left[\frac{x - x_s}{x}\right]^{0.5} \cdot \left[\frac{\mathrm{M}_e}{\mathrm{M}_f}\right]^{m} \tag{5.6}$$

and for turbulent flows

$$St = St_0 \cdot \left[\frac{\omega}{e^{\omega} - 1}\right], \qquad \omega = D \cdot B_h \cdot \left[\frac{x - x_s}{x}\right]^{0.8} \cdot \left[\frac{\mathrm{M}_e}{\mathrm{M}_f}\right]^{n}. \tag{5.7}$$

The factors C, D, m and n are constants which need to be determined either experimentally or numerically for a given freestream flow condition. The application of this modified relation to experimental data is explored further in Section 5.5.3.

5.4 Experimental Methodology

5.4.1 Experimental Model

Experimental testing was conducted on a flat plate model used in previous studies [73, 99, 100, 152] at 0° angle of attack. Figure 5.1 shows a schematic of the experimental model. A porous injector of 39.5 x 39.5 mm^2 was placed 160 mm downstream of the model's sharp leading edge (see Section 5.4.2 for more details about the injector). A plenum is located underneath the injector and pipework is placed to feed the injection gas to the injector. The temperature and pressure in the plenum were measured by a fast response (response time $<$ 0.1 ms) K-type thermocouple ($\varnothing$0.0762 mm) and a Kulite pressure transducer (HEL-375-35BARA). Downstream of the porous injector, the model features a 340 mm long PEEK surface for downstream infrared measurements (material properties in Table 5.1). For a secondary verification of the surface heat transfer, 13 quartz-based platinum individual thin film gauges are mounted both upstream and downstream of the porous injector as well as one OMEGA CO2-K surface-mounted thermocouple. The thermocouple is made from 0.13 mm thermocouple alloy and has a response time in the range of 2-5 ms. Finally, 3D printed trips may be added to a pocket 25.7 mm downstream of the

leading edge to aid transition for the turbulent test cases. A diamond transition trip was used with a span-wise length of 90 mm and a height of 0.1 mm. A flush insert was used for the laminar experiments.

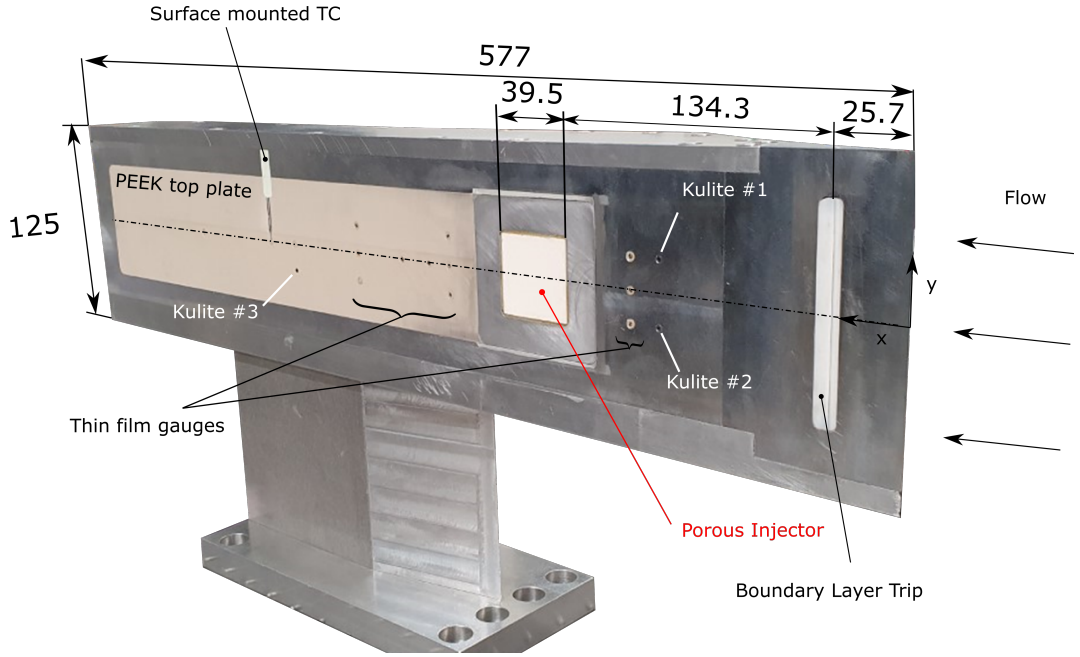

Figure 5.1: Flat plate model instrumented with Kulite pressure transducers, thin film gauges and a porous injector with a PEEK top plate for infrared measurements. Dimensions in mm.

In addition, the surface static pressure was measured using two surface-mounted Kulite pressure transducers (XCS-093-5A). The Total temperature was measured in the test section using differentially heated aspirated thermocouples. The measured data was acquired using a National Instruments PXIe-8135 controller with one PXIe-6368 card. A sample rate of 125 kHz was used to record all signals of the measurement which includes model and wind tunnel instrumentation. A separate heat transfer amplifier unit, HTA5, is also used for thin film gauge data acquisition. This forms a stand-alone unit, run at a matching sample rate to the main data acquisition (DAQ) system.

Primarily, surface heat transfer measurements were acquired using infrared thermography and a schematic of the optical setup is shown in Fig. 5.2. The experimental test piece is orientated in a vertical configuration such that the field of view (FoV) of the IR camera is nearly normal to the model surface. Two infrared

cameras are used for these experiments, the FLIR A6751 SLS long-wave infrared (LWIR) camera with a wavelength band of 7.5-11μm fitted with a 17 mm lens and a Telops M3K FAST mid-wave (MWIR) camera with a wavelength range of 1.5-5.2 μm fitted with a 100 mm lens. The LWIR camera was used to give a broad image of the flat plate including up to 100 mm downstream of the porous injector whilst the MWIR camera was used to support the LWIR camera with detailed close-up images of the porous sample. Due to the spectral emissivity dependence of porous Zirconia (the emissivity of Zirconia is very low in the mid-wave region), it was only possible to obtain LWIR images for the tests with the Zirconia injector. The experimental model was viewed through a 50 mm coated germanium and 100 mm sapphire window respectively for the long-wave and mid-wave cameras. The LWIR camera was operated at a windowed spatial resolution of 320 x 256 at a frame rate of 400 Hz and the MWIR operated at 320 x 256 with a frame rate of 2 kHz. This corresponds to approximately 7 pixels/mm with the MWIR and 2 pixels/mm with the LWIR camera.

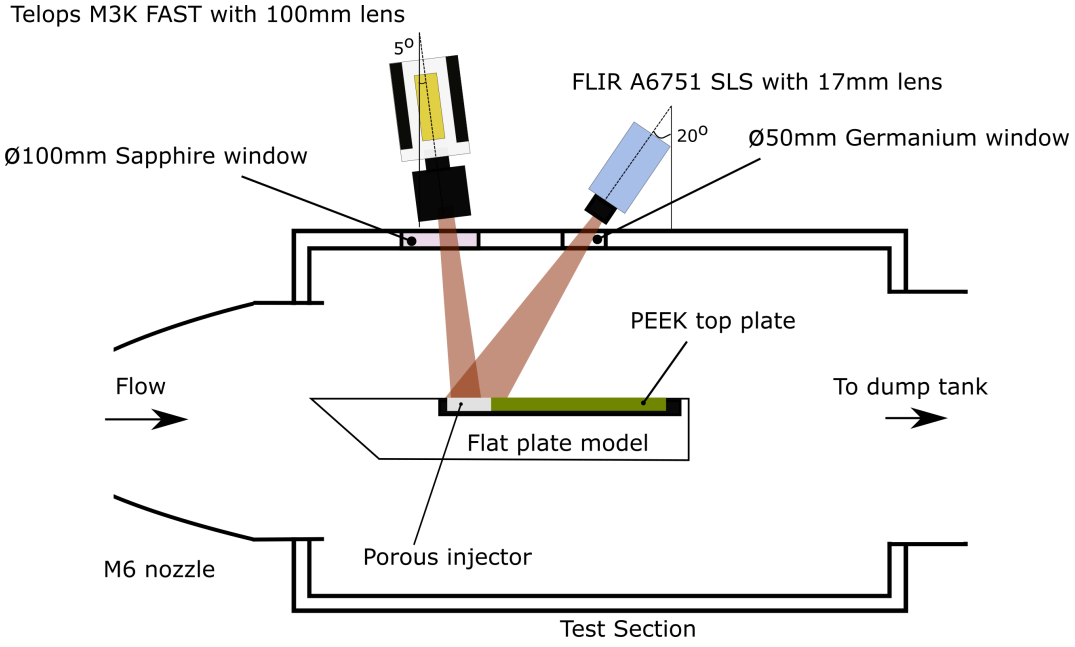

Figure 5.2: Top view of the experimental model in the test section.

5.4.2 Porous Injector

Various porous materials have been used for transpiration cooling experiments including Ultra-High-Temperature-Ceramic (UHTCs) such as ZrB_2 [65] and carbon-carbon (C/C) composites [96]. $ZrBr_2$ in particular is a candidate flight material with a melting point of 3505 K and the extremely fine port structure (on the order of 1μm) which allows for a very even injection with no localized jets from fissures in the material. However, the high thermal product of this material leads to a very low signal-to-noise ratio for infrared measurements in transient hypersonic wind tunnels. Thus, an alternative material for the purpose of wind tunnel experiments with a similar internal structure (pore diameters of the order of 2 μm) but lower conductivity is porous Zirconia (ZrO_2) manufactured by Imperial College London. Yttria-Stabilized Zirconia, 3-5 μm was sintered in air at 1200°C for 45 minutes yielding a 40% porous substrate. The resulting sample combines a very low thermal product with the pore size and therefore outflow homogeneity of candidate materials for transpiration cooling. An alternative, commercially available micro-porous material is METAPOR CE170 which is made of aluminium hydroxide bonded to a resin system (pore diameter 20μm). This material has an order of magnitude larger pore sizes than Zirconia (Fig. 5.3) and is an interesting material for comparison as the cooling effectiveness of porous injectors may be a function of surface geometry, roughness and coolant outflow. The properties of both materials are summarised in Table 5.1.

The permeability of the samples was measured using an ISO 4022 standard test rig pre and post-experiment according to the procedure detailed in Ifti et al. [65]. The outflow distribution of the employed porous injectors was characterised by hot-wire anemometry with air injection. Due to the large differences in absolute outflow velocities between the two injectors, the obtained normalised velocity maps are shown in Fig. 5.4. The normalisation is conducted by dividing the velocity at each point against the mean value over the entire porous surface. The resultant span and stream-wise averages are shown in Fig. 5.5. Porous Zirconia exhibited a predominantly uniform outflow with some local densification towards the bottom

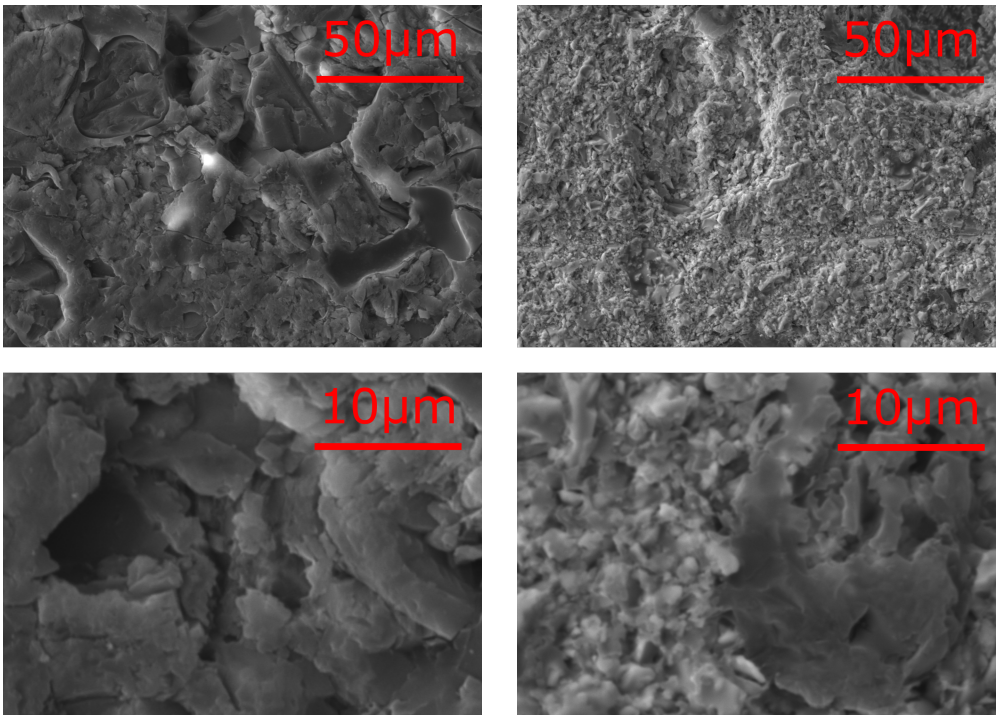

(a) METAPOR CE170 **(b)** Zirconia

Figure 5.3: Microscopic images of the porous injectors at different magnification factors.

Table 5.1: Properties of porous Zirconia (ZrO_2), METAPOR CE170 and PEEK. The thermal properties (ρ,c_p,k) were measured by Netzsch Instruments and the emissivity, ε, was measured using an in-house benchtop setup.

Parameter	ZrO_2	METAPOR CE170	PEEK
Thickness, L / mm	7	7	10
Porosity, ϕ	0.40	0.20	-
Density, ρ_s / $\mathrm{kg\,m^{-3}}$	3140	1710	1310
Thermal Conductivity, k_s / $\mathrm{W\,m^{-}\,K^{-1}}$	0.556	1.662	0.25
Specific Heat Capacity, $c_{p,s}$ / $\mathrm{J\,kg^{-1}\,K^{-1}}$	462	1177	1201
Thermal Product, $(\sqrt{\rho c_p k})$ / $\mathrm{J\,m^{-2}\,K^{-1}\,s^{-0.5}}$	1039	1565	627
Darcy Coefficient, K_D / $\mathrm{m^2}$	$1.12 \cdot 10^{-14}$	$1.86 \cdot 10^{-13}$	-
Forchheimer Coefficient, K_F / m	$1.51 \cdot 10^{-10}$	$7.44 \cdot 10^{-9}$	-
Emissivity, ε	0.93	0.95	0.93

right of the injector whilst highly localised jets and regions with almost no outflow were present on the METAPOR CE170 surface. Further comments regarding the permeability distributions of both injectors and the implication to experimental results are explored in Section 5.5.

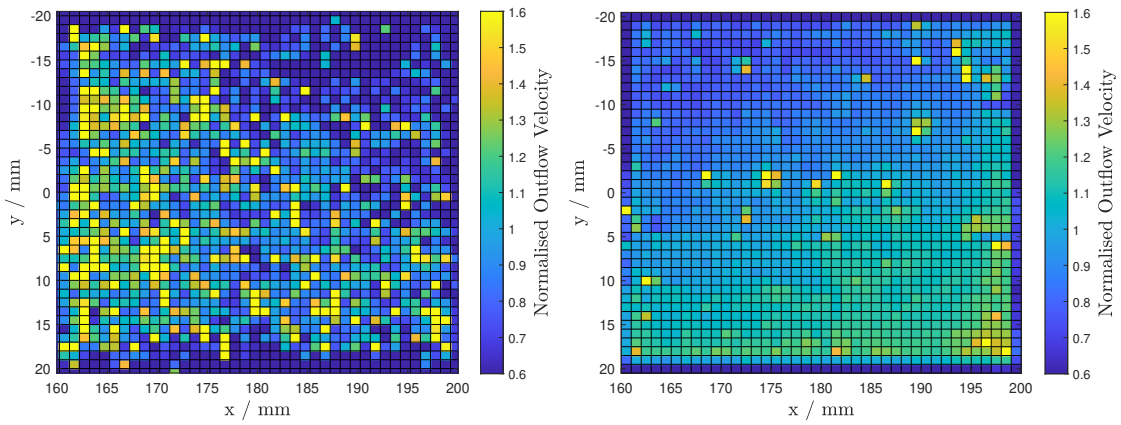

(a) METAPOR CE170 **(b)** Zirconia

Figure 5.4: Outflow velocity maps normalised with the average flow velocity across the sample at 3 bar differential pressure. This was measured with a hot wire with no cross-flow. The x and y coordinates correspond to the distance from the leading edge and the distance from the model centre-line respectively.

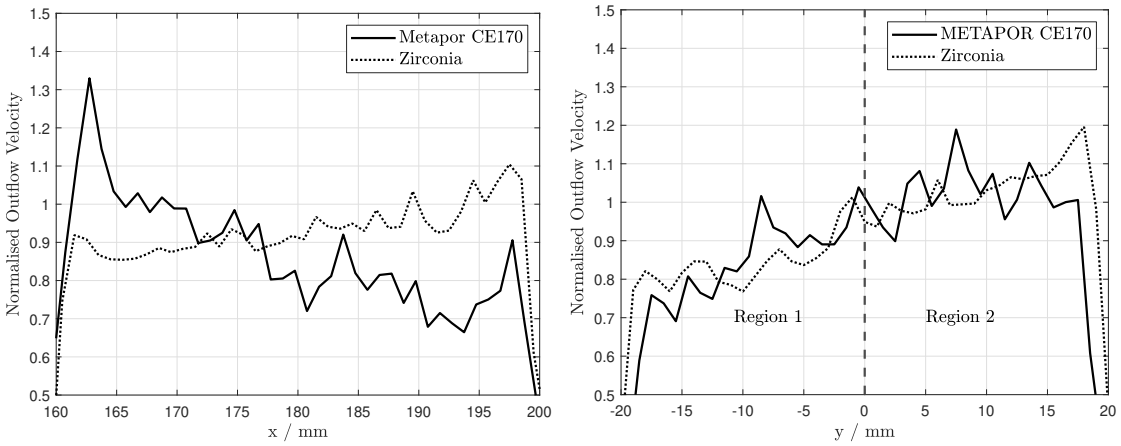

(a) Stream-wise variation **(b)** Span-wise variation

Figure 5.5: Span-wise and Stream-wise average outflow velocities for Zirconia and METAPOR CE170 from the hot wire measurements. Region 1 and 2 will be referred to later in Fig. 5.19.

5.4.3 Heat Transfer Measurements

The surface heat flux was primarily measured by employing infrared thermography with additional individual thin film gauges to support and validate the infrared measurements. infrared thermography spatially resolves the 2D flow structures

at the wall and crucially, the non-intrusive [139, 169] nature of this technique permits measurements directly on the porous injector without impeding or otherwise disturbing the coolant outflow. A series of calibration steps, further detailed in Ref. [59], were followed to obtain quantitative transient temperature maps of the flat plate surface including the transpiration-cooled injector from the raw infrared signal.

1. Multipoint calibration: Firstly, a multipoint calibration was carried out in situ using a black body calibrator (CI-Systems SR-33-7 infrared calibrator) to relate the camera raw signal to the true black body temperature inside the wind tunnel test section. This step calibrates the camera and optical system by and spatial non-uniformities or offsets due to the detector or the wider optical system.

2. Emissivity measurement: Secondly, to relate the black body temperature to the true material temperature, a material emissivity measurement was performed pre-experiment by using a bench-top setup. The measured emissivity values for both porous injectors and the PEEK surface upstream and downstream of the injector are recorded in Table 5.1. For these experiments, the directional dependence of emissivity was not required as the maximum angle between the camera and the normal to the flat plate surface was 20° wherein the emissivity is roughly constant [161].

3. Image Processing: Finally, the images were spatially transformed to a rectangle that represents the physical geometry and passed through an image stabilisation algorithm prior to final post-processing.

After the corrected temperature profile, ΔT, was obtained the heat flux, $\dot{q}_w$, was determined by applying the impulse response method of Oldfield [162]. A fully coupled transpiration-cooled impulse response method such as in Hermann et al. [74] is not required as the convective heat transfer process between the coolant fluid and porous solid was accounted for by a separate calibration procedure as detailed in Ref. [59]. The thermal product for the porous injector and the downstream

PEEK surface is detailed in Table 5.1. The impulse response is calculated with the assumption that the material thermal response is one-dimensional and semi-infinite. According to Schultz and Jones [131], this assumption is valid as long as the thermal penetration depth is shorter than the thickness of the material. Over a time period of 0.5 s, the penetration depth for METAPOR CE170, Zirconia and PEEK is 2.6, 1.7 and 1.3 mm respectively. These values are all below the recorded values of material thickness given in Table 5.1.

Finally, the Stanton number was found by applying the boundary layer edge flow properties as follows

$$St = \frac{\dot{q}_c}{\rho_e u_e c_p (T_r - T_w)} \tag{5.8}$$

where $\dot{q}$ is the convective heat flux, ρ_e is the freestream density, u_e is the freestream velocity, c_p is the specific heat capacity at constant pressure, T_r is the recovery temperature and T_w is the wall temperature. The recovery temperature is found as per

$$T_r = T_e \left[1 + r \left(\frac{\gamma - 1}{2}\right) M_e^2\right] \tag{5.9}$$

where γ is the ratio of specific heats, and r is the recovery factor where $r = \sqrt{Pr}$ for laminar flows and $r = 0.89$ for turbulent flows. Figure 5.6 shows infrared images from both the LWIR and MWIR cameras for helium injection onto laminar flow. The LWIR captures a wide field of view of the flat plate whilst the MWIR images the porous injector only with a greater resolution on the surface. Due to the spectral emissivity dependence of Zirconia detailed above, MWIR images are only presented for the METAPOR CE170 injector.

5.4.4 Flow Conditions

The experiments were conducted in the Oxford High-Density Tunnel (HDT) at the Oxford Thermofluids Institute operated in Ludweig tube mode. A detailed description of the facility may be found in [138, 170]. The tunnel was operated using nitrogen as the driver gas as described in Appendix C. The Mach 6 nozzle was selected and two different freestream conditions were chosen to achieve laminar and

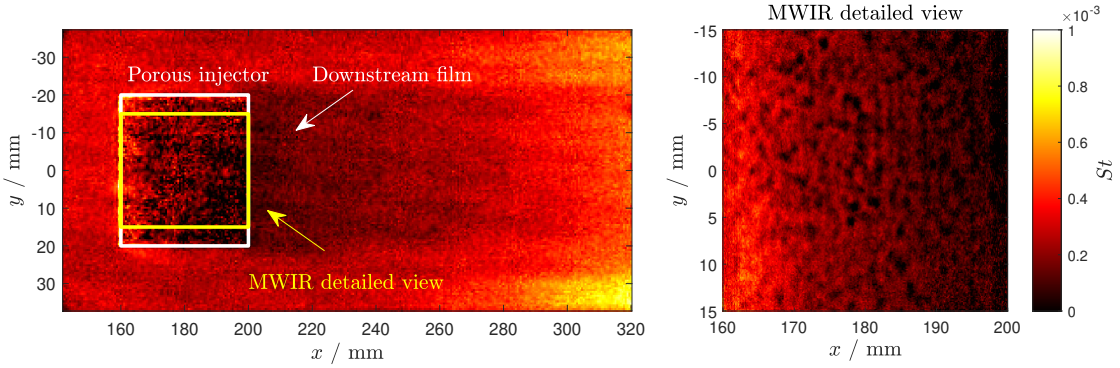

Figure 5.6: Illustration of the processed infrared images captured by the two cameras. The presented contours represent helium injection on the METAPOR CE170 injector at $F = 0.028\%$ at laminar conditions. The LWIR camera has a pixel density of 2 pixels/mm and the MWIR image which focuses on the porous injector has a pixel density of 7 pixels/mm.

turbulent boundary layer states on the model surface. The freestream properties are calculated from measured stagnation pressures upstream of the nozzle throat, pitot pressures, and temperatures using isentropic relations. This is justified as the value of the viscous interaction parameter, $\bar{\chi}$, at $x = 140\,\text{mm}$ (the furthest upstream measurement point), is below 0.18, i.e. viscous effects are negligible [8]. The viscosity was determined using Keyes model [158] and Table 5.2 presents an overview of the flow conditions. The total test time for each individual experimental point was approximately 30 ms.

Table 5.2: Freestream flow conditions.

Parameter	Laminar	Turbulent
Pressure, p_∞ / Pa	786	1737
Temperature, T_∞ / K	49.6	42.6
Velocity, u_∞ / m s^{-1}	861	798
Density, ρ_∞ / kg m^{-3}	0.0552	0.142
Mach number, M_∞	6.1	6.1
Unit Reynolds number, Re_u / m^{-1}	$13.4{\cdot}10^6$	$37.2{\cdot}10^6$
Estimated boundary layer height, δ_{99}/ mm at $x = 160\,\text{mm}$	2.36	4.44

The blowing ratio, F (Eq. (5.4)), is determined from the measured plenum and freestream pressures and temperatures according to the Darcy-Forchheimer equation [62]

$$\frac{p_f^2 - p_e^2}{2LR_fT_f} = \frac{\mu_f \rho_f u_f}{K_D} + \frac{(\rho_f u_f)^2}{K_F} \tag{5.10}$$

where the values of the permeability coefficients, K_D and K_F are given in Table 5.1. For the blowing parameter (Eq. (5.3)), St_0 is the experimentally measured Stanton number when $F = 0$. Table 5.3 presents an overview of all the cases considered in this study.

Table 5.3: Overview of blowing cases at both laminar and turbulent conditions (Table 5.2). Note: The value of blowing parameter requires St_0 and has thus been calculated based on the surface heat transfer without injection for the laminar and turbulent cases respectively.

Boundary layer state	Laminar				Turbulent		
Injector	Metapor 170CE		Zirconia		Metapor 170CE		Zirconia
Coolant gas	N_2	He	N_2	He	N_2	He	N_2
Mass flux, $\rho_f u_f$ / kg s^{-1} m^{-2}	0.012-0.081	0.0071-0.013	0.0078-0.032	0.0050	0.049-0.30	0.017-0.027	0.021-0.046
Blowing ratio, F / %	0.026-0.17	0.015-0.028	0.016-0.067	0.011	0.043-0.26	0.015-0.024	0.019-0.040
Blowing Parameter, B_h	0.99-6.45	0.57-1.06	0.63-2.60	0.406	0.65-3.78	0.18-0.36	0.26-0.56

5.5 Results and Discussion

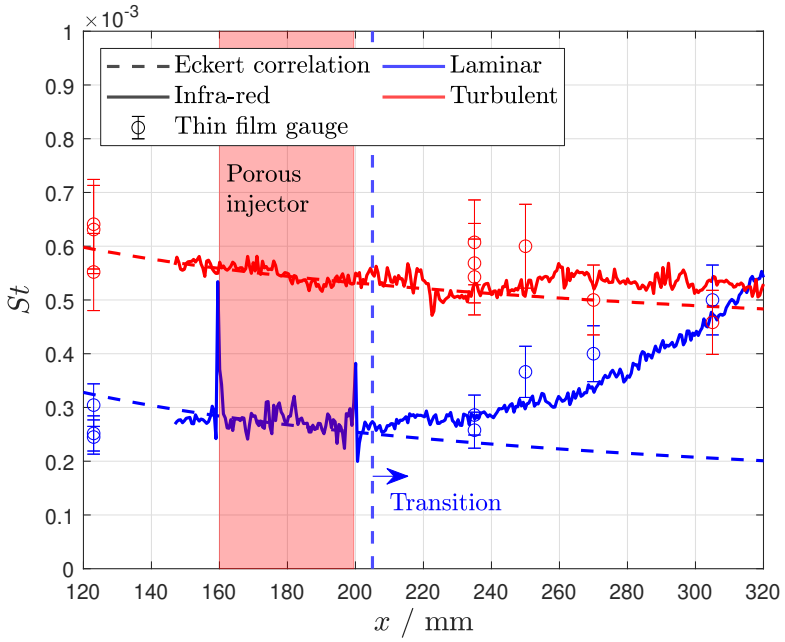

Figure 5.7: Comparison of measured Stanton numbers with the Eckert laminar and turbulent correlations [171]. The span-wise average is taken between y = -15 mm and y = 15 mm.

For both the laminar and turbulent cases described in Table 5.2, it was first necessary to ascertain that the correct boundary layer state was achieved without blowing. This was confirmed by measuring the surface heat flux and comparing to the values to Eckert's heat flux correlations for laminar and turbulent boundary layers on a flat plate [89]. Figure 5.7 shows the span-wise averaged line plots between y = -15 mm and y = 15 mm for the two conditions. Both the laminar and turbulent cases match well with the Eckert curves and the individual thin film gauges on and upstream of the porous injector. For the laminar case, it is clear that the boundary layer then transitions at approximately x = 205 mm to the turbulent level after 320 mm. This is satisfactory as the primary purpose of these experiments is to present heat transfer measurements purely on the porous injector region. Later in Section 5.5.4, the downstream results will be presented only for the turbulent cases. Estimated boundary layer thicknesses at the start of the porous injector (x = 160 mm) are recorded in Table 5.2. The values are estimated by assuming a Blasius boundary layer profile for both the laminar and turbulent cases [172]. Compressibility is accounted for by calculating the Reynolds number based on the reference temperature [89]. It must be noted that the estimate for the turbulent boundary layer assumes that the flow is fully turbulent from the start of the flat plate. This is not true for these experiments (turbulence is incited by a boundary layer trip) and therefore the quoted boundary layer thickness for the turbulent case is likely to be an overestimate.

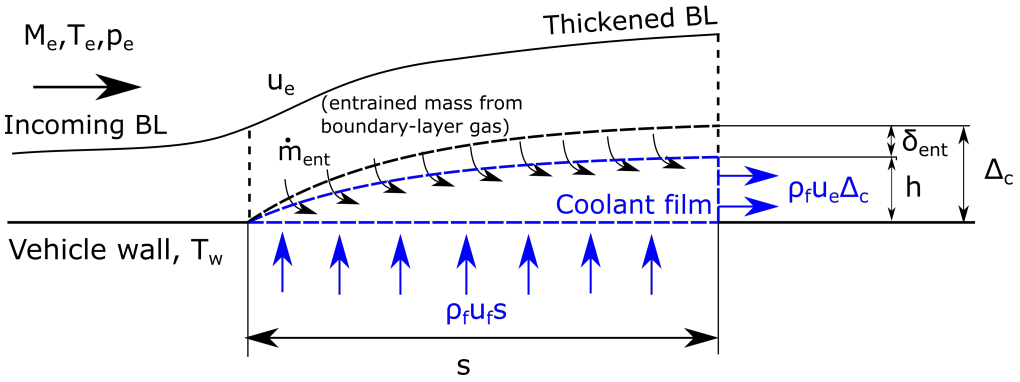

Figure 5.8: Control volume around the injected gas and the mass entrainment into the coolant gas over the injector. Adapted from Ifti [173]; reprinted by permission of the authors

It is well established by previous studies [99, 106] that the introduction of the coolant layer thickens the incoming boundary layer. The height of the coolant sub-layer is modelled by considering the continuity equation across a simple control volume as presented in Fig. 5.8. As detailed by Ifti et al. [173], by assuming that the coolant is at the same temperature as the vehicle wall, T_w, and that the coolant reaches the edge velocity, u_e, after becoming tangential to the wall; the resultant height of the coolant layer at the end of the injector is

$$\Delta_c = h + \delta_{ent} \tag{5.11}$$

where

$$h = \frac{\mathrm{M}_e T_w}{\mathrm{M}_f T_e} Fs \tag{5.12}$$

and δ_{ent}, which is the growth of the coolant layer due to the entrained boundary layer gas. s in Eq.5.11 is the stream-wise length of the porous injector. δ_{ent} is approximated as a Blasius laminar or turbulent boundary layer thickness solutions (depending on whether this analysis is undertaken for a laminar or turbulent boundary layer) beginning at the injector's starting point. Figure 5.9 shows the variation in Δ_c for the experimentally tested conditions with blowing ratio. Due to the approximately seven times smaller molecular weight of helium compared to nitrogen, there is a corresponding change in the coolant layer height due to injection for a given blowing ratio. In the following sections, the effect of blowing on the surface heat transfer at both laminar and turbulent conditions is examined in detail.

5.5.1 Laminar Flow on Injector

Several different blowing ratios were tested for the METAPOR CE170 and Zirconia injectors with both nitrogen and helium coolant gases. An overview of these cases are presented in Table 5.3. Relatively low blowing ratios were selected to ensure that the flow remains laminar along the injector; previous studies by Tanno et al. [42] have shown that at high blowing ratios, injection may lead to early transition. Contour plots of the surface Stanton reduction (St/St_0) on the porous injector are

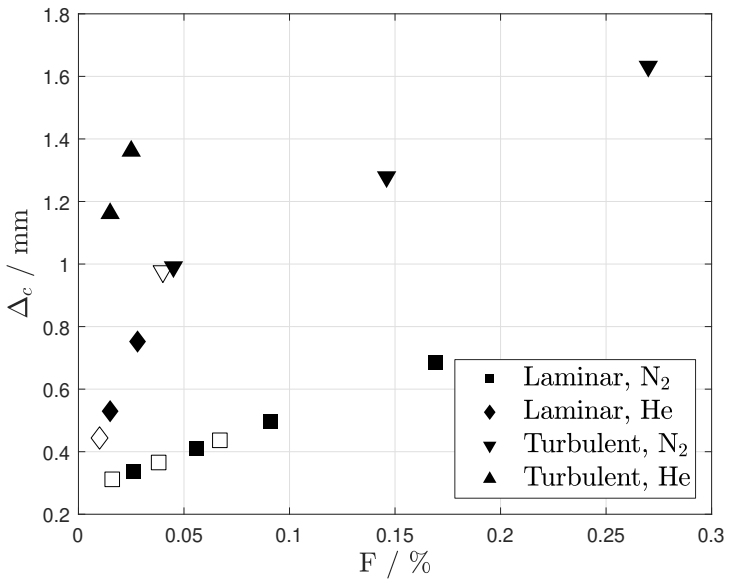

Figure 5.9: Estimated change in the coolant layer height, Δ_c, with blowing ratio for the experimentally tested laminar and turbulent conditions. The filled points refer to conditions tested using the METAPOR CE170 injector and the unfilled points for the Zirconia injector.

presented in Fig. 5.10 for a subset of blowing cases where both the METPAOR CE170 and Zirconia injectors have similar blowing ratios. The introduction of the low-momentum coolant into the sublayer of the boundary layer can significantly reduce the temperature and velocity gradients close to and at the wall. This is demonstrated in Fig. 5.10 where both the nitrogen and helium injection cases exhibit a gradual decrease in Stanton number reduction downstream from the start of the injector. Both injectors show similar trends with a generally uniform, 2D heat transfer distribution even for the highly non-uniform METAPOR CE170 injector.

The span-wise averaged values of the Stanton number reduction are plotted versus the stream-wise direction, x, in Fig. 5.11. As the blowing ratio, F, increases the Stanton number reduces, reaching essentially zero for the highest nitrogen injection case. The rise in the experimental points at around $x = 170\,\text{mm}$ for nitrogen injection with the METAPOR CE170 injector may be due to either the non-uniformity of the porous injector or perhaps a sign of earlier transition than expected. Whilst nitrogen injection gives a very uniform coverage over the porous sample, the helium cases show an initial heat flux augmentation at x $\approx$ 160-162 mm

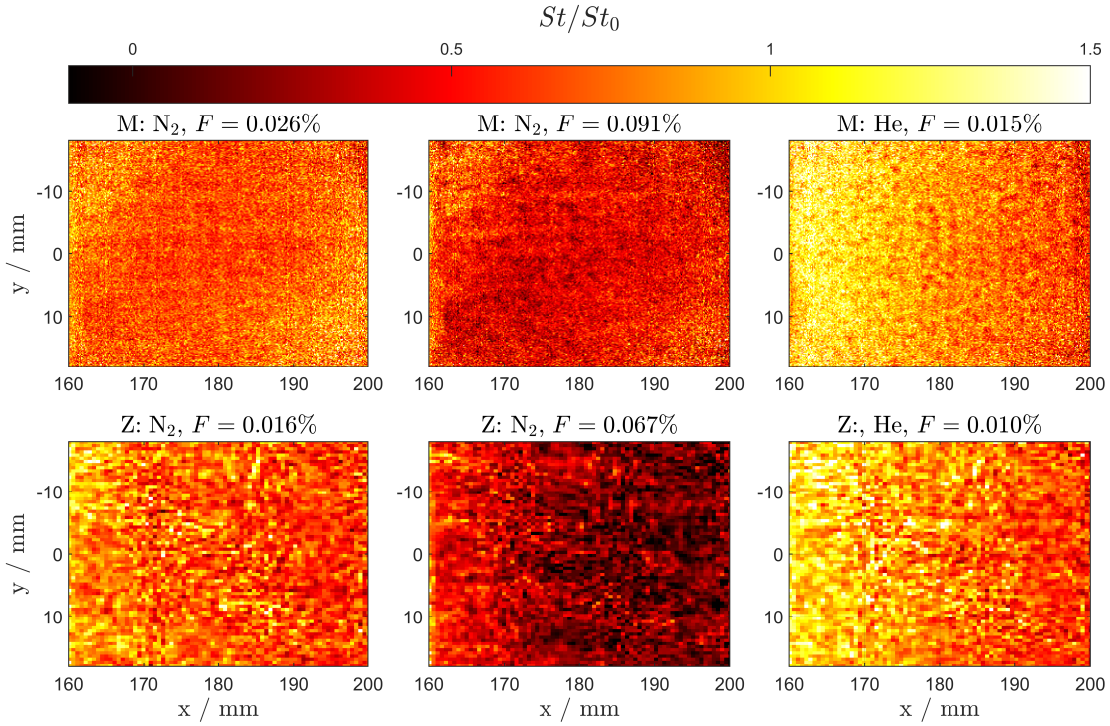

Figure 5.10: Comparison between the METAPOR CE170 and Zirconia injector for the laminar condition. Note: the Zirconia images have lower resolution due to the FLIR camera. M represents the METAPOR CE170 injector and Z the Zirconia.

and thereafter a very steep drop towards the end of the injector. The initial increase in surface heat flux is likely due to the fact that at the very start of the injector, the wall temperature gradient does not change significantly due to the inclusion of helium injection. However, due to the high concentration of helium at the wall, the effective mixture thermal conductivity at the wall is higher than the free-stream air. Thus, it is possible for a higher resulting heat flux close to the interface between the injector and the wall with blowing than the wall heat flux without injection.

It is notable that at the end of the injector ($x = 195\,\text{mm}$), a helium blowing ratio of 0.028% achieves a comparable level of cooling to nitrogen at 0.091% - over a factor of three times larger. This is consistent with the findings from other experiments [39] where helium was found to be significantly more effective in terms of heat transfer reduction compared to nitrogen due to both its higher specific heat capacity and lower molecular weight. The lower molecular weight of helium means that a higher plenum pressure is needed for a given mass flux through the

injector. Thus both helium exits at a higher velocity due to its lower density and, in addition, there is a larger volume of helium at the exit.

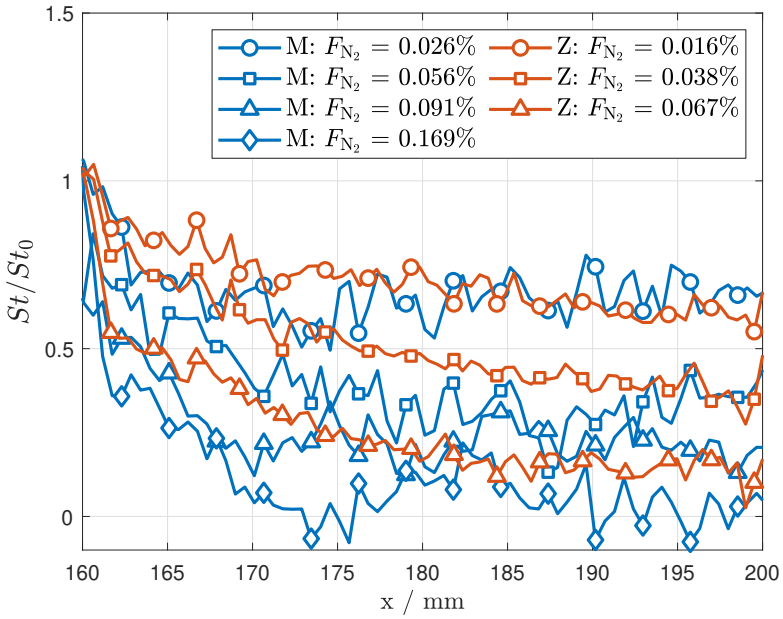

(a) Nitrogen injection

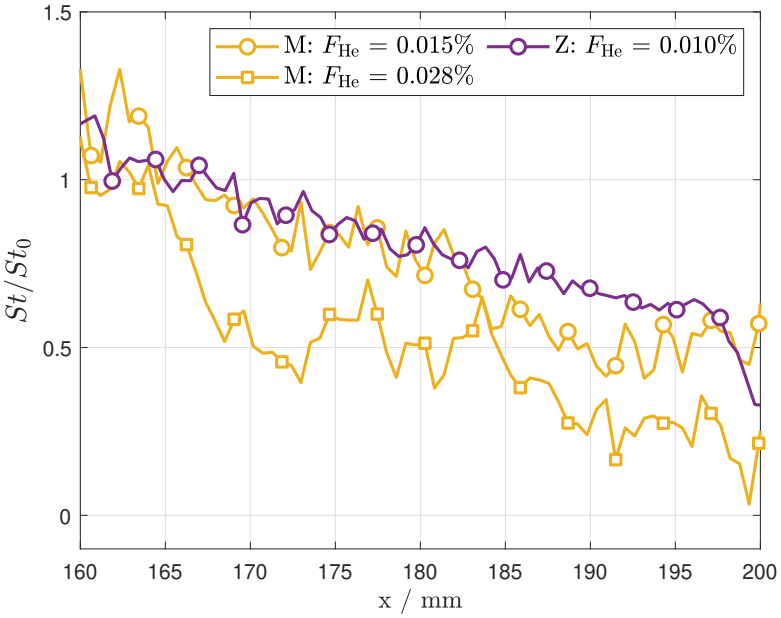

(b) Helium injection

Figure 5.11: Span-wise averaged Stanton number reduction along the porous injector at the laminar condition. The average is taken between y = -15 mm and 15 mm assuming a two-dimensional injector. M represents the METAPOR CE170 injector and Z the Zirconia.

5.5.2 Turbulent Flow on Injector

Figure 5.12 shows contours of Stanton number reduction for different nitrogen and helium blowing ratios for both the Zirconia and METAPOR CE170 injectors. For nitrogen injection, similar to the laminar cases, both injectors exhibit a very uniform heat transfer distribution on the surface. Compared to the laminar cases, there is little visible change in Stanton number reduction along the sample. For high blowing ratios ($F = 0.27\%$), a region of heat transfer enhancement is present at the beginning of the injector (x = 165-175 mm) before a gradual reduction downstream. A highly non-uniform distribution is exhibited by the helium case with the individual 'cold' spots akin to the hot wire map in Fig. 5.4.

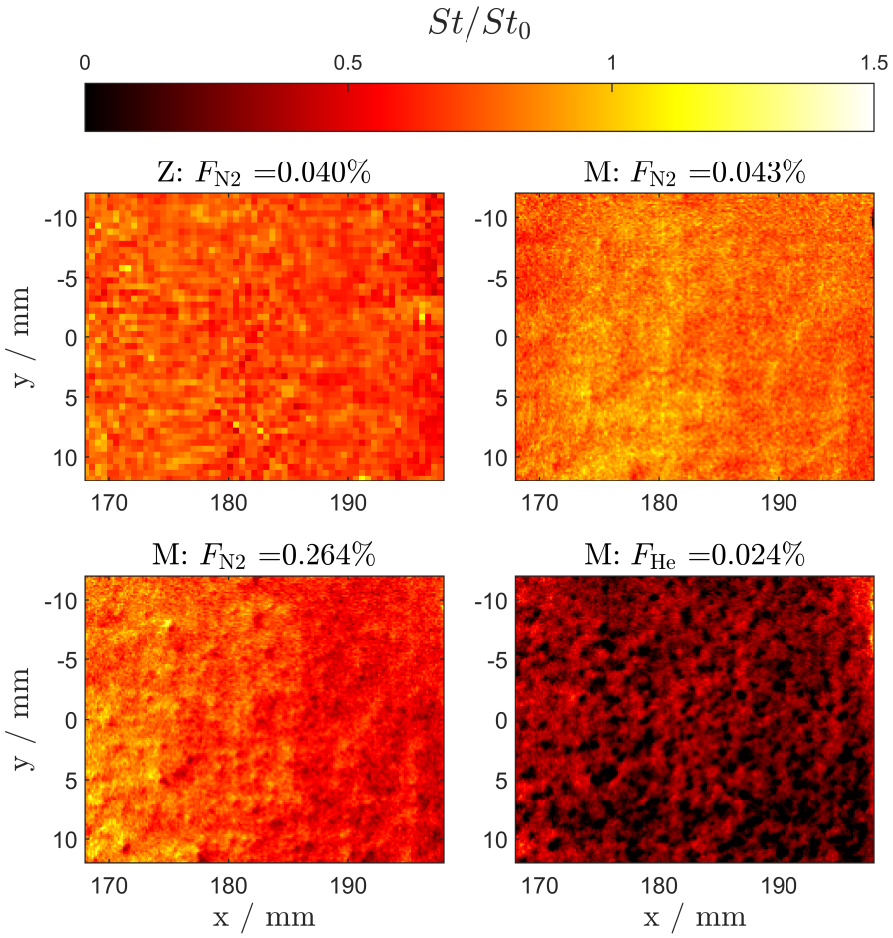

Figure 5.12: Comparison between the METAPOR 170CE and Zirconia injector for the turbulent condition. Note: the Zirconia images have lower resolution due to the FLIR camera. M represents the METAPOR CE170 injector and Z the Zirconia.

Figure 5.13 depicts span-wise averaged values of the Stanton number reduction versus the stream-wise direction, x. As the the blowing ratio, F, increases the Stanton number reduces. The profiles are fairly flat with little variation with stream-wise direction after around $x = 170\,\text{mm}$. For nitrogen injection, as the blowing ratio increases, there is an increase in Stanton number over the uncooled case at the beginning of the injector (see inset Fig. 5.13). This suggests that, for turbulent flow, the compression shock formed by the thickening of the boundary layer increases in strength with a higher blowing ratio and gives rise to up to 40% promotion in Stanton number for the highest blowing case. Both the METAPOR CE170 and Zirconia injectors behave similarly with the same flat Stanton reduction profiles at comparable blowing ratios. There is a marked reduction for even very low blowing ratios of helium injection. For a blowing ratio of 0.25%, the surface Stanton number with nitrogen is roughly 40% of the uncooled case at the end of the porous injector whilst for helium only a blowing ratio of 0.015% is required for a comparative heat reduction. The substantial heat reduction due to helium is well beyond expected values based on known correlations for turbulent flows [36].

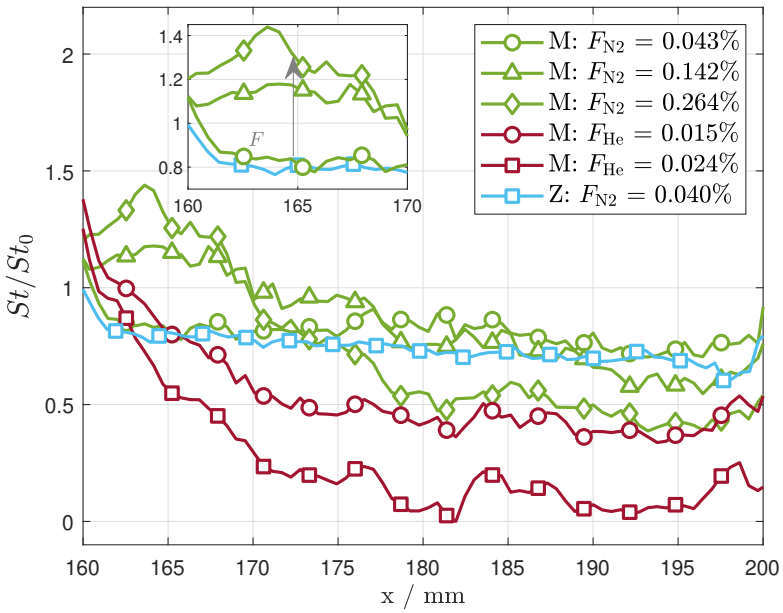

Figure 5.13: Span-wise averaged Stanton number reduction along the porous injector at the turbulent condition. M represents the METAPOR CE170 injector and Z the Zirconia. The average is taken between y = -15 mm and y = 15 mm assuming a two-dimensional injector.

5.5.3 Correlations

In previous works [92, 101], the heat transfer reduction across different blowing ratios and coolants were correlated against the blowing parameter, B_h, by employing one of either Eq. (5.2) or (5.5) for laminar or turbulent flows respectively. Figure 5.14 shows the experimental blowing parameters at each stream-wise axial location on the injector plotted against the span-wise average Stanton number reduction for both the laminar and turbulent cases. Each data point represents the span-wise average over a particular location x, i.e. on a pixel row. Whilst there is a clear trend of increased cooling with higher blowing parameter and there is an intersection between the theoretical curves of Mickley and Moyer-Rindal, especially for the laminar cases, the stream-wise heat transfer distribution on the injector is not captured. This is because St_0 does not change appreciably over the length of the injector and F is a single value for the constant mass injection cases presented in this study.

Clearly, the influence of the injector needs to be accounted for to capture the axial variation in heat transfer on the injector. For this purpose, a correction to account for the boundary layer development as shown in Eqs. (5.6) and (5.7) may be applied to the experimental data points. Figure 5.15 shows all the experimental data points plotted for both laminar and turbulent conditions. Whilst good agreement is observed for the laminar cases with nitrogen injection and turbulent with low nitrogen injection, the other cases all exhibit a divergence from the correlation. This is because one of the inherent assumptions of this model is that when $x = x_s$, the value of $St/St_0 = 1$; i.e. any cooling begins at the exact start of the injector. However, this may not always be true for all cases, especially for high-blowing cases where the boundary layer may grow slightly upstream of the injector or if, like in the turbulent cases, there is a region of heat flux enhancement near the start of the injector. The proposed correlation parameters do not capture the complex interaction between the coolant outflow and the incoming boundary layer at the very start of the injector but, rather, predict the evolution from an initial point. For this reason, to correlate the experimental data points, the modified correlation parameter may be plotted not against St/St_0 but rather against $\frac{St/St_0}{(St/St_0)_{\max}}$, i.e.

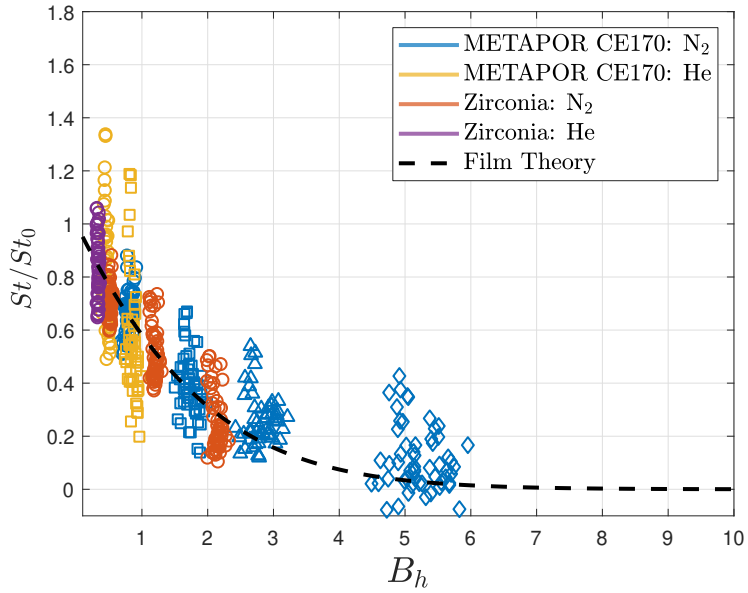

(a) Laminar

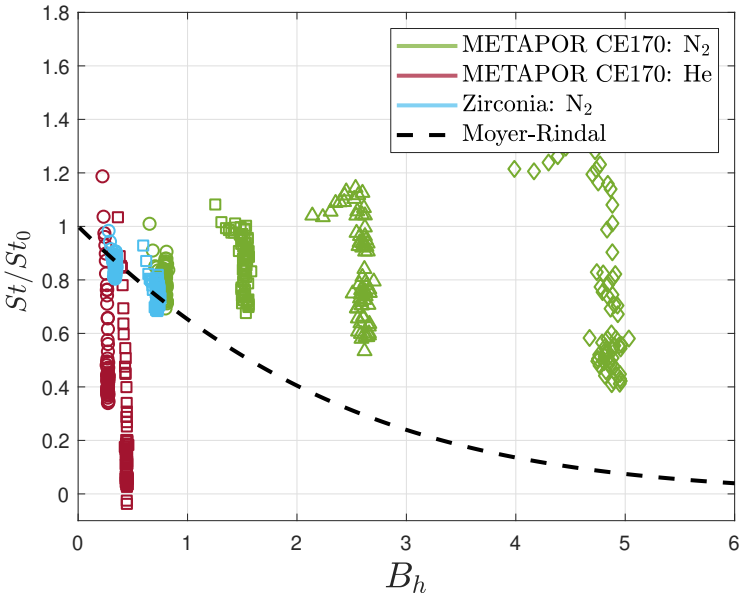

(b) Turbulent

Figure 5.14: Span-wise averaged Stanton reduction between $y = 15$ to -15 mm on the porous injector against the blowing parameter, B_h (based on the local St_0 at each location) for all injection cases.

normalised against the peak value of St/St_0. The chosen $(St/St_0)_{\max}$ values are the cyan filled symbols in Fig. 5.15. Generally speaking, this occurs at start of the injector, x_s, but may also be a few mm downstream as is the case for the higher blowing turbulent cases with nitrogen injection (Fig. 5.13).

Figure 5.16 shows the same experimental points as above but with the x axis

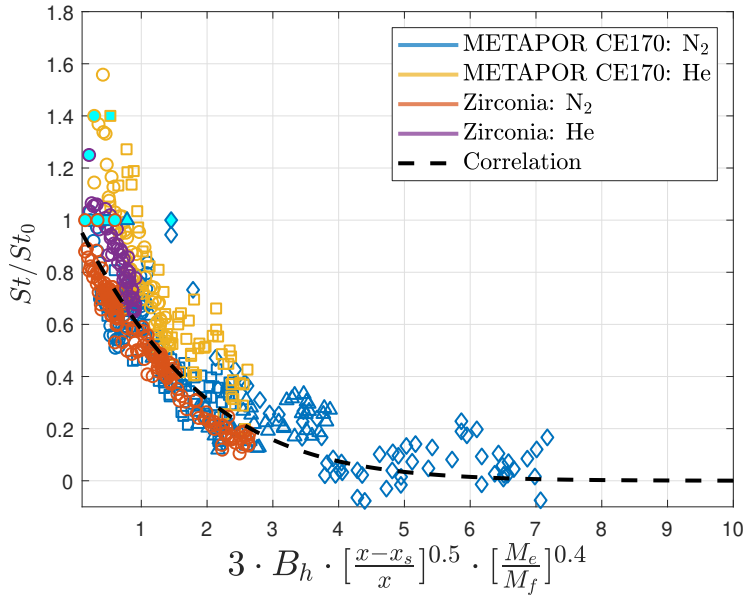

(a) Laminar

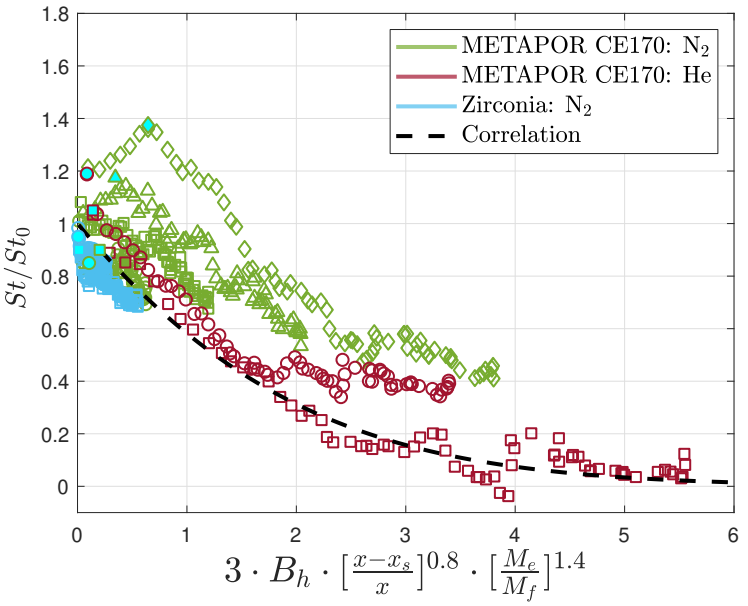

(b) Turbulent

Figure 5.15: Span-wise averaged Stanton reduction between $y = 15$ to -15 mm on the porous injector against the blowing parameter, B_h (based on the local St_0 at each location) for all injection cases. Correlation refers to Eqs (5.6) and (5.7). The filled cyan points are selected values of $(St/St_0)_{\max}$ for each case.

replaced with λ and ω from Eqs. (5.6) and (5.7) as well as the y axis replaced with $\frac{St/St_0}{(St/St_0)_{\max}}$ as discussed above. To achieve a good fit with experimental data a value of $C = 3$ and $m = 0.4$ for the laminar cases and $D = 3$ and $n = 1.4$ for the turbulent cases was chosen. Overall, both correlations reasonably capture the

effect of the injected mass flux, the growth of the boundary layer at the injector and the differences in molecular properties of the nitrogen and helium coolants. Whilst C and D are purely empirically derived factors for the present freestream test conditions, there is a greater significance to the chosen value of the exponents m and n. For the laminar case, the value of $m = 0.4$ is also referenced by Marvin and Pope [117] as an upper bound correction factor to account for differing fluid properties between the injected and freestream gas in laminar stagnation point flows. For the turbulent cases, several values for the exponent between 0.5 and 1 have been stated depending on the experimental data [45, 174]. An exponent of 1.4 is higher than expected, suggesting that helium injection is a more effective coolant in turbulent flows than previously observed for these freestream conditions and geometry. In fact, the factor

$$\left(\frac{\mathrm{M}_e}{\mathrm{M}_f}\right)^{1.4} \tag{5.13}$$

translates to helium possessing 16 times the cooling effectiveness of an equivalent blowing parameter of nitrogen. However, it must be stressed that this is based on only two helium injection cases and further experimental and computational studies are required to fully understand this effect.

Figure 5.17 show both correlations applied to a subset of span-wise averaged experimental data points. For the laminar cases, an extremely good fit within 5% of the experimental data is attained for the Zirconia injector for both the nitrogen and helium injection cases. This material, as demonstrated above produces an extremely uniform outflow, closely resembling the assumed uniform mass injection boundary condition. Greater scatter with up to 30% deviation is present for the METAPOR CE170 cases though the trend is again clear. The sharp local variations present for all the cases with this injector highlight the importance of selecting an injector with a uniform outflow to ensure that all regions on the surface are cooled to the required degree. A similar level of agreement is seen for the turbulent cases wherein, with nitrogen injection, the correlation lies within 10% of the experimental points when the correlation curves are set to begin at the point of maximum heat transfer

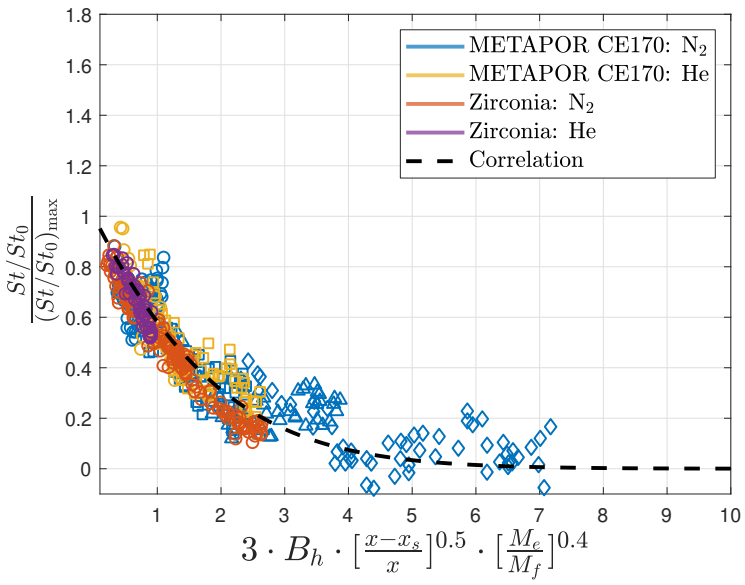

(a) Laminar

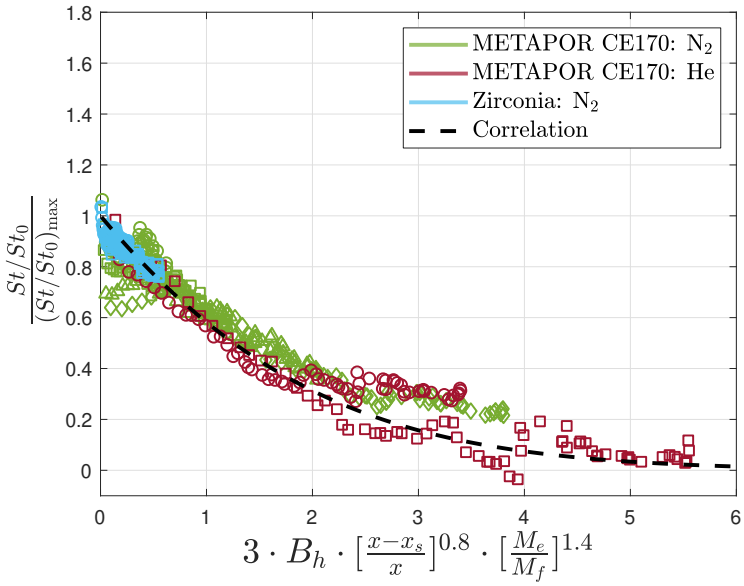

(b) Turbulent

Figure 5.16: Span-wise averaged $\frac{St/St_0}{(St/St_0)_{max}}$ between $y = 15$ to -15 mm on the porous injector against the correlation factors in Eqs. (5.6) and (5.7) for all cases. Correlation refers to Eqs. (5.6) and (5.7).

at $x = 164$ mm. For the helium case presented, whilst the correlation follows the general trend, there is greater scatter in the experimental curve and the correlation under-predicts the heat transfer reduction, especially from $x = 160$ to 182 mm.

Overall, the presented correlation parameters correctly capture the axial heat transfer distribution at the start of a finite-length porous injector for both laminar

and turbulent cases. In particular, this shows that in certain scenarios, it may be more beneficial to begin the transpiration-cooled wall upstream of a predicted high heat flux region than to inject at higher mass fluxes so that the film is fully developed by the time it arrives at that region.

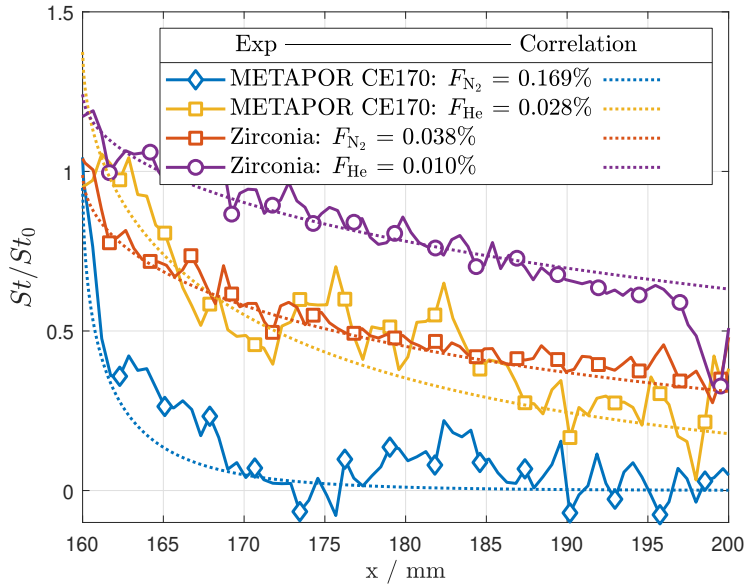

(a) Laminar

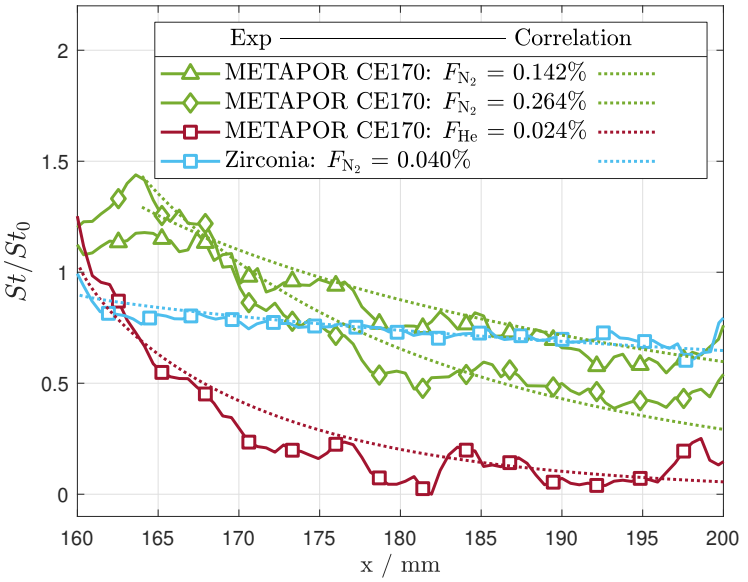

(b) Turbulent

Figure 5.17: Comparison between the span-wise averaged experimental heat transfer reduction and predicted by the correlations in Eqs. (5.6) and (5.7).

5.5.4 Turbulent Downstream Effectiveness

As noted previously, for the laminar cases, transition began right after the end of the porous injector and thus it is not possible to comment on the effectiveness of injection as it mixes downstream with the external boundary layer for laminar flows. Several studies have been completed on this topic for slot injectors [122–124] and more recently, Ifti et al. [100], characterised the downstream laminar effectiveness for Mach 7 flows on the same experimental model as this paper. However, as indicated by Fig 5.7, for the turbulent case, the boundary layer was fully turbulent up to the end of the field of view of the infrared camera and thus the downstream mixing may be compared.

To compare with existing literature [124], the heat flux reduction can also be formulated as an isothermal cooling effectiveness

$$\eta_{th} = 1 - \frac{St}{St_0}, \tag{5.14}$$

where the subscript '0' denotes the uncooled case. A case of 100% cooling, i.e. zero Stanton number to the wall, would result in an effectiveness of 1. Contour plots of the thermal effectiveness are plotted in Fig. 5.18 for the highest injection cases using nitrogen and helium respectively. Whilst both cases have a similar trend of diminishing effectiveness as the coolant mixes further downstream, it is notable that for the highest nitrogen injection, the coolant film diffuses laterally and is wider than the span of the injector. In addition, significant non-uniformity in the film coverage downstream is present with greater coverage between 10 and 20 mm compared to -10 and -20 mm displaying fully three-dimensional behaviour.

Furthermore, Fig. 5.19 shows the span-wise average cooling efficiency from the end of the injector ($x = 200$ mm) to 310 mm from the leading edge. All of the cases exhibit a similar, close to linear, monotonic trend of reduced thermal efficiency as the coolant traverses further downstream. Essentially, with an increased blowing ratio, i.e. coolant mass flux, the film coverage improves on the injector as well as downstream. For low nitrogen blowing ratios, there is little reduction in the

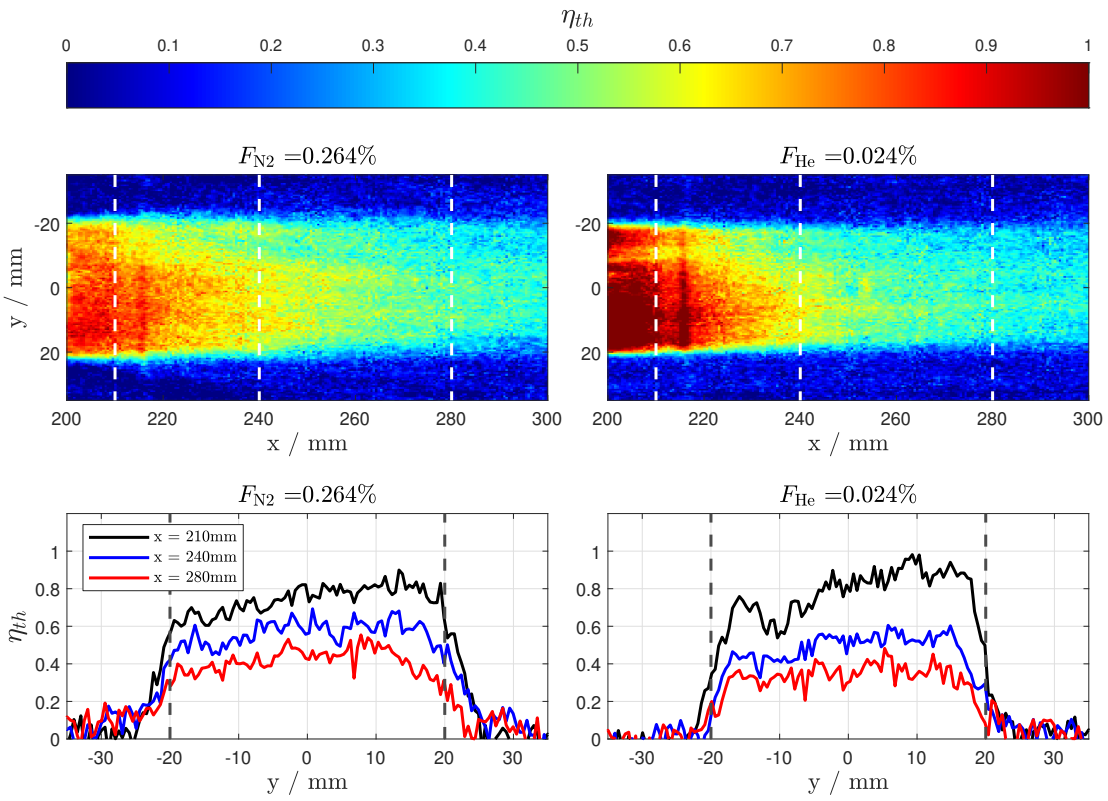

Figure 5.18: Contour plots of downstream isothermal efficiency for the highest nitrogen and helium injection cases in turbulent flow with the METAPOR CE170 injector. The three span-wise slices are taken at $x = 210$, 240 and 280 mm.

thermal efficiency as the film convects downstream, i.e. the gradient is relatively shallow. The coolant film retains a baseline level of thermal efficiency even at $x = 300$ mm with a drop from 0.08 to 0.05 for $F_{N2} = 0.040\%$. In contrast, the highest nitrogen injection cases display a very steep drop off from an efficiency of almost 1 at the end of the injector for $F_{N2} = 0.264\%$ to 0.3 just 100 mm downstream. For helium injection, the trend is slightly dissimilar to nitrogen with a marginally steeper gradient. This is expected due to the higher volume and different molecular properties of the helium film.

The obtained values of η may be correlated by a factor defined by Hombsch and Olivier [124] (using the same approach as Goldstein)

$$\xi = \left(\frac{C^*}{Re_u}\right)^{0.2} \left(\frac{T_e}{T^*}\right)^{0.6} \frac{x'^{0.8}}{F \cdot s} \tag{5.15}$$

where x' is the distance from the start of the injector, $C*$ is the Chapman-Rubesin

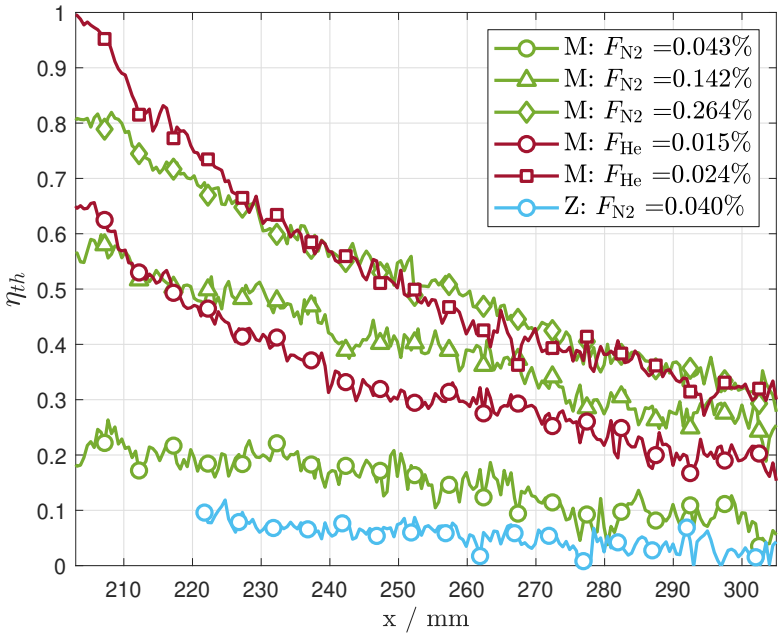

Figure 5.19: Span-wise average thermal efficiencies from the end of the injector to 310 mm from the leading edge. M represents the METAPOR CE170 injector and Z the Zirconia injector. The span-wise averages are taken from y = -15 to 15 mm.

factor evaluated at Eckert's reference temperature ($(T_e/T^*)(\mu^*/\mu_e)$), and s is the stream-wise length of the injector. Whilst this correlation factor is strictly speaking for when the injected gas is the same as the freestream, a scaling factor of $(\frac{c_{p,f}}{c_{p,e}})^{1.4}$ is used to account for the helium cases. Note that for the instance of correlating the effectiveness downstream of the porous injector, a correction factor based on the heat capacity, c_p is more appropriate than the molecular weight ratio as full coverage of coolant downstream can no longer be assumed. In fact, as the coolant diffuses downstream, it will mix with the external turbulent boundary layer. Thus, we can no longer assume the coolant is at an equal temperature to the wall and the rate at which the coolant will rise in temperature will be largely governed by the heat capacity.

This factor essentially translates to a factor of 10 which is in between the factor $(\frac{\mathrm{M}_e}{\mathrm{M}_f})^{0.4}$ for laminar flow over the injector and $(\frac{\mathrm{M}_e}{\mathrm{M}_f})^{1.4}$ for turbulent referred to by the correlations above (Fig. 5.17). The fact that the dissimilar gas correlation factor varies between on and downstream of the injector and for different flow conditions reinforces the fact that a more complex physical model is required to accurately capture the effect of dissimilar gases across different flow scenarios.

Homsbsch and Olivier [124] proposed the following correlation for turbulent cases

$$\eta_{th} = \begin{cases} 1 & \text{for } \xi \leq 1.85, \\ [1 + 0.32(\xi - 1.85)]^{-0.8} & \text{for } \xi > 1.85, \end{cases} \tag{5.16}$$

for blowing ratios from 18-53%. For the lower blowing ratios and higher Mach number in this study ($M = 6.1$ and $F = 0.019$-0.264%), the authors propose the following modification to the correlation

$$\eta_{th} = \begin{cases} 1 & \text{for } \xi \leq 4.5, \\ [1 + 0.15(\xi - 4.5)]^{-0.8} & \text{for } \xi > 4.5. \end{cases} \tag{5.17}$$

which successfully lines up with the experimental data (Fig. 5.20). Due to the large difference in blowing ratio between the experiments conducted in Ref. [124] and the present work, it is not surprising that there is a difference between Eqs. (5.16 and 5.17). The current data set demonstrates the shortcomings of existing general models of downstream effectiveness for turbulent flows and further experiments at a wider range of conditions will help develop confidence in this model to accurately model these flows.

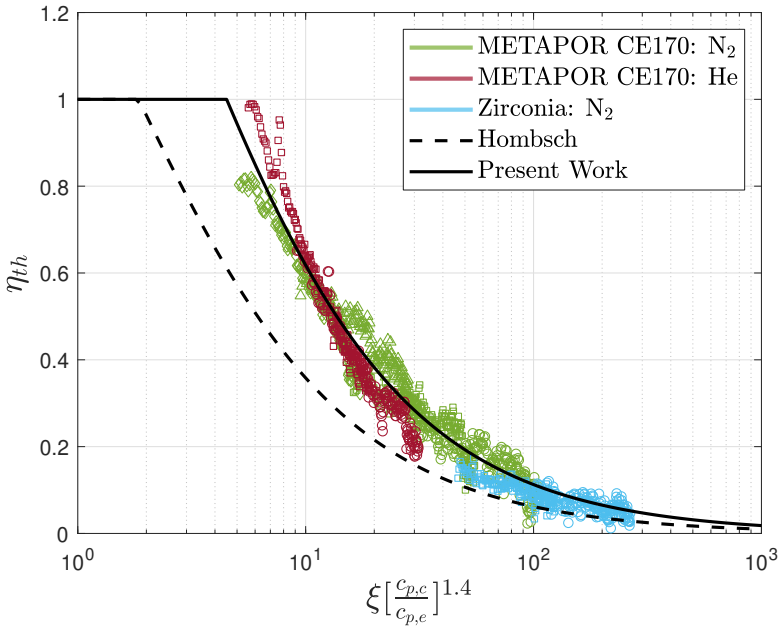

Figure 5.20: Thermal effectiveness, η_{th}, verses the correlation factor, ξ. The present work represents Eq. (5.17).

As per Fig. 5.4 and 5.5, there is significant non-uniformity in the METAPOR CE170 sample with greater outflow at the bottom half of the injector ($y < 0\,\text{mm}$) compared to the top half. The averaged normalised outflow velocity for the top half of the injector is 55% of the whole injector compared to 45% at the bottom. Theoretically, the asymmetric outflow should affect the downstream effectiveness and this may be accounted for by tuning the correlation in Eq. (5.17) to account for the variable blowing rates across the injector. Figure 5.21 plot the thermal effectiveness downstream from the edge of the injector for nitrogen injection at the highest blowing ratio for different span-wise regions downstream of the injector and compares this to the appropriate downstream effectiveness predicted by the correlation. At the very edge of the injector, the correlation presented in Eq. (5.17) models the thermal effectiveness very closely, with the change in localised blowing ratio reflected as a shift in the dashed curves. However, as the film convects downstream, the 3D nature of the film close to the injector gradually reduces as the film mixes with the hypersonic crossflow at higher rates downstream until the film is almost totally uniform in the span-wise direction. This limits the validity of the correlation proposed above to regions up to 50 mm from the injector. Before this point, the film remains one-dimensional and a simple 1D correlation may be applied locally at each stream-wise 'slice' to model the evolution of the thermal film effectiveness downstream of the injector.

5.6 Conclusions

In this study, the spatial, two-dimensional surface heat transfer of two transpiration-cooled micro-porous injectors was measured in laminar and turbulent hypersonic flow. It was found that a modification to film theory which accounts for the boundary layer growth at the start of the injector successfully correlates the heat transfer reduction across different blowing rates for nitrogen and helium injection. Injection in the laminar regime results in a steady, monotonic reduction in heat transfer whilst a much flatter profile was observed in the turbulent regime. helium was found to be more effective at cooling in both laminar and turbulent flows than

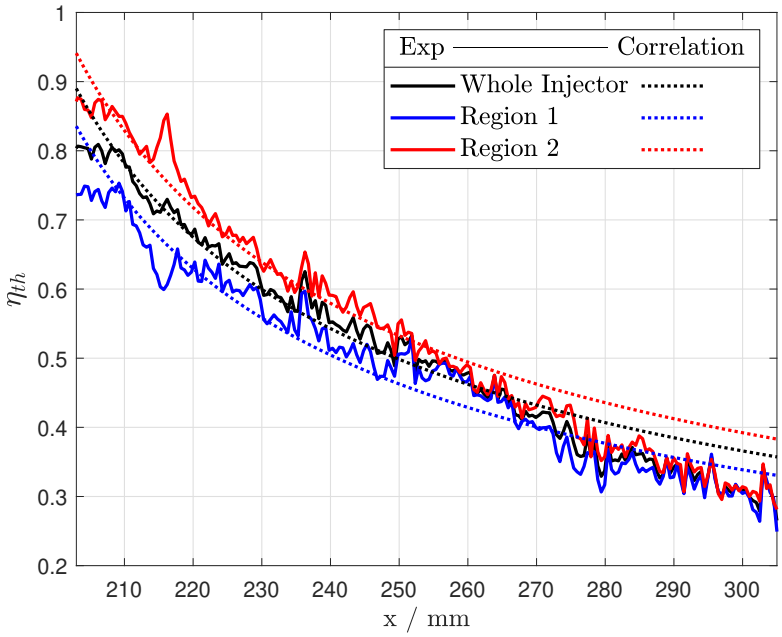

Figure 5.21: Experimental span-wise averaged thermal effectiveness, η_{th}, at $F = 0.264\%$ of N_2. Region 1 and 2 refer to indicated locations in Fig. 5.5 and 'Correlation' refers to Eq. (5.17).

reported previously in the literature. In the turbulent regime, helium exhibited a cooling effectiveness 16 times greater than nitrogen. The outflow uniformity of a porous injector was found to have a great impact on the spatial heat transfer distribution. A uniform outflow leads to consistent coverage of coolant over the injector with no local hot spots.

Overall, the results published add insight into the spatial variation in local heat transfer on the injector surface and how the film build-up differs between laminar and turbulent flows. Whilst the presented correlations are specific to the flow conditions used in these experiments, they may still be used as a preliminary design tool for sizing a transpiration-cooled system. Further experimental and numerical studies covering a wider parameter space of freestream conditions and coolant gases may yield a generalised correlation applicable across a wider range of flight conditions.

5.7 Uncertainty Analysis

The main independent quantities measured in this paper are the Stanton number, the blowing ratio, the blowing parameter and the unit Reynolds number. To

find the total uncertainty, the Taylor Series Method by Coleman and Steele [167] was employed where, for a function $r = r(X_1, X_2, ...X_n)$, the uncertainties in the individual measurements are assumed to be uncorrelated. Thereafter, gradients $\frac{\partial r}{\partial X_i}$ are calculated numerically by perturbing the variables X_i in the data reduction processing steps. First of all, the unit Reynolds number is calculated according to the following equation

$$Re_u = \frac{\rho_e u_e}{\mu_e} \tag{5.18}$$

where u_e and ρ_e are a function of the Mach number, M, total pressure, P_0, and total temperature, T_0. The Stanton number is calculated according to

$$St = \frac{\dot{q}_w}{\rho_e u_e c_p (T_r - T_w)} \tag{5.19}$$

where the heat flux at the wall, $\dot{q}_w$, is a function of the material thermal product, $\sqrt{\rho c_p k}$, and the temperature, T_w, obtained through infrared camera measurements. The blowing ratio is calculated using Eq. 5.4, which depends on T_e and ρ_e as well as the injected mass flux, $\rho_f u_f$. This is calculated assuming a linear pressure gradient through the porous injector and a constant solid temperature by employing Eq. (5.10). The uncertainties in the Darcy and Forchheimer coefficients were determined using the same Monte Carlo simulation procedure detailed in Ref. [65]. The blowing parameter relates the uncooled Stanton number and the blowing ratio as per Eq. (5.3). The freestream mass flux cancels out in this equation and can be written as

$$B_h = \frac{\rho_f u_f c_p (T_r - T_w)}{\dot{q}_w} \tag{5.20}$$

where, in this case, there is no dependency on Mach number, M, or total pressure, P_0.

The wall temperature, T_w is determined via infrared thermography and a key figure of merit used to qualify the temperature output of infrared cameras is the noise equivalent differential temperature (NETD) [135]. This is a signal-to-noise figure that represents the temperature difference which would produce a signal

equal to the camera's temporal noise. For both the FLIR A6751 SLS and Telops M3K cameras used in this work, a factory calibration determined that the NETD was below 40 mK over the observed range of temperatures. This is significantly smaller than the expected temperature rise of the injector of 0.5-5 K. In addition to the NETD, there are additional sources of error from the infrared calibration system. This includes the error in the measurement of the reflected temperature when conducting the multipoint calibration, T_{ref}, and the error in the temperature measurement of the CI-Systems black body calibrator, $T_{\text{calibrator}}$. Finally, to go from the black body temperature to the temperature of the material of interest, the emissivity of the material, ε, is required.

Table 5.4 lists the different uncertainty contributions to the overall uncertainty in the measurement of Reynolds number, Stanton number, blowing ratio and blowing parameter for the case of an injected mass flux of $0.833\,\text{kg}\,\text{s}^{-1}\,\text{m}^{-2}$. This represents a medium level of nitrogen injection for the METAPOR CE170 injector. The main drivers of uncertainty, especially for the Stanton number and blowing parameter are the total temperature, T_0, and the material thermal product. The uncertainty in blowing parameter is 14.0% where the main source of uncertainty is the total temperature (60%). A tighter measurement of total temperature in future experimental campaigns and higher accuracy materials may yield uncertainties well below 10% for all of the key independent quantities.

Table 5.4: Uncertainty contributions and overall uncertainties in unit Reynolds number, uncooled Stanton number, blowing ratio, and blowing parameter. This is for the laminar freestream condition with nitrogen injection at $0.833\,\mathrm{kg\,s^{-1}\,m^{-2}}$ and a METAPOR CE170 injector.

Parameter	Baseline value	Absolute uncertainty	Relative uncertainty
NETD / K	0.04	±0.02	50%
T_{ref} / K	296	±2	<1%
$T_{\mathrm{calibrator}}$ / K	296	±0.1	<1%
ε	0.95	±0.04	4.2%
$(\sqrt{\rho c k})$ / $\mathrm{Jm^{-2}K^{-1}s^{-0.5}}$	1565	±78.25	5%
P_0 / Pa	1204	±24.08	2%
T_0 / K	420	±10	2.4%
M	6.1	±0.1	1.6%
T_{pl} / K	293	±2	<1%
p_{pl} / Pa	$3.89 \cdot 10^5$	$\pm 1 \cdot 10^4$	2.5%
K_D / $\mathrm{m^2}$	$2.52 \cdot 10^{-13}$	$\pm 1.74 \cdot 10^{-14}$	6.9%
K_F / m	$1.03 \cdot 10^{-8}$	$\pm 1.06 \cdot 10^{-9}$	10.3%
Re_u / $\mathrm{m^{-1}}$	$13.3 \cdot 10^6$	$6.26 \cdot 10^5$	4.7%
St_0	$5 \cdot 10^{-3}$	$6.45 \cdot 10^{-4}$	12.9%
F	$1.7 \cdot 10^{-2}$	$1.2 \cdot 10^{-3}$	7.1%
B_h	3.43	0.48	14.0%

Chapter 6

Experimental Studies of Hypersonic Shock Impingement on a Transpiration-Cooled Flat Plate

Contents

6.1 Foreword

In this chapter, the novel infrared-based diagnostic method to measure surface heat transfer on transpiration-cooled porous injectors is applied to the generic case of a flat plate with shock impingement in hypersonic flow. For the first time, two-dimensional spatial heat transfer distributions of transpiration cooling applied to SWBLI in hypersonic conditions have been experimentally captured. Both fully

turbulent and transitional cases exhibit a similar response to coolant injection and transpiration cooling is found to be highly effective for these cases. As a result, simplified correlations are proposed. The following work has been published in the *Journal of Spacecraft and Rockets*. It is presented in this chapter with small layout changes, but unaltered content. The author contributions are as follows

- Imran Naved: Conceptualisation, Methodology, Investigation, Data Analysis, Writing
- Matthew McGilvray, Tobias Hermann, and Chris Hambidge: Supervision

6.2 Introduction

Shock-wave-boundary-layer interactions (SWBLIs) often take place on deployed control surfaces, at the juncture between vertical fins and the fuselage, and the inlets of hypersonic vehicles [18]. The impinging SWBLIs can lead to harsh adverse pressure gradients which may result in boundary layer separation with correspondingly high surface pressures and heat loads. Depending on the state of the incoming boundary layer as well as the shock strength, SWBLIs may be broadly divided into three types based in the state of the boundary layer downstream of shock impingement: laminar, transitional, and turbulent. The second of these types generally occurs where the incoming boundary layer is laminar but the free-stream Reynolds number is in the upper end of the laminar regime and the strength of the incident shock causes the boundary layer to separate and rapidly transition to turbulence [175]. Hypersonic transitional SWBLIs can result in significantly greater peak surface heat transfer than laminar or turbulent interactions [176–179] and are a phenomenon of great interest, especially for the outer surfaces of hypersonic cruise vehicles where in many cases the boundary layer is laminar up to the shock interaction. This is a particular concern for hypersonic cruise vehicles wherein the actuation of control surfaces may lead to an SWBLI interaction, triggering transition or even boundary layer separation and leading to very high off-design thermal and pressure loads. Turbulent interactions on the other hand are common

in the walls of scramjet combustors [18] which whilst promoting mixing, can result in very high localised heat loads and dynamic pressure which need to be mitigated.

Designing a thermal protection system (TPS) that is able to withstand these high heat fluxes is challenging. One candidate is transpiration cooling which is an active thermal protection system that can be applied to hypersonic vehicles. This involves passing a cool fluid through a porous material into the external boundary layer. Cooling is achieved through a combination of the coolant creating a thin film which thickens the boundary layer and insulates the wall from the hot external gas, internal convection between the coolant and porous medium, and, in certain cases if an inert gas is used, the coolant film can protect the wall from surface oxidation and catalytic recombination. The advantage of transpiration cooling is the flexibility of using this technique for a wide range of free-stream conditions. In addition, the introduction of the low-velocity coolant gas reduces the velocity gradient in the boundary layer, and therefore the skin friction, which for internal walls of combustion chambers, is a major contribution to engine drag [18].

However, this is balanced out by the additional complexity budget introduced to implement this system. In particular, transpiration cooling is a good candidate for cooling local hot spots caused by SWBLIs as this TPS system may be applied locally to regions where these interactions are likely to occur. However, a critical aspect of these flows is whether the coolant layer can withstand the disturbances caused by the shock wave and remain intact throughout the interaction region. If the coolant layer remains intact, then it is likely that a marked reduction in peak heating is possible [45].

There are limited previous experimental studies exploring the effectiveness of transpiration cooling for SWBLIs, especially at hypersonic conditions. The most extensive experiments were carried out by Holden and Sweet [45] in the 1990s where the surface heat transfer and pressure on a flat plate with a transpiration-cooled wall in turbulent hypersonic flow was characterised by a range of varying blowing rates and incident shock strengths. Nitrogen and helium were used as coolants and a range of shock generator angles between 5-10° were employed to generate the

incident shock. It was found that the interaction region between the incident shock and the low-momentum transpiration-cooled boundary layer did not result in a significant increase in the size of attached or separated interaction regions, and did not result in significant flow-field distortions above the interaction region. Thus, the heating downstream of the shock-impingement point could easily be reduced to values without shock impingement by a relatively small increase in transpiration cooling in this region. For supersonic flows, Strauss et al. [121] found that impinging a shock with a 9.3° ramp angle shock generator at Mach 2.5 led to only moderate reductions ($\approx 5\%$) in cooling efficiency (i.e. $\frac{T_r - T_w}{T_r - T_f}$) compared to the case without impingement. This is a promising result though the authors note that hotspots due to shock-boundary layer interaction on the porous wall can be an issue, with locally high thermal loads and, therefore, an increase in the risk of structural failure in the porous material, especially so if the wall segment is thin.

The work reported in this paper presents experimental results concerning shock impingement onto a transpiration-cooled porous wall at Mach 6.1 laminar and turbulent conditions. In this study, a 10° shock generator was installed to generate a strong oblique shock to impinge onto a flat plate model. The effectiveness of transpiration cooling for a transitional SWBLI case has never been reported before even though some of the highest heat fluxes occur in this case. The surface heat transfer of the transpiring porous injector is characterised using high-speed infrared thermography which spatially resolves the 2D flow structures at the wall and crucially, the non-intrusive nature of this technique enables measurements directly on the porous injector without impeding or otherwise disturbing the coolant outflow. Infrared thermography has been previously tested and validated for transpiration-cooled surfaces in hypersonic flows by Naved et al. [59] and this technique is the basis for the heat transfer measurements presented in this paper.

6.3 Experimental Methodology

6.3.1 Experimental Model

The experiments were conducted on a flat plate model at 0° angle of attack as described in Naved et al. [60]. Figure 6.1 shows a cross-section of the experimental model. A porous injector of 39.5 x 39.5 mm was placed 160 mm downstream of the sharp (radius < 0.1 mm) leading edge. A plenum is located underneath the injector and pipework is placed to feed the injection gas to the injector. The temperature and pressure in the plenum were measured by a fast response K-type thermocouple (⌀0.0762 mm) and a Kulite pressure transducer (HEL-375-35BARA). Downstream of the porous injector, the model features a 340 mm long PEEK surface for downstream infrared measurements. For a secondary verification of the surface heat transfer, 13 quartz-based platinum individual thin film gauges were mounted both upstream and downstream of the porous injector. Finally, 3D printed trips were added to a pocket 25.7 mm downstream of the leading edge to aid transition for the turbulent test cases. A diamond transition trip was used with a span-wise length of 90 mm and a height of 0.1 mm. A flush insert was used for the cases where a laminar undisturbed boundary layer was desired.

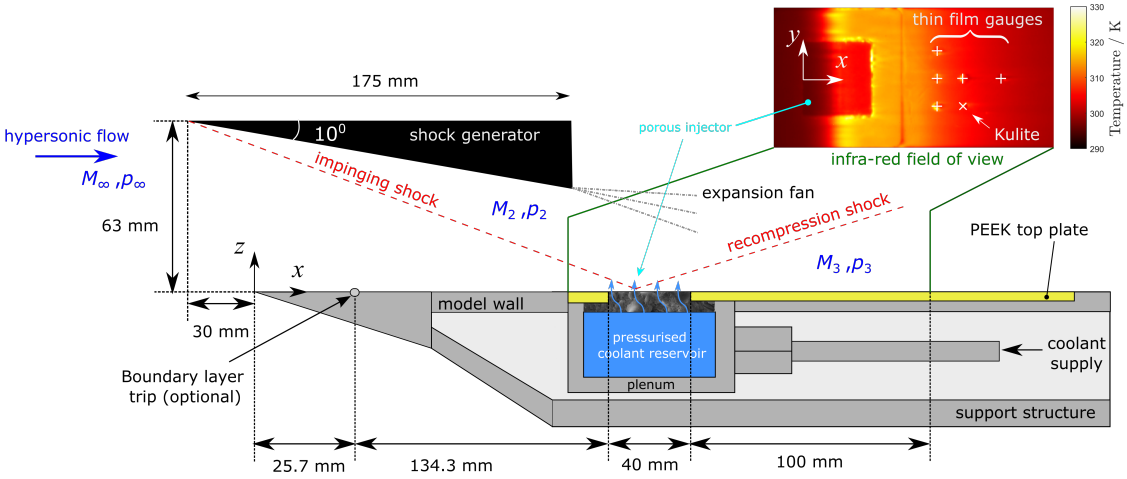

Figure 6.1: Schematic of the flat plate model with the position of the shock generator and the field of view for infrared thermography. Not to scale.

In addition, the surface static pressure was measured using two surface-mounted Kulite pressure transducers (XCS-093-5A). The freestream total temperature

was measured prior to these experiments using differentially heated aspirated thermocouples. The measured data was acquired using a National Instruments PXIe-8135 controller with one PXIe-6368 card. A sample rate of 125 kHz was used to record all signals of the measurement which includes model and wind tunnel instrumentation. A separate in-house heat transfer amplifier unit, HTA5, is also used for thin film gauge data acquisition. This forms a stand-alone unit, run at a matching sample rate to the main DAQ system.

Primarily, surface heat transfer measurements were acquired using infrared thermography and a schematic of the optical setup is shown in Fig. 6.2. The experimental test piece was orientated in a vertical configuration such that the field of view (FoV) of the IR camera is nearly normal to the model surface. The FLIR A6751 SLS long-wave infrared (LWIR) camera with a wavelength band of 7.5-11μm was used for these experiments. The experimental model was viewed through a 50 mm coated Germanium window and the camera was operated at a windowed spatial resolution of 256 x 320 at a frame rate of 400 Hz. This results in approximately 15 frames over the steady tunnel test time.

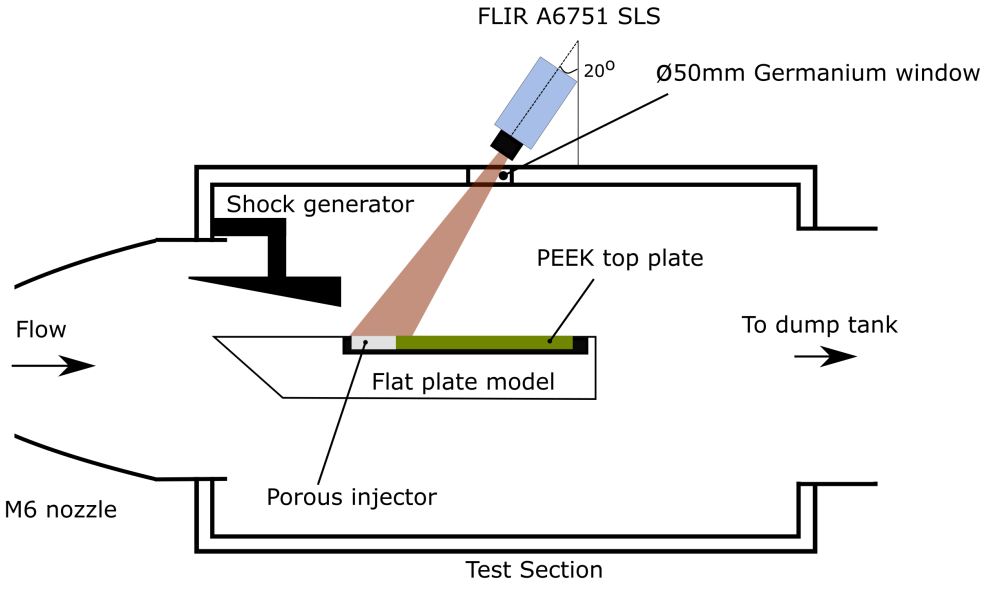

Figure 6.2: Top view of the experimental model in the test section.

Table 6.1: Properties of porous METAPOR CE170 and PEEK. The thermal properties (ρ,c_p,k) were measured by Netzsch Instruments and the emissivity, ε, was measured using an in-house benchtop setup [59]

Parameter	METAPOR CE170	PEEK
Thickness, L / mm	7	10
Porosity, ϕ	0.20	-
Density, ρ_s / $\mathrm{kg\,m^{-3}}$	1710	1310
Thermal Conductivity, k_s / $\mathrm{W\,m^{-}\ K^{-1}}$	1.662	0.25
Specific Heat Capacity, $c_{p,s}$ / $\mathrm{J\,kg^{-1}\,K^{-1}}$	1177	1201
Thermal Product, $(\sqrt{\rho c_p k})$ / $\mathrm{J\,m^{-2}\,K^{-1}\,s^{-0.5}}$	1565	627
Darcy Coefficient, K_D / $\mathrm{m^2}$	$1.86 \cdot 10^{-13}$	-
Forchheimer Coefficient, K_F / m	$7.44 \cdot 10^{-9}$	-
Emissivity, ε	0.95	0.93

The porous injector used for these experiments was the METAPOR CE170 which is a commercially available micro-porous material made of aluminium hydroxide bonded to a resin system (pore diameter 20 μm). The properties of both METAPOR CE170 and PEEK are available in Table 6.1. Due to a lack of available manufacturer data for the thickness of the porous injector used for these experiments and to determine the localised permeability for the relatively small samples used in the experiment (39.5 x 39.5 x 7 mm), the outflow and permeability of the porous injector were measured according to the procedure detailed by Ifti et al. [65]. This was completed pre and post-experiment and both measurements were within the uncertainty bounds of the permeability measurement - i.e. there was no significant difference between the two measurements.

The 10° shock generator deflects the flow by 17° and is positioned above the main plate such that the inviscid shock impingement position is approximately 165 mm from the leading edge. The wedge was manufactured from a single block of aluminium, with a length of 175 mm and width of 200 mm and was mounted onto the test section wall. The width of the shock generator was maximized in order to minimize 3D effects on the 100 mm wide flat plate. The resulting inviscid shock strength at $M_\infty = 6.1$ is $p_2/p_\infty = 3.73$.

6.3.2 Heat Transfer Measurements

The surface heat flux was primarily measured by employing infrared thermography with additional individual thin film gauges to support and validate the infrared measurements. A series of calibration steps, further detailed in Ref. [59], were followed to obtain quantitative transient temperature maps of the flat plate surface including the transpiration-cooled injector from the raw infrared signal.

1. Multipoint calibration: Firstly, a multipoint calibration was carried out in-situ using a black body calibrator (CI-Systems SR-33-7 infrared calibrator) to relate the camera raw signal to the true black body temperature inside the wind tunnel test section. This step calibrates the camera and optical system by correcting any detector or optical system spatial non-uniformity or offsets.

2. Emissivity measurement: Secondly, to relate the black body temperature to the true material temperature, a material emissivity measurement was performed pre-experiment by using a bench-top setup. The measured emissivity values for both the porous injector and the PEEK surface upstream and downstream of the injector are recorded in Ref. [59].

3. Image Processing: Finally, the images were spatially transformed to a rectangle that represents the physical geometry and passed through an image stabilisation algorithm prior to final post-processing.

After the corrected temperature profile, ΔT, was obtained the heat flux, $\dot{q}_w$, was determined by applying the impulse response method of Oldfield [162] employing the local material thermal properties of METAPOR CE170 (porous injector) and PEEK (the remainder of the flat plate), respectively. A fully coupled transpiration-cooled impulse response method such as in Hermann et al. [74] was not required as the convective heat transfer process between the coolant fluid and porous solid was accounted for by the calibration procedure. Further justification for this assumption and details of the calibration process are presented in Ref. [59].

6.3.3 Flow Conditions and Parameters

Table 6.2: Free-stream and post-recompression shock flow conditions. The post-recompression shock values are calculated from isentropic relations.

Parameter	Laminar		Turbulent	
	Freestream (∞)	Post-recompression shock (3)	Freestream (∞)	Post-recompression shock (3)
Pressure, p / Pa	786	8413	1985	21246
Temperature, T / K	49.6	107.8	44.0	95.6
Velocity, u / m s^{-1}	861	791	811	745
Density, ρ / kg m^{-3}	0.0552	0.272	0.157	0.774
Mach Number, M	6.1	3.80	6.1	3.80
Unit Reynolds Number Re_u / m^{-1}	$13.4{\cdot}10^6$	$28.2{\cdot}10^6$	$40.5{\cdot}10^6$	$84.8{\cdot}10^6$
Estimated boundary layer height, δ_{99}/ mm at $x = 160\,\text{mm}$	2.36	-	4.44	-

The experiments were conducted in the Oxford High-Density Tunnel (HDT) at the Oxford Thermofluids Institute operated in Ludweig tube mode. A detailed description of the facility may be found in Refs. [138, 170]. The Mach 6 nozzle was selected and two different freestream conditions were chosen to achieve both laminar and turbulent boundary layer states at the porous injector. The free-stream properties are calculated from measured stagnation pressures, pitot pressures, and temperatures using isentropic relations. The viscosity was determined using Keyes model [158] and Table 6.2 presents an overview of the flow conditions.

For direct comparison with previous investigations of transpiration-cooled walls without shock impingement, the experimental heat fluxes are expressed as a Stanton number which is based on the free-stream conditions upstream of the shock impingement

$$St = \frac{\dot{q}_w}{\rho_\infty u_\infty c_p (T_0 - T_w)} \tag{6.1}$$

where $\dot{q}_w$ is the heat flux at the wall, ρ_∞ is the free-stream density, u_∞ is the free-stream velocity, c_p is the specific heat capacity at constant pressure, T_0 is the total temperature and T_w is the wall temperature. Due to a lack of information regarding the local recovery factor in the shock interaction region as well as to maintain consistency with the aforementioned experiments conducted by Holden

and Sweet [45], the more conventionally used recovery temperature is replaced by the total temperature in the equation above.

The blowing ratio, which is defined as the ratio of the coolant mass flux to the free stream mass flux at the boundary layer edge, is determined from the measured plenum and free-stream pressures and temperatures according to the Darcy-Forchheimer equation

$$\frac{p_f^2 - p_e^2}{2LR_fT_f} = \frac{\mu_f \dot{m}_f}{K_D} + \frac{\dot{m}_f^2}{K_F} \tag{6.2}$$

where the values of the permeability coefficients, K_D and K_F are given in Table 6.1 for the METAPOR CE170 injector used in this study. The free stream mass flux at the boundary layer edge may be defined either upstream of injection, $\rho_\infty u_\infty$, or downstream of the re-compression shock, $\rho_3 u_3$. Thus two blowing ratios may be defined

$$F = \frac{\dot{m}_f}{\rho_\infty u_\infty} = \frac{\rho_f u_f}{\rho_\infty u_\infty} \tag{6.3}$$

and

$$F_3 = \frac{\dot{m}_f}{\rho_3 u_3} = \frac{\rho_f u_f}{\rho_3 u_3} \tag{6.4}$$

where the subscript 'f', '∞', and '3' denotes the coolant, the boundary layer edge value upstream of the shock interaction region, and the boundary layer edge value downstream of the re-compression shock. The boundary layer edge values downstream of the re-compression shock ('3' in Fig. 6.1) are found by applying oblique shock relations across the impinging and re-compression shocks.

As the surface pressure rises rapidly over the porous injector, there is a risk that the constant mass flux assumption does not hold over the injector as, from the Darcy-Forchheimer equation, the injected mass flux depends both on the plenum pressure and surface pressure. To assess whether this occurs, the lowest plenum pressure tested for the turbulent condition (where the surface pressure is the highest) is 2.7 bar. The corresponding surface pressure downstream of the re-compression

shock (from Table 6.2) is 0.212 bar - just under 8% of the plenum pressure - whilst upstream of the shock, it is 0.0198 bar. Applying the two surface pressures to the Darcy-Forchheimer equation, the difference in coolant mass flux between the two scenarios is less than 0.45 %. Higher plenum pressures and lower surface pressures would lead to an even smaller difference. This value is within the error of mass flux measurement and, therefore, it may be assumed that the injected mass flux is constant within reasonable accuracy over the porous injector for all the test cases presented in this work.

Table 6.3 presents an overview of all the cases considered in this study. The quoted values of the blowing ratio in the subsequent results section are all based on F, the blowing ratio based on the boundary layer edge values upstream of impingement. The corresponding blowing ratios downstream of the re-compression shock may be read off the table. Some of the values of F, especially for the laminar cases, are very high compared to previous experiments in a similar setup [60]. This is due to the higher free-stream mass flux post-recompression shock which then requires higher coolant mass fluxes to result in a significant heat transfer reduction.

Table 6.3: Overview of blowing cases at both laminar and turbulent conditions. F is the blowing ratio based on the boundary layer edge conditions upstream of shock impingement, '∞', and F_3 is the blowing ratio based on the boundary layer edge conditions downstream of shock impingement, '3'. T_f and p_f are the measured coolant temperature pressure.

Coolant	Boundary layer state	$\dot{m}_\mathrm{f}$ / kg m^{-3}	F / %	F_3 / %	T_res / K	P_res / kPa
N_2	Laminar	0.11	0.24	0.052	293	108
N_2	Laminar	0.26	0.55	0.13	292	177
N_2	Laminar	0.81	1.71	0.38	293	389
He	Laminar	0.014	0.030	0.0070	291	100
He	Laminar	0.022	0.046	0.010	291	124
He	Laminar	0.042	0.088	0.019	292	173
He	Laminar	0.10	0.21	0.047	292	279
N_2	Turbulent	0.48	0.38	0.084	292	268
N_2	Turbulent	0.74	0.58	0.13	294	365
He	Turbulent	0.056	0.044	0.0097	291	202
He	Turbulent	0.14	0.11	0.024	291	335

6.4 Results and Discussion

For the targeted laminar and turbulent conditions on the flat plate, it is necessary to first ascertain that the correct boundary layer state is achieved before shock impingement. Figure 6.3 presents the span-wise averaged surface Stanton number (between y = -15 to 15 mm) for both the laminar and turbulent shock impingement cases as well as the equivalent without shock impingement. Without impingement, the boundary layer remains laminar and turbulent, respectively, within the porous domain. For the laminar boundary layer, transition occurs from x = 200 mm onwards. Overall, there is a great agreement to within 5% with the flat plate correlations of Eckert [89].

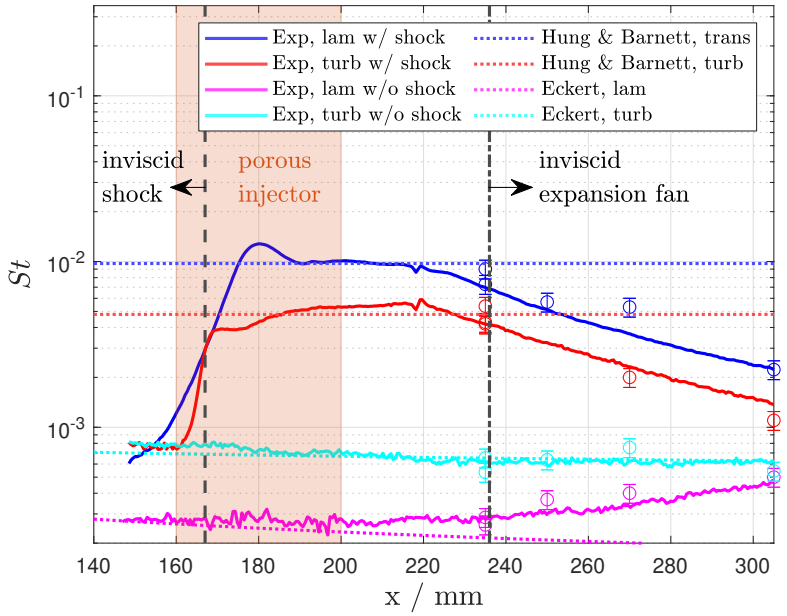

Figure 6.3: Span-wise averaged surface Stanton number (averaged between y = -15 to 15 mm) of the uncooled shock impingement and unshocked cases at both laminar (Re_u = 13.4·10^6 m^{-1}) and turbulent (Re_u = 40.5·10^6 m^{-1}) conditions. The circular points represent thin film gauges. The discontinuity at x ≈216 mm is due to the joint between the model and the plate that holds the injector.

Once the shock generator was installed, the generated impinging shock interacts with the flat plate on the porous injector. The SWBLI increases the boundary layer thickness and there is likely to be at least some flow separation due to the shock intensity and boundary layer state. The expansion waves from the rear of

the shock generator increase the Mach number and interact with the reflected shock. These expansion waves impinge onto the boundary layer far downstream of the SWBLI region and do not influence the interaction region. The inviscid shock impingement location and the position where expansion waves emanating from the end of the shock generator interact with the model surface are marked in Fig. 6.3. The position of the expansion fan correlates well with the position at which the surface heat transfer begins to reduce agreeing with previous experiments for a turbulent boundary layer by Schluein [180].

For the incoming laminar boundary layer, a clear location of peak heating is located at $x \approx$178 mm. After that point, the heat flux reduces gradually plateauing from 190-210 mm to $St = 0.01$. This curve is characteristic of a transitional shock interaction where due to the relatively high Reynolds number at the shock impingement location ($Re_L > 2.4 \cdot 10^6$) and the large shock generator angle (10°), shock-induced transition occurs leading to significantly higher heating rates than even purely turbulent flows [179]. As noted by Currao et al. [176] for a similar configuration (Mach 5.8, shock generator angle of 10° and $Re_u = 7 \cdot 10^6$ m^{-1}), shock-induced transition caused separation to occur well ahead of the shock impingement location with the reattachment region very close to the inviscid shock impingement location. The fact that peak heating rates are well above the fully turbulent level suggests that a similar flow topology was attained in these experiments with the transition to turbulence occurring prior to the inviscid shock impingement point.

Following previous flowfield studies by Schluein [180], for a fully turbulent incoming boundary layer, the interaction of the oblique shock with the boundary layer is likely to cause a separation zone upstream of the shock impingement point. For large wedge angles (i.e. greater than 10°), it is noted that whilst the skin friction decreases in the vicinity of the separation point, the heat flux increases. The increase in heat flux is present in these experimental heat transfer measurements (Fig. 6.3) and is indicative of the complex non-equilibrium behaviour in such turbulent interacting flows where the Reynolds analogy between momentum and heat transfer is not valid. Such an increase in the heat flux rate for separated flow regions has

also been observed in other studies of two-dimensional interactions [178]. The amplification of turbulence in the boundary layer and in the external flow due to the shock wave interaction, as well as the higher surface pressure and density due to the stronger separation shock (compared to similar interactions in purely laminar flows) are possible explanations for the observed increase in the surface heat transfer in the interaction region. From Fig. 6.3, a peak of $St \approx 0.0055$ is reached towards the end of the porous injector for the turbulent SWBLI. This is closely in line with previous investigations with shock impingement at Mach 5 turbulent flow by Schülein [180].

The peak heating rates for laminar, turbulent, and transitional shock impingement regions have been correlated by Hung and Barnett [177]. It was found that when $Re_L > 5 \cdot 10^5$ the boundary layer flow is sufficiently disturbed that SWBLI disturbance promotes transition. The expressions for transitional and turbulent flows are

$$\left[\frac{St}{St_0}\right]_{\max} = 0.468 \cdot (Re_L \cdot 10^{-6}) \cdot \left(\frac{p_3}{p_\infty}\right)^{1.13} \qquad \text{Transitional (6.5)}$$

$$\left[\frac{St}{St_0}\right]_{\max} = 0.13 \cdot \left(\frac{p_3}{p_\infty}\right)^{0.8} \qquad \text{Turbulent (6.6)}$$

where, for these experiments, $\left[\frac{St}{St_0}\right]_{\max} = 34.9$ for the transitional and 6.7 for the fully turbulent scenarios. As shown by Fig. 6.3, both values under-predict the experimentally measured peak heating. This has also been observed by Heffner et al. [181] and Holden and Sweet [45] but, nonetheless, the correlations are useful to benchmark the experimental data.

The following experimental results with the inclusion of transpiration cooling are discussed in terms of the boundary layer state downstream of shock impingement, i.e. transitional or turbulent. The experimental results are split into three sections. The first section details the case where the strong shock impinges onto a laminar boundary layer with nitrogen and helium injection, the second concerns the respective turbulent cases, and in the final section correlations are developed to predict the effectiveness

of transpiration cooling for turbulent and transitional shock interaction regions for system design purposes. The results are normalised either in relation to St_0, the Stanton number without shock impingement when $F = 0\%$ or $St_{0,s}$, the Stanton number with shock impingement when $F = 0\%$.

6.4.1 Transitional

Contour plots of the Stanton number ratio between the shocked and unshocked experimental data (St/St_0) are plotted in Fig 6.4. For the uncooled case, a rapid rise in heat transfer occurs across the injector peaking at over 50 times higher than the nominal laminar boundary layer without injection. Clear span-wise periodical variations are present on the porous injector surface. These have also been observed by Currao et al. [176] for similar transitional SWBLIs who attributed them to Görtler instability and the associated contra-rotating stream-wise vortices. Whilst these vortices likely do not cause transition themselves, they lead to other forms of instability that eventually result in transition [182]. With coolant injection, there are prominent 'cold' patches for the helium case downstream of impingement at approximately x = 195 mm. This may be attributed to non-uniformities in the coolant outflow for this porous injector [60]. These patches are not present for the nitrogen case likely due to the higher outflow velocity of helium for a given injected mass flux (due to its lower density) exacerbating local flow structures.

Figure 6.5 shows spanwise averaged (between y = -15 to 15 mm) heat transfer reduction curves based on either the uncooled case without shock impingement, St_0, or the uncooled case with shock impingement, $St_{0,s}$. The contours show a slightly asymmetric Stanton number distribution relative to the freestream, especially for the uncooled case. This is likely due to a slight misalignment of the shock generator relative to the flat plate whilst with the inclusion of cooling, the blockage effect of the coolant on the SWBLI smoothes out the asymmetry. From Fig 6.5a, it is clear that both nitrogen and helium injection have little effect on the overall stream-wise heat transfer profile but rather lower the surface heat flux over the entire injector. For the highest nitrogen injection, the value of St_s/St_0 is reduced to below

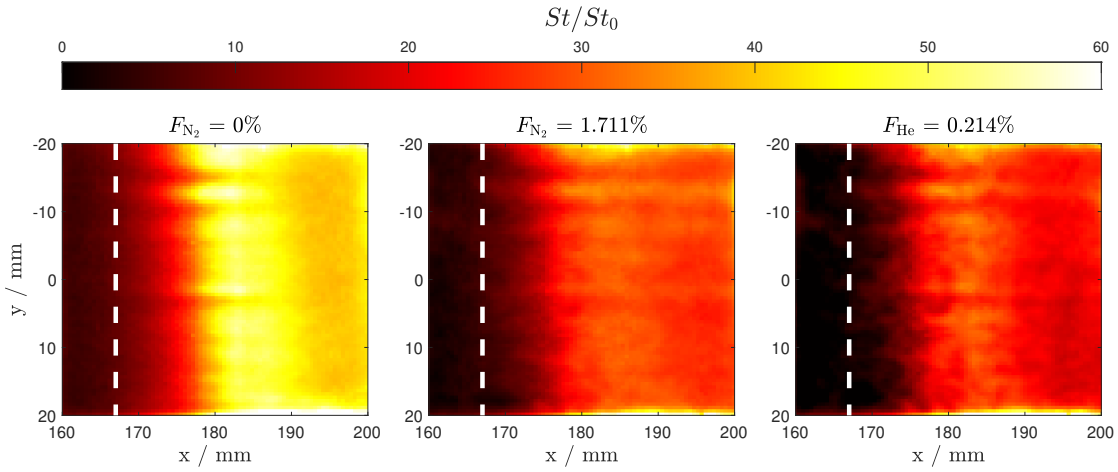

Figure 6.4: Contour plots of three transitional cases normalised against the nominal laminar case without shock impingement (St/St_0). The white dashed line indicates the inviscid shock impingement location.

30 which corresponds to over 60% less heat transfer compared to the unshocked case. Considering Fig. 6.5b, it is interesting to note the very steep reduction in heat transfer upstream of impingement. This is likely due to a combination of the lower surface pressures (leading to a higher local blowing ratio) upstream of the interaction region (denoted approximately by the inviscid shock line) and the laminar nature of the flow before the strong separation caused by the shock. Downstream of the interaction region ($x > 180\,\text{mm}$), the heat transfer reduction is very flat, characteristic of previous measurements of transpiration cooling in turbulent flows without SWBLI [60].

For helium injection, a blowing ratio of 0.214% essentially achieves a similar $St_s/St_{0,s}$ downstream of the shock interaction ($x > 180\,\text{mm}$) as nitrogen with 1.711%; i.e. only 12.5% the mass flux of helium is required to achieve the same cooling efficiency as nitrogen, highlighting the increased effectiveness of helium for these cases. A combination of the higher specific heat capacity of helium which provides the capacity to absorb roughly 5 times greater quantities of heat than nitrogen for the same mass flow rate, and the lower molecular weight likely contribute to the increased effectiveness. As helium's molecular weight is lower than that of nitrogen, a higher plenum pressure is required to achieve the same mass flux through the injector. This leads to two differences at the exit: helium

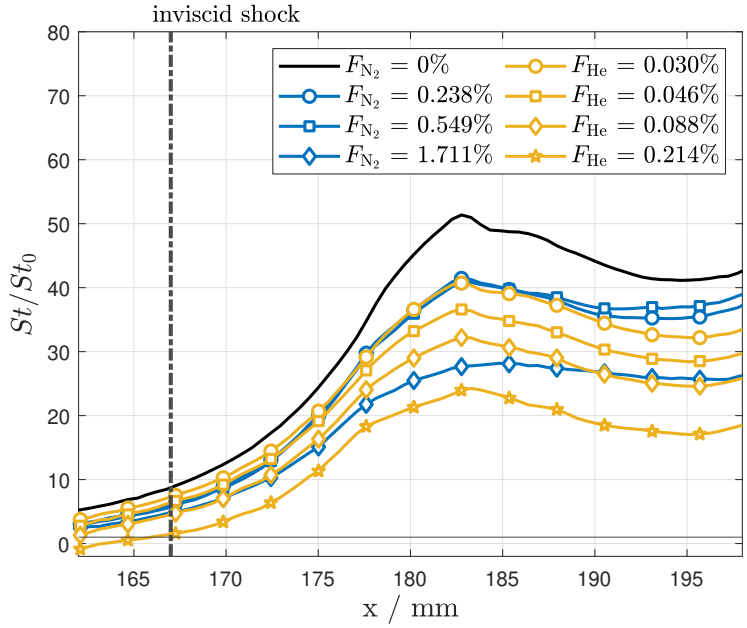

(a) In terms of the heat transfer reduction relative to the uncooled case without shock impingement, St/St_0.

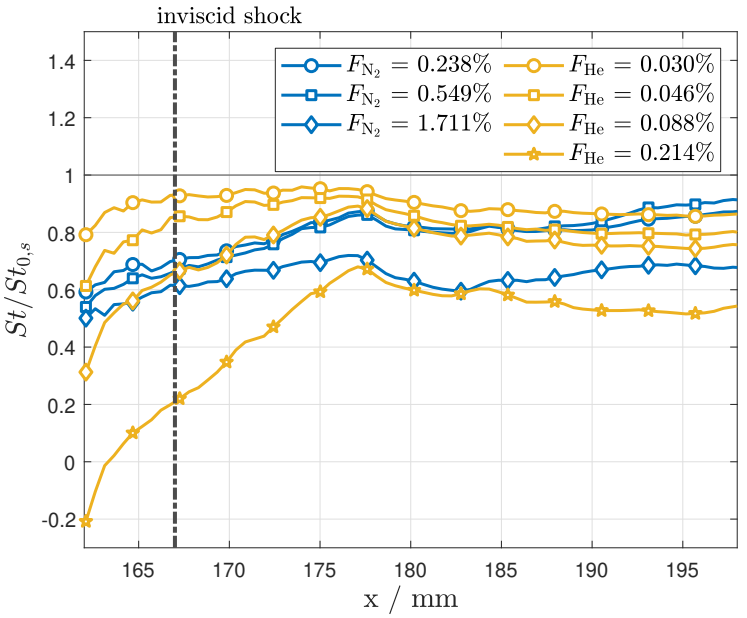

(b) In terms of the heat transfer reduction relative to the uncooled case with shock impingement, $St/St_{0,s}$.

Figure 6.5: Span-wise averaged Stanton number ratio between y = -15 to 15 mm for the transitional condition. The data is constrained to the range of x = 162-198 mm to disregard non-physical rises at the intersection between the injector and the cover plate.

exits at a higher velocity due to its lower density at a given edge pressure, p_e, and helium contain more gas particles than nitrogen since a higher plenum pressure

results in a higher mole number; i.e., a higher mole number leads to a larger volume of helium at the exit. In combination, these two effects result in seven times the higher volumetric flow rate of helium when its mass flow rate is matched with nitrogen. This likely thickens the boundary layer at the shock impingement location and results in a reduced wall temperature gradient.

For $F_{N_2} = 1.711\%$, a negative Stanton number is recorded at $x = 163\,\text{mm}$. For very high blowing ratios, where the boundary layer close to the wall is almost entirely comprised of coolant, a negative Stanton number may arise when the coolant gas layer is rapidly accelerated due to the shear stress of the external flow. This would lead to the coolant gas itself establishing a velocity profile akin to the external boundary layer which leads to a dissipation of thermal energy. Since the injected coolant gas starts at near-zero stream-wise velocity close to the wall and the coolant temperature is very near to the wall temperature (Table 6.3), the total temperature of the coolant layer is similar to the wall temperature. This means that the effective driving temperature of the wall heat transfer (generally represented by the recovery temperature) has to be lower than the wall temperature and therefore a negative heat flux (and therefore Stanton number) may occur. A similar phenomenon has been observed by Ifti et al. [106] for a transpiration cooling in a laminar hypersonic boundary layer and by Keller et al. [125] and Hombsch and Olivier [124] for slot injection in supersonic and hypersonic flows.

6.4.2 Turbulent

The turbulent cases manifest a markedly different profile from the transitional cases. Fig 6.6 shows three contour plots for the turbulent flow condition normalised against the nominal turbulent case without shock impingement. There is a sudden jump at $\approx 165\,\text{mm}$ for the uncooled case and then a shallower gradient until the end of the porous injector at $x = 200\,\text{mm}$. With coolant injection, a consistent 'smoothing' of the heat transfer profile in the stream-wise direction over the injector is observed with higher heat transfer upstream of the shock impingement location for the nitrogen and low helium cases. However, with sufficient injected mass flux,

such as for helium injection at $F = 0.110\%$, the heat transfer upstream also reduces to below the uncooled case. Once again, similar to the transitional cases, significant spatial non-uniformities are present in the helium case.

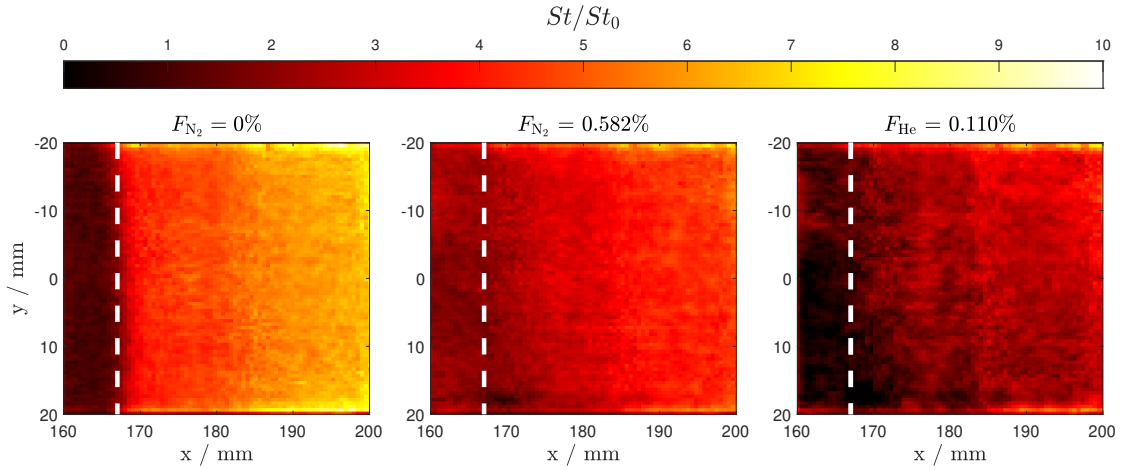

Figure 6.6: Contour plots of three turbulent cases normalised against the nominal turbulent case without shock impingement (St/St_0). The white dashed line indicates the inviscid shock impingement location.

From Fig. 6.7b, it is observed that on and upstream of the shock impingement location, the heat transfer enhancement is over double the nominal uncooled case. This effect has not been reported previously in literature though it may be due to the introduction of the subsonic coolant layer moving the separation bubble caused by the impinging shock further upstream compared to the uncooled case. Heat transfer rates are particularly strong in the vicinity of the point at which the separated flow re-attaches and an earlier reattachment point would shift the rapid change in heat transfer further upstream [183]. Further computational and experimental studies would be valuable to provide insight. Downstream of impingement, a very similar profile is present as the transitional cases discussed previously. This confirms that a fully turbulent region remains downstream of the interaction and the flat profile is similar to cases where transpiration is applied to turbulent flow without impingement. Once again helium is significantly more effective than nitrogen. A blowing ratio, F, of 0.582% of nitrogen is sufficient to reduce peak heat transfer to just under 70% of the uncooled case whilst only 0.110% of helium is sufficient to reduce it to under

50%. Helium is approximately 8 times more efficient for the same blowing ratio of nitrogen which is a similar ratio to the transitional cases described previously.

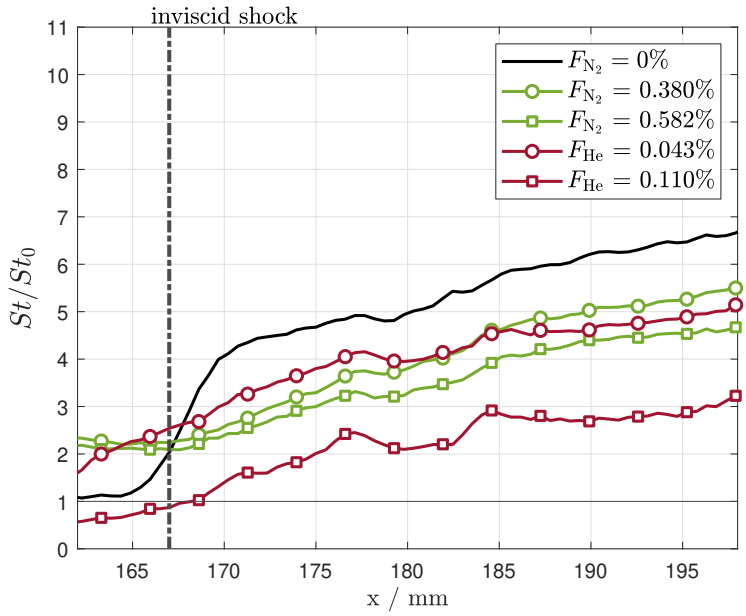

(a) In terms of the heat transfer reduction relative to the uncooled case without shock impingement, St/St_0.

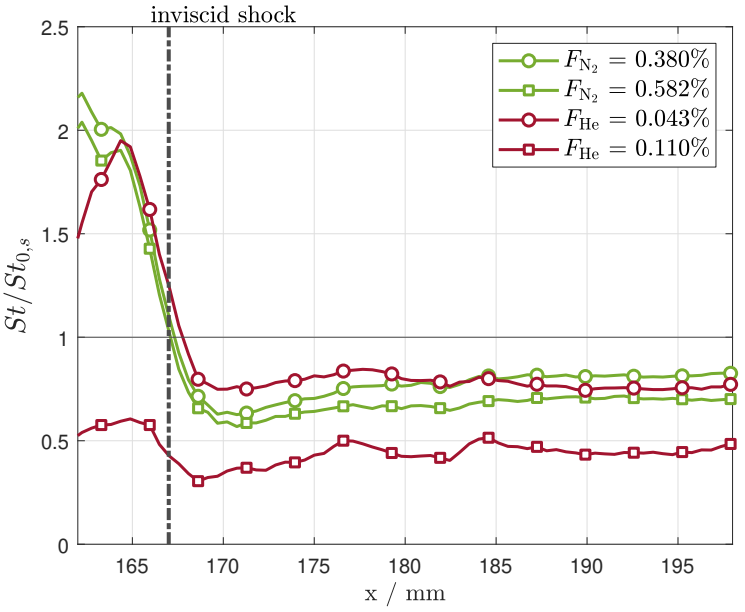

(b) In terms of the heat transfer reduction relative to the uncooled case with shock impingement, $St/St_{0,s}$.

Figure 6.7: Span-wise averaged Stanton number ratio (averaged between y = -15 to 15 mm) for the turbulent condition. The data is constrained to the range of x = 162-198 mm to disregard non-physical rises at the intersection between the injector and the cover plate.

6.4.3 Correlation

For system design purposes, it is useful to define the cooling requirements necessary to reduce the peak heat transfer downstream of the shock interaction region to acceptable levels. Whilst, a full range of blowing ratios that reduce the wall heat transfer to or below the upstream turbulent/laminar levels have not been tested in this experimental campaign, it is possible to correlate the experimental data concisely using a blowing parameter defined by the local inviscid conditions downstream of the re-compression shock (henceforth defined as the blowing parameter, $B_{h,s}$). This parameter has also been used by Holden and Sweet to correlate similar experimental data [45]. The blowing parameter is defined as

$$B_{h,s} = \frac{F_3}{St_3} = \frac{\dot{m}_f}{\rho_3 u_3} \cdot \frac{\rho_3 u_3 c_p (T_0 - T_w)}{\dot{q}_w} = \frac{\dot{m}_f c_p (T_0 - T_w)}{\dot{q}_w} \tag{6.7}$$

where St_3 is the Stanton number based on the boundary layer edge parameters downstream of the re-compression shock. These are defined by the subscript '3' from Fig 6.1. Based on this, Holden and Sweet correlated the heat transfer reduction downstream of the shock interaction region in turbulent flows [45] with the following expression

$$\frac{St}{St_{0,s}} = 1 - 0.92 \cdot \left[1 - \exp\left(- \frac{\left(\frac{\mathrm{M}_\infty}{\mathrm{M}_\mathrm{f}} \right) \cdot B_{h,s}}{4} \right) \right] \tag{6.8}$$

where $(\frac{\mathrm{M}_\infty}{\mathrm{M}_\mathrm{f}})$ is a molecular weight correction to account for the differing molecular weights of helium and nitrogen. This correlation was based on fitting a large number of test points with 5°, 7.5° and 10° shock generator angles at Mach 6 and 8 in which transpiration cooling was introduced with both nitrogen and helium gases. The molecular weight correction may be understood physically as akin to accounting for the differences in the volume of gas that is introduced. If it is assumed that on the porous injector, there is at least some coverage of coolant at all locations which are likely to be at the same temperature as the wall, then the major difference between injecting a heavier and lighter gas is the effect on the oncoming boundary

layer. If the gas is lighter, it will take up more volume for a given mass flow rate and thus displace the boundary layer by a greater factor.

To correlate the experimental data, Fig. 6.7 shows span-wise and stream-wise averaged (between y = -15 to 15 mm and x = 185-195 mm) Stanton number ratio ($St/St_{0,s}$) against the blowing parameter. From Fig. 6.8a, there is a clear trend of increased cooling with higher blowing parameter with helium performing, as noted above, significantly better than nitrogen. A blowing parameter of approximately

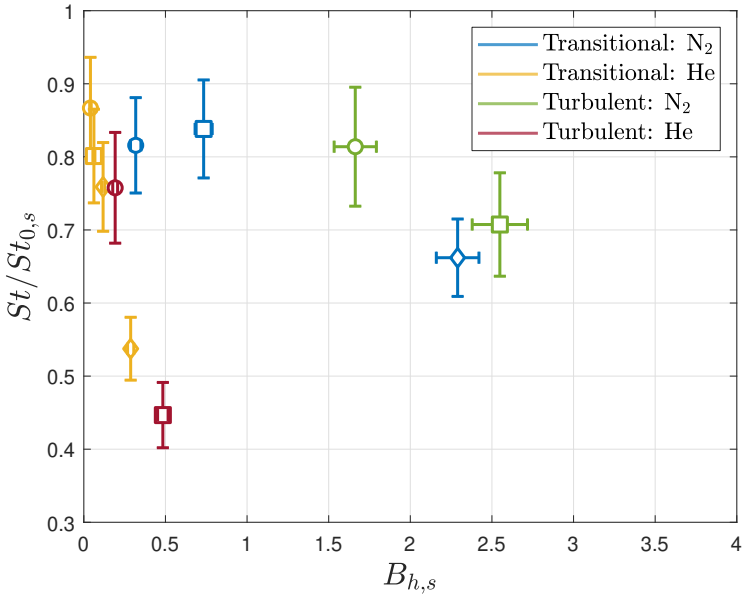

(a) No correction

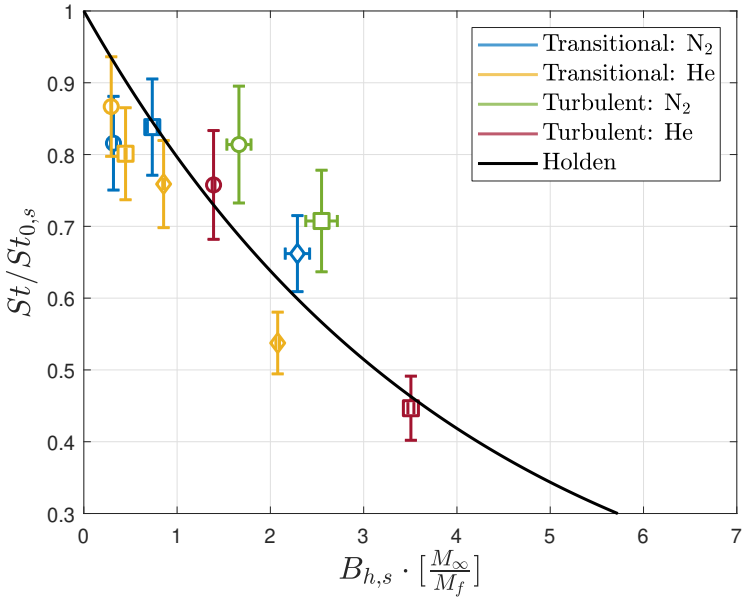

(b) With (M_∞/M_f) correction

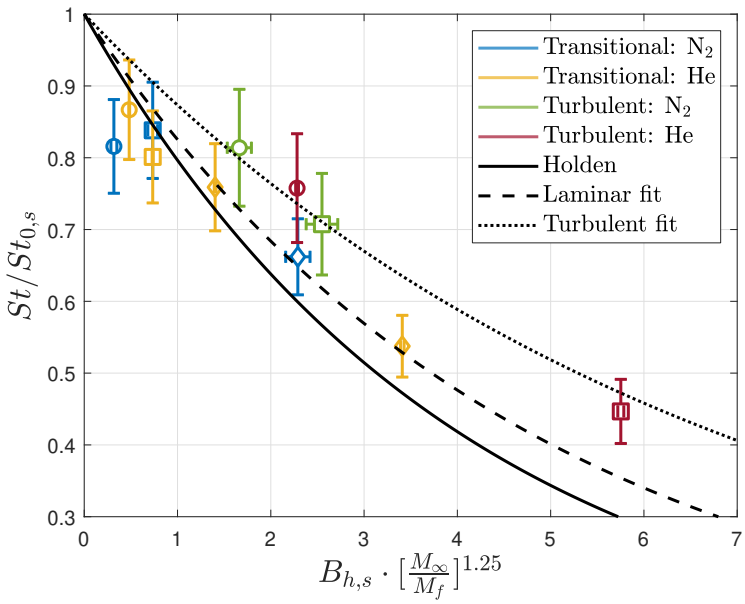

(c) With $(M_\infty/M_f)^{1.25}$ correction. The transional and turbulent fits refer to Eqs (6.9) and (6.10).

Figure 6.8: Span-wise and stream-wise averaged (between y = -15 to 15 mm and x = 185-195 mm) Stanton number ratio ($St/St_{0,s}$) for transitional and turbulent case. The symbols correspond to different blowing rates from Fig. 6.5 and 6.7 and the error bars to the uncertainty values presented in the Appendix.

0.4 leads to a heat reduction of 0.45 for helium as opposed to 0.85 for nitrogen. Both the transitional and turbulent cases show similar levels suggesting that as the shock interacts with the laminar boundary, there is a very rapid transition of the boundary layer to turbulence and therefore the region downstream of the shock impingement is fully turbulent. First of all, the experimental data from these tests may be compared directly to Holden's correlation, Eq. (6.8), as displayed in Fig 6.8b. There is reasonable agreement with the experimental measurements with the turbulent cases consistently under-predicting the level whilst transitional displays the opposite. The scatter in the points may be attributed either to the chosen molecular weight correction or the decision to compare both the transitional and turbulent cases against the same curve.

If the molecular weight correction is modified to include an exponent of 1.25, correlations with a better fit to the experimental data may be developed. Treating the transitional and turbulent cases separately, adjusted forms of Eq. (6.8) may

be fitted against the experimental results (Fig. 6.8c)

$$\frac{St}{St_{0,s}} = 1 - 0.92 \cdot \left[1 - \exp\left(-\frac{\left(\frac{\mathrm{M}_\infty}{\mathrm{M}_\mathrm{f}}\right)^{1.25} \cdot B_{h,s}}{4.75}\right)\right] \qquad \text{Transitional} \quad (6.9)$$

$$\frac{St}{St_{0,s}} = 1 - 0.92 \cdot \left[1 - \exp\left(-\frac{\left(\frac{\mathrm{M}_\infty}{\mathrm{M}_\mathrm{f}}\right)^{1.25} \cdot B_{h,s}}{6.75}\right)\right] \qquad \text{Turbulent} \quad (6.10)$$

where the factor 4 in the denominator of the exponential has been changed to 4.75 and 6.75 respectively for the transitional and turbulent cases. It is difficult to isolate the exact reason for the differences between the Holden and Sweet correlation and the two conditions tested in this study. It was noted by Holden that the experimental points for strong shock impingement with a 10° shock generator did not correlate as well as for lower shock strengths; the current experiment exclusively uses a 10° shock generator. From Fig. 6.5b, it appears that for the nitrogen cases in particular, the downstream heat transfer reduction continues to rise slightly from 185-200 mm. It is possible that in the 30 mm of length between the shock impingement location and the end of the injector, the flow field has not reached a fully turbulent condition. In addition, the differences in injector geometry and flow conditions may all have an impact on the cooling efficiency which would need to be explored either numerically or with a more detailed experimental parameter study. The choice of molecular weight correction, $(\frac{\mathrm{M}_\infty}{\mathrm{M}_\mathrm{f}})^{1.25}$, lies in between the correction factors for laminar, $(\frac{\mathrm{M}_\infty}{\mathrm{M}_\mathrm{f}})^{0.4}$, and turbulent, $(\frac{\mathrm{M}_\infty}{\mathrm{M}_\mathrm{f}})^{1.4}$, flows from prior experiments with the same porous injector and geometry without shock impingement [60]. Clearly, the thermal efficiency with dissimilar gas injection is tightly coupled to the nature of the external flow field. For example, whether it's laminar, turbulent, shock disturbed, etc. all require a different molecular weight correction. A complex, physics-based model is likely required to universally account for dissimilar gas injection for a broader range of external flow fields and injected gases.

Overall, it is encouraging that for both the fully turbulent and transitional cases, the peak heat fluxes can be reduced significantly with relatively small injection

mass fluxes of nitrogen or helium. helium in particular proves to be more effective than previously suggested by Holden and Sweet. The empirical fits in Eqs. (6.9) and (6.10) may be used as a basis for simplified correlations to predict the peak heating for a given blowing rate for initial systems design.

Whilst these experiments have shown the potential benefits of applying transpiration cooling to cool regions of SWBLI, in a flight scenario instead of the heat flux reaching a peak with a cold wall, the wall temperature will rise to a steady level. At high temperatures, a further challenge in cooling these regions is viscosity-driven blockage where due to the higher viscosity at high temperatures, high plenum pressures are required to deliver a given mass flux compared to for a cold wall [46]. In fact, if the surface temperature is in the order of 2300 K, the viscosity increases by approximately four times for nitrogen injection, and therefore the injected mass flux reduces by the same factor assuming the external pressure is the same. This issue coupled with the high surface pressures at the shock-interaction region adds to the overall challenge of transpiration cooling SWBLI regions.

6.5 Conclusions

Cooling regions of peak heating caused by SWBLIs remain a topic of active research to this day. However, there is a lack of experimental data in the open literature exploring the effectiveness of transpiration cooling in mitigating heat transfer in regions of SWBLI, especially in the case of a transitional SWBLI which often produces the highest heat fluxes. In this paper, transpiration-cooling experiments have been conducted in the Oxford High Density Tunnel (HDT) to measure the surface heat transfer of a transpiration-cooled porous injector subjected to a strong oblique shock from a 10° shock generator.

For the laminar freestream condition, due to the strength of the incident shock, a transitional SWBLI region was formed with peak heating over 50 times greater than the nominal laminar level. The introduction of coolant injection led to a reduction in surface heat transfer for all cases. Relatively low blowing rates were sufficient to greatly reduce the heat transfer downstream of shock interaction with a blowing

rate of 1.711% of nitrogen and 0.214% sufficient to reduce levels to 55-60% of the maximum in the transitional case. helium was significantly more effective than nitrogen with only 12.5% of the injected mass flux of helium sufficient to achieve a comparable heat flux reduction to nitrogen. The experimental data are correlated and both the transitional and turbulent cases display a similar trend. Two empirical fits have been proposed for the presented experimental data which can be valuable for aiding initial systems-level design for a transpiration-cooled system. In addition, the presented high-resolution, 2D heat transfer data can be useful validation tools to compare against high-fidelity CFD simulations in the future.

6.6 Uncertainty Analysis

The main independent quantities reported in this paper are the Stanton number, the blowing ratio, the blowing parameter and the unit Reynolds number. To find the total uncertainty, the Taylor Series Method by Coleman and Steele [167] was employed where, for a function $r = r(X_1, X_2, ...X_n)$, the uncertainties in the individual measurements are assumed to be uncorrelated. Thereafter, gradients $\frac{\partial r}{\partial X_i}$ are calculated numerically by perturbing the variables X_i in the data reduction processing steps. First of all, the unit Reynolds number is calculated according to the following equation

$$Re_u = \frac{\rho_e u_e}{\mu_e} \tag{6.11}$$

where u_e and ρ_e are a function of the Mach number, M, total pressure, P_0, and total temperature, T_0. The Stanton number is calculated according to Eq X where the heat flux at the wall, $\dot{q}_w$, is a function of the material thermal effusivity, $\sqrt{\rho c_p k}$, and the temperature, T_w, obtained through infrared camera measurements. The blowing ratio is calculated using Eq. (6.3), which depends on T_e and ρ_e as well as the injected mass flux, $\rho_f u_f$. This is calculated assuming a linear pressure gradient through the porous injector and a constant solid temperature by employing Eq. (6.2). The uncertainties in the Darcy and Forchheimer coefficients were determined using the same monte carlo simulation procedure detailed in Ref. [65].

The wall temperature, T_w is determined via infrared thermography and a key figure of merit used to qualify the temperature output of infrared cameras is the noise equivalent differential temperature (NETD) [135]. In this work, a factory calibration determined that the NETD was below 40 mK over the observed range of temperatures. This is significantly smaller than the expected temperature rise of the injector of 0.5-10 K. In addition to the NETD, there are additional sources of error from the infrared calibration system. This includes the uncertainties in the measurement of the reflected temperature when conducting the multipoint calibration, T_{ref}, the error in the temperature measurement of the CI-Systems black body calibrator, $T_{\text{calibrator}}$, and the emissivity of the material, ε.

Table 6.4 details the different uncertainty contributions to the overall uncertainty in the measurement of Reynolds number, Stanton number, blowing ratio, and blowing parameter for the case of an injected mass flux of $0.81\,\text{kg}\,\text{s}^{-1}\,\text{m}^{-2}$. The main drivers of uncertainty, especially for the Stanton number and blowing parameter are the total temperature, T_0, and the material thermal effusivity. The uncertainty in the blowing parameter is 11.4% where the main source of uncertainty is the total temperature (60%). In future experiments, the uncertainty may be reduced with a tighter measurement of total temperature and higher accuracy measurements of material thermophysical properties.

Table 6.4: Uncertainty contributions and overall uncertainties in unit Reynolds number, uncooled Stanton number, blowing ratio and blowing parameter for the laminar freestream condition with nitrogen injection at $0.81\,\mathrm{kg\,s^{-1}\,m^{-2}}$ and a METAPOR CE170 injector.

Parameter	Baseline value	Absolute uncertainty	Relative uncertainty
NETD / K	0.04	±0.02	50%
T_{ref} / K	296	±2	<1%
$T_{\mathrm{calibrator}}$ / K	296	±0.1	<1%
ε	0.95	±0.04	4.2%
$(\sqrt{\rho c_p k})$ / $\mathrm{Jm^{-2}K^{-1}s^{-0.5}}$	1565	±78.25	5%
P_0 / kPa	1204	±24.08	2%
T_0 / K	420	±10	2.4%
M	6.1	±0.1	1.6%
T_{pl} / K	293	±2	<1%
p_{pl} / K	$3.89\cdot10^{5}$	$\pm1{\cdot}10^{4}$	2.5%
K_D / $\mathrm{m^2}$	2.52 / m $\cdot10^{-13}$	$\pm1.74\cdot10^{-14}$	6.9%
K_F / m	1.03 / $\mathrm{m^2}$ $\cdot10^{-8}$	$\pm1.06\cdot10^{-9}$	10.3%
Re_u / m^{-1}	$13.3\cdot10^{6}$	$6.26\cdot10^{5}$	4.7%
St_0	$5\cdot10^{-3}$	$6.62\cdot10^{-4}$	13.2%
F	$1.72\cdot10^{-2}$	$1.24\cdot10^{-3}$	7.2%
$B_{h,s}$	2.3	0.27	11.4%

Chapter 7

Conclusions and Future Work

This thesis aimed to investigate the application of transpiration cooling to reduce the surface heat transfer on hypersonic vehicles. In this chapter, the key findings are presented from a combined systems-level and experimental approach. The original research contributions are highlighted, and their impact on the current state-of-the-art models is discussed. Finally, suggestions are made for future work.

First of all, a systems-level study was conducted to assess the suitability of transpiration cooling on a generic flight vehicle. A 15° half-angle 2D wing leading edge with a nose radius of 0.1 m was chosen as the geometry of interest with the Space Shuttle re-entry trajectory. The PIRATE numerical code was employed to perform these calculations. The model was extended to incorporate the effects of 2D lateral conduction and a substructure to represent an actual flight vehicle better. It is shown that transpiration cooling reduces outer wall and substructure temperatures throughout the re-entry trajectory. By applying a moderate level of coolant injection ($F = 0.04$ of helium), the maximum temperature of the substructure reduces from over 700 K to 450 K. Furthermore, transpiration cooling can reduce the thermal stresses at the substructure, with a 65% reduction in the temperature gradient of the substructure surface for moderate coolant injection. This is a key result as choosing appropriate materials for the substructure is a major factor for a given flight vehicle and mission trajectory.

Whilst the systems-level study relied on simple, analytical correlations to predict the heat transfer reduction due to transpiration cooling, vehicle designers

require detailed, local heat transfer information on and in the vicinity of the porous injector. This is required for more complex flowfields or if transpiration cooling is utilised as a localised cooling solution. To enable these measurements, a novel heat transfer measurement method is developed to measure the surface heat transfer of transpiration-cooled porous injectors in short-duration hypersonic facilities. Traditional surface heat flux methods such as discrete thin film gauges or thermocouples are not suitable for modern micro-porous materials with pore sizes of the order of $10\,\mu\,\mathrm{m}$. Discrete gauges would impede or otherwise disturb the outflow from the porous material. High-speed infrared thermography was employed to measure the surface temperature of the porous material. A bespoke calibration system was developed, and the method was validated experimentally in the Oxford High-Density Tunnel on a flat-faced hemispherical probe at a single Mach 7 freestream condition with nitrogen, air, argon, krypton and helium injection gases and mass flow rates ranging from 0.01-0.235 $\mathrm{kg\,s^{-1}\,m^{-2}}$. It was found that the Stanton number reduction matched to within 10% of both CFD results and correlations, verifying this measurement technique and providing a novel experimental dataset to the open literature.

After developing the infrared measurement technique, this was applied to two different scenarios that are of interest to vehicle designers. The first scenario concerns the need for detailed local heat transfer information on and in the vicinity of the porous injector if this technique is applied for local cooling. Limited spatially resolved experimental studies exist, particularly in hypersonic flows. Experiments were conducted in the Oxford High-Density Tunnel at Mach 6.1 in both laminar and turbulent regimes. Spatially resolved 2D surface heat transfer measurements were acquired by imaging directly on and downstream of two very different micro-porous transpiration-cooled injectors (METAPOR CE170 and Zirconia) using high-speed infrared thermography. It was found that a modification to existing relations from film theory successfully correlates the stream-wise heat transfer distribution on the injector for different blowing rates of nitrogen and helium injection. For the first time, a model that accounts for a finite length injector that does not begin

at a model's leading edge or stagnation point has been developed. A key result is that helium performs much better than reported in previous experiments. The downstream thermal effectiveness was also characterised for turbulent flows. These datasets add important spatial two-dimensional information on the effectiveness of transpiration cooling to the open literature and characterise the performance of a UHTC-like porous injector for the first time (Zirconia).

The second of the two scenarios is applying transpiration cooling to mitigate the peak heat fluxes caused by shock-wave boundary layer interactions. In this work, experiments were once again conducted in the Oxford High-Density Tunnel at Mach 6.1 in both laminar and turbulent regimes where a 10° shock generator impinged a strong oblique shock wave onto a transpiration-cooled injector. For the laminar condition, due to the strength of the incident shock, a laminar-transitional shock-wave boundary-layer interaction region was formed with peak heating over 50 times greater than the nominal laminar level. Both nitrogen and helium were used as coolants, and relatively low injection rates were sufficient to greatly reduce the heat transfer downstream of shock interaction for both regimes. The experimental data are correlated, and both fully turbulent and laminar-transitional cases display a similar trend, with helium, in particular, performing better than suggested by existing studies. Thus, these experiments have established that transpiration cooling is an excellent cooling system to mitigate the high heat fluxes for these regimes and have contributed a clean dataset that may be used for future CFD validation studies.

A key output from the experimental studies in Chapters 5 and 6 are relatively simple correlations that may be used by vehicle designers to make an initial assessment of the effectiveness of transpiration cooling for a given flight scenario. Table 7.1 details the various correlations and the inputs required for each of them. A handful of parameters, many of which can be readily estimated are sufficient to apply these correlations. Whilst the correlations may be applied to any freestream condition, ultimately they have been devised based on a limited set of experimental data at the Mach 6 condition. The robustness of these correlations can only be determined with further experimental and/or numerical studies

A key outcome of these correlations is the startling effectiveness of helium compared to nitrogen as the cooling gas - in some scenarios, helium shows 16 times more cooling effectiveness than nitrogen for the same injected mass flux. However, such advantages of helium must be balanced against managing the larger volume of helium at a given pressure. For most flight vehicles, there is a premium of available space and a requirement to either pressure helium to very high pressures or store it in large tanks makes the usage of this gas less attractive.

There are several avenues for future work. First of all, the limited laminar and turbulent correlations from the flat plate experiments proposed in Chapter 6 can be extended to apply to a greater range of flow conditions. This should be pursued mainly from a CFD and analytical viewpoint with judicious experimental testing to verify key points. Furthermore, an extension of the experimental dataset to chemically reacting flows would be beneficial. Real gas effects become important at velocities above 3-4 $\mathrm{km\,s^{-1}}$ and an extension of the proposed correlations to those regimes will be important for broader applicability. This is particularly important for shock-interaction regions, which are highly sensitive to real gas effects. From a systems-level standpoint, the clear next step is applying these techniques to complex, realistic geometries. An obvious candidate would be a wing leading edge design, perhaps even replicating the shock-wave interaction region experienced by the Skylon vehicle as described in Fig. 1.4 and assessing the effectiveness of transpiration cooling in mitigating the expected high surface temperatures in those regions. Understanding the effectiveness of different leading-edge designs and coolant gases in a holistic fashion; including the overall mass budget for a given mission, the sizing of the gas injection system and implications on thermal stress/wear will be important in bringing a transpiration-cooled system closer to flight readiness.

Ultimately, this thesis has assessed the performance of transpiration cooling if applied to a wing leading edge, revealing additional benefits (cooling the substructure and reducing thermal stresses) which have not been elaborated on in previous works. Furthermore, for the first time, it has provided fully two-dimensional heat transfer information on the surface of a transpiration-cooled porous injector in simple and

complex hypersonic flowfields, including developing simple correlations. Hopefully, all of this will enable future vehicle designers to better qualify and design a working transpiration-cooled system for real vehicles.

Table 7.1: An overview of the heat transfer correlations developed in this work.

Scenario		Inputs	Correlation	Output
Flat plate, on the injector	Laminar	$\dot{q}_0$, T_r, T_w, c_p, $\dot{m}_f$, x, x_s, M_e, M_f	$\dfrac{3B_h\left(\frac{x-x_s}{x}\right)^{0.5}\left(\frac{\mathrm{M}_e}{\mathrm{M}_f}\right)^{0.4}}{\exp\left[3B_h\left(\frac{x-x_s}{x}\right)^{0.5}\left(\frac{\mathrm{M}_e}{\mathrm{M}_f}\right)^{0.4}\right]-1}$	$\frac{St/St_0}{(St/St_0)_{\max}}$
	Turbulent		$\dfrac{3B_h\left(\frac{x-x_s}{x}\right)^{0.8}\left(\frac{\mathrm{M}_e}{\mathrm{M}_f}\right)^{1.4}}{\exp\left[3B_h\left(\frac{x-x_s}{x}\right)^{0.8}\left(\frac{\mathrm{M}_e}{\mathrm{M}_f}\right)^{1.4}\right]-1}$	
Flat plate, downstream of injector	Turbulent	u_e, ρ_e, μ_e, T_e, T_0, T_w, x', $\dot{m}_f$, s	$\left[1+0.15\left[\left(\frac{C^*}{Re_u}\right)^{0.2}\left(\frac{T_e}{T^*}\right)^{0.6}\frac{x'^{0.8}}{Fs}-4.5\right]\right]^{-0.8}$	$1-St/St_0$
Flat plate, shock impingement, on the injector	Transitional	$\dot{q}_0$, T_0, T_w, c_p, $\dot{m}_f$, M_e, M_f	$\dfrac{1-0.92\left[1-\exp\left(-\frac{\left(\mathrm{M}_\infty/\mathrm{M}_\mathrm{f}\right)^{1.25}B_{h,s}}{4.75}\right)\right]}{1-0.92\left[1-\exp\left(-\frac{\left(\mathrm{M}_\infty/\mathrm{M}_\mathrm{f}\right)^{1.25}B_{h,s}}{6.45}\right)\right]}$	$St/St_{0,s}$
	Turbulent			

Appendices

Appendix A

PIRATE Model

The ***P**orous **I**mpulse **R**esponse **A**nalysis for **T**ranspiration cooling **E**valuation* (PIRATE) numerical code calculates the transient temperature response of a one dimensional porous transpiration cooled material that is subject to aerodynamic surface heating. Figure A.1 presents an outline of the code. A majority of the model of this study has been based on the work of Böhrk et al. who developed a heat balance for porous materials and the associated external flow boundary layer (HEATS) [38]. In contrast to the work of Böhrk et al., the current model does not employ finite differences to solve the heat transfer in the material, but uses an approach based on impulse response convolution. The incentive for the layout of the code, i.e. mostly analytical or low-cost numerical schemes, is to apply the correlations from the large body of literature to assess the viability of transpiration cooling for a wide parameter space of hypersonic flight conditions. This requires a large amount of calculations to be performed and hence necessitates a quick convergence time for the numerical simulation.

The details of the aerodynamic model used in PIRATE as well as the local cooling and film models are detailed in the full paper [86].

A.1 Temperature in the Porous Material

The temperature of the solid and fluid phases within the vehicle wall is calculated, based on a given coolant mass flow rate, porous wall thickness and thermophysical properties of the solid and fluid phases. A semi-analytical approach is used utilising

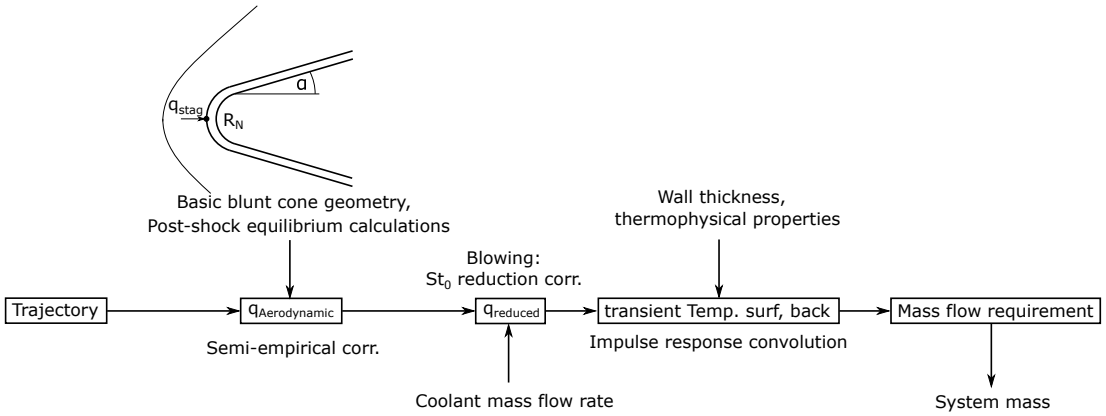

Figure A.1: Flow chart of the computational approach.

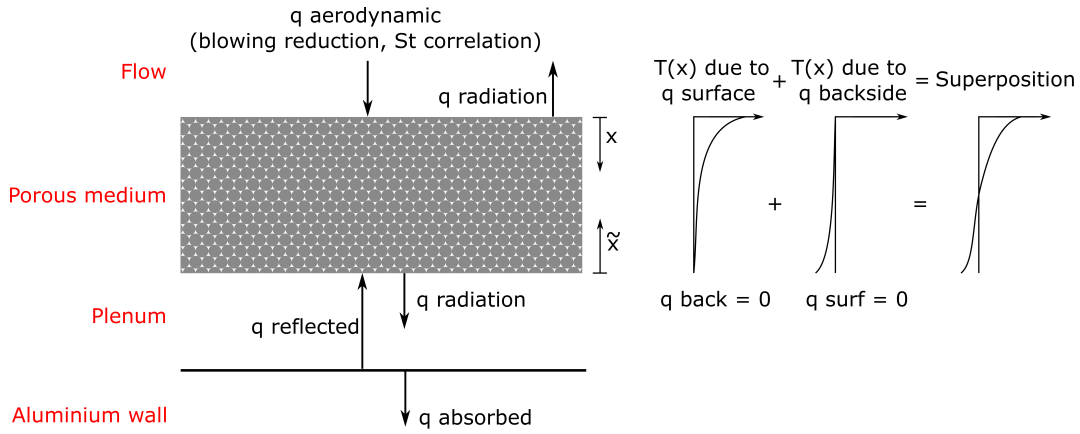

Figure A.2: Schematic of the one-dimensional thermal model.

impulse or step responses of the porous material. The only temperatures calculated in the procedure are of the porous material surface and backside. The procedure does account for the entire temperature field within the material, but, in contrast to a finite element approach, does not calculate it at every point. In essence, this is what provides a much faster computation time. The thermal model used is one-dimensional and is therefore only suitable for cases where the lateral heat flux is negligible when compared to the normal heat transfer, i. e. $\dot{q}_{\text{normal}} >> \dot{q}_{\text{lateral}}$ (the model was subsequently updated to account for 2D conduction as detailed in Chapter 3). In the following, the boundary conditions of the thermal model and the calculation methodology are presented. A schematic overview of the wall model is shown in Fig. A.2.

The net surface heat flux is calculated based on the cooled aerodynamic heat

flux and also accounts for radiative cooling via

$$\dot{q}_{\text{surface}} = \dot{q}_{\text{reduced}} - \sigma \varepsilon_s T^4_{\text{surface}} \tag{A.1}$$

with the Stefan-Boltzmann constant, σ, and the surface emissivity, ε_s. It is assumed that an aluminium plenum is located behind the porous material. Between the plenum surface and the backside of the porous wall, heat transfer in form of radiation can occur. This leads to a negative net backside heat flux that is calculated from the balance of the radiative heat exchange terms,

$$\dot{q}_{\text{backside}} = -\frac{\sigma \left(T^4_{\text{backside}} - T^4_{\text{pl}} \right)}{\frac{1}{\varepsilon_s} + \frac{1}{\varepsilon_{\text{pl}}} - 1} \tag{A.2}$$

with the aluminium plenum emissivity $\varepsilon_{\text{pl}} = 0.07$ and the respective temperature T_{pl} which is assumed to be at ambient conditions. Through the variation of the plenum temperature and reflectivity, different rear boundary conditions can be set, e. g. a fully adiabatic backside for $\varepsilon_{\text{pl}} = 0$. In the following, the derivation of the step and impulse responses of porous media are presented. Thereafter, their application in the current model is discussed.

Derivation of Step and Impulse Responses

The governing equations are the energy equations for solid and fluid phase are [76]

$$(1-\phi)\,\rho_s c_{p,s} \frac{\partial T_s}{\partial t} = k_s\,(1-\phi)\,\frac{\partial^2 T_s}{\partial x^2} + h_v\,(T_f - T_s) \tag{A.3}$$

and

$$\phi \rho_f c_{p,f} \frac{\partial T_f}{\partial t} = \phi \rho_f c_{p,f} \frac{v_f}{\phi} \frac{\partial T_f}{\partial x} + h_v\,(T_s - T_f)\,, \tag{A.4}$$

with (s) denoting the solid phase, (f) denoting the fluid phase, the thermal conductivity, k, the porosity, ϕ, the volumetric heat transfer coefficient, h_v, the time, t, and the location, x, measured from the surface. Note that the convention used in these equations is a temperature difference to the initial starting temperature,

T_{start}. The equations are solved for the boundary conditions of a constant fluid temperature at the plenum side with material thickness, L,

$$x = L, \qquad T_f = 0, \tag{A.5}$$

an adiabatic backside

$$x = L, \qquad \frac{\partial T_s}{\partial x} = 0, \tag{A.6}$$

and a unit surface heat flux

$$x = 0, \qquad \dot{q} = -\left(1-\phi\right) k_s \frac{\partial T_s}{\partial x} = 1\,\mathrm{Wm}^{-2}. \tag{A.7}$$

for steady state calculations or a Dirac impulse

$$x = 0, \qquad \dot{q}(t) = -\left(1-\phi\right) k_s \frac{\partial T_s(t)}{\partial x} = \delta(t=0), \quad \text{where} \quad \int_0^\infty \dot{q}(t)\mathrm{d}t = 1\,\mathrm{Jm}^{-2} \tag{A.8}$$

for transient calculations.

In the case of a steady state, i. e. a time derivative of zero in Eqs. (A.3) and (A.4), the employed approach is similar to the work of Schweikert et al. [82]. The calculation results in the steady state temperature (i. e. the step response at a time of infinity) for a continuous unit surface heat flux of

$$H_{s,\,\text{steady}} = \sum_{i=1}^{3} C_i \exp\left(\lambda_i x\right) \tag{A.9}$$

for the solid phase and

$$H_{f,\,\text{steady}} = \sum_{i=1}^{3} C_i \left(1 - \lambda_i^2 \frac{k_s(1-\phi)}{h_v}\right) \exp\left(\lambda_i x\right) \tag{A.10}$$

for the fluid phase with the Eigenvalues

$$\lambda_{1,2} = \frac{h_v}{2\rho_f c_{p,f} v_f} \pm \sqrt{\left(\frac{h_v}{2\rho_f c_{p,f} v_f}\right)^2 + \frac{h_v}{k_s\left(1-\phi\right)}}, \text{ and } \lambda_3 = 0. \tag{A.11}$$

The coefficients C_i are obtained from solving the linear system of equations

$$\begin{pmatrix} B_1\exp(\lambda_1 L) & B_2\exp(\lambda_2 L) & 1 \\ \lambda_1\exp(\lambda_1 L) & \lambda_2\exp(\lambda_2 L) & 1 \\ \lambda_1 & \lambda_2 & 1 \end{pmatrix} \cdot \begin{pmatrix} C_1 \\ C_2 \\ C_3 \end{pmatrix} = \begin{pmatrix} 0 \\ 0 \\ \frac{-1}{k_s(1-\phi)} \end{pmatrix} \tag{A.12}$$

with

$$B_{1,2} = 1 - \lambda_{1,2}^2 \frac{k_s(1-\phi)}{h_v}. \tag{A.13}$$

Equations (A.12) and (A.13) are a representation of the boundary conditions (A.5)-(A.7) in the Laplace space.

For transient calculations, impulse responses of both solid and fluid phases are required. They are calculated analytically in the Laplace-space (variable $\tilde{s}$) after transforming the time domain (variable t) of Eqs. (A.3) and (A.4). The solid impulse response, i. e. the temperature evolution after the exposure to a unit Dirac impulse of surface heat flux, is determined to be

$$H_{s,\,\mathrm{trans}} = \sum_{i=1}^{3} C_i \exp(\lambda_i x) \tag{A.14}$$

and the fluid impulse response is calculated by

$$H_{f,\,\mathrm{trans}} = \sum_{i=1}^{3} C_i \left(\frac{\tilde{s}(1-\phi)\rho_s c_{p,s}}{h_v} + \frac{k_s(1-\phi)}{h_v}\lambda_i^2 \right) \exp(\lambda_i x). \tag{A.15}$$

The eigenvalues, λ_i, are calculated by solving the characteristic equation

$$A_3\lambda_{1-3}^3 + A_2\lambda_{1-3}^2 + A_1\lambda_{1-3} + A_0 = 0. \tag{A.16}$$

with the coefficients

$$A_0 = \frac{h_v}{(1-\phi)\rho_s c_{p,s}} \frac{h_v}{\phi\rho_f c_{p,f}} - \left(\tilde{s} + \frac{h_v}{(1-\phi)\rho_s c_{p,s}} \right) \left(\tilde{s} + \frac{h_v}{\phi\rho_f c_{p,f}} \right), \tag{A.17}$$

$$A_1 = \frac{v_f}{\phi} \left(\tilde{s} + \frac{h_v}{(1-\phi)\rho_s c_{p,s}} \right), \tag{A.18}$$

$$A_2 = \frac{k_s}{\rho_s c_{p,s}} \left(\tilde{s} + \frac{h_v}{\phi \rho_f c_{p,f}} \right), \tag{A.19}$$

$$A_3 = -\frac{v_f}{\phi} \frac{k_s}{\rho_s c_{p,s}}. \tag{A.20}$$

The coefficients C_i are again a function of the boundary conditions (A.5), (A.6) and (A.8) in the Laplace space and are determined from solving the linear system of equations

$$\begin{pmatrix} B_1 \exp(\lambda_1 L) & B_2 \exp(\lambda_2 L) & B_3 \exp(\lambda_3 L) \\ \lambda_1 \exp(\lambda_1 L) & \lambda_2 \exp(\lambda_2 L) & \lambda_3 \exp(\lambda_3 L) \\ \lambda_1 & \lambda_2 & \lambda_3 \end{pmatrix} \cdot \begin{pmatrix} C_1 \\ C_2 \\ C_3 \end{pmatrix} = \begin{pmatrix} 0 \\ 0 \\ \frac{-1}{k_s(1-\phi)} \end{pmatrix} \tag{A.21}$$

with

$$B_i = \frac{\tilde{s}(1-\phi)\rho_s c_{p,s}}{h_v} + \frac{k_s(1-\phi)}{h_v} \lambda_i^2. \tag{A.22}$$

The so determined analytical solution in the Laplace space is transformed back to the time domain by using the algorithm of Gaver and Stehfest [184, 185]. Further details of the derivation of these porous medium impulse responses are presented in detail in Ref. [74].

Additionally, the transient change in plenum coolant temperature is considered that can lead to a further source of heating of the porous material, an effect that was present in some of the validation cases. To account for this phenomenon the same methodology is used as described above. However, the boundary conditions are changed appropriately to a Dirac impulse of coolant temperature,

$$x = L, \qquad T_f = \delta(t=0), \quad \text{where} \quad \int_0^\infty T_f(t) \mathrm{d}t = 1\,\mathrm{Ks}, \tag{A.23}$$

an adiabatic backside

$$x = L, \qquad \frac{\partial T_s}{\partial x} = 0, \tag{A.24}$$

and an adiabatic surface

$$x = 0, \qquad \frac{\partial T_s}{\partial x} = 0. \tag{A.25}$$

This results in the alteration to (1 0 0) of the right hand side of Eq. (A.21). The obtained impulse response of the solid material is labelled as $H_{s,\,\mathrm{trans},\,T}$ and describes the solid temperature evolution at a given depth after a unit temperature impulse of the plenum coolant.

A.1.1 Steady State Temperature Calculation

This section describes how the step responses are used to calculate the surface and backside temperatures of the porous material. As the used differential equation system, Eqs. (A.3) and (A.4), is linear, it is possible to superpose different solutions and thus account for a non-adiabatic backside or for the change in plenum coolant temperature. As depicted in Fig. A.2, the different heating sources are used to calculate the respective temperature fields in the material. Every heating source, e. g. surface or backside heat flux, leads to a temperature change. All the temperature changes are then superposed to obtain the combined temperature field. As the heat flux terms also depend on these temperature fields, an iterative approach is used to calculate the heat flux boundary conditions and the temperature fields until convergence is obtained.

For steady state cases (no transient change in plenum coolant temperature is considered here), the solid temperatures at the surface and backside are calculated via

$$T_{s,\mathrm{surface}} = H_{s,\,\mathrm{steady}}(x = 0) \cdot \dot{q}_{\mathrm{surface}} + H_{s,\,\mathrm{steady}}(x = L) \cdot \dot{q}_{\mathrm{backside}} + T_{\mathrm{start}} \tag{A.26}$$

and

$$T_{s,\mathrm{backside}} = H_{s,\,\mathrm{steady}}(x = L) \cdot \dot{q}_{\mathrm{surface}} + H_{s,\,\mathrm{steady}}(x = 0) \cdot \dot{q}_{\mathrm{backside}} + T_{\mathrm{start}}. \tag{A.27}$$

The surface fluid temperature is determined by

$$T_f = H_{f,\,\mathrm{steady}}(x=0)\cdot\dot{q}_{\mathrm{surface}} + T_{\mathrm{start}}, \tag{A.28}$$

with the initial temperature T_{start}.

A.1.2 Transient Temperature Calculation

The transient calculations are based on the impulse response principle [162]. The same linear superposition approach is used as described in section A.1.1. The solid material temperatures at the surface and backside are determined via the discrete convolutions

$$T_{s,\mathrm{surface}}(t_i) = \sum_{t_j=t_0}^{t_i} H_{s\,\mathrm{trans}}(t_j, t_{i-j}, x=0)\cdot\dot{q}_{\mathrm{surface}}(t_j) + \sum_{t_j=t_0}^{t_i} H_{s\,\mathrm{trans}}(t_j, t_{i-j}, x=L)\cdot\dot{q}_{\mathrm{backside}}(t_j) + \sum_{t_j=t_0}^{t_i} H_{s\,\mathrm{trans},\,T}(t_j, t_{i-j}, x=0)\cdot T_{f,\,pl}(t_j) + T_{\mathrm{start}} \tag{A.29}$$

and

$$T_{s,\mathrm{backside}}(t_i) = \sum_{t_j=t_0}^{t_i} H_{s\,\mathrm{trans}}(t_j, t_{i-j}, x=L)\cdot\dot{q}_{\mathrm{surface}}(t_j) + \sum_{t_j=t_0}^{t_i} H_{s\,\mathrm{trans}}(t_j, t_{i-j}, x=0)\cdot\dot{q}_{\mathrm{backside}}(t_j) + \sum_{t_j=t_0}^{t_i} H_{s\,\mathrm{trans},\,T}(t_j, t_{i-j}, x=L)\cdot T_{f,\,pl}(t_j) + T_{\mathrm{start}}. \tag{A.30}$$

The surface fluid temperature is calculated by

$$T_f(t_i) = \sum_{t_j=t_0}^{t_i} H_{f\,\mathrm{trans}}(t_j, t_{i-j}, x=0)\cdot\dot{q}_{\mathrm{surface}}(t_j) + T_{f,\,pl}(t_i) + T_{\mathrm{start}}. \tag{A.31}$$

The inclusion of a time-varying coolant mass flux results in a change of the impulse response over time. The change in the thermal properties of the porous

medium is approximated by combining different impulse responses which correspond to different coolant mass fluxes, $\dot{m}_A$. This strategy has been employed for inverse heat transfer investigations in the past, where time-varying impulse responses are considered [186, 187]. It is usually referred to as the sequential function specification method [188] and the details of the approach are given in the following. An impulse response $H_{s,f\,\mathrm{trans}}(t_j, t_i, x) = f(v_f(t_j))$ is calculated for each time step, where t_j is the starting time of the impulse response and t_i is the temperature evolution of this particular impulse response. However, the changing coolant velocity of the following time steps will also affect the evolution of the impulse response. This is approximated by changing the normalised gradient of the impulse response $H_{s,f\,\mathrm{trans}}(t_j, t_{i-j}, x)$ to be equal to the normalised gradient of the impulse response $H_{s,f\,\mathrm{trans}}(t_i, t_{i-j}, x)$ and thus accounting for the change in coolant velocity with time,

$$H_{s,f\,\mathrm{trans}}(t_j, t_{i-j}, x) = H_{s,f\,\mathrm{trans}}(t_j, t_{i-j-1}, x)\Big[1+ \frac{H_{s,f\,\mathrm{trans}}(t_i, t_{i-j}, x) - H_{s,f\,\mathrm{trans}}(t_i, t_{i-j-1}, x)}{H_{s,f\,\mathrm{trans}}(t_i, t_{i-j-1}, x)}\Big], \quad \text{(A.32)}$$

for $t_i > t_j$ and $t_0 < t_j < t_{\mathrm{end}}$.

A.2 Reservoir Pressure

The calculated fluid temperatures in the material will have an effect on the plenum pressure p_{pl} since a higher coolant temperature leads to a higher viscosity in the material and this will therefore lead to a higher required plenum pressure for a given mass flux. The governing equation of this process is the Darcy-Forchheimer equation,

$$-\frac{\partial p}{\partial x} = \frac{\mu_f}{K_D} v_f + \frac{\rho_f}{K_F} v_f^2, \quad \text{(A.33)}$$

with pressure, p, coolant dynamic viscosity, μ_f, Darcy-coefficient, K_D, and Forchheimer coefficient, K_F. Analogous to Langener [46], a simplified linear solution of the temperature field in the medium can be used to solve the Darcy-Forchheimer equation analytically to

$$p_{\mathrm{pl}}^2 = p_g^2 + \frac{2L}{T_f - T_{s,\mathrm{backside}}} \Big[\frac{\dot{m}_A R\, \mu_{f,\mathrm{ref}}}{(n+2)\, K_D\, T_{\mathrm{ref}}^n} \left(T_f^{n+2} - T_{s,\mathrm{backside}}^{n+2} \right) + \frac{\dot{m}_A^2 R}{2K_F} \left(T_f^2 - T_{s,\mathrm{backside}}^2 \right) \Big] \quad \text{(A.34)}$$

with the viscosity law exponent, $n = 0.69$, the specific gas constant, R, and the viscosity reference temperature, T_{ref} [46]. The coolant density is then obtained by using the ideal gas law and is used to update the impulse responses. The described procedure is conducted for every segment along the vehicle surface.

A.3 Validation

This code has been validated against a range of both experimental studies and flight data from the SHEFEX II flight test. Only one of those validation cases is presented here and the other cases are detailed in Ref. [86]

Flat Plate Plasma Wind Tunnel Experiments: Transient Transpiration Cooling

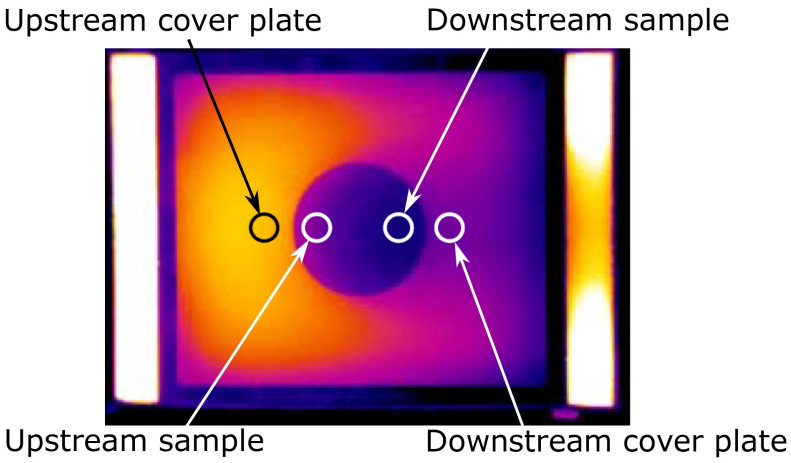

Figure A.3: Infrared thermography image of L2K experiments [37].

In this validation study, transpiration-cooled porous materials were investigated. The same experimental campaign described in Ref. [37] investigated the effectiveness of transpiration cooling for various coolant mass flow rates of nitrogen. In the study, continuous plasma wind tunnel freestream conditions were maintained,

while the coolant mass flow rate was varied in steps over the test time of the experiment. Infrared thermography was used to determine the transient surface temperature of the porous sample, denoted as the downstream sample in Fig. A.3. By applying the same freestream conditions as presented in Table A.1, the transient wall temperatures with the coolant gas are simulated.

Table A.1: Flow conditions for the plasma wind tunnel experiments.

Condition	L2K
M	7.0
p_∞, Pa	47
T_∞, K	378
Total enthalpy, $\mathrm{MJ\,kg^{-1}}$	8.4

Figure A.4 shows the variation in mass flow rate and the measured transient surface temperature. The experiment used a carbon-carbon (C/C) standard porous material located approximately 200 mm from the model stagnation point. In the PIRATE simulation of the experiment, the coolant temperature in the plenum is increasing to a maximum of 422 K, which was also measured in the experiment. The linear rise and fairly constant plateau at later times are representative of a typical test condition as presented in Ref. [37]. The C/C-SiC plenum behind the porous sample is modeled by accounting for the respective radiation loss at the backside. This is taken into account by using a radiative back boundary condition as described in Section A.1. Additionally, the results obtained by a HEATS simulation of this experiment are included. At short times, both simulations and the experimental data agree well, whereas at long times, the PIRATE simulation slightly underpredicts the porous sample surface temperature, and the respective HEATS simulation results in an overprediction. As the HEATS simulation used an adiabatic backside condition, the higher predicted temperature seems reasonable. The additional radiative losses at the plenum side result in a lower temperature for the PIRATE simulation. A reason for the higher measured surface temperature at approximately 300 s could be the result of an increase in the temperature of the structure below the cooled surface. The overall agreement between the PIRATE simulation and the experimental data

is very good. Hence, transient transpiration cooling effects at the injection location are sufficiently captured by the model approach.

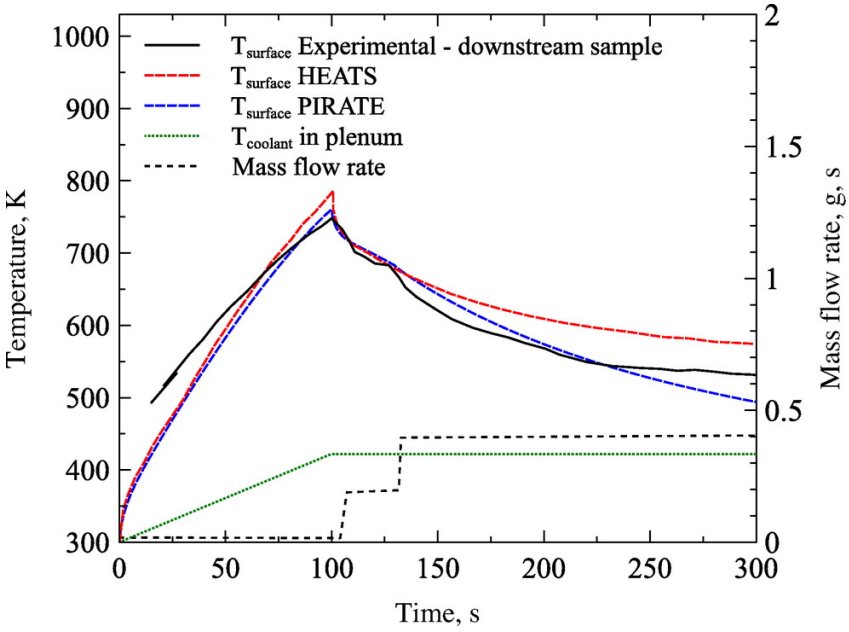

Figure A.4: Comparison between PIRATE, HEATS, and experimental measurements of a C/C sample [37, 38].

Appendix B

Principles of Infrared Thermography

Infrared thermography is a two-dimensional, optical, non-contact technique of temperature measurement. It is the process of measuring the infrared radiation emitted from an object and then using these measurements to calculate the temperature T of the object. Radiation is a means of energy transfer via electromagnetic waves. Radiation can be absorbed, reflected, and transmitted by a body. For a given body, the conservation of energy can therefore be expressed by

$$\alpha(\lambda) + \rho(\lambda) + \tau(\lambda) = 1 \tag{B.1}$$

where α, ρ, and τ are the absorptivity, reflectivity, and transmissivity coefficients of the body, respectively. Each of these coefficients may depend on both radiation wavelength, λ, (spectral) and propagation direction (directional). Radiation is emitted by all bodies with a temperature $T > 0\,\mathrm{K}$. If the body is opaque (that is, when $\tau = 0$), then radiation is only emitted from the surface of the body and not from any point within the body. Fundamentally, the simplest concept in infrared thermography is the concept of a black body. A black body is a hypothetical body which absorbs all incident radiation, at all wavelengths, i.e. $\alpha = \varepsilon = 1$. The electromagnetic radiative power of a black body is given by Planck's law

$$L_{bb}(\lambda, T) = \frac{2hc^2}{\lambda^5} \frac{1}{\exp \frac{hc}{\lambda k_B T} - 1} \tag{B.2}$$

where $L_{bb}(\lambda, T)$ is the electromagnetic power radiated per unit area of an emitting black body, in the normal direction, per unit solid angle per unit wavelength, h is Planck's constant, c is the speed of light in a vacuum, k_B is the Boltzmann constant, λ is the wavelength of the electromagnetic radiation, and T is the absolute temperature of the black body. By using Planck's law, the radiative power emitted by a body over a known spectral range can be directly related to the temperature of the body. For ambient temperatures, the greatest radiation intensity from a black body is emitted in the infrared band, which is why infrared cameras are frequently used for thermography applications. Figure B.1 shows the solution to Eq. (B.2) for a variety of black body temperatures. It is apparent that for ambient temperature measurements, the infrared signal is highest in the long-wave region, and thus a long-wave camera is typically used for those applications. At higher temperatures (over 500 K), a mid-wave camera becomes more appropriate. The wavelength at which the radiance is maximal for a given temperature can be found from Wien's displacement law which states that the spectral radiance of black-body radiation per unit wavelength peaks at the wavelength λ_{peak} given by

$$\lambda_{\text{peak}} = \frac{b}{T} \tag{B.3}$$

where b is a constant of proportionality called the Wien's displacement constant, equal to $2.897771955 \cdot 10^{-3}\,\text{m K}$.

The radiative properties for real materials (known as grey bodies) are characterised by the emissivity, $\varepsilon(\lambda, T, \theta)$ which is a function of the wavelength of the radiation, λ, the temperature of the body, T, and the angle of emission from the surface normal, θ. The emissivity specifies the radiance from a grey body as a proportion of the radiance from a black body at the same temperature. The absorptivity of a grey body is defined as the radiative power absorbed as a proportion of that absorbed by a black body under the same conditions (a black body absorbing all radiation). Kirchoff's law of thermal radiation states that the emissivity of a body is equal to its absorptivity. This is necessarily true to satisfy the conservation of energy. Consequently, if the emissivity of the body is less than one (as with all

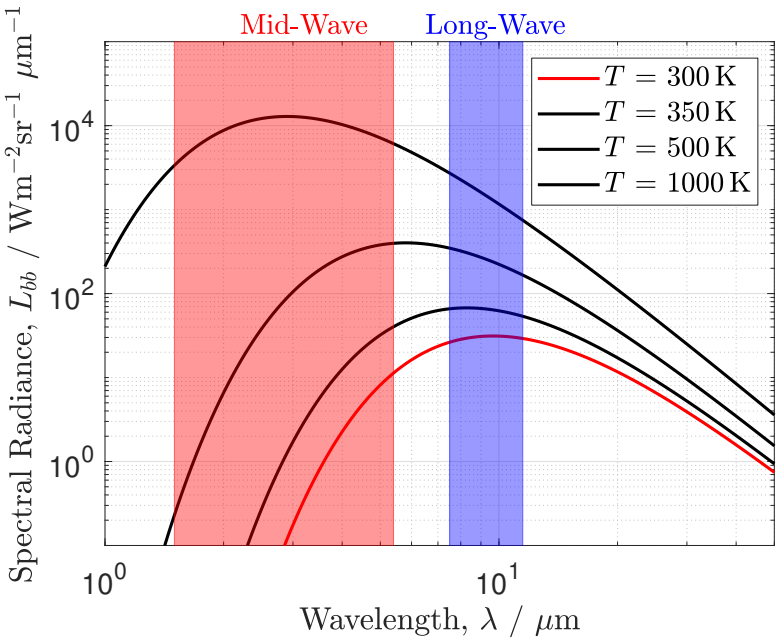

Figure B.1: The spectral radiance of a black body at a variety of temperatures. The red and blue shaded regions represent typical wavelength bands for mid- and long-wave cameras, respectively [135].

real materials), then the absorptivity is also less than one, and a portion of incident radiation arriving at the surface of a grey body will be reflected.

An infrared detector measuring the radiance from the surface of a grey body will therefore be receiving both emitted and reflected radiation. If air, or some other transparent medium, with non-zero emissivity is present between the surface and the detector, the radiation will be both attenuated and contributed to by the transparent medium. In practice, therefore, calibration procedures are needed to accurately determine the surface temperature of a grey body from measurements of surface radiance. A detailed, practical, in-situ calibration methodology is provided in Chapter 4.

B.1 Infrared Cameras

Infrared camera technology has advanced rapidly over the past few decades, to the extent that it has now found wide usage in a variety of research areas. In this section, a short overview of infrared camera detectors is provided. A more detailed discussion

on the theoretical basis and operation of different infrared cameras is presented by Astarita and Carlomagno [135]. There are two main types of infrared detector

- Microbolometer: Within a microbolometer, infrared radiation arrives at the detector pixels, which causes a local increase in the detector temperature. This increase in temperature leads to a change in the electrical resistance of the detector material. The change in electrical resistance is then measured and related to incident radiation intensity (and subsequently temperature). The detector usually consists of a matrix of microbolometers, allowing a spatially resolved image to be formed.

- Photo-detector: This type of infrared camera consist of a series of sensors within which low energy state electrons are contained. When an incident photon arrives, which has appropriate energy, an electron within the sensor is excited to a higher energy state. When at the higher state, the electron is able to move and thereby conduct electricity, doing so under the influence of a driving voltage potential. The incident radiation thereby allows a current to flow, which can be measured and related to the incident radiation. Photo-detectors require cooling in order to function, which is often provided by an integrated Stirling heat pump. Operating detector temperatures of approximately 70 K are common. Photo-detectors typically have a lower NETD[1] than microbolometers and are often used in scientific applications for this reason, but are more expensive. Nowadays, the most commonly used types of photo-detector infrared scanners are *mercury cadmium telluride* (HgCdTe, also called CMT or MCT), *indium antimonide* (InSb) and the *quantum well infrared photodetector* (QWIP).

In recent years, manufacturers have started producing very high-speed infrared cameras, with frame rates up to 100 kHz [189]. This has enabled a wider usage of such cameras in short duration high-speed facilities where the test time can be in the order of ms.

[1] NETD (Noise Equivalent Temperature Difference) is the value of a signal temperature variation which would match the noise of the camera - as some reference condition

B.2 Optical Access

(a) Sapphire, coated [190]
.

(b) Zinc Selenide, uncoated [191].

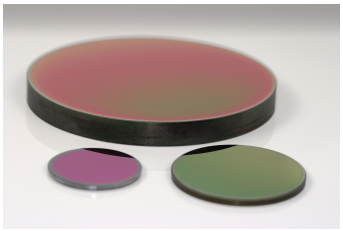

(c) Germanium [192].

Figure B.2: A selection of optical windows.

A range of different materials have been used as infrared transparent windows (some examples in Fig. B.2), providing optical access to wind tunnels. The windows are usually designed such that they form part of the wind tunnel enclosure. A common infrared window material is Sapphire which has a high transmissivity only in the short and medium-wave infrared band (0.75-5 μm) and consequentially can only be used effectively with short- and medium-wave infrared cameras (or wide-band cameras combined with filters). The high hardness and durability of Sapphire are significant attributes, and such windows are often supplied with anti-reflective coatings. For wider applicability, Zinc Selenide is appropriate for the short-, mid- and long-wave cameras where the transmissivity drops off above 15 μm. These windows require anti-reflective coatings to achieve their high transmissivity. It is also one of the softest commonly used infrared windows and damages easily. Another option for long-wave measurements is Germanium which is a tough, durable material that can easily be machined into complex shapes (making it ideal for the complex window geometries). The transmissivity of Germanium, however, exhibits a strong dependence on both temperature and wavelength, and this must be considered for facilities in which the environment temperature is likely to change significantly [193]. There are other choices of optical windows available, and the best choice will depend on the infrared camera used and the temperature at which the window is operated.

B.3 Emissivity Dependence of Porous Materials

The choice of infrared camera for a given experiment will also depend on the spectral emissivity dependence of the material of interest. A higher material emissivity is desirable to maximise the signal from the

Whilst some materials have essentially broadband emissivity curves in the infrared spectrum, one class of materials which actually show strong spectral emissivity dependence are ceramics which may be used in transpiration cooling experiments. Two such materials are Alumina (Al2O3) and Zirconia (ZrO2) which have been used as materials for experimental tests in Chapters 4 and 5. Figure B.3 shows the spectral emissivity dependence for solid Alumina and Zirconia. There is a region of reduced emissivity in the mid-wave region which corresponds to an effective emissivity of between 0.1-0.2. This has been verified through benchtop testing with the Telops M3K FAST mid-wave camera. On the other hand, the emissivity is between 0.8-0.9 in the long-wave region. Thus, a LWIR camera (such as the FLIR A6751) is required for infrared measurements with Zirconia and Alumina.

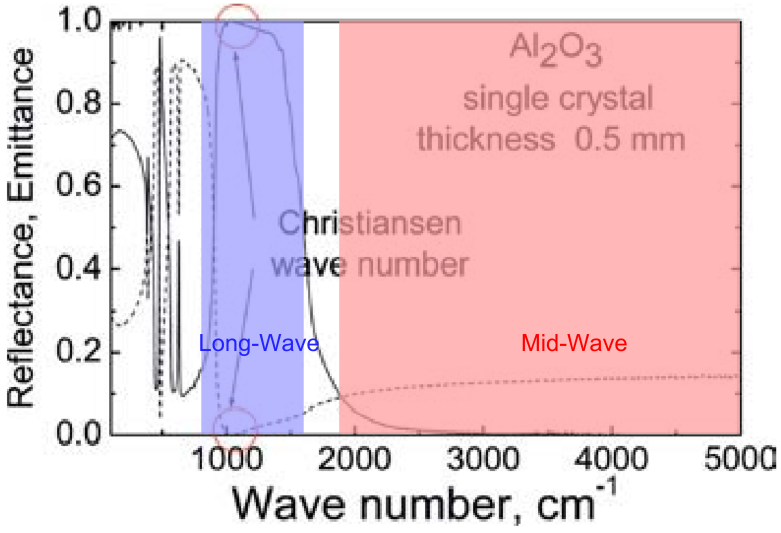

(a) Alumina [194]

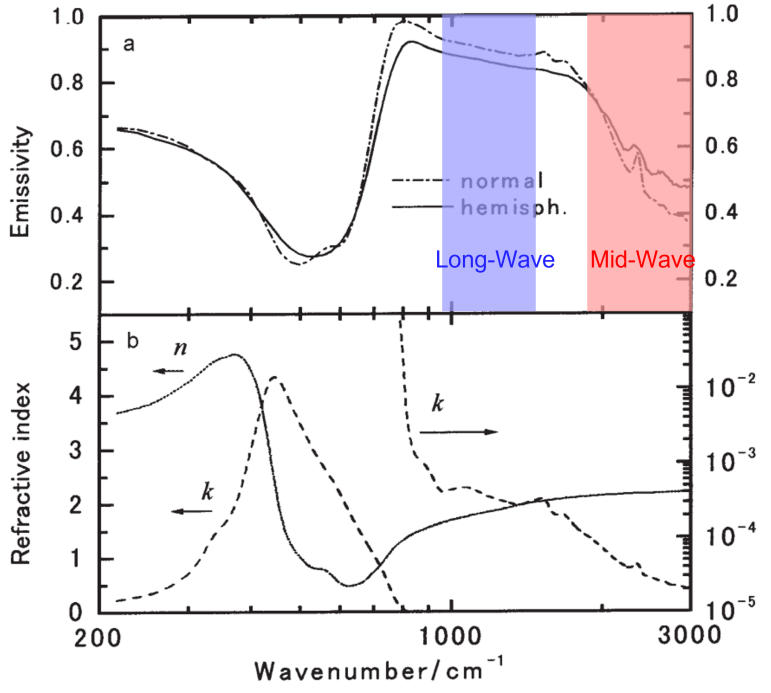

(b) Zirconia [195]

Figure B.3: Spectral emissivity dependence.

Appendix C

Infrared Experiments in the HDT

Over the course of experimental testing in the HDT, it was observed that when using the mid-wave infrared camera to image the surface temperature of a model; sudden, non-physical temperature rises were observed. This was initially attributed to either error in the calibration or potential spurious reflections from the inside of the test section. However, after several investigations, it was identified that the cause of these effects was due to the atmospheric transmittance of air in the Mid Wave Infrared. As Fig. C.1 shows, there are significant regions with low transmission due to CO_2 or H_2O in the mid-wave region. Further testing identified the ppm of CO_2 in the air bottle banks was negligible. However, there is significant H_2O content in the air and it is envisaged that due to the very low static temperature of the free-stream gas as it exits the nozzle (below the liquefaction temperature if the gas was stationary), the effect of water vapour is magnified and not captured by static bench-top calibrations prior to the experiment.

To eliminate this issue, the HDT can also be operated using nitrogen as the driver gas (instead of air). After this modification was implemented, an initial test was conducted on a 7 deg half-angle cone (as part of a larger set of experimental testing with that model) with the Mach 7 nozzle. The test was run at 37 bar fill pressure and a total temperature of 500 K. Figure C.2 shows the results of two tests conducted using the Telops M3K FAST mid-wave camera with the nitrogen and air driver, respectively. Whilst the infrared red result with the air driver exhibits a sudden peak at time = 0.11 s, this non-physical temperature spike was eliminated

using the nitrogen driver. As a result of these findings, the HDT was run with the nitrogen driver gas for the experiments in Chapter 5. The experiments in Chapters 4 and 6 did not require the nitrogen driver gas as the infrared camera used for those experiments was the LWIR camera.

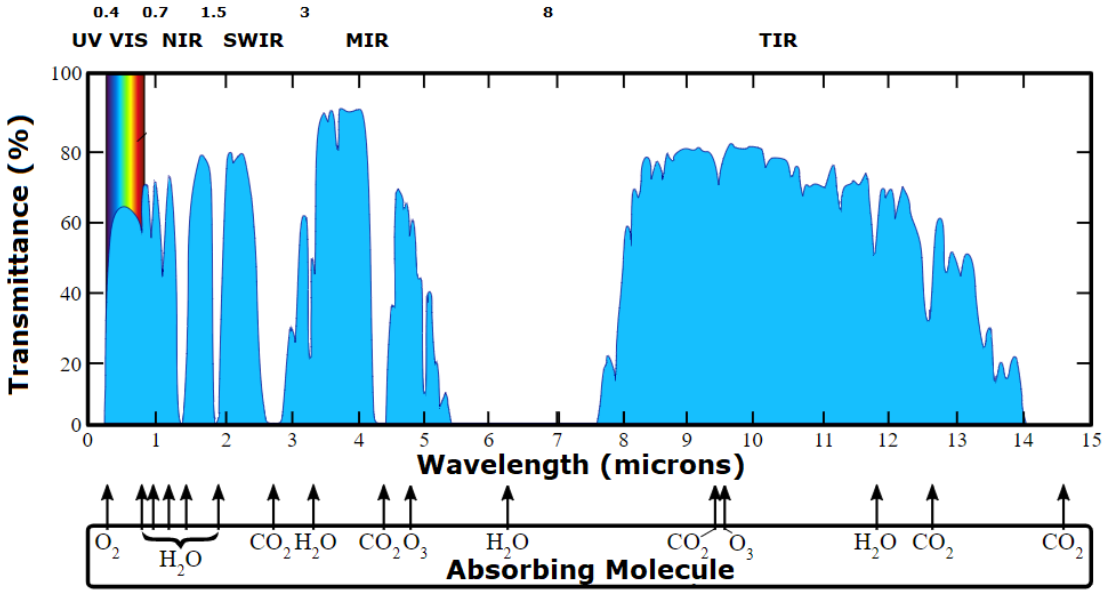

Figure C.1: Atmospheric transmission at different wavelengths. Adapted from Ref. [196].

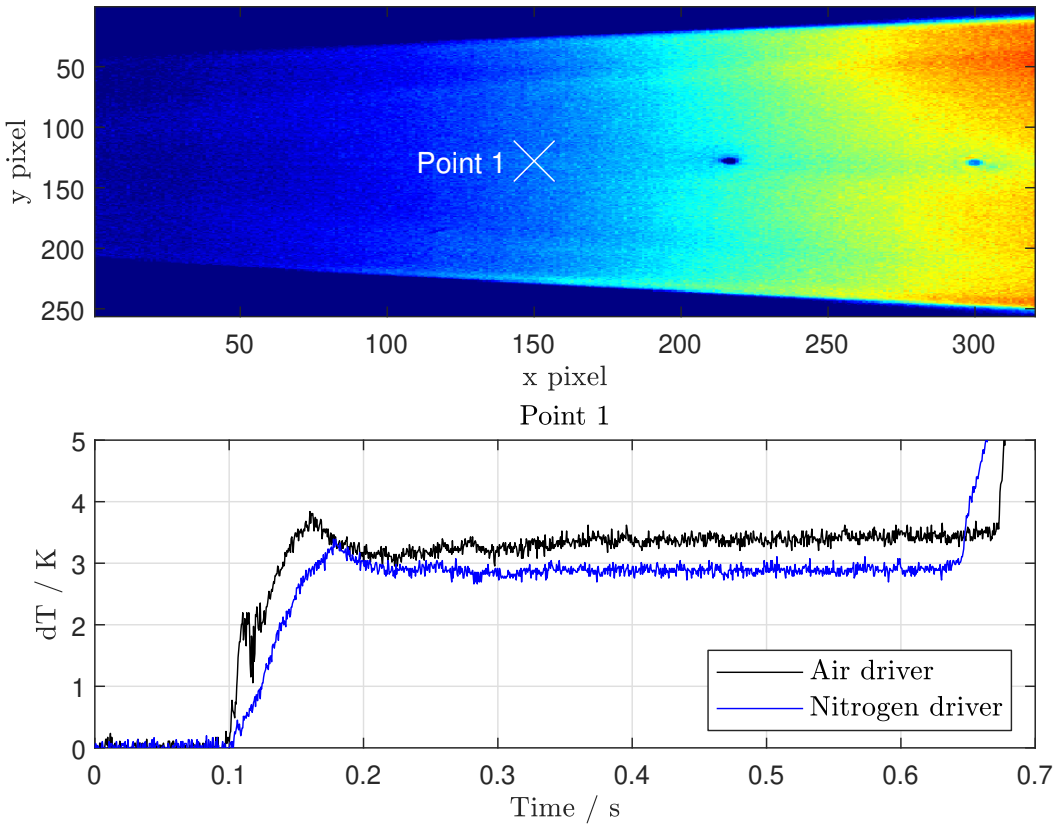

Figure C.2: Infrared image of the cone at $t = 0.375\,\mathrm{s}$ (top) and the respective line plot at point 1 (bottom) with the air and nitrogen driver, respectively. The non-physical spike is evident at $t = 0.115\,\mathrm{s}$ on the black trace.

Appendix D

Infrared Measurement Sensitivity

Table D.1: Sensitivity of each variable to the final detected radiance (I_D) – assuming $T_{obj} = 300\,\mathrm{K}$.

Parameter	r	X_i	$\frac{\mathrm{UMF}}{\sum_{i=1}^{J}\mathrm{UMF}_i} * 100$ (%)
$T_{\mathrm{atm,ext}}$ / K	293	2	0.2
$\varepsilon_{\mathrm{atm,ext}}$	0.02	2	6.1
T_{wind} / K	293	2	4.3
$\varepsilon_{\mathrm{wind}}$	0.05	2	15.1
$\tau_{\mathrm{atm,ext}}$	0.05	2	6.7
$T_{\mathrm{atm,int}}$ / K	293	10	0.8
τ_{wind}	0.77	0.05	16.7
$\varepsilon_{\mathrm{atm,int}}$	0.02	2	4.6
$\varepsilon_{\mathrm{obj}}$	0.9	0.05	11.5
$\tau_{\mathrm{atm,int}}$	0.01	0.05	5.6
T_{wall} / K	293	5	3.7
$\varepsilon_{\mathrm{wall}}$	0.05	2	1.1
ρ_{obj}	0.1	0.05	17.2
T_{env} / K	293	2	1.5
ρ_{wind}	0.03	0.01	2.4
$\varepsilon_{\mathrm{env}}$	0.8	2	2.6

In Chapter 4, it was mentioned that the series of equations representing the various sources of radiation in the tunnel (Fig 4.7) may be simplified into one equation of the form

$$I_D(t) = \varepsilon_{\mathrm{obj}} \cdot A1 \cdot I_{bb}^{\mathrm{obj}}(t) + \rho_{\mathrm{obj}} \cdot A2 \cdot I_{bb}^{\mathrm{amb}} \tag{D.1}$$

where $A1$ and $A2$ parameters are obtained by performing an in-situ calibration.

This assumes that none of these sources changes temperature appreciably during a test, which is a reasonable assumption for a short-duration facility such as the HDT with a total test time of below 1 s.

To substantiate this assumption, a sensitivity study has been conducted using the Taylor Series method [167] to ascertain the effect of each of the above terms on the detector radiant intensity, $I_D(t)$. Table D.1 summarises the sensitivity of each variable, r, to an uncertainty, X_i, where the sensitivity is quantified as a relative Uncertainty Magnification Factor (UMF) in %. The relative UMF relates the sensitivity of each of the input variables to the final result. As the results show, any variation in temperature by 2 K of all the sources has a maximum UMF of 3.7% for the test section wall. This is essentially negligible compared to variations in properties such as emissivity, reflectivity and transmissivity.

Appendix E

List of Experiments

The experiments completed over the course of this research were conducted over two separate test campaigns - namely the stagnation probe experiments detailed in Chapter 4 and the flat plate experiments detailed in Chapters 5 and 6. The tables contained in this appendix are as follows

- Table E.1: Tunnel operating and derived values for the stagnation probe experimental campaign.
- Table E.2: Tunnel operating and derived values for the flat plate laminar experiments without shock impingement and no boundary layer trip.
- Table E.3: Tunnel operating and derived values for the flat plate turbulent experiments without shock impingement and with a diamond boundary layer trip.
- Table E.4: Tunnel operating and derived values for the flat plate laminar experiments with shock impingement and no boundary layer trip.
- Table E.4: Tunnel operating and derived values for the flat plate turbulent experiments with shock impingement and with a diamond boundary layer trip.

Table E.1: Overview of the stagnation probe experiments in Chapter 4. The values below refer to steady condition three. Note: For these experiments, the Mach number and the total temperature were determined based on a pitot rake survey prior to the experimental campaign.

Shot number	Tunnel parameters		Measured values		Derived values							Material	Injected gas	Gas injection measured		Derived gas injection values		
	P_{fill} / kPa	T_{fill} / K	P_0 / kPa	T_0	M	P_∞ / Pa	T_∞ / K	u_∞ / m s^{-1}	ρ_∞ / kg m^{-3}	μ_∞ / Pa s	Re_∞ / m^{-1}			P_{pl} / kPa	T_{pl} / K	$\dot{m}_{\text{f}}$ / kg m^{-3}	St_0	B_h
1763	777	500	645.48	459.21	7.03	151.59	42.18	915.32	$1.25{\cdot}10^{-2}$	$3.02{\cdot}10^{-6}$	$3.80{\cdot}10^{6}$	Alumina	- -	-	-	-	$1.26{\cdot}10^{-2}$	-
1744	777	500	637.33	459.21	7.03	149.67	42.18	915.32	$1.24{\cdot}10^{-2}$	$3.02{\cdot}10^{-6}$	$3.75{\cdot}10^{6}$	Alumina	N_2	279.24	295.00	$1.49{\cdot}10^{-2}$	$1.26{\cdot}10^{-2}$	0.104
1748	777	500	643.53	459.21	7.03	151.13	42.18	915.32	$1.25{\cdot}10^{-2}$	$3.02{\cdot}10^{-6}$	$3.79{\cdot}10^{6}$	Alumina	N_2	614.60	294.18	$7.17{\cdot}10^{-2}$	$1.26{\cdot}10^{-2}$	0.498
1750	777	500	644.61	459.21	7.03	151.38	42.18	915.32	$1.25{\cdot}10^{-2}$	$3.02{\cdot}10^{-6}$	$3.79{\cdot}10^{6}$	Alumina	N_2	1041.04	296.70	$2.00{\cdot}10^{-1}$	$1.26{\cdot}10^{-2}$	1.390
1746	777	500	637.40	459.21	7.03	149.69	42.18	915.32	$1.24{\cdot}10^{-2}$	$3.02{\cdot}10^{-6}$	$3.75{\cdot}10^{6}$	Alumina	Air	278.77	295.67	$1.50{\cdot}10^{-2}$	$1.26{\cdot}10^{-2}$	0.105
1747	777	500	635.35	459.21	7.03	149.21	42.18	915.32	$1.23{\cdot}10^{-2}$	$3.02{\cdot}10^{-6}$	$3.74{\cdot}10^{6}$	Alumina	Air	617.89	296.31	$7.28{\cdot}10^{-2}$	$1.26{\cdot}10^{-2}$	0.513
1762	777	500	634.17	459.21	7.03	148.93	42.18	915.32	$1.23{\cdot}10^{-2}$	$3.02{\cdot}10^{-6}$	$3.73{\cdot}10^{6}$	Alumina	Air	1043.66	299.06	$2.02{\cdot}10^{-1}$	$1.26{\cdot}10^{-2}$	1.426
1730	777	500	645.71	459.21	7.03	151.64	42.18	915.32	$1.25{\cdot}10^{-2}$	$3.02{\cdot}10^{-6}$	$3.80{\cdot}10^{6}$	Alumina	Kr	150.94	292.69	$9.26{\cdot}10^{-3}$	$1.26{\cdot}10^{-2}$	0.064
1732	777	500	645.43	459.21	7.03	151.58	42.18	915.32	$1.25{\cdot}10^{-2}$	$3.02{\cdot}10^{-6}$	$3.80{\cdot}10^{6}$	Alumina	Kr	488.58	293.61	$9.61{\cdot}10^{-2}$	$1.26{\cdot}10^{-2}$	0.666
1733	777	500	645.16	459.21	7.03	151.51	42.18	915.32	$1.25{\cdot}10^{-2}$	$3.02{\cdot}10^{-6}$	$3.80{\cdot}10^{6}$	Alumina	Kr	717.61	293.18	$2.05{\cdot}10^{-1}$	$1.26{\cdot}10^{-2}$	1.424
1781	777	500	642.27	459.21	7.03	150.83	42.18	915.32	$1.25{\cdot}10^{-2}$	$3.02{\cdot}10^{-6}$	$3.78{\cdot}10^{6}$	Alumina	-	-	-	-	$1.26{\cdot}10^{-2}$	-
1780	777	500	607.24	459.21	7.03	142.61	42.18	915.32	$1.18{\cdot}10^{-2}$	$3.02{\cdot}10^{-6}$	$3.57{\cdot}10^{6}$	Alumina	Ar	258.02	314.42	$1.34{\cdot}10^{-2}$	$1.26{\cdot}10^{-2}$	0.099
1779	777	500	642.15	459.21	7.03	150.81	42.18	915.32	$1.25{\cdot}10^{-2}$	$3.02{\cdot}10^{-6}$	$3.78{\cdot}10^{6}$	Alumina	Ar	582.23	296.02	$7.21{\cdot}10^{-2}$	$1.26{\cdot}10^{-2}$	0.502
1778	777	500	640.88	459.21	7.03	150.51	42.18	915.32	$1.24{\cdot}10^{-2}$	$3.02{\cdot}10^{-6}$	$3.77{\cdot}10^{6}$	Alumina	Ar	1031.57	295.73	$2.23{\cdot}10^{-1}$	$1.26{\cdot}10^{-2}$	1.554
1791	777	500	642.22	459.21	7.03	150.82	42.18	915.32	$1.25{\cdot}10^{-2}$	$3.02{\cdot}10^{-6}$	$3.78{\cdot}10^{6}$	Alumina	- -	-	-	-	$1.26{\cdot}10^{-2}$	-
1790	777	500	643.35	459.21	7.03	151.09	42.18	915.32	$1.25{\cdot}10^{-2}$	$3.02{\cdot}10^{-6}$	$3.79{\cdot}10^{6}$	Alumina	He	1075.36	300.07	$2.78{\cdot}10^{-2}$	$1.26{\cdot}10^{-2}$	0.193
1789	777	500	642.36	459.21	7.03	150.86	42.18	915.32	$1.25{\cdot}10^{-2}$	$3.02{\cdot}10^{-6}$	$3.78{\cdot}10^{6}$	Alumina	He	1540.89	298.76	$5.71{\cdot}10^{-2}$	$1.26{\cdot}10^{-2}$	0.397
1788	777	500	642.86	459.21	7.03	150.97	42.18	915.32	$1.25{\cdot}10^{-2}$	$3.02{\cdot}10^{-6}$	$3.78{\cdot}10^{6}$	Alumina	He	1873.42	294.72	$8.52{\cdot}10^{-2}$	$1.26{\cdot}10^{-2}$	0.593

Table E.2: Overview of the laminar flat plate experiments from Chapter 5. The values below refer to steady condition two. Note: the total temperature values were determined based on total temperature measurements taken prior to the experimental campaign at the same condition. The Mach number was determined based on the edge pressure on the flat plate.

Shot number	Tunnel parameters		Measured values			Derived values							Material	Injected gas	Gas injection measured		Gas injection derived	
	P_{fill} / kPa	T_{fill} / K	P_0 / kPa	T_0 / K	P_{Kulite} / Pa	M	P_e / Pa	T_e / K	u_e / ms^{-1}	ρ_e / kg m^{-3}	μ_e / Pa s	Re_u / m^{-1}			P_{pl} / kPa	T_{pl} / K	$\dot{m}_f$ / kg m^{-3}	F / %
2094	1800	500	1370.98	418.93	803.71	6.08	803.71	49.97	860.95	$5.60{\cdot}10^{-2}$	$3.58{\cdot}10^{-6}$	$1.35{\cdot}10^{7}$	METAPOR CE170	-	-	-	-	-
2097	1800	500	1364.49	418.93	780.34	6.10	780.34	49.62	861.36	$5.48{\cdot}10^{-2}$	$3.55{\cdot}10^{-6}$	$1.33{\cdot}10^{7}$	METAPOR CE170	N_2	33.54	293.58	$1.26{\cdot}10^{-2}$	0.027
2096	1800	500	1371.58	418.93	790.67	6.09	790.67	49.73	861.23	$5.54{\cdot}10^{-2}$	$3.56{\cdot}10^{-6}$	$1.34{\cdot}10^{7}$	METAPOR CE170	N_2	50.25	293.68	$2.76{\cdot}10^{-2}$	0.058
2095	1800	500	1369.88	418.93	794.02	6.09	794.02	49.81	861.14	$5.55{\cdot}10^{-2}$	$3.57{\cdot}10^{-6}$	$1.34{\cdot}10^{7}$	METAPOR CE170	N_2	64.66	293.98	$4.47{\cdot}10^{-2}$	0.094
2093	1800	500	1369.42	418.93	792.01	6.09	792.01	49.78	861.17	$5.54{\cdot}10^{-2}$	$3.56{\cdot}10^{-6}$	$1.34{\cdot}10^{7}$	METAPOR CE170	N_2	90.31	296.25	$8.26{\cdot}10^{-2}$	0.173
2098	1800	500	1366.10	418.93	777.73	6.10	777.73	49.56	861.43	$5.47{\cdot}10^{-2}$	$3.55{\cdot}10^{-6}$	$1.33{\cdot}10^{7}$	METAPOR CE170	He	69.75	292.61	$7.10{\cdot}10^{-3}$	0.015
2099	1800	500	1370.49	418.93	778.44	6.11	778.44	49.52	861.47	$5.48{\cdot}10^{-2}$	$3.54{\cdot}10^{-6}$	$1.33{\cdot}10^{7}$	METAPOR CE170	He	95.70	292.27	$1.32{\cdot}10^{-2}$	0.028
2128	1800	500	1370.07	418.93	788.80	6.09	788.80	49.72	861.25	$5.53{\cdot}10^{-2}$	$3.56{\cdot}10^{-6}$	$1.34{\cdot}10^{7}$	Zirconia	-	-	-	-	-
2129	1800	500	1372.80	418.93	784.68	6.10	784.68	49.61	861.37	$5.51{\cdot}10^{-2}$	$3.55{\cdot}10^{-6}$	$1.34{\cdot}10^{7}$	Zirconia	N_2	107.82	299.52	$8.00{\cdot}10^{-3}$	0.017
2130	1800	500	1369.58	418.93	776.58	6.11	776.58	49.50	861.50	$5.47{\cdot}10^{-2}$	$3.54{\cdot}10^{-6}$	$1.33{\cdot}10^{7}$	Zirconia	N_2	167.10	300.33	$1.82{\cdot}10^{-2}$	0.039
2132	1800	500	1369.20	418.93	776.10	6.11	776.10	49.49	861.50	$5.46{\cdot}10^{-2}$	$3.54{\cdot}10^{-6}$	$1.33{\cdot}10^{7}$	Zirconia	N_2	230.58	303.24	$3.25{\cdot}10^{-2}$	0.069
2133	1800	500	1370.04	418.93	774.27	6.11	774.27	49.45	861.55	$5.46{\cdot}10^{-2}$	$3.54{\cdot}10^{-6}$	$1.33{\cdot}10^{7}$	Zirconia	He	235.56	298.02	$5.00{\cdot}10^{-3}$	0.011

Table E.3: Overview of flat plate turbulent experiments from Chapter 5. The values below refer to steady condition two. Note: the total temperature values were determined based on total temperature measurements taken prior to the experimental campaign at the same condition. The Mach number was determined based on the mean Mach number from Table E.2 due to a higher Kulite pressure likely caused by the boundary layer trip.

Shot number	Tunnel parameters		Measured values			Derived values							Material	Injected gas	Gas injection measured		Gas injection derived	
	P_{fill} / kPa	T_{fill} / K	P_0 / kPa	T_0 / K	P_{Kulite} / Pa	M	P_e / Pa	T_e / K	u_e / ms^{-1}	ρ_e / kg m^{-3}	μ_e / Pa s	Re_u / m^{-1}			P_{pl} / kPa	T_{pl} / K	$\dot{m}_f$ / kg m^{-3}	F / %
2111	4000	400	3008.40	357.44	1923.52	6.10	1723.76	42.36	795.61	$1.42{\cdot}10^{-1}$	$3.03{\cdot}10^{-6}$	$3.72{\cdot}10^{7}$	METAPOR CE170	-		-	-	-
2112	4000	400	3002.28	357.44	1865.26	6.10	1720.25	42.36	795.61	$1.41{\cdot}10^{-1}$	$3.03{\cdot}10^{-6}$	$3.72{\cdot}10^{7}$	METAPOR CE170	N_2	68.91	295.09	$5.02{\cdot}10^{-2}$	0.045
2113	4000	400	2994.55	357.44	1941.02	6.10	1715.82	42.36	795.61	$1.41{\cdot}10^{-1}$	$3.03{\cdot}10^{-6}$	$3.71{\cdot}10^{7}$	METAPOR CE170	N_2	97.97	293.05	$9.66{\cdot}10^{-2}$	0.086
2114	4000	400	2994.68	357.44	1935.04	6.10	1715.89	42.36	795.61	$1.41{\cdot}10^{-1}$	$3.03{\cdot}10^{-6}$	$3.71{\cdot}10^{7}$	METAPOR CE170	N_2	132.77	292.46	$1.64{\cdot}10^{-1}$	0.146
2115	4000	400	2995.99	357.44	1936.38	6.10	1716.65	42.36	795.61	$1.41{\cdot}10^{-1}$	$3.03{\cdot}10^{-6}$	$3.71{\cdot}10^{7}$	METAPOR CE170	N_2	194.23	291.91	$3.05{\cdot}10^{-1}$	0.271
2116	4000	400	3003.46	357.44	1968.86	6.10	1720.92	42.36	795.61	$1.42{\cdot}10^{-1}$	$3.03{\cdot}10^{-6}$	$3.72{\cdot}10^{7}$	METAPOR CE170	-		-	-	-
2118	4000	400	2995.51	357.44	2205.32	6.10	1716.37	42.36	795.61	$1.41{\cdot}10^{-1}$	$3.03{\cdot}10^{-6}$	$3.71{\cdot}10^{7}$	METAPOR CE170	He	107.89	291.33	$1.67{\cdot}10^{-2}$	0.015
2117	4000	400	2996.39	357.44	2101.75	6.10	1716.87	42.36	795.61	$1.41{\cdot}10^{-1}$	$3.03{\cdot}10^{-6}$	$3.71{\cdot}10^{7}$	METAPOR CE170	He	139.07	291.13	$2.75{\cdot}10^{-2}$	0.024
2125	4000	400	3000.44	357.44	2272.62	6.10	1719.19	42.36	795.61	$1.41{\cdot}10^{-1}$	$3.03{\cdot}10^{-6}$	$3.71{\cdot}10^{7}$	Zirconia	-		-	-	-
2126	4000	400	2997.36	357.44	2230.20	6.10	1717.43	42.36	795.61	$1.41{\cdot}10^{-1}$	$3.03{\cdot}10^{-6}$	$3.71{\cdot}10^{7}$	Zirconia	N_2	184.03	298.70	$2.00{\cdot}10^{-2}$	0.020
2127	4000	400	2991.36	357.44	2257.55	6.10	1713.99	42.36	795.61	$1.41{\cdot}10^{-1}$	$3.03{\cdot}10^{-6}$	$3.70{\cdot}10^{7}$	Zirconia	N_2	281.72	298.64	$5.00{\cdot}10^{-2}$	0.040

Table E.4: Overview of flat plate shock impingement transitional experiments from Chapter 6. The values below refer to steady condition two. Note: the total temperature values were determined based on total temperature measurements taken prior to the experimental campaign at the same condition. The Mach number was determined based on the mean Mach number from Table E.2 due to a higher Kulite pressure likely caused by the SWBLI.

Shot number	Tunnel parameters		Measured values			Derived values							Material	Injected gas	Gas injection measured		Gas injection derived	
	P_{fill} / kPa	T_{fill} / K	P_0 / kPa	T_0 / K	P_{Kulite} / Pa	M	P_e / Pa	T_e / K	u_e / ms^{-1}	ρ_e / kg m^{-3}	μ_e / Pa s	Re_u / m^{-1}			P_{pl} / kPa	T_{pl} / K	$\dot{m}_f$ / kg m^{-3}	F / %
2102	1800	500	1375.04	418.93	788.13	6.10	788.13	49.65	861.32	$5.53{\cdot}10^{-2}$	$3.55{\cdot}10^{-6}$	$1.34{\cdot}10^{7}$	METAPOR CE170	-	-	-	-	-
2107	1800	500	1367.59	418.93	788.13	6.09	788.13	49.73	861.23	$5.52{\cdot}10^{-2}$	$3.56{\cdot}10^{-6}$	$1.34{\cdot}10^{7}$	METAPOR CE170	N_2	108.02	292.93	$1.15{\cdot}10^{-1}$	0.242
2108	1800	500	1365.72	418.93	788.13	6.09	788.13	49.75	861.21	$5.52{\cdot}10^{-2}$	$3.56{\cdot}10^{-6}$	$1.33{\cdot}10^{7}$	METAPOR CE170	N_2	177.39	292.45	$2.64{\cdot}10^{-1}$	0.556
2109	1800	500	1367.51	418.93	788.13	6.09	788.13	49.73	861.23	$5.52{\cdot}10^{-2}$	$3.56{\cdot}10^{-6}$	$1.34{\cdot}10^{7}$	METAPOR CE170	N_2	389.38	292.88	$8.18{\cdot}10^{-1}$	1.719
2103	1800	500	1366.85	418.93	788.13	6.09	788.13	49.74	861.22	$5.52{\cdot}10^{-2}$	$3.56{\cdot}10^{-6}$	$1.34{\cdot}10^{7}$	METAPOR CE170	He	99.79	291.46	$1.44{\cdot}10^{-2}$	0.030
2104	1800	500	1368.28	418.93	788.13	6.09	788.13	49.72	861.24	$5.52{\cdot}10^{-2}$	$3.56{\cdot}10^{-6}$	$1.34{\cdot}10^{7}$	METAPOR CE170	He	123.69	291.42	$2.19{\cdot}10^{-2}$	0.046
2105	1800	500	1364.47	418.93	788.13	6.09	788.13	49.76	861.19	$5.52{\cdot}10^{-2}$	$3.56{\cdot}10^{-6}$	$1.33{\cdot}10^{7}$	METAPOR CE170	He	173.19	291.77	$4.18{\cdot}10^{-2}$	0.088
2106	1800	500	1368.68	418.93	788.13	6.09	788.13	49.72	861.24	$5.52{\cdot}10^{-2}$	$3.56{\cdot}10^{-6}$	$1.34{\cdot}10^{7}$	METAPOR CE170	He	279.30	292.18	$1.02{\cdot}10^{-1}$	0.214

Table E.5: Overview of flat plate shock impingement turbulent experiments from Chapter 6. The values below refer to steady condition one. Note: the total temperature values were determined based on total temperature measurements taken prior to the experimental campaign at the same condition. The Mach number was determined based on the mean Mach number from Table E.2 due to a higher Kulite pressure likely caused by the SWBLI.

Shot number	Tunnel parameters		Measured values			Derived values							Material	Injected gas	Gas injection measured		Gas injection derived	
	P_{fill} / kPa	T_{fill} / K	P_0 / kPa	T_0 / K	P_{Kulite} / Pa	M	P_e / Pa	T_e / K	u_e / ms^{-1}	ρ_e / kg m^{-3}	μ_e / Pa s	Re_u / m^{-1}			P_{pl} / kPa	T_{pl} / K	$\dot{m}_f$ / kg m^{-3}	F / %
2119	4000	400	3460.01	357.44	2289.11	6.10	1982.52	42.36	795.61	$1.63{\cdot}10^{-1}$	$3.03{\cdot}10^{-6}$	$4.28{\cdot}10^{7}$	METAPOR CE170	-	-	-	-	-
2122	4000	400	3453.43	357.44	2076.92	6.10	1978.75	42.36	795.61	$1.63{\cdot}10^{-1}$	$3.03{\cdot}10^{-6}$	$4.27{\cdot}10^{7}$	METAPOR CE170	N_2	267.57	292.22	$4.90{\cdot}10^{-1}$	0.379
2123	4000	400	3464.35	357.44	2183.86	6.10	1985.01	42.36	795.61	$1.63{\cdot}10^{-1}$	$3.03{\cdot}10^{-6}$	$4.29{\cdot}10^{7}$	METAPOR CE170	N_2	365.36	293.85	$7.50{\cdot}10^{-1}$	0.577
2120	4000	400	3467.32	357.44	2228.88	6.10	1986.71	42.36	795.61	$1.63{\cdot}10^{-1}$	$3.03{\cdot}10^{-6}$	$4.29{\cdot}10^{7}$	METAPOR CE170	He	202.12	291.13	$5.62{\cdot}10^{-2}$	0.043
2121	4000	400	3465.73	357.44	2241.95	6.10	1985.79	42.36	795.61	$1.63{\cdot}10^{-1}$	$3.03{\cdot}10^{-6}$	$4.29{\cdot}10^{7}$	METAPOR CE170	He	336.12	291.22	$1.41{\cdot}10^{-1}$	0.109

References

[1] T.A. Heppenheimer. *Facing the Heat Barrier: A History of Hypersonics*. 1947.

[2] *NASA Picks SpaceX to Land Next Americans on Moon*. Mar. 2021. URL: https://www.nasa.gov/press-release/as-artemis-moves-forward-nasa-picks-spacex-to-land-next-americans-on-moon (visited on 12/03/2022).

[3] Missile Defense Project. *Avangard | Missile Threat*. July 2021. URL: https://missilethreat.csis.org/missile/avangard/ (visited on 12/03/2022).

[4] R. Jeffrey Smith. *Hypersonic Missiles Are Unstoppable. And They're Starting a New Global Arms Race*. 2019. URL: https://www.nytimes.com/2019/06/19/magazine/hypersonic-missiles.html (visited on 12/03/2022).

[5] Jeremy Hsu. *Hypersonic 'SpaceLiner' Aims to Fly Passengers in 2050*. 2013.

[6] Richard Varvill and Alan Bond. "The SKYLON Spaceplane - Progress to Realisation". In: *Journal of the British Interplanetary Society* 61 (2008), pp. 412–418.

[7] E R Van Driest. "Investigation of Laminar Boundary Layer in compressive Fluids Using the Crocco Method". In: *NACA TN 2597* (1952).

[8] John D. Anderson. "Hypersonic and High-Temperature Gas Dynamics, Third Edition". In: *Hypersonic and High-Temperature Gas Dynamics, Third Edition* (Mar. 2019). DOI: 10.2514/4.105142.

[9] Prasun N. Desai, Dan T. Lyons, Jeff Tooley, and Julie Kangas. "Entry, Descent, and Landing Operations Analysis for the Stardust Entry Capsule". In: *Journal of Spacecraft and Rockets* 45.6 (May 2012), pp. 1262–1268. DOI: 10.2514/1.37090.

[10] Daniel A Boyd. "Aerothermodynamic Analysis of a Mars Sample Return Earth-Entry Vehicle". PhD thesis. Old Dominion University, 2018. DOI: 10.25777/xhmz-ax21.

[11] Michael E. Tauber, Gene P. Menees, and Henry G. Adelman. "Aerothermodynamics of transatmospheric vehicles". In: *Journal of Aircraft* 24.9 (May 1987), pp. 594–602. DOI: 10.2514/3.45483.

[12] J. A. Fay and F. R. Riddell. "Theory of Stagnation Point Heat Transfer in Dissociated Air". In: *Journal of the Aerospace Sciences* 25.2 (Feb. 1958), pp. 73–85. DOI: 10.2514/8.7517.

[13] Kenneth Sutton and Randolph A Graves Jr. "A general stagnation-point convective heating equation for arbitrary gas mixtures". In: *NASA TR R-376* (1971).

[14] Michael E Tauber. “A Review of High-Speed, Convective, Heat-Transfer Computation Methods”. In: *NASA TP-2914* (May 1989).

[15] R. W. Detra and H. Hidalgo. “Generalized Heat Transfer Formulas and Graphs for Nose Cone Re-Entry Into the Atmosphere”. In: *Journal of the American Rocket Society* 31.3 (June 1961), pp. 318–321. DOI: 10.2514/8.5471.

[16] Thomas Reimer, Markus Kuhn, Ali Gülhan, Burkhard Esser, Martin Sippel, and Arnold Van Foreest. “Transpiration Cooling Tests of Porous CMC in Hypersonic Flow”. In: *17th AIAA International Space Planes and Hypersonic Systems and Technologies Conference*. 2011. DOI: 10.2514/6.2011-2251.

[17] Charles Camarda. “Space Shuttle Design and Lessons Learned”. In: *NATO Science and Technology Lecture Series on "Hypersonic Flight Testing"*. Rhodes-St-Genese, Mar. 2014. DOI: 10.13140/RG.2.1.2635.2405.

[18] Holger Babinsky and John K. Harvey. *Shock wave-boundary-layer interactions*. Cambridge University Press, Jan. 2011, pp. 1–461. DOI: 10.1017/CBO9780511842757.

[19] Barry E. Edney. “Effects of shock impingement on the heat transfer around blunt bodies”. In: *AIAA Journal* 6.1 (May 1968), pp. 15–21. DOI: 10.2514/3.4435.

[20] Th. Eggers. “Numerical Investigation on the Potential of Steam Cooling for the Skylon Spaceplane in Hypersonic Flow”. In: *28th International Congress of the Aeronautical Sciences*. 2012.

[21] Roger D. Launius and Dennis R. Jenkins. *Coming Home: Reentry and Recovery from Space*. NASA, 2011, pp. 1–339.

[22] Joe D. Watts. “Flight Experience with Shock Impingement and Interference Heating on the X-15 Research Airplane”. In: *NASA TM X-1669* (1968), pp. 1–25.

[23] *PICA Heat Shield Technology Used by SpaceX | NASA*. Mar. 2017. URL: https://www.nasa.gov/offices/oct/images/phenolic-impregnated-carbon-ablator-pica-heat-shield-technology-is-used-by-spacex (visited on 12/03/2022).

[24] R. J. Swigart, W. C.L. Shih, J. H. Wang, R. Snow, J. W. Trolier, S. A. Leone, A. Martellucci, and A. L. Laganelli. “Hypersonic film cooling effectiveness and aero-optical effects”. In: *AIAA 1st National Fluid Dynamics Conference, 1988* (1988). DOI: 10.2514/6.1988-3824.

[25] Caihong Su. “Aero-optical analysis of a film-cooled optical window based on linear stability analysis”. In: *AIAA Journal* 57.7 (Apr. 2019), pp. 2840–2850. DOI: 10.2514/1.J058150/ASSET/IMAGES/LARGE/FIGURE17.JPEG.

[26] “Integral cooling system for high-temperature missile structures”. US4739952A. Daniel N. Giles. Apr. 26, 1988.

[27] Marc Ewenz Rocher, Tobias Hermann, Matthew McGilvray, Hassan Saad Ifti, Fabian Hufgard, Martin Eberhart, Arne Meindl, Stefan Löhle, Tommaso Giovannini, and Luc Vandeperre. “Testing a Transpiration Cooled Zirconium-Di-Boride sample in the Plasma Tunnel at IRS”. In: *AIAA Scitech 2019 Forum*. American Institute of Aeronautics and Astronautics Inc, AIAA, 2019, pp. 1–17. DOI: 10.2514/6.2019-1552.

[28] George M Low. "The Compressible Laminar Boundary Layer with Fluid Injection". In: *NACA TN 2404* (1955).

[29] W.D. Rannie. *A simplified theory of porous wall cooling*. Tech. rep. Pasadena: Jet Propulsion Laboratory, Nov. 1947, pp. 1–24.

[30] Morris W. Rubesin. "An Analytical Estimation of the Effect of Transpiration Cooling on the Heat-Transfer and Skin-Friction Characteristics of a Compressible, Turbulent Boundary Layer". In: *NACA TN 3341* (1954), pp. 1–56.

[31] M.W. Rubesin and C.C. Pappas. "An Analysis of the Turbulent Boundary Layer Characteristics of a Flat Plate with Distributed Light Gas Injection". In: *NAVA TN 4149* (Feb. 1958).

[32] C.C. Pappas and Arthur F. Okuno. "Heat-transfer measurement for binary gas laminar boundary layers with high rates of injection". In: *NASA TN D-2473* (1964), pp. 1–45.

[33] C.J. Stalmach, J.J. Bertin, and T.C. Pope. "A Study of Boundary Layer Transition on Outgassing Cones in Hypersonic Flow". In: *NASA CR-1908* (1971).

[34] C. R. Wimberly, F. K. McGinnis, and J. J. Bertin. "Transpiration and film cooling effects for a slender cone in hypersonic flow". In: *AIAA Journal* 8.6 (May 1970), pp. 1032–1038. DOI: 10.2514/3.5827.

[35] E. P. Volchkov, E. G. Zaulichnyi, S. S. Kutateladze, and A. I. Leont'ev. "Film cooling by injection into a turbulent boundary layer". In: *Journal of Applied Mechanics and Technical Physics* 8.2 (Mar. 1967), pp. 63–64. DOI: 10.1007/BF00918038.

[36] W. M. Kays. "Heat transfer to the transpired turbulent boundary layer". In: *International Journal of Heat and Mass Transfer* 15.5 (May 1972), pp. 1023–1044. DOI: 10.1016/0017-9310(72)90237-2.

[37] Markus Kuhn and H. Hald. "Application of transpiration cooling for hot structures". In: *Notes on Numerical Fluid Mechanics and Multidisciplinary Design* 98 (2008), pp. 82–103. DOI: 10.1007/978-3-540-77819-6{_}6.

[38] Hannah Boehrk, Olivier Piol, and Markus Kuhn. "Heat Balance of a Transpiration-Cooled Heat Shield". In: *Journal of Thermophysics and Heat Transfer* 24.3 (July 2010), pp. 581–588. DOI: 10.2514/1.47172.

[39] A. Gülhan and S. Braun. "An experimental study on the efficiency of transpiration cooling in laminar and turbulent hypersonic flows". In: *Experiments in Fluids* 50.3 (Mar. 2011), pp. 509–525. DOI: 10.1007/s00348-010-0945-6.

[40] A. Brune, S. Hosder, S. Gulli, and L. Maddalena. "Variable Transpiration Cooling Effectiveness in Laminar and Turbulent Flows for Hypersonic Vehicles". In: *AIAA Journal* 53.1 (Dec. 2014), pp. 176–189. DOI: 10.2514/1.j053053.

[41] Hannah Böhrk. "Transpiration-Cooled Hypersonic Flight Experiment: Setup, Flight Measurement, and Reconstruction". In: *Journal of Spacecraft and Rockets* 52.3 (Apr. 2015), pp. 674–683. DOI: 10.2514/1.a33144.

[42] H. Tanno, T. Komuro, K. Itoh, Markus Kuhn, Ivaylo Petkov, and Burkard Esser. "Transpiration cooling experiments in free-piston shock tunnel HIEST". In: *8th European Workshop on Thermal Protection Systems and Hot Structures*. Noordwijk, Niederlande, 2016.

[43] Steven P. Schneider. "Hypersonic Boundary-Layer Transition with Ablation and Blowing". In: *Journal of Spacecraft and Rockets* 47.2 (May 2010), pp. 225–237. DOI: 10.2514/1.43926.

[44] Nicolas Gascoin, Guillaume Fau, Philippe Gillard, Markus Kuhn, Marc Bouchez, and Johan Steelant. "Comparison of Two Permeation Test Benches and of Two Determination Methods for Darcy's and Forchheimer's Permeabilities." In: *Journal of Porous Media* 15.8 (2012), pp. 705–720. DOI: 10.1615/JPORMEDIA.V15.I8.10.

[45] Michael S. Holden and Shirley J. Sweet. "Studies of transpiration cooling with shock interaction in hypersonic flow". In: *AIAA 25th Plasmadynamics and Lasers Conference, 1994*. American Institute of Aeronautics and Astronautics Inc, AIAA, 1994. DOI: 10.2514/6.1994-2475.

[46] Tobias Langener, Jens Von Wolfersdorf, and Johan Steelant. "Experimental Investigations on Transpiration Cooling for Scramjet Applications Using Different Coolants". In: *AIAA Journal* 49.7 (Apr. 2011), pp. 1409–1419. DOI: 10.2514/1.j050698.

[47] Stefan Löhle, Sven Schweikert, and Jens von Wolfersdorf. "Method for Heat Flux Determination of a Transpiration-Cooled Wall from Pressure Data". In: *Journal of Thermophysics and Heat Transfer* 30.3 (Jan. 2016), pp. 567–572. DOI: 10.2514/1.t4815.

[48] Christian Dittert, Markus Selzer, and Hannah Böhrk. "Flowfield and Pressure Decay Analysis of Porous Cones". In: *AIAA Journal* 55.3 (Jan. 2017), pp. 874–882. DOI: 10.2514/1.j055298.

[49] Kevin Basore, Markus Selzer, Vincent Wheatley, Russell R. Boyce, David J. Mee, Bianca R. Capra, Markus Kuhn, and Stefan Brieschenk. "Performance Comparison of Distributed Injection Methods for Hypersonic Film-Cooling". In: *20th Australasian Fluid Mechanics Conference*. 2016.

[50] J. Wang and L. J. Vandeperre. "Deformation and Hardness of UHTCs as a Function of Temperature". In: *Ultra-High Temperature Ceramics: Materials for Extreme Environment Applications* 9781118700785 (Nov. 2014), pp. 236–266. DOI: 10.1002/9781118700853.CH10.

[51] John J. Bertin and Russell M. Cummings. "Critical Hypersonic Aerothermodynamic Phenomena". In: *Annual Review of Fluid Mechanics* 38 (Dec. 2006), pp. 129–157. DOI: 10.1146/ANNUREV.FLUID.38.050304.092041.

[52] M. Ewenz Rocher, T Hermann, and M McGilvray. "Oxidation response of transpiration cooled ZrB2 on a hypersonic stagnation point". In: *Journal of Spacecraft and Rockets* (2022).

[53] D. G. Fletcher. "Fundamentals of Hypersonic Flow - Aerothermodynamics". In: *Tech. Rep. RTO-EN-AVT-116,* RO AVT Lecture Series, 2004.

[54] Martin Sippel and Tobias Schwanekamp. "The SpaceLiner Hypersonic System-Aerothermodynamic Requirements and Design Process". In: *8th European Symposium on Aerothermodynamics for Space Vehicles*. 2015.

[55] R. Longstaff and R. Varvill. "SKYLON D1 – Preliminary re-entry trajectory analysis." In: *SKY-REL-RP-0013* (Aug. 2012), pp. 1–47.

[56] Michael S. Holden and Joseph M. Kolly. "Measurements of heating in regions of shock/shock interaction in hypersonic flow". In: *33rd Aerospace Sciences Meeting and Exhibit*. American Institute of Aeronautics and Astronautics Inc, AIAA, 1995. DOI: 10.2514/6.1995-640.

[57] Tobias Hermann, Matthew McGilvray, and Imran Naved. "Performance of Transpiration-Cooled Heat Shields for Reentry Vehicles". In: *AIAA Journal* 58.2 (Feb. 2020), pp. 830–841. DOI: 10.2514/1.J058515.

[58] Imran Naved, Tobias Hermann, and Matthew McGilvray. "Numerical Simulation of Transpiration Cooling for a High-Speed Vehicle with Substructure". In: *AIAA Journal* (Mar. 2021), pp. 1–12. DOI: 10.2514/1.J059771.

[59] Imran Naved, Tobias Hermann, Matthew McGilvray, Marc Ewenz Rocher, Chris Hambidge, Luke Doherty, Laurent Le Page, Madeleine Grossmann, and Luc Vandeperre. "Heat Transfer Measurements of a Transpiration Cooled Stagnation Point in Transient Hypersonic Flow". In: *Journal of Thermophysics and Heat Transfer* (2022).

[60] Imran Naved, Tobias Hermann, Chris Hambidge, Chiara Falsetti, Hassan Saad Ifti, Matthew McGilvray, Lullia Elizarova, and Luc Vandeperre. "Transpiration Cooling Heat Transfer Experiments in Laminar and Turbulent Hypersonic Flow". In: *Journal of Thermophysics and Heat Transfer* (2022).

[61] Imran Naved, Tobias Hermann, Chris Hambidge, and Matthew McGilvray. "Experimental Studies of Hypersonic Shock Impingement on a Transpiration-Cooled Flat Plate". In: *Journal of Spacecraft and Rockets* (2022).

[62] D.A. Nield and A. Bajan. *Convection in Porous Media*. 4th ed. New York: Springer, 2013, pp. 1–35.

[63] Tobias Langener, Jens Von Wolfersdorf, Markus Kuhn, and Johan Steelant. "Transpiration cooling with supersonic flows and foreign gas injection". In: *46th AIAA/ASME/SAE/ASEE Joint Propulsion Conference and Exhibit*. American Institute of Aeronautics and Astronautics Inc., 2010. DOI: 10.2514/6.2010-6794.

[64] Sabri Ergun and A. A. Orning. "Fluid Flow through Randomly Packed Columns and Fluidized Beds". In: *Industrial & Engineering Chemistry* 41.6 (Mar. 2005), pp. 1179–1184. DOI: 10.1021/ie50474a011.

[65] Hassan Saad Ifti, Tobias Hermann, Matthew McGilvray, Laura Larrimbe, Rowan Hedgecock, and Luc Vandeperre. "Flow Characterisation of Porous Ultra-High-Temperature Ceramics for Transpiration Cooling". In: *AIAA Journal* (2022). DOI: https://doi.org/10.2514/1.J061009.

[66] M. D.M. Innocentini, A. C. Rizzi, L. A. Nascimento, and V. C. Pandolfelli. "The pressure-decay technique for air permeability evaluation of dense refractory ceramics". In: *Cement and Concrete Research* 34.2 (Feb. 2004), pp. 293–298. DOI: 10.1016/j.cemconres.2003.08.006.

[67] Tobias Hermann and M. McGilvray. "Analytical solution of flows in porous media for transpiration cooling applications". In: *Journal of Fluid Mechanics* 915 (2021), p. 38. DOI: 10.1017/JFM.2021.126.

[68] Daniel Prokein, Jens von Wolfersdorf, and Hannah Böhrk. "Analysis of anisotropy effects for transpiration cooled CMC leading edges using OpenFOAM". In: *20th AIAA International Space Planes and Hypersonic Systems and Technologies Conference, 2015* (2015). DOI: 10.2514/6.2015-3552.

[69] V. König, M. Rom, S. Müller, M. Selzer, S. Schweikert, and J. Von Wolfersdorf. "Numerical and experimental investigation of transpiration cooling with carbon/carbon characteristic outflow distributions". In: *Journal of Thermophysics and Heat Transfer* 33.2 (Jan. 2019), pp. 449–461. DOI: 10.2514/1.T5457/ASSET/IMAGES/LARGE/FIGURE15.JPEG.

[70] Behzad Ghanbarian, Allen G. Hunt, Robert P. Ewing, and Muhammad Sahimi. "Tortuosity in Porous Media: A Critical Review". In: *Soil Science Society of America Journal* 77.5 (Sept. 2013), pp. 1461–1477. DOI: 10.2136/SSSAJ2012.0435.

[71] Yvan Champoux, Michael R. Stinson, and Gilles A. Daigle. "Air-based system for the measurement of porosity". In: *The Journal of the Acoustical Society of America* 89.2 (June 1998), p. 910. DOI: 10.1121/1.1894653.

[72] Josef Prokop, Libor Švéda, Alexandr Jančárek, and Ladislav Pína. "Porosity Measurement Method by X-Ray Computed Tomography". In: *Key Engineering Materials* 409 (2009), pp. 402–405. DOI: 10.4028/WWW.SCIENTIFIC.NET/KEM.409.402.

[73] Hassan Saad Ifti, Tobias Hermann, and Matthew McGilvray. "Transpiration Cooling at Mach 5 Employing Porous UHTC". In: *Conference on Flight vehicles, Aerothermodynamics and Re-entry Missions and Engineering (FAR)*. 2019, p. 8.

[74] Tobias Hermann, Matthew McGilvray, Hassan Saad Ifti, Fabian Hufgard, and Stefan Löhle. "Thermal impulse response in porous media for transpiration-cooling systems". In: *Journal of Thermophysics and Heat Transfer* 34.2 (Jan. 2020), pp. 447–456. DOI: 10.2514/1.T5841.

[75] John Florio, Jack B. Henderson, Frederick L. Test, and Ramamurthy Hariharan. "Characterization of Forced Convection Heat Transfer in Decomposing, Glass-Filled Polymer Composites:" in: *Journal of Composite Materials* 25.11 (July 2016), pp. 1515–1539. DOI: 10.1177/002199839102501108.

[76] David E. Glass, Arthur D. Dilley, and H. Neale Kelly. "Numerical Analysis of Convection / Transpiration Cooling". In: *Journal of Spacecraft and Rockets* 38.1 (Aug. 2008), pp. 15–20. DOI: 10.2514/2.3666.

[77] L. B. Younis and R. Viskanta. "Experimental determination of the volumetric heat transfer coefficient between stream of air and ceramic foam". In: *International Journal of Heat and Mass Transfer* 36.6 (Jan. 1993), pp. 1425–1434. DOI: 10.1016/S0017-9310(05)80053-5.

[78] X. Fu, R. Viskanta, and J. P. Gore. "Measurement and correlation of volumetric heat transfer coefficients of cellular ceramics". In: *Experimental Thermal and Fluid Science* 17.4 (Aug. 1998), pp. 285–293. DOI: 10.1016/S0894-1777(98)10002-X.

[79] Tzer Ming Jeng, Meng Ping Wang, Guang Jyh Hwang, and Ying Huei Hung. "A new semi-empirical model for predicting heat transfer characteristics in porous channels". In: *Experimental Thermal and Fluid Science* 29.1 (Dec. 2004), pp. 9–21. DOI: 10.1016/J.EXPTHERMFLUSCI.2003.12.019.

[80] B. Mayer, Hassan Gomaa, Bernhard Weigand, and Yuri Zudin. "An Analytical Model to Evaluate Heat Transfer Characteristics in Porous Media by a Periodic Quasi Steady-State Technique". In: *ISROMAC 2012—14th International Symposium on Transport Phenomena and Dynamics of Rotating Machinery*. 2012.

[81] Hui Wang and Liejin Guo. "Volumetric Convective Heat Transfer Coefficient Model for Metal Foams". In: *https://doi.org/10.1080/01457632.2018.1432045* 40.5-6 (Apr. 2018), pp. 464–475. DOI: 10.1080/01457632.2018.1432045.

[82] Sven Schweikert, Jens von Wolfersdorf, Markus Selzer, and Hermann Hald. "Characterization of Actively Cooled Porous C / C Wall Segments According to Pressure Loss and Internal Temperature Distribution". In: *7th European Workshop on Thermal Protection Systems & Hot Structures*. 2013.

[83] Kharthik Chakravarthy, Laurent Le Page, Tobias A. Hermann, Matthew McGilvray, and Benjamin A O Williams. "Characterisation of internal heat transfer in transpiring porous media using optical diagnostics". In: *International Conference on Flight vehicles, Aerothermodynamics and Re-entry Missions and Engineering*. Monopoli, 2019.

[84] Rui Ding, Jianhua Wang, Fei He, Guangqi Dong, and Longsheng Tang. "Numerical investigation on the performances of porous matrix with transpiration and film cooling". In: *Applied Thermal Engineering* 146 (Jan. 2019), pp. 422–431. DOI: 10.1016/J.APPLTHERMALENG.2018.09.134.

[85] Daniel Prokein, Christian Dittert, Hannah Böhrk, and Jens von Wolfersdorf. "Numerical simulation of transpiration cooling experiments in supersonic flow using OpenFOAM". In: *CEAS Space Journal* 12.2 (June 2020), pp. 247–265. DOI: 10.1007/S12567-019-00292-6.

[86] Tobias Hermann, Imran Naved, and Matthew McGilvray. "Tool for Rapid Transient Transpiration-Cooled Reentry Simulation". In: *AIAA Journal* 58.2 (Feb. 2020), pp. 842–853. DOI: 10.2514/1.j058516.

[87] Wesley M. Mann. "Effective displacement thickness for boundary layers with surface mass transfer". In: *AIAA Journal* 1.5 (May 1963), pp. 1181–1182. DOI: 10.2514/3.1749.

[88] Nisiki Hayasi. "Displacement thickness of the boundary layer with blowing". In: *AIAA Journal* 3.12 (May 1965), pp. 2348–2349. DOI: 10.2514/3.3372.

[89] E. R. G. Eckert. "Engineering Relations for Heat Transfer and Friction in High-Velocity Laminar and Turbulent Boundary-Layer Flow Over Surfaces With Constant Pressure and Temperature". In: *Journal of Fluids Engineering* 78.6 (Aug. 1956), pp. 1273–1283. DOI: 10.1115/1.4014011.

[90] E. R. G. Eckert, P. J. Schneider, A. A. Hayday, and R. M. Larson. "Mass-Transfer Cooling of a Laminar Boundary Layer by Injection of a Light-Weight Foreign Gas". In: *Journal of Jet Propulsion* 28.1 (June 1958), pp. 34–39. DOI: 10.2514/8.7218.

[91] William M Kays, Michael E Crawford, and Bernhard Weigand. *Convective Heat and Mass Transfer*. 4th. New York: McGraw-Hill, 2005.

[92] H. S. Mickley, R. C. Ross, A. L. Squyers, and W. E. Stewart. "Heat, Mass, and Momentum Transfer for Flow Over a Flat Plate With Blowing or Suction". In: *NACA TN 3208* (1954).

[93] Morris W Rubesin. "The influence of surface injection on heat-transfer and skin friction associated with the high-speed turbulent boundary layer". In: *NACA Research Memorandum* (1956).

[94] E. Roy Bartle and Bernard M. Leadon. "Experimental Evaluation of Heat Transfer with Transpiration Cooling in a Turbulent Boundary Layer at M = 3.2". In: *Journal of the Aerospace Sciences* 27.1 (Jan. 1960), pp. 78–80. DOI: 10.2514/8.8397.

[95] Jens Meinert, J-ograve, rg Huhn, Erhan Serbest, and Oskar J. Haidn. "Turbulent Boundary Layers with Foreign Gas Transpiration". In: *Journal of Spacecraft and Rockets* 38.2 (Mar. 2008), pp. 191–198. DOI: 10.2514/2.3693.

[96] Hannah Boehrk, Viola Wartemann, Thino Eggers, Jan Martinez Schramm, Alexander Wagner, and Klaus Hannemann. "Shock Tube Testing of the Transpiration-Cooled Heat Shield Experiment AKTiV". In: *18th AIAA/3AF International Space Planes and Hypersonic Systems and Technologies Conference*. American Institute of Aeronautics and Astronautics (AIAA), Dec. 2012, pp. 1–8. DOI: 10.2514/6.2012-5935.

[97] Zheng Huang, Yin-hai Zhu, Yan-bin Xiong, and Pei-Xue Jiang. "Investigation of Supersonic Transpiration Cooling through Sintered Metal Porous Flat Plates". In: *Journal of Porous Media* 18.11 (Sept. 2015), pp. 1047–1057. DOI: 10.1615/jpormedia.2015012159.

[98] S. Mohammed Ibrahim, P. Vivek, and K. P. J. Reddy. "Experimental Investigation on Transpiration Cooling Effectiveness for Spacecraft Entering Martian Atmosphere". In: *AIAA Journal* 54.9 (May 2016), pp. 2922–2926. DOI: 10.2514/1.j054757.

[99] Tobias Hermann, Hassan Saad Ifti, Matthew Mcgilvray, Luke Doherty, and Rowland Penty Geraets. "Mixing Characteristics in a Hypersonic Flow around a Transpiration Cooled Flat Plate Model". In: *HiSST: International Conference on High-Speed Vehicle Science Technology* November (2018), pp. 1–15.

[100] Hassan Saad Ifti, Tobias Hermann, Marc Ewenz Rocher, Luke Doherty, Christopher Hambidge, Matthew McGilvray, and Luc Vandeperre. "Laminar transpiration cooling experiments in hypersonic flow". In: *Experiments in Fluids* 63.6 (June 2022), pp. 1–14. DOI: 10.1007/S00348-022-03446-1/FIGURES/12.

[101] Richard A. Thompson and Peter A. Gnoffo. "Implementation of a blowing boundary condition in the LAURA code". In: *46th AIAA Aerospace Sciences Meeting and Exhibit*. American Institute of Aeronautics and Astronautics Inc., 2008. DOI: 10.2514/6.2008-1243.

[102] Junxiang Shi and Jianhua Wang. "A Numerical Investigation on the Laminar Boundary Flow Layer with Transpiration Cooling". In: *Transport in Porous Media* 78.1 (Sept. 2009), pp. 37–46. DOI: 10.1007/S11242-008-9279-8.

[103] S. Gulli, L. Maddalena, and S. Hosder. "Variable transpiration cooling for the thermal management of reusable hypersonic vehicles". In: *Aerospace Science and Technology* 29.1 (Aug. 2013), pp. 434–444. DOI: 10.1016/J.AST.2013.05.002.

[104] W. Dahmen, T. Gotzen, S. Müller, and M. Rom. "Numerical simulation of transpiration cooling through porous material". In: *International Journal for Numerical Methods in Fluids* 76.6 (2014), pp. 331–365. DOI: 10.1002/fld.3935.

[105] Adriano Cerminara, Tobias Hermann, Hassan Saad Ifti, Ralf Deiterding, Neil Sandham, and Matthew McGilvray. "Influence of instability modes on cooling performance in hypersonic boundary layer with slot injection". In: *Aerospace Science and Technology* 109 (Feb. 2021), p. 106409. DOI: 10.1016/J.AST.2020.106409.

[106] Hassan Saad Ifti, Tobias Hermann, Matthew McGilvray, and Jim Merrifield. "Numerical Simulation of Transpiration Cooling in a Laminar Hypersonic Boundary-Layer". In: *Journal of Spacecraft and Rockets* (2022).

[107] By W Morris Rubesin, Constantine C Pappas, Arthur F Okuno, and Moffett Field. "The Effect of Fluid Injection on the Compressible Turbulent Boundary Layer - Preliminary Tests of Transpiration Cooling of a Flat Plate at M=2.7 with Air as the Injected Gas". In: *NACA Research Momorandum* (1955).

[108] Robert T. Swann and Claud M. Pittman. "Numerical Analysis of the Transient Response of Advanced Thermal Protection Systems for Atmospheric Entry". In: *NASA TN D-1379* (1962).

[109] John T. Howe and Yvonne S. Sheaffer. "Mass Addition in the Stagnation Region for Velocity up to 50,000 Feet Per Second". In: *NASA TR R-207* (1964).

[110] C. B. Moyer and R. Rindal. "An analysis of the coupled chemically reacting boundary layer and charring ablator. Part 2 - Finite difference solution for the in-depth response of charring materials considering surface chemical and energy balances". In: *NASA CR-1061* (1968).

[111] Sreekanth and N. M. Reddy. "Numerical simulation of transpiration cooling over blunt bodies at hypersonic mach numbers". In: *30th Thermophysics Conference*. American Institute of Aeronautics and Astronautics Inc, AIAA, 1995. DOI: 10.2514/6.1995-2082.

[112] J. Hartnett and C. Liu. "Transpiration Cooling Correlations for Air and Non-Air Free Streams". In: *AIAA 3rd Thermophysics Conference*. American Institute of Aeronautics and Astronautics (AIAA), June 1968. DOI: 10.2514/6.1968-758.

[113] Kenneth K. Yoshikawa. "Linearised Theory of Stagnation Point Heat and Mass Transfer at Hypersonic Speeds". In: *NASA TN D-5246* (1969).

[114] C.C. Pappas and George Lee. "Heat transfer and pressure on a hypersonic blunt cone with mass addition". In: *AIAA Journal* 8.5 (May 1970), pp. 954–956. DOI: 10.2514/3.5801.

[115] G.E. Kaattari. "Effects of mass addition on blunt-body boundary-layer transition and heat transfer". In: *NASA TP-1139* (Jan. 1978).

[116] Arnold Van Foreest, Martin Sippel, Ali Gülhan, Burkard Esser, B. A.C. Ambrosius, and K. Sudmeijer. "Transpiration Cooling Using Liquid Water". In: *Journal of Thermophysics and Heat Transfer* 23.4 (May 2012), pp. 693–702. DOI: 10.2514/1.39070.

[117] Joseph G. Marvin and Ronald B. Pope. "Laminar convective heating and ablation in the Mars atmosphere." In: *AIAA Journal* 5.2 (May 1967), pp. 240–248. DOI: 10.2514/3.3948.

[118] Dennis D. Stalmach and John J. Bertin. "The Analysis of a Nonsimilar Laminar Boundary Layer". In: *NASA CR 151658* (1978).

[119] Robert J. Nowak, Michael S. Hoiden, and Allan R. Wieting. "Shock/shock interference on a transpiration cooled hemispherical model". In: *AIAA 21st Fluid Dynamics, Plasma Dynamics and Lasers Conference, 1990*. American Institute of Aeronautics and Astronautics Inc, AIAA, 1990. DOI: 10.2514/6.1990-1643.

[120] Peixue Jiang, Zhiyuan Liao, Zheng Huang, Yanbing Xiong, and Yinhai Zhu. "Influence of shock waves on supersonic transpiration cooling". In: *International Journal of Heat and Mass Transfer* 129 (Feb. 2019), pp. 965–974. DOI: 10.1016/J.IJHEATMASSTRANSFER.2018.10.043.

[121] Friedolin Strauss, Jan Witte, Matthias Weißwange, Chiara Manfletti, and Stefan Schlechtriem. "Experiments on shock-boundary layer interaction and cooling efficiency in a transpiration cooled model scramjet". In: *53rd AIAA/SAE/ASEE Joint Propulsion Conference, 2017* (2017). DOI: 10.2514/6.2017-4833.

[122] Richard J. Goldstein. "Film Cooling". In: *Advances in Heat Transfer* 7.C (Jan. 1971), pp. 321–379. DOI: 10.1016/S0065-2717(08)70020-0.

[123] K. A. Heufer and H. Olivier. "Experimental and Numerical Study of Cooling Gas Injection in Laminar Supersonic Flow". In: *AIAA Journal* 46.11 (May 2008), pp. 2741–2751. DOI: 10.2514/1.34218.

[124] M. Hombsch and H. Olivier. "Film cooling in laminar and turbulent supersonic flows". In: *Journal of Spacecraft and Rockets* 50.4 (July 2013), pp. 742–753. DOI: 10.2514/1.A32346/ASSET/IMAGES/LARGE/FIGURE27.JPEG.

[125] Michael A. Keller and Markus J. Kloker. "Direct Numerical Simulation of Foreign-Gas Film Cooling in Supersonic Boundary-Layer Flow". In: *AIAA Journal* 55.1 (Nov. 2016), pp. 99–111. DOI: 10.2514/1.j055115.

[126] Lawrence W. Woodruff and George C. Lorenz. "Hypersonic turbulent transpiration cooling including downstream effects". In: *AIAA Journal* 4.6 (May 1966), pp. 969–975. DOI: 10.2514/3.3589.

[127] Richard P. Fogaroli and Alan R. Saydah. "Turbulent heat-transfer and skin-friction measurements on a porous cone with air injection at high Mach numbers." In: *AIAA Journal* 4.6 (May 1966), pp. 1116–1117. DOI: 10.2514/3.3627.

[128] H. Olivier and H. Gronig. "Instrumentation Techniques of the Aachen Shock Tunnel TH2". In: *ICIASF '95 Record. International Congress on Instrumentation in Aerospace Simulation Facilities*. Institute of Electrical and Electronics Engineers (IEEE), Nov. 2002, pp. 1–116. DOI: 10.1109/iciasf.1995.519106.

[129] Yuan Qing Liu, Pei Xue Jiang, Yan Bin Xiong, and Yang Ping Wang. "Experimental and numerical investigation of transpiration cooling for sintered porous flat plates". In: *Applied Thermal Engineering* 50.1 (Jan. 2013), pp. 997–1007. DOI: 10.1016/J.APPLTHERMALENG.2012.08.028.

[130] Sven Schweikert, Jens Von Wolfersdorf, Markus Selzer, and Hermann Hald. "Experimental Investigation on Velocity and Temperature Distributions of Turbulent Cross Flows over Transpiration Cooled C/C-Wall Segments". In: *5th European Conference for Aeronautics and Space Sciences (EUCASS)*. 2013.

[131] D. L. Schultz and T. V. Jones. "Heat-Transfer Measurements In Short-Duration Hypersonic Facilities". In: *AGARDograph No.165* (1973).

[132] H. Ozawa, S. J. Laurence, J. Martinez Schramm, A. Wagner, and K. Hannemann. "Fast-response temperature-sensitive-paint measurements on a hypersonic transition cone". In: *Experiments in Fluids* 56.1 (Nov. 2015), pp. 1–13. DOI: 10.1007/S00348-014-1853-Y/FIGURES/19.

[133] Walter H. Beck, Christian Klein, Ulrich Henne, Werner Sachs, Jan Martinez Schramm, Alexander Wagner, Klaus Hannemann, Thomas Gawehn, and Ali Gülhan. "Application of temperature and pressure sensitive paints to DLR hypersonic facilities: "Lessons learned"". In: *53rd AIAA Aerospace Sciences Meeting*. American Institute of Aeronautics and Astronautics Inc, AIAA, 2015. DOI: 10.2514/6.2015-0023.

[134] Jan Martinez Schramm, Frank Edzards, and Klaus Hannemann. "Calibration of fast-response temperature sensitive paints for their application in hypersonic high enthalpy flows". In: *Notes on Numerical Fluid Mechanics and Multidisciplinary Design* 136 (2018), pp. 141–151. DOI: 10.1007/978-3-319-64519-3{_}13/FIGURES/4.

[135] Tommaso Astarita and Giovanni Maria Carlomagno. *Infrared Thermography for Thermo-Fluid-Dynamics*. Springer Berlin Heidelberg, Jan. 2013, pp. 1–224. DOI: 10.1007/978-3-642-29508-9.

[136] Ranjini Ramesh, Richard G. Morgan, and David J. Mee. "Heat Transfer Measurements in an Expansion Tube Using Infrared Thermography". In: *AIAA Journal* 60.2 (Feb. 2022), pp. 883–891. DOI: 10.2514/1.J059919.

[137] Matthew McGilvray, Luke J. Doherty, Richard G. Morgan, and David Gildfind. "T6: The Oxford University Stalker Tunnel". In: *20th AIAA International Space Planes and Hypersonic Systems and Technologies Conference*. American Institute of Aeronautics and Astronautics (AIAA), July 2015, pp. 1–11. DOI: 10.2514/6.2015-3545.

[138] Matthew McGilvray, Luke J. Doherty, Andrew J. Neely, Robert Pearce, and Peter Ireland. "The Oxford High Density Tunnel". In: *20th AIAA International Space Planes and Hypersonic Systems and Technologies Conference, 2015*. AIAA American Institute of Aeronautics and Astronautics, 2015.

[139] Mirko Zaccara, Joshua B. Edelman, and Gennaro Cardone. "A general procedure for infrared thermography heat transfer measurements in hypersonic wind tunnels". In: *International Journal of Heat and Mass Transfer* 163 (Dec. 2020), p. 120419. DOI: 10.1016/J.IJHEATMASSTRANSFER.2020.120419.

[140] P. J. Schneider, R. E. Maurer, and M. G. Strapp. "Two-Dimensional Transpiration Cooling". In: *AIAA 7th Aerospace Sciences Meeting*. American Institute of Aeronautics and Astronautics (AIAA), Jan. 1969. DOI: 10.2514/6.1969-96.

[141] Gene T. Colwell and James M. Modlin. "Heat pipe and surface mass transfer cooling of hypersonic vehicle structures". In: *Journal of Thermophysics and Heat Transfer* 6.3 (May 1992), pp. 492–499. DOI: 10.2514/3.387.

[142] J M Modlin and G T Colwell. "Surface cooling of scramjet engine inlets using heat pipe, transpiration, and film cooling". In: *Journal of Thermophysics and Heat Transfer* 6.3 (1992), pp. 500–504. DOI: 10.2514/3.388.

[143] Christian Dittert, Hannah Böhrk, and Hendrik Weihs. "Wall thickness optimization of a transpiration-cooled sharp leading edge at atmospheric re-entry". In: *5th International Conference on Porous Media and its Applications in Science and Engineering*. Kona, Hawaii: Engineering Conferences International, June 2014.

[144] Ko L. W., Quinn R. D., and Gong L. "Finite-Element Reentry Heat-Transfer Analysis of Space Shuttle Orbiter". In: *NASA TP 2657* (1986).

[145] J Steelant, M Dalenbring, and G Wang. "The Thermal and Structural Paradox for Hypersonic Cruisers". In: *Proceedings of the 8th European Symposium on Aerothermodynamics for Space Vehicles* 1 (2015).

[146] Barry Edney. *Anomalous Heat Transfer and Pressure Distributions on Blunt Bodies at Hypersonic Speeds in the Presence of an Impinging Shock.* Tech. rep. 1968. DOI: https://doi.org/10.2172/4480948.

[147] Thomas J.R. Hughes. "Unconditionally stable algorithms for nonlinear heat conduction". In: *Computer Methods in Applied Mechanics and Engineering* 10.2 (1977), pp. 135–139. DOI: 10.1016/0045-7825(77)90001-9.

[148] COMSOL AB. *COMSOL Multiphysics®*. Stockholm, Sweden. URL: www.comsol.com (visited on 12/03/2022).

[149] Lester Lees. "Laminar Heat Transfer Over Blunt-Nosed Bodies at Hypersonic Flight Speeds". In: *Journal of Jet Propulsion* 26.4 (Sept. 1956), pp. 259–269. DOI: 10.2514/8.6977.

[150] R. Feldhuhn. "Heat transfer from a turbulent boundary layer on a porous hemisphere". In: *AIAA 14th Aerospace Sciences Meeting*. American Institute of Aeronautics and Astronautics (AIAA), Jan. 1976. DOI: 10.2514/6.1976-119.

[151] G.E. Kaattari. "The Effect of Simulated Ablation-Gas Injection on the Shock Layer of Blunt Bodies at Mach Numbers of 3 and 5". In: *NASA TN D-2954* (1965).

[152] Marc Ewenz Rocher, Tobias Hermann, Matthew McGilvray, Hassan Saad Ifti, Joao Vieira, Chris Hambidge, Mark Kenneth Quinn, Madeleine Grossman, and Luc Vandeperre. "Pressure-sensitive paint diagnostic to measure species concentration on transpiration-cooled walls". In: *Experiments in Fluids* 63.1 (Jan. 2022), pp. 1–11. DOI: 10.1007/S00348-021-03355-9/FIGURES/15.

[153] Pertti Auerkari. *Mechanical and physical properties of engineering alumina ceramics*. Tech. rep. 1996, p. 26.

[154] Marc Ewenz Rocher, Tobias Hermann, Matthew McGilvray, Madeleine Grossman, and Luc Vandeperre. "Measuring the concentration of freestream species on a hypersonic transpiration cooled stagnation point". In: *Journal of Spacecraft and Rockets* (2022).

[155] O. Rozenbaum, D. De Sousa Meneses, Y. Auger, S. Chermanne, and P. Echegut. "A spectroscopic method to measure the spectral emissivity of semi-transparent materials up to high temperature". In: *Review of Scientific Instruments* 70.10 (Sept. 1999), p. 4020. DOI: 10.1063/1.1150028.

[156] Jack Hillyer, Luke Doherty, Chris Hambidge, and Matthew McGilvray. "Extension of Test Time in Ludweig Tunnels". In: *The 2nd International Conference on Flight Vehicles, Aerothermodynamics and Re-entry Missions Engineering*. Heilbronn, 2022.

[157] T Hermann, M Mcgilvray, C Hambidge, L Doherty, and D Buttsworth. "Total Temperature Measurements in the Oxford High Density Tunnel". In: *International Conference on Flight vehicles, Aerothermodynamics and Re-entry Missions and Engineering*. Monopoli, Italy, 2019.

[158] Frederick G. Keyes. *The Heat Conductivity, Viscosity, Specific Heat and Prandtl Numbers for Thirteen Gases*. Tech. rep. 1952, pp. 1–35.

[159] William Playford. "Well-Conditioned Heat Transfer Measurements on Engine Scale Gas Turbine Rigs". PhD thesis. Cambridge: University of Cambridge, May 2018. DOI: https://doi.org/10.17863/CAM.22150.

[160] Fluke. *Emissivity compensation for Fluke Calibration 4180 Series Precision Infrared Calibrators*. Tech. rep. 2012.

[161] Hans Dieter Baehr and Karl Stephan. *Heat and Mass Transfer*. Berlin, Heidelberg: Springer Berlin Heidelberg, 2011. DOI: 10.1007/978-3-642-20021-2.

[162] M. L.G. Oldfield. "Impulse response processing of transient heat transfer gauge signals". In: *Proceedings of the ASME Turbo Expo*. Vol. 3 PART A. American Society of Mechanical Engineers Digital Collection, Sept. 2006, pp. 739–750. DOI: 10.1115/GT2006-90949.

[163] R.J. Gollan and P.A. Jacobs. "About the formulation, verification and validation of the hypersonic flow solver Eilmer". In: *International Journal for Numerical Methods in Fluids* 73.1 (Sept. 2013), pp. 19–57. DOI: 10.1002/FLD.3790.

[164] Peter Jacobs and Rowan Gollan. "Implementation of a Compressible-Flow Simulation Code in the D Programming Language". In: *Applied Mechanics and Materials* 846 (July 2016), pp. 54–60. DOI: 10.4028/WWW.SCIENTIFIC.NET/AMM.846.54.

[165] Marc Ewenz Rocher, Tobias Hermann, Matthew McGilvray, and Rowan Gollan. "Correlation for Species Concentration on a Hypersonic Stagnation Point with Mass Injection". In: *AIAA Journal* (Jan. 2022), pp. 1–12. DOI: 10.2514/1.J061159.

[166] Periklis Papadopoulos, Ethiraj Venkatapathy, Dinesh Prabhu, Mark P. Loomis, and Dave Olynick. "Current grid-generation strategies and future requirements in hypersonic vehicle design, analysis and testing". In: *Applied Mathematical Modelling* 23.9 (Sept. 1999), pp. 705–735. DOI: 10.1016/S0307-904X(99)00007-4.

[167] Hugh W. Coleman and W. Glenn Steele. *Experimentation, Validation, and Uncertainty Analysis for Engineers: Third Edition*. Hoboken, NJ, USA: John Wiley and Sons, July 2009, pp. 1–317. DOI: 10.1002/9780470485682.

[168] Daniel Prokein, Jens von Wolfersdorf, Christian Dittert, and Hannah Böhrk. "Transpiration cooling experiments on a CMC wall segment in a supersonic hot gas channel". In: *2018 International Energy Conversion Engineering Conference* (2018). DOI: 10.2514/6.2018-4696.

[169] C. Falsetti, M. Sisti, and P. F. Beard. "Infrared thermography and calibration techniques for gas turbine applications: A review". In: *Infrared Physics and Technology* 113 (Mar. 2021), p. 103574. DOI: 10.1016/j.infrared.2020.103574.

[170] Sebastien Wylie, Luke Doherty, and Matthew McGilvray. "Commissioning of the oxford high density tunnel (HDT) for boundary layer stability measurements at mach 7". In: *2018 Fluid Dynamics Conference* (2018). DOI: 10.2514/6.2018-3074.

[171] E. R. G. Eckert. "Engineering Relations for Heat Transfer and Friction in High-Velocity Laminar and Turbulent Boundary-Layer Flow Over Surfaces With Constant Pressure and Temperature". In: *Journal of Fluids Engineering* 78.6 (1956), pp. 1273–1283. DOI: 10.1115/1.4014011.

[172] Hermann Schlichting and Klaus Gersten. "Boundary-Layer Theory". In: *Boundary-Layer Theory* (Oct. 2016), pp. 1–799. DOI: 10.1007/978-3-662-52919-5/COVER.

[173] Hassan Saad Ifti. "Transpiration Cooling of a Hypersonic Vehicle". PhD thesis. University of Oxford, 2021.

[174] C.C Pappas and Arthur F Okuno. "The Relation between Skin Friction and Heat Transfer for the Compressible Turbulent Boundary Layer with Gas Injection". In: *NASA TN D-2957* (1965), p. 32.

[175] Doyle Knight and Mahsa Mortazavi. "Hypersonic shock wave transitional boundary layer interactions - A review". In: *Acta Astronautica* 151 (Oct. 2018), pp. 296–317. DOI: 10.1016/J.ACTAASTRO.2018.06.019.

[176] Gaetano M. D. Currao, Rishabh Choudhury, Sudhir L. Gai, Andrew J. Neely, and David R. Buttsworth. "Hypersonic Transitional Shock-Wave–Boundary-Layer Interaction on a Flat Plate". In: *AIAA Journal* 58.2 (Feb. 2020), pp. 814–829. DOI: 10.2514/1.J058718.

[177] F. Hung and D. Barnett. "Shockwave-boundary layer interference heating analysis". In: *AIAA 11th Aerospace Sciences Meeting*. American Institute of Aeronautics and Astronautics (AIAA), Jan. 1973. DOI: 10.2514/6.1973-237.

[178] J. Lunte and E. Schülein. "Heat transfer amplification in transitional shock-wave/boundary-layer interactions". In: *AIAA Aviation 2019 Forum* (2019), pp. 1–20. DOI: 10.2514/6.2019-3440.

[179] N. D. Sandham, E. Schülein, A. Wagner, S. Willems, and J. Steelant. "Transitional shock-wave/boundary-layer interactions in hypersonic flow". In: *Journal of Fluid Mechanics* 752 (Aug. 2014), pp. 349–382. DOI: 10.1017/JFM.2014.333.

[180] Erich Schülein. "Skin Friction and Heat Flux Measurements in Shock/Boundary Layer Interaction Flows". In: *AIAA Journal* 44.8 (May 2006), pp. 1732–1741. DOI: 10.2514/1.15110.

[181] K. S. Heffner, A. Chpoun, and J. C. Lengrand. "Experimental study of transitional axisymmetric shock-boundary layer interactions at Mach 5". In: *AIAA 23rd Fluid Dynamics, Plasmadynamics, and Lasers Conference, 1993* (1993). DOI: 10.2514/6.1993-3131.

[182] Jie Ren and Song Fu. "Secondary instabilities of Görtler vortices in high-speed boundary layer flows". In: *Journal of Fluid Mechanics* 781 (2015), pp. 388–421. DOI: 10.1017/JFM.2015.490.

[183] Daniel Arnal and Jean Délery. "Laminar-Turbulent Transition and Shock Wave/Boundary Layer Interaction". In: *RTO-EN-AVT-116 — Critical Technologies for Hypersonic Vehicle Development*. 2004, pp. 1–46.

[184] Jr. Gaver Donald P. "Observing Stochastic Processes, and Approximate Transform Inversion". In: *Operations Research* 14.3 (June 1966), pp. 444–459. DOI: 10.1287/OPRE.14.3.444.

[185] H. Stehfest. "Algorithm 368: Numerical inversion of Laplace transforms [D5]". In: *Communications of the ACM* 13.1 (1970), pp. 47–49. DOI: 10.1145/361953.361969.

[186] James Vere Beck. "Inverse heat conduction : ill-posed problems / James V. Beck, Ben Blackwell, Charles R. St. Clair, Jr." In: *Inverse heat conduction : ill-posed problems* (1985).

[187] Keith A. Woodbury and Sunil K. Thakur. "Redundant data and future times in the inverse heat conduction problem". In: *Inverse Problems in Engineering* 2.4 (July 2007), pp. 319–333. DOI: 10.1080/174159796088027610.

[188] James V. Beck. "Nonlinear estimation applied to the nonlinear inverse heat conduction problem". In: *International Journal of Heat and Mass Transfer* 13.4 (Apr. 1970), pp. 703–716. DOI: 10.1016/0017-9310(70)90044-X.

[189] Telops. *High-Performance FAST Cameras*. URL: https://www.telops.com/products/high-performance-fast-cameras/ (visited on 12/03/2022).

[190] Thorlabs. *Sapphire Windows*. URL: https://www.thorlabs.com/NewGroupPage9.cfm?ObjectGroup_ID=3982 (visited on 12/03/2022).

[191] Knoght Optical. *ZnSe/ZnS Windows*. URL: https://www.knightoptical.com/stock/default/windows-and-diffusers/ir-windows/znse-zns-windows.html (visited on 12/03/2022).

[192] Knight Optical. *Germanium Windows*. URL: https://www.knightoptical.com/stock/default/windows-and-diffusers/ir-windows/germanium-windows.html (visited on 12/03/2022).

[193] Gary J. Hawkins and Thomine Stolberg-Rohr. "Spectral design of temperature-invariant narrow bandpass filters for the mid-infrared". In: *Optics Express, Vol. 23, Issue 1, pp. 580-596* 23.1 (Jan. 2015), pp. 580–596. DOI: 10.1364/OE.23.000580.

[194] B. Rousseau, J. F. Brun, D. De Sousa Meneses, and P. Echegut. "Temperature Measurement: Christiansen Wavelength and Blackbody Reference". In: *International Journal of Thermophysics 2005 26:4* 26.4 (July 2005), pp. 1277–1286. DOI: 10.1007/S10765-005-6726-4.

[195] H. Tanaka, S. Sawai, K. Morimoto, and K. Hisano. "Measurement of Spectral Emissivity and Thermal Conductivity of Zirconia by Thermal Radiation Calorimetry". In: *Journal of Thermal Analysis and Calorimetry 2001 64:3* 64.3 (2001), pp. 867–872. DOI: 10.1023/A:1011538022439.

[196] 450000E Avionics Department Code. *Electronic Warfare and Radar Systems Engineering Handbook*. 4th. 2013. URL: https://apps.dtic.mil/sti/citations/ADA617071.